Aerodynamic shape optimisation of conceptual over-body designs for heavy goods vehicles

By

Haithem Hadi Aburebaiya

The University of Leeds

School of Mechanical Engineering

October 2020

The candidate confirms that the work submitted is his own. No publications have been written to date therefore the contribution of other authors is not relevant to other publications. The candidate confirms that appropriate credit has been given within the thesis where reference has been made to the work of others. This copy has been supplied on the understanding that it is copyright material and that no quotation from the thesis may be published without proper acknowledgement.

This work is dedicated to:

My beloved parents

My beloved wife, sons and daughters

My beloved brothers and sisters;

My friends who encourage and support me, especially,

Acknowledgements

All the praises be to Allah, the Most Beneficent, the Most Merciful.

I would first like to thank sponsor the Libyan government. I would also like to express my grateful to my supervisors Dr Andrew Shires, Dr Carl Gilkeson and Dr Greg de Boer.

Abstract

Heavy goods vehicles (HGVs) are extensively used in the UK transport sector, and an ever-increasing volume of traffic on the roads has led to an increase in total fuel consumption. Over the years, different strategies have been employed in the design of HGVs including shape changes or use of add-on devices at various positions. More recently, a popular option has been to change the traditional rectangular longitudinal sectional shape of typical HGVs and to modify the over-body shape with curvature. However, there is no clear guidance on how to do this effectively and the variety of approaches seen on the roads suggests that there are no universally accepted design rules. Furthermore, most aerodynamics studies in the literature focus primarily on minimising drag; far too little attention has been paid to enhance stability, handling and safety operation due to shape changes, especially due to side winds or gusts. The purpose of this work is to address these issues using Computational Fluid Dynamics (CFD) simulations with aerodynamic shape optimisation.

A simplified generic HGV, the Ground Transportation System (GTS), is investigated in this thesis because it closely resembles a typical European HGV and there is an abundance of high-quality experimental data available. A rigorous verification and validation study using the commercial CFD package, ANSYS Fluent, found agreement to within 15% between experiments and the numerical results. Following this, an aerodynamic shape optimisation study was formulated. The shape of the over-body profile was parameterised using a 3rd order polynomial with three design variables determining the shape of the vehicle, namely, the height of the base region, the angle of the trailing edge of the roof and the radius of curvature of the longitudinal roof edges. Using a 125-point Design of Experiments (DoE) approach, high-fidelity CFD simulations were carried out for yaw angles of 0°, 5°, 6° and 8°. These angles were determined from analysis of a typical Leeds-London-Leeds motorway journey.

Moving Least Squares (MLS) metamodels were used in conjunction with Genetic Algorithms (GAs) and gradient-based techniques to identify optimum HGV designs. Results show that a minimum-drag design can accomplish drag reduction of around 40% compared to a baseline (rectangular) vehicle, however, weathercock stability is 11% poorer at a slip angle of 5° increasing to 35%, at 8°. The best stability design was found to achieve a 33% drag improvement, compared to the baseline and weathercock stability is between 8% and 25% worse, for 5° and 8° of yaw, respectively. However, the reduction in weathercock stability, compared to the baseline design, naturally leads to better directional stability and road holding capability. The height of the base of the vehicle is the dominant design parameter with small values leading to improved drag but large values inducing greater weathercock stability due to increased rear side area. From this, design guidelines are proposed.

Table of Contents

List of Figures

List of Tables

Nomenclature

Symbol	**Quantity**	**SI Unit**
c_p	specific heat capacity	J kg^{-1}K^{-1}
$\dot{m}$	mass flowrate	kg s^{-1}
A	area	m^2
L	length	m
T	temperature	K or °C
t	thickness	m
V	total velocity vector	m s^{-1}
c	specific heat capacity	J kg^{-1} K^{-1}
k	thermal conductivity	W m^{-1} K^{-1}
l	turbulence length scale	m
u	velocity component in x-direction	m s^{-1}
v	velocity component in y-direction	m s^{-1}
w	velocity component in z-direction	m s^{-1}
C_D	Drag Coefficient	
C_L	Lift Coefficient	
C_M	Moment Coefficient	
C_p	Pressure Coefficient	
p	Pressure	Pa
Re	Reynolds number	
U_∞	Free stream wind velocity	m s^{-1}
$y+$	Nondimensional cell wall distance	

Greek symbols

σ	Stefan-Boltzmann constant (5.67×10^{-8})	W m^{-2} K^{-4}
β	slip angle	Rad or degree
μ	dynamic viscosity	kg m^{-1} s^{-1}
ρ	density	kg m^{-3}
ν	kinematic viscosity	m^2 s^{-1}
σ	Stefan-Boltzmann constant (5.67×10^{-8})	W m^{-2} K^{-4}
ρ	density	kg m^{-3}

Abbreviations

CFD	computational fluid dynamics
2D	Two-dimensional
3D	Three-dimensional
DNS	Direct numerical simulation
FDM	Finite difference method
FEM	Finite element method

LES	Large Eddy Simulation
NACA	National advisory committee for aeronautics
RANS	Reynolds Averaged Navier-Stokes
SA	Spalart-Allmaras
SIMPLE	Semi implicit method for pressure linked equations
SST	Shear Stress Transport

1 : Introduction

This chapter introduces the general subject area of heavy goods vehicles with an overview of their purpose, design characteristics and energy considerations. In addition, the concept of the curved over-body design is briefly described with related gaps in knowledge in the literature highlighted. This is the basis of the major research question to be addressed in the thesis as a whole which forms the aims and objectives. These and the thesis structure are described before relevant literature is explored in chapters 2 and 3.

1.1 Energy Efficiency, Transport and the Environment

In the past 20 years fuel costs have increased within the UK so the need to improve Heavy Goods Vehicle (HGV) design to decrease fuel consumption is becoming ever more crucial. The aerodynamic performance of HGV's is one of the most important considerations of vehicle design which should be improved in order to reduce the amount of fuel consumed and to realise significant reductions in greenhouse gases. For example, a tractor-trailer weighing 36 tons and moving at a speed of 105 km/h consumes about 21% of its fuel due to aerodynamic losses, with 60% attributable to thermal efficiency of the engine, 13% due to rolling resistance and other losses representing 6% (Choi et al., 2014).

Many research studies have investigated the aerodynamic performance of HGVs with a focus on the structure of the flow field to explain the mechanisms which generate the aerodynamic forces, especially drag (Choi et al., 2014). These are very important to allow substantial reductions in aerodynamic drag, to save energy and decrease fuel consumption. As an illustration, in the example above it is feasible to save about 4% in fuel if aerodynamic drag can be reduced by 20% (Choi et al., 2014). Although such reductions may seem ambitious, it is clear that design improvements will have a beneficial impact both economically and environmentally.

In 2018, transport in the UK accounted for 27% of all carbon dioxide emissions which was equivalent to 121.4 million tonnes (Mt)(Penistone, 2019). This was greater than the second largest sector, energy supply (24%). Fig. 1.1 shows the breakdown of the major sources of total UK greenhouse gas emissions in 2017.

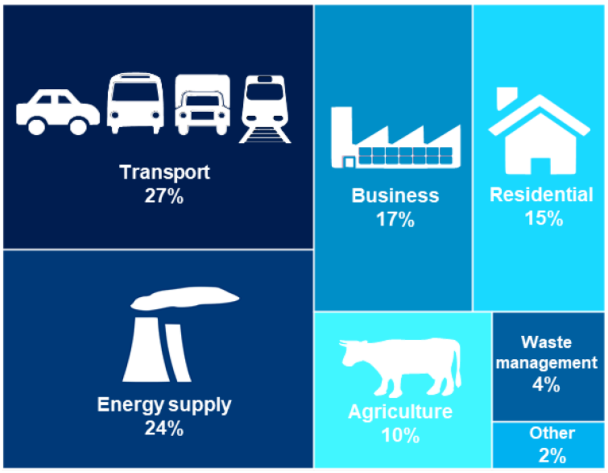

Fig. 1.1. Domestic Road Freight Statistics, United Kingdom 2017 (Penistone, 2018).

In 2018, UK net emissions of CO_2 were provisionally estimated to be 364.1 Mt, 2.4% lower than the 2017 figure of 373.2 Mt. An important point is that CO_2 is the most abundant greenhouse gas, accounting for 81% of total UK greenhouse gas emissions. Observing the trends over a long period, provisional estimates suggest that in 2018, total UK greenhouse gas emissions were 43.5% lower than in 1990 and 2.5% lower than 2017. This shows the long-term benefits of reducing emissions across all sectors with advances in understanding and technology. These trends are clearer in Fig. 1.2 and it is encouraging to see that the rate of decrease in emissions is greater in the last decade in particular.

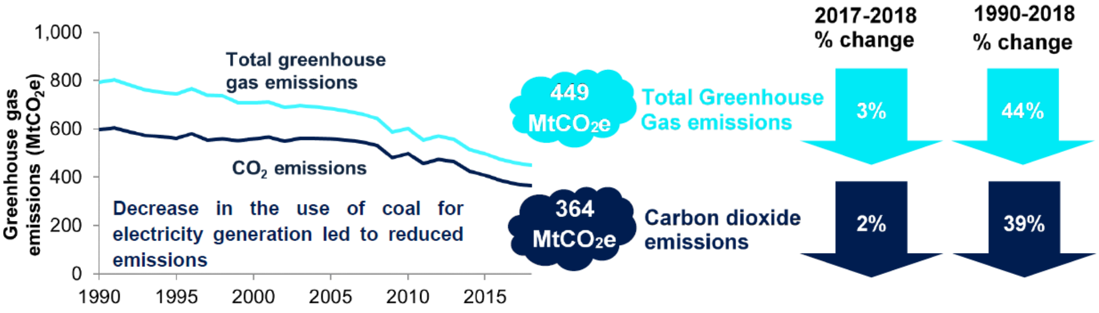

Fig. 1.2. Illustration of the reduction on energy demand in the UK, since 1990 (Penistone, 2019).

Despite the overall improvement, the actual reduction in transport emissions is comparatively modest with energy reduction in this sector of only 3.2% in 2018, compared to 1990. The largest reductions since 1990 are due to efficiency improvements in the business, public and energy sectors, see Fig. 1.3. The vast majority of emissions from transport are due to road transport; rail contributes comparatively little. Nevertheless, the 3.2% decrease in transport CO_2 emissions from 1990 to 2018 has been achieved by improvements in fuel efficiency of modern vehicles and lower traffic growth as a result of a dip following the 2008/2009 recession.

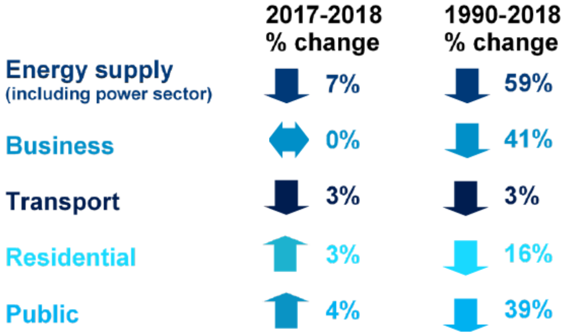

For the sectors not included here, provisional CO_2 estimates for 2018 cannot be made as they cannot be derived from the energy statistics. Final 2018 estimates for all sectors will be published in February 2020, which will include total emissions by sector.

Fig. 1.3. Comparison of the change in energy consumption in five sectors in the UK over two time periods (Penistone, 2019).

Looking to the future, the UK has domestic targets for reducing greenhouse gas emissions under the Climate Change Act 2008, which established a long-term legally-binding framework to reduce greenhouse gas emissions, committing the UK to reducing emissions by at least 80 per cent below 1990 baselines by 2050, with an interim target to reduce greenhouse gas emissions by at least 34 per cent compared to the 1990 baseline by 2020. Therefore, in the context of this thesis, identifying design improvements to reduce transport emissions is relevant to the UK government's vision for drastically reducing energy.

1.2 **Heavy Goods Vehicles**

HGV's are extensively used in the UK transport sector. The number of HGVs in the UK freight sector was approximately 2.6 million in 2018, contributing £12 billion to the UK economy in 2017 as the Annual Business Survey showed (DfT, 2019). Fig. 1.4 shows some key figures resulting from the UK freight sector based on Domestic Road Freight Statistics (DfT, 2019). It can be seen that in the UK, in 2018, goods lifted, goods moved and vehicle kilometres travelled by HGV's increased by 1%, 3% and 1%, respectively, compared to 2017. In terms of raw figures, 1.41 billion tonnes of goods were lifted on journeys covering 18.7 billion vehicle kilometres.

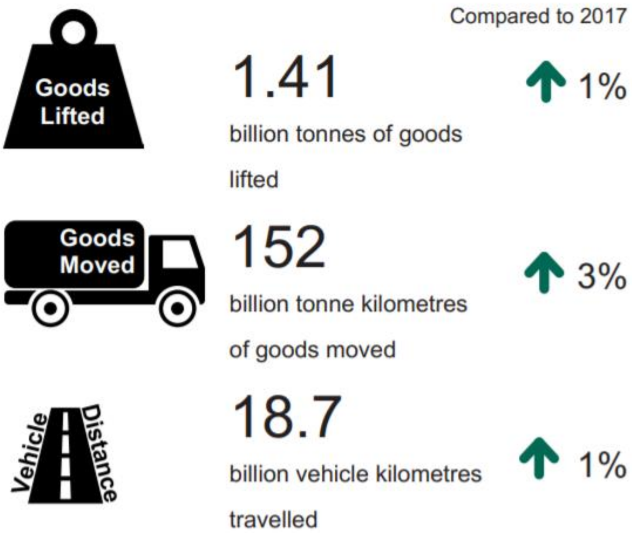

Fig. 1.4. Domestic Road Freight Statistics, United Kingdom 2018 (DfT, 2019).

Considering the overall design philosophy of HGV's, Fig. 1.5 shows the difference in appearance between typical European and American HGV's. It can be seen that there is a difference in the shape of the tractor unit which pulls the trailer behind it; American trucks have a longer tractor unit with the engine situated at the front, whereas European semi-trucks have a more compact bluff shape. The main reason for this difference is that HGV lengths are strictly regulated in Europe, therefore, the cabin is situated above the engine for European designs. The cab-over-engine trucks are easier to handle as well. As can be seen in Fig. 1.5, the trailer units of European HGV's have a cuboid shape.

Fig. 1.5. Images showing typical (a) European and (b) American HGV's(NODUM, 2018)

The length restrictions in the US are less demanding and so “conventional” HGV’s there have a cabin behind the engine, making the vehicle longer than cab-over-engine designs. A major advantage of a conventional cab design is that the truck can be more comfortable to drive because of the increase in the size of the cabin. Furthermore, the engine and drivetrain is easier to service and maintain from better accessibility. However, traditional European HGV’s must be used in the UK.

1.3 Size and Weight Limits of UK HGV’s

HGVs in the UK range from a gross vehicle weight of 3.5 tonnes to 44 tonnes, with articulated vehicles (which tend to be longer, larger, heavier vehicles) carrying more freight. In 2018, articulated vehicles carried 889 million tonnes (63%) of freight, whereas rigid vehicles only carried 517 million tonnes (37%) of freight (Table 1.1). Fig. 1.6 shows the main difference between these two vehicle types. In terms of size, typical articulated HGV’s are 16.5m in length, 2.55m in width and there is a maximum height of 4.95m. Different classifications exist for vehicle length, see Table 1.1.

Table 1.1.Current UK limits lorry sizes and weights (Butcher, 2009).

weight	44 tonnes for lorries with 6 axles 40 tonnes for lorries with 5 axles
length	12 metres for a rigid vehicle 16.5 metres for an articulated vehicle 18.75 metres for a road train (a combination of a lorry and a trailer)
width	2.55 metres excluding driving mirrors
height	no limit, but wherever possible a maximum of 4.95 metres should be adhered to in order to make maximum use of the motorway and trunk road network

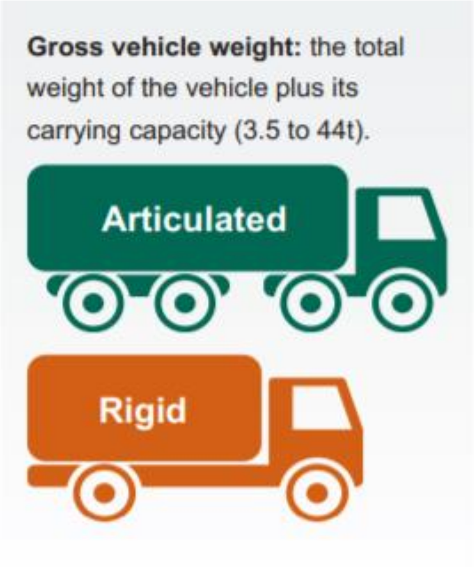

Fig. 1.6. Types of HGVs in the UK (DfT, 2019)

1.4 Purpose of the work

In the last 10 years, roof curvature has been used extensively in practice for HGVs on the UK road network. However, the wind tunnel testing of (Holt et al., 2015) is, to the author's knowledge, the only known example in the literature of a systematic investigation of roof curvature for bluff road vehicles. Despite the large number of different curved roof shapes seen on HGV's in the UK in recent years, there is no clear indication of which design may offer the best results to a generic HGV. A visual survey of HGV road traffic currently travelling on UK roads does suggest that vast improvements can be realised, especially with respect to the over-body shape.

Fig. 1.7. Examples of HGVs with a traditional rectangular shape (De Boer et al., 2016).

Fig. 1.8. Examples of curved roof HGVs (Cooper, 2004) (De Boer et al., 2016).

Fig. 1.7 shows some examples of typical UK HGVs with flat roof sections, whereas Fig. 1.8 illustrates some relatively new designs from the past 10 years; the exception is the image of the Labatt's streamliner from 1947 (Cooper, 2004) in the top right of Fig. 1.8. In all of these designs, the objective is to reduce aerodynamic drag. In addition to roof curvature, historically, different strategies have been used to reduce drag on bluff vehicles such as add-on devices including cab roof fairings, (Malviya et al., 2009) and on various positions in the vehicle (Wong and Mair, 1983, Choi et al., 2014). A thorough review of this literature is provided later (chapter 3), however, it is worthwhile stating here that add-on devices may lead to greater instability due to greater side area; far too little attention has been paid to enhance stability, handling and safety operation of HGVs especially, under challenging conditions such gusts and side winds. Historically, many drag reduction studies focus mainly on zero yaw conditions (Ortega and Salari, 2004).

1.5 Scope of Research

The main focus of this PhD is to explore HGV roof curvature using aerodynamic shape optimisation. The purpose will be to minimise aerodynamic drag without negatively impacting the static stability in yaw. The impact of dynamic stability would require the use of transient simulations which is beyond the scope of this work, therefore only static stability will be considered. The overall aim is to produce design guidance for HGV over-body design which may be useful for legislators and vehicle manufacturers/operators. This aim will be achieved by addressing the following objectives:

1. Understand the fundamentals of fluid mechanics, bluff-body aerodynamics and stability considerations for HGVs.
2. Determine the range of typical wind angles for a motorway journey from Leeds to London and back, which is one of the major HGV hauling routes in the UK.
3. Develop a validated CFD simulation approach to accurately determine aerodynamic parameters including forces and moments so that energy efficiency and stability can be evaluated.
4. Explore potential design parameters which can positively influence the aerodynamic behaviour of HGVs
5. Formulate a design optimisation problem, with design objectives of minimising drag and maximising stability, to explore the best design directions for HGVs with a particular focus on curved roof sections.

6. Determine the best design compromises for optimal energy consumption and stability considerations to produce design guidance which informs manufacturers, operators and legislators of better potential design characteristics.

1.6 Thesis structure

Chapter 2 reviews basic principles of fluid mechanics and Computational Fluid Dynamics (CFD) which are relevant to the subject area. In Chapter 3, a detailed review of bluff body aerodynamics is presented with a focus on past drag reduction strategies. This chapter concludes with a summary of the main gaps in knowledge which will be addressed in subsequent chapters. Chapter 4 presents a detailed validation and verification exercise on relevant HGV shapes to develop a suitable numerical method which can determine aerodynamic characteristics. In Chapter 5, some analysis of a typical Leeds-London motorway route is presented to identify the range of yaw angles experienced by an HGV on a typical haulage route, with prevailing wind conditions. Suitable HGV shape parameters are also evaluated with some preliminary 2D and 3D analyses. Chapter 6 presents a rigorous design optimisation method which is used to optimise a typical HGV in various wind conditions; these results are used to provide design guidance. Finally, the discussion and conclusions, Chapter 7, focus on the key outcomes of this research with suggestions for future work.

Chapter 2 : Review of Fluid Mechanics, CFD, Stability of Heavy Goods Vehicles and Optimisation

In this chapter the fundamentals of fluid mechanics and Computational Fluid Dynamics (CFD) relevant to road vehicles are discussed. These concepts form the basis of the work carried out in later chapters. Road vehicle aerodynamics and stability are also considered in this chapter as a precursor to a more detailed review of bluff body aerodynamics, including HGVs, in chapter 3. Design optimisation is also briefly described.

2.1 Reynolds Number and Flow Regimes

The Reynolds number is a dimensionless parameter which is very important in fluid mechanics, given by:

$$Re = \frac{\rho V l}{\mu} \tag{2.1}$$

where ρ,V, l and μ are the fluid density (kg/m^3), velocity (m/s), characteristic length (m) and the viscosity (kg/m-s) respectively (Fox et al., 2010, Moran et al., 2003). The flow is classified into laminar or turbulent depending on the Reynolds number, *Re*. A low value of *Re* means laminar flow, high means the flow regime is turbulent and there is a transition between the two, for example in the case of a flow in a pipe, the flow is laminar when the Reynolds Number is less than 2100 and it is turbulent when the Reynolds Number is greater than 4000. In a laminar flow, the paths of moving fluid particles are parallel and they do not cross each other. However, in a turbulent flow, the particles move in a churned up, chaotic manner without a clear structure, see Fig. 2.2 (Fox et al., 2010, Moran et al., 2003, Anderson, 2011). The features of a given flow structure around a body are dependent on and change dramatically with different Reynolds numbers. In aerodynamic investigations scale models can be used instead of full-scale objects, provided that the Reynolds numbers are similar and in the same flow regime e.g. turbulent. Often, increasing the free-stream velocity is required to fulfil this requirement to ensure the condition of dynamic similarity is met, especially when using scale models smaller than the original (Hucho, 1986). In road vehicle aerodynamics the Reynolds number is usually high enough that the flow field is assumed to be turbulent.

2.2 **Mach number, Compressible and Incompressible flow**

The Mach number is a dimensionless parameter which is very important in fluid mechanics (especially in gases such as air) which is used to distinguish if the flow is compressible or incompressible. It is given by:

$$M = \frac{V}{C} \tag{2.2}$$

Where V and c are the velocity (m/s) and to the local speed of sound, c (m/s), in the gas, respectively (Fox et al., 2010, Moran et al., 2003). The flow is considered incompressible when the density of the fluid changes by less than 5%, whereas the flow is classified as compressible when density changes of more than 5% are observed (Anderson, 2011). When dealing with incompressible flows, these are easier to model numerically whereas simulations of compressible flow are more challenging due to additional flow physics such as the appearance of shock and expansion waves. Fortunately, in analysing the aerodynamics of a typical road vehicle such as an HGV, the flow speeds are low enough to be considered incompressible because they are far less than the speed of sound, c, and below the threshold of compressibility i.e. M < 0.3. Therefore, the flow fields analysed in this thesis will be based on the incompressible assumption.

2.3 **Pressure Coefficient**

An important property of a fluid is the viscosity, which is related to internal friction between particles of a fluid (Fox et al., 2010, Moran et al., 2003) . Inviscid flow implies that no energy is dissipated through viscosity and Bernoulli's equation can be applied to reveal insights into flow physics, namely:

$$p + \frac{1}{2}\rho V^2 = \text{constant} \tag{2.3}$$

where ρ is the fluid density (kg/m^3), p is the static pressure (Pa) and V is the velocity (m/s). This equation can be applied to a simple example related to vehicle aerodynamics to provide insight into the relationship between velocity and pressure at various points along any given streamline around a vehicle. Fig. 2.1 shows the streamlines of the 2D flow around the centreline of a vehicle and the resulting pressure distribution expressed as the pressure coefficient, C_p, given by:

$$C_p = \frac{p - p_\infty}{1/_2\ \rho\, V_\infty^2} \tag{2.4}$$

where p_∞ is the free-stream static pressure (pa) and V_∞ is the free-stream velocity (m/s). From Bernoulli's equation the relationship between pressure coefficient and velocity can be expressed as:

$$C_p = 1 - \left(\frac{V}{V_\infty}\right)^2 \tag{2.5}$$

where V is the local velocity at any point on the streamline.

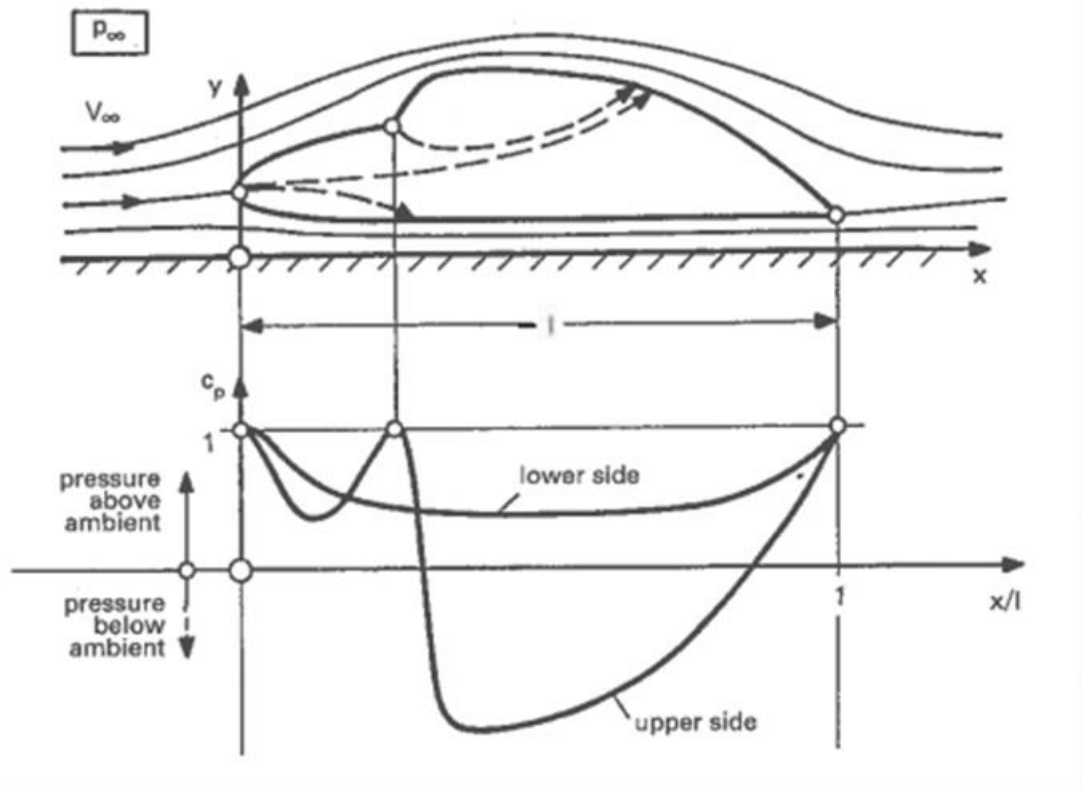

Fig. 2.1. Streamlines of the 2D flow around a body of a vehicle including the pressure distribution (Hucho, 1986).

By following the pressure distribution on the surface of the vehicle, this reveals three stagnation points: one at the nose region, one in the cover between the bonnet and windscreen and another at the trailing edge. According to Bernoulli's equation, at these three stagnation points (where the velocity is zero) the pressure coefficient has its maximum value ($C_p\ = 1$). On the lower surface of the vehicle the local velocity increases but is still lower than the free-stream velocity so the pressure is higher than the free-stream value and $C_p > 0$. On the other hand, in the case of very small ground clearances (with a smooth underbody), the velocity can increase dramatically which reduces pressure until it may reach a level which is even lower than the free stream pressure, where $C_p < 0$. This scenario normally only applies to racing car aerodynamics.

Following the upper surface contour of the vehicle, positive pressure coefficients extend from the stagnation point all the way to the windscreen, before local acceleration over the roof leads to low pressures, where $C_p < 0$. Moving downstream, at the trailing edge of the roof the pressure returns to the stagnation value i.e. $C_p = 1$. At this point there are considerable differences between the idealised non-viscous representation of a fluid and real, viscous fluids; in practice, stagnation at the rear of the vehicle is impossible due to viscous drag contributions. For the inviscid case shown in Fig. 2.1, the net drag force is equal to zero as with all cases of incompressible, inviscid, two-dimensional flows; this is widely known in fluid mechanics as D'Alembert's paradox (Scibor-Rylski, 1984, Hucho, 1986, Schuetz, 2015). Also, it is noticeable that the pressure on the lower side of the vehicle is higher than the upper side so a lift force is observed.

2.4 Effects of Viscosity

In real engineering applications, fluids have viscosity which is highly influential. Viscosity leads to friction and resistive forces inside fluids, both between the fluid particles, and in the contact area between a fluid and the surface of a submerged body. This causes velocity gradients near walls leading to boundary layers. An example of a boundary layer growing along a flat plate is shown in Fig. 2.2.

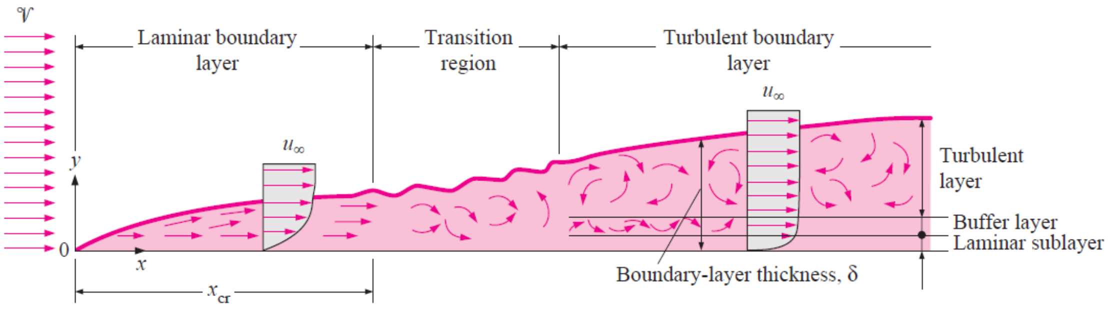

Fig. 2.2. Boundary layer velocity distribution on flat plate (Cengel et al., 1998).

The extent of the boundary layer is typically 2 or 3 mm away from the surface of a moderately sized external body, whereas it can grow to many centimeters on a large aircraft for example (Anderson, 2011). The viscous effects are concentrated within boundary layers and they are very influential with decreasing velocities from the free-stream until it is zero at the surface of the body such as an HGV, for example (Rajput, 2002). The flow within the boundary layer itself is also classified into laminar or turbulent depending on the Reynolds number of the external flow field. In viscous flow, molecular friction acts as a shear stress on the surface of the body. This tangential force is called friction drag, D_f, which is given by:

$$D_f = \oint \tau_w \cos \varphi ds \tag{2.6}$$

where τ_w is Shear stress at the surface and φ is angle between the direction of τ_w and the horizontal axis, see Fig. 2.3.

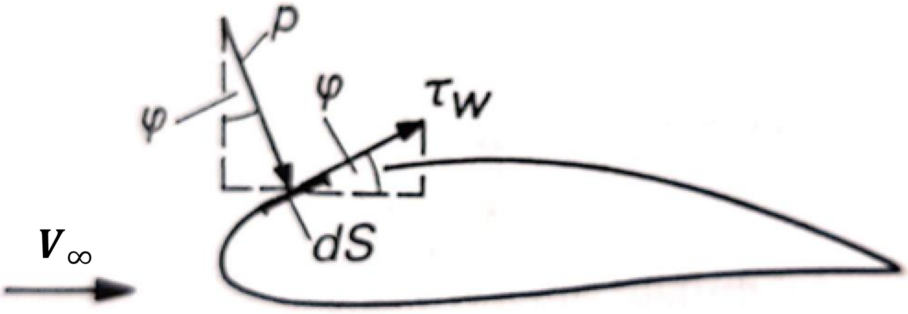

Fig. 2.3. The relation between friction drag and Shear stress, and pressure drag and pressure (Hucho, 1986).

In general, friction drag depends strongly on Reynolds number. In cases of bluff bodies it can be negligible compared to pressure drag. One of the most important phenomena related to flow around a bluff body is flow separation. When a boundary layer is subjected to a pressure gradient where pressure increases in the flow direction, the flow is retarded and in some cases it can reverse as shown in Fig. 2.4. It can be seen that the separation streamline begins at the separation point (where the velocity is zero) and it divides the boundary layer into two distinct regions. In the region above the separation streamline the flow moves forward in the free-stream direction but below the streamline the flow is reversed because the boundary layer has lost significant energy. At this separation point the velocity gradient is,

$$\left(\frac{du}{dy}\right)_w = 0 \tag{2.7}$$

where u is the local flow velocity (m/s), y is the distance away from the wall (m) and the subscript w denotes the wall condition. Usually, an adverse pressure gradient occurs when the shape of the body changes suddenly, especially in the case of blunt bodies. This can lead to the phenomena of flow separation and a wake usually forms. Related to this, drag on a bluff body experiences significant pressure drag which dominates friction drag. The resulting modification to the flow structure around such a body drives the overall pressure distribution around the body and in turn these effects generate the aerodynamic forces and moments acting on it.

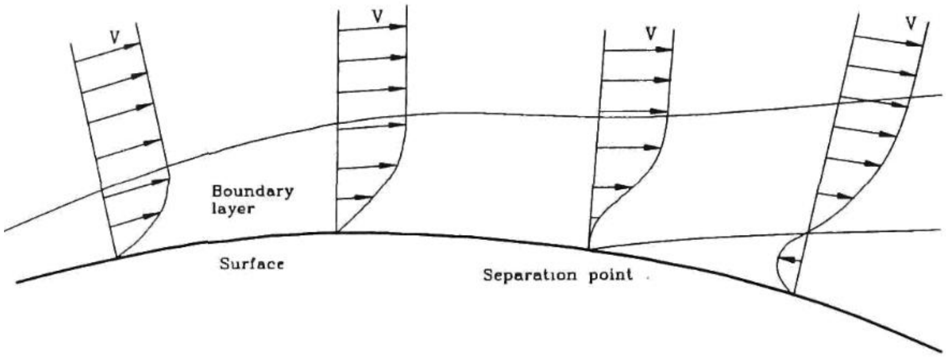

Fig. 2.4. Boundary layer and velocity distribution around the external surface of a curved body (Genta, 1997).

2.5 Steady and Unsteady Flows

Steady-state flow fields commonly occur in many applications and this applies when the fluid properties at a specific locations remain constant. However, these flow features may be changing from point to point in a given flow field. In contrast, the flow is considered to be unsteady or transient when fluid properties change as a function of time. Generally, steady-state flow occurs when boundary conditions are constant, but not always. For example, in the case of external flow past a bluff body, at certain Reynolds numbers the flow may not be steady and vortex shedding can occur, see Fig. 2.5 (Griffin, 1995).

Fig. 2.5. Experimental results showing vortex shedding behind a circular cylinder (Griffin, 1995).

In the case of HGVs, real flow fields will typically be unsteady (Cooper, 2004), however, steady-state flow fields are often computed with high accuracy using CFD (Roy et al., 2006). This will be discussed in more detail later.

2.6 Aerodynamic Drag and Flow Separation

The pressure drag is found from the integration of the forces acting over a body which results from the pressure distribution, namely:

$$D_p = \oint p \sin\varphi dS \tag{2.8}$$

For bluff bodies the pressure drag is significantly larger than the friction drag which itself occurs due to the shear stresses at the surface of the body. The total drag can be written as:

$$D = D_f + D_p \tag{2.9}$$

The total drag force can now be defined by the dimensionless drag coefficient, namely:

$$C_D = \frac{D}{\frac{\rho}{2} V_\infty^2 A} \tag{2.10}$$

where $\frac{\rho}{2} V_\infty^2$ denotes the free-stream dynamic pressure and, in the case of vehicle aerodynamics, A is the largest cross-section of the body, projected in the free-stream direction. The behavior of the drag coefficient is dependent on whether the body has sharp edges or rounded ones. Fig. 2.6 shows the drag coefficient for a circular cylinder and a flat plate which is perpendicular to the direction of a flow as a function of Reynolds number. As can be seen, in the case of bodies which have sharp edges the drag coefficient is insensitive to the Reynolds number and flow separation occurs at the sharp edges of the body. On the other hand, bodies which have slightly rounded edges show behavior in which the drag coefficient does depend on the Reynolds number, especially for high *Re*.

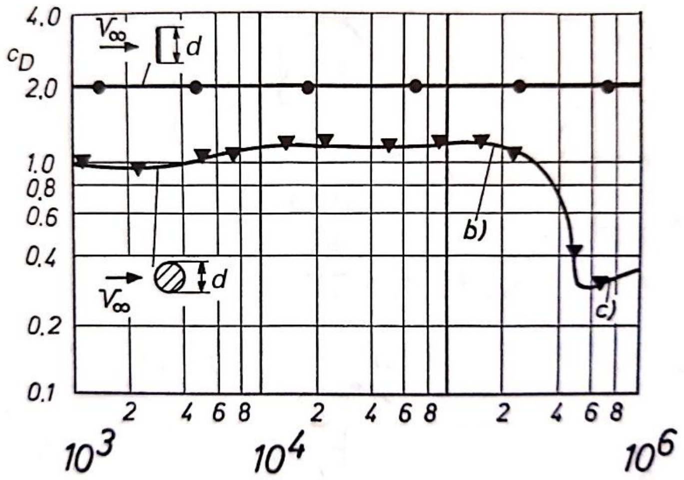

Fig. 2.6. Drag coefficients of blunt bodies (a circular cylinder and a flat plate perpendicular to the flow) as function of Reynolds number (Hucho, 1986). Points (b) and (c) relate to Fig. 2.7.

The position of where the separation occurs is dependent on whether the flow is laminar or turbulent which in turn depends on the state of the boundary layer. As can be seen in case (b) labelled in Fig. 2.6 and Fig. 2.7., when a laminar boundary layer exists (at low *Re*), the drag coefficient is high because the wake region immediately downstream of the cylinder is broad. The size of this wake region is also a result of the location of the separation points which coincide with the points of maximum thickness. In contrast, for turbulent boundary layers the drag coefficient and the size of wake region is lower because the flow remains attached for longer.

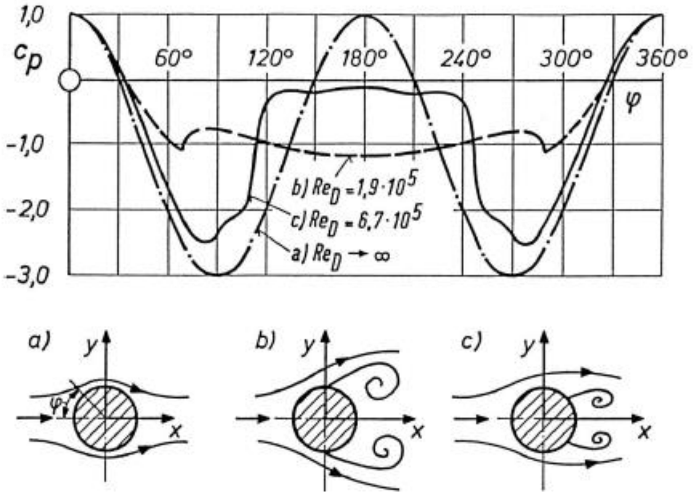

Fig. 2.7. pressure distribution and flow structure around a circular cylinder at different Reynolds numbers: (a) inviscid flow; (b)laminar flow (c) turbulent flow (Hucho and Sovran, 1993).

Extending this to vehicle aerodynamics, the state of the boundary layer has an impact on the size of the wake and thus the overall drag coefficient. Although flow separation is responsible for a large proportion of pressure drag, this phenomenon is not yet fully understood (Choi et al., 2014). There are two general types of flow separation which depend on whether the separation line is perpendicular to the flow direction or not. These are contrasted in Fig. 2.8. with the separation line occurring perpendicular to the flow direction in the wake of bluff bodies (Fig. 2.8. a) and parallel to the axes of the vortex structures which develop downstream of the leading edge of slanted bodies (Fig. 2.8. b).

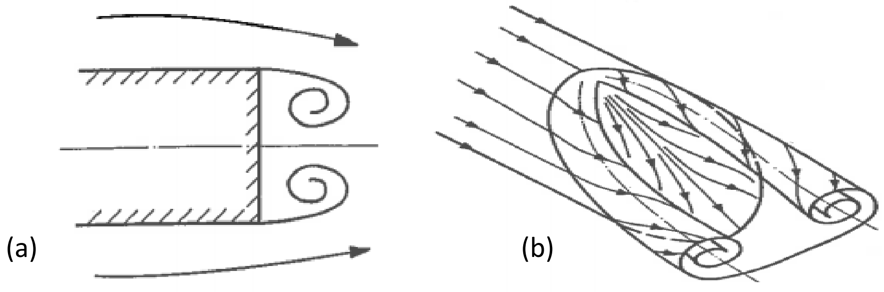

Fig. 2.8. Illustration of separation lines which are (a) normal to the direction of flow and (b) along a slanted surface for which the separation line is not perpendicular to direction of flow (Hucho and Sovran, 1993, Choi et al., 2014).

The behavior of these vortices and the flow in the separated wake region, is dependent on Reynolds the number. For low Reynolds numbers, the vortices and the flow structure in the wake region behind the bluff body are symmetrical. However, for high Reynolds numbers the phenomena of alternating periodic vortex shedding occurs from the side of the body. These vortices, known as a von Karman vortex street (Griffin, 1995), move downstream into the wake and the time-dependent nature of these means the flow will be unsteady, see Fig. 2.5. Due to periodic vortex shedding, all flow properties in the wake change periodically at a frequency, n, which is contained within a dimensionless coefficient, the Strouhal number:

$$S_t = \frac{nd}{V_\infty} \tag{2.11}$$

where d is the width of the body (m). This coefficient is a function only of the Reynolds number. This periodic flow separation and vortex shedding causes pressure loss in the wake region as a result of dissipation of the kinetic energy from the large vortices to frictional heat by strong turbulent mixing (Choi et al., 2014).

Returning to Fig. 2.8. , when the separation is inclined to the flow direction, the axes of generated vortices are roughly parallel to both the lines of separation and the direction of the flow. Therefore, the velocity component in the direction of the vortex axis cannot be neglected and steady three dimensional flow separation is present. This type of separated flow is often seen in road vehicle aerodynamics and it also contributes to greater pressure drag.

2.7 Aerodynamic Forces and Moments

Generally, bluff bodies, such as ground vehicles produce a drag force which is small at the front of the body, whereas a considerable proportion of drag force occurs at the rear part of the body. Flow separation can be minimised at the front but it is difficult to avoid this in the base region. To quote Hucho (1986) “it is not so important to find a proper shape to divide the oncoming flow but it is very important to design a rear body surface which brings the divided streamlines smoothly together”. Although streamlined bodies have favourable aerodynamic properties and they bring streamlines smoothly together to avoid flow separation, it is not practical for road vehicles, especially large bluff ones such as HGVs.

Aerodynamic flows around a given bluff body leads to three sets of forces and moments as shown in Fig. 2.9. For symmetrical oncoming flow($\beta = 0$, which is the angle between the resultant velocity vector and the direction of travel of the HGV) the drag force, D, is accompanied by a lift force, L, and a pitching moment, M. When the approaching flow has a slip angle ($\beta \neq 0$), an asymmetric flow field is produced and this leads to other forces and moments including the side force, Y, a rolling moment, R, and a yawing moment, N.

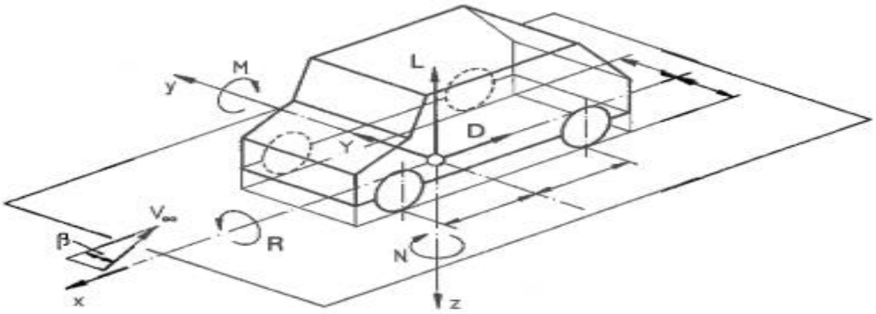

Fig. 2.9. Forces and moments acting on a vehicle (Hucho, 1986).

All of these forces and moments can be expressed as non-dimensional aerodynamic coefficients, namely:

$$c_L = \frac{L}{\frac{\rho}{2} V_\infty^2 A} \tag{2.12}$$

$$c_D = \frac{D}{\frac{\rho}{2} V_\infty^2 A} \tag{2.13}$$

$$c_M = \frac{M}{\frac{\rho}{2} V_\infty^2 A l} \tag{2.14}$$

$$c_Y = \frac{Y}{\frac{\rho}{2} V_\infty^2 A} \tag{2.15}$$

$$c_R = \frac{R}{\frac{\rho}{2} V_\infty^2 A l} \tag{2.16}$$

$$c_N = \frac{N}{\frac{\rho}{2} V_\infty^2 A l} \tag{2.17}$$

Where C_L, C_D, C_M, C_Y, C_R, and C_N are the coefficients of lift, drag, pitching moment, side force, rolling moment and yawing moment, respectively. In addition, $\frac{\rho}{2} V_\infty^2$, A and l are the free-stream dynamic pressure, the largest cross-section of the body and the length of the vehicle (or sometimes the wheelbase), respectively. They are dependent on the angle of yaw, β, and *Re* and they are also highly sensitive to the shaping of the body of the vehicle. For example, lift decreases as the ground clearance reduces due to a higher velocity on the underside surface of the vehicle. The vortices generated on slanted surfaces may also influence all three sets of forces and moments, some more so than others.

2.8 Basics of vehicle stability

As already stated, the flow around a vehicle produces three different forces and moments which has an effect on fuel consumption as well as a notable influence on vehicle stability and safety. These forces and moments affect the directional stability of road vehicles in different ways. For example, the lift force and pitching moment changes the traction of tyres due to changes in the download acting on the wheels (Scibor-Rylski, 1984, Hucho, 1986, Schuetz, 2015). In addition, when a vehicle is subject to a side wind gust, this introduces a side force, a yawing moment and rolling action. These cause a change in attitude of the vehicle impacting its direction and this invariably requires intervention from a driver to prevent course deviation (Scibor-Rylski, 1984, Hucho, 1986, Schuetz, 2015). Stability is also important when ground vehicles are travelling in the straight-ahead position, during cornering and under braking conditions. In the case of straight driving, the lift force affects wheel download at high speed. For example, a notchback car at high speed loses about 10% from its rear axle load due to increased aerodynamic lift at its rear (Scibor-Rylski, 1984, Hucho, 1986, Schuetz, 2015). In such cases, stability can be impaired because steering response of the vehicle can reduce. In general, a vehicle with no big difference in lift between rear and front axles is more stable. However, it should be noted that large vehicles such as HGVs are very unlikely to be susceptible to this issue due to their huge mass and comparatively low speed.

In the case of cornering, generally, increasing lift on the front axle makes the vehicle understeer, while increasing lift force on the rear axle makes it oversteer more. For braking manoeuvres, the behaviour of vehicles which are moving at high speed (prior to braking), is changed significantly by aerodynamic forces. The drag force can complement the braking system with resistance to motion whereas the lift force typically impairs stability by changing the download on both the front and rear axles. When a vehicle undergoes a braking manoeuvre due to front axle braking, the vehicle is still stable even though the steering ability can be lost. On the other hand, when the rear axle brakes are applied, the vehicle can become unstable, especially at high speeds. All of these elements show that aerodynamic design plays in important role in controlling the forces and moments to improve stability.

2.8.1 Lift and Pitching Moment

The shape of the front and back of ground vehicles has an important effect on stability. The front stagnation position and flow separation height at the rear can change the front-to-rear lift distribution thus influencing the pitching moment. In addition, if the edges of a vehicle are perpendicular to the flow direction, their shape (e.g. sharp or rounded) and position can affect lift and pitching moment. Rounded edges on upper surfaces can decrease and even prevent flow separation so the local velocity will increase and static pressure will reduce. These decreases in static pressure on upper surfaces causes an increase in overall lift, however, because it is concentrated at the front of the vehicle, this usually increases nose-up pitching moments (Hucho, 1986, Schuetz, 2015).

2.8.2 Side Force, Roll and Yaw

Unsurprisingly, the side force acting on a vehicle increases when the lateral projection area increases. However, the yawing moment change may increase or decrease, depending on the side area distribution and whether it is skewed more to the front or rear. Accordingly, the yawing moment will decrease as rear area increases and so will the rear side force (Hucho, 1986, Schuetz, 2015). The yawing moment is affected by the degree of rounding of vehicle edges and it is dependent on their size and location (front, rear, lateral etc). For example, the rounding of all rear lateral edges usually causes a reduction of the rear side force, resulting in an increase in yawing moment (Hucho, 1986, Schuetz, 2015). Moreover, although the inclination angle between the side of a vehicle and the vertical axis has no effect on yaw, an increase in this inclination angle can decrease the overall side force as well as the rolling moment. In addition, the slope angle of the rear has two conflicting effects on drag and yawing moment; when the slope angle increases, the drag will decease until a certain point (a local minima) and then it typically increases again (Ahmed et al., 1984), however, the yawing moment can increase slightly (Hucho, 1986).

2.8.3 Directional Stability

The yawing moment and corresponding coefficient, C_N, has an important role in directional stability because it has the tendency to rotate the vehicle around the vertical axis. When a vehicle is disturbed (e.g. due to a side wind), if the response is to oppose the disturbance then the vehicle is statically stable and it will yaw against the disturbance. Mathematically this stability criterion is given by: $\frac{dc_N}{d\beta} < 0$. In contrast, if the yawing moment further exaggerates the disturbance then the vehicle is statically unstable and the stability criterion is: $\frac{dc_N}{d\beta} > 0$ (Hucho, 1986, Schuetz, 2015). Fig. 2.10 shows three different shapes which have different sensitivities to the side wind angle, β. The differences in pressure distribution on side area for each shape gives a different response to side wind as shown in the figure. It can be seen that separation behind bluff box-type vehicles (case b) favourably alters the pressure distribution which improves stability, compared to rounded (streamlined) vehicles (case a). In case c, stability increased even further because of the large tail fin; its comparatively large rear side area produces a restorative side force (Hucho, 1986, Schuetz, 2015).

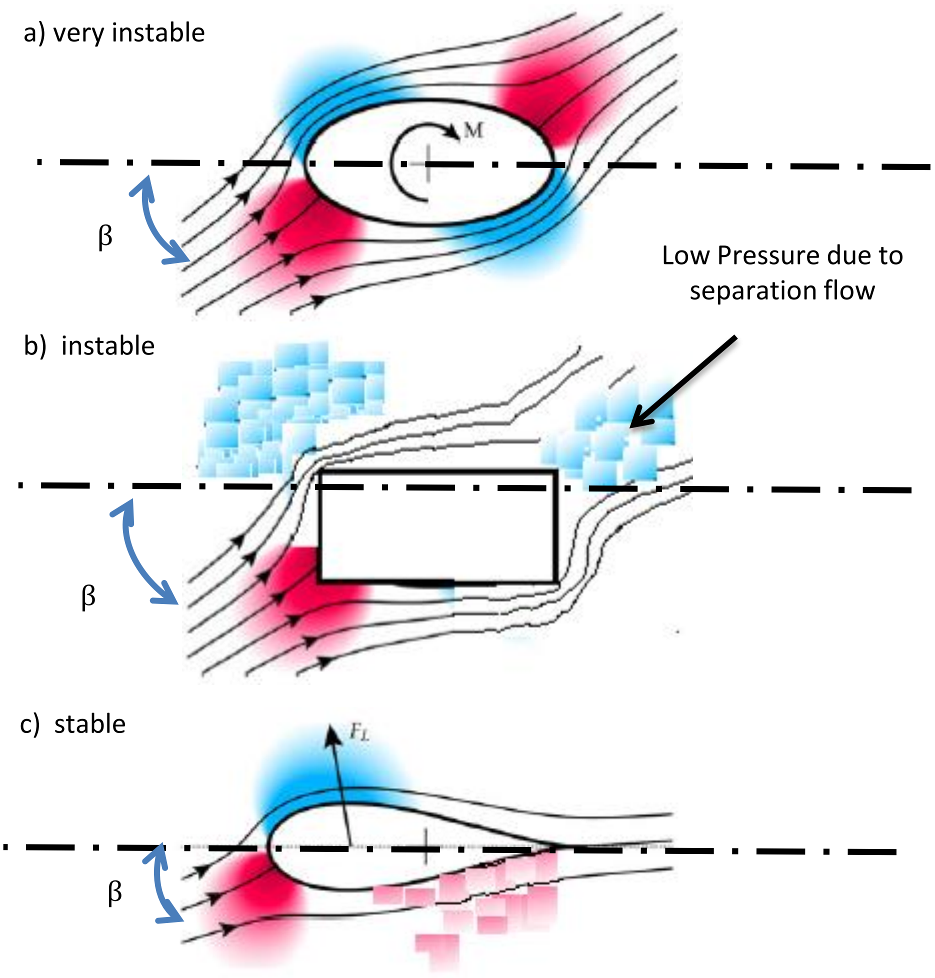

Fig. 2.10. Aerodynamic directional stability in side winds (Red colour = High pressure and blue colour = low pressure): (a) Attached flow; (b) Separated flow at the rear edge, (c) with large tail fin (Schuetz, 2015).

2.8.4 Static Margin and Side Wind Effect

When a vehicle is in motion, the presence of a side wind impacts the resultant velocity of the free-stream of airflow over it. The resultant velocity, V_{res}, is expressed from the summation of vectors:

$$V_{res} = \sqrt{V_D^2 + V_S^2 + 2V_D V_S \cos\beta} \qquad (2.18)$$

where: V_S and V_D are the speeds of the crosswind and road, respectively, see Fig. 2.11. Furthermore, the angle of the side wind is given by:

$$\cos\beta = \frac{V_{res}^2 - V_D^2 - V_S^2}{2V_{res}V_D} \qquad (2.19)$$

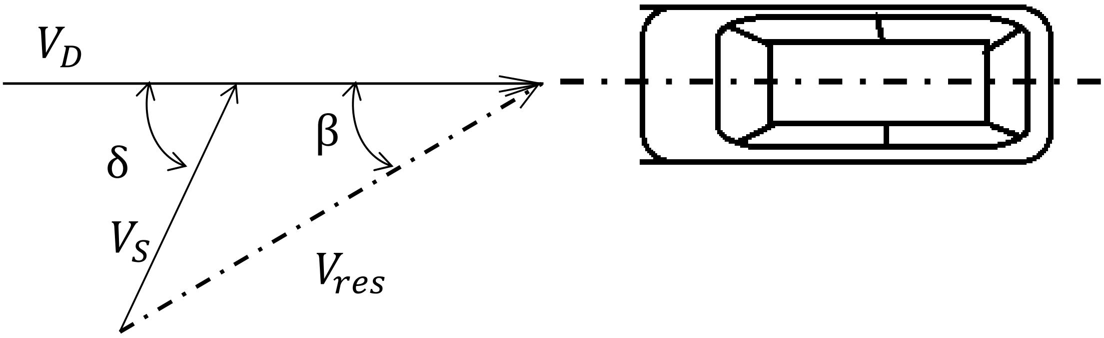

Fig. 2.11. Velocity vectors for a road vehicle experiencing a side wind whilst in motion.

The effects of side forces and the lateral deviation are dependent on different factors. One of these is the static margin which determines how longitudinally stable a vehicle is. To illustrate this, consider the vehicle shown in Fig. 2.12. The static margin is found from the distance between the centre of gravity (CG) and centre of pressure (CoP) or the neutral point (Gillespie, 1992), see Fig. 2.12.

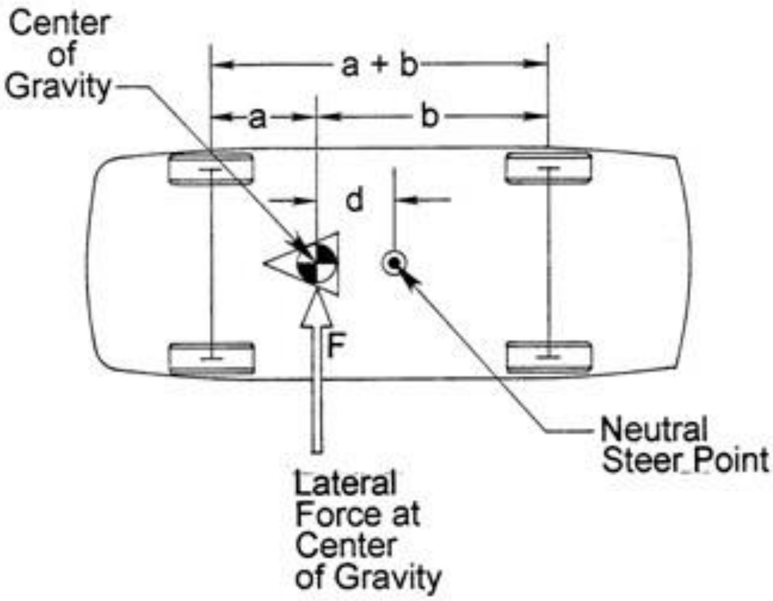

Fig. 2.12. Illustration of the static margin (Gillespie, 1992)

Usually the CoP is located behind the CG of road vehicles which is known as a positive static margin and it means the vehicle is stable. Conversely, if the CoP is ahead of the CG, this represents an unstable vehicle (longitudinally) and the static margin is negative. The static margin, SM, is defined as the ratio of the distance between CG and CoP, *d*, and the wheelbase (a+b), see Fig. 2.12. Normal road vehicles are stable and they operate with a positive SM in the range of 3-7% (Gillespie, 1992). In vehicle design it is important to tune the positions of both CG and CoP to obtain an acceptable SM. It is known that the magnitude of the static margin affects yaw response because it determines how strong the reaction to a disturbance is (Hucho, 1986). Generally, for yaw angles of up to 20 degrees, the yawing moment coefficient, C_N, has a linear response as shown in Fig. 2.13(a). Furthermore, the smaller the area at the rear of a vehicle, the greater the yawing moment but conversely, the side force coefficient, C_Y, particularly at the rear (C_{YR}) reduces, as shown in Fig. 2.13 (b) (Hucho, 1986).

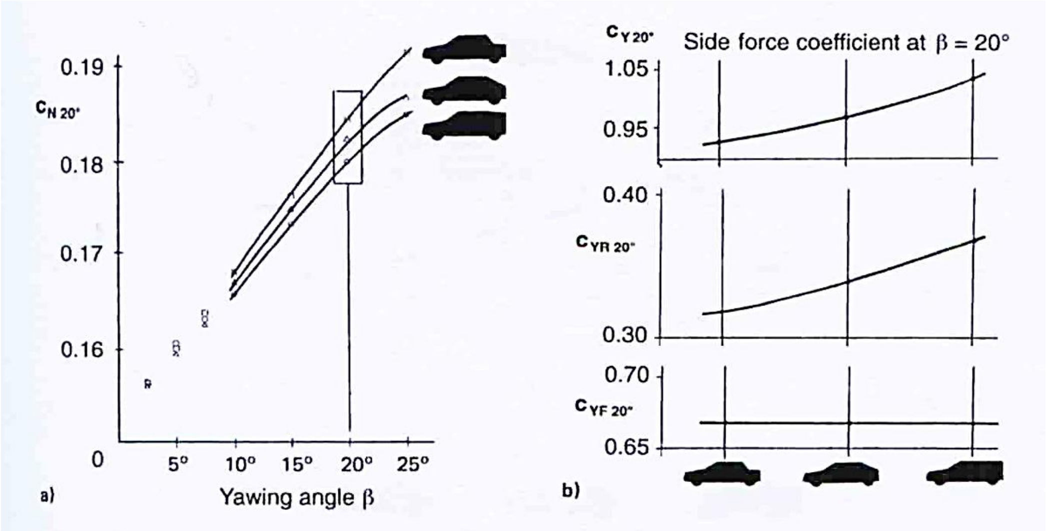

Fig. 2.13. I Typical changes in (a) CN and (b) CY in response to side winds (Hucho, 1986).

The response of vehicle in roll as a result of side winds is shown in Fig. 2.14. It is similar to yaw i.e. as the side wind and thus yaw angle increases, the rolling moment increases (Hucho, 1986). This occurs because as the wind approaches from the side of a given vehicle, it tends to push it over. Clearly, as the side area at the top of the vehicle increases, the rolling moment coefficient, C_R also increases as shown in Fig. 2.14. Again, the response is mostly linear up to about 20 degrees of yaw. Naturally, the interaction between the different forces and moments due to side winds is a complex issue due to the interaction between vehicle design and aerodynamics.

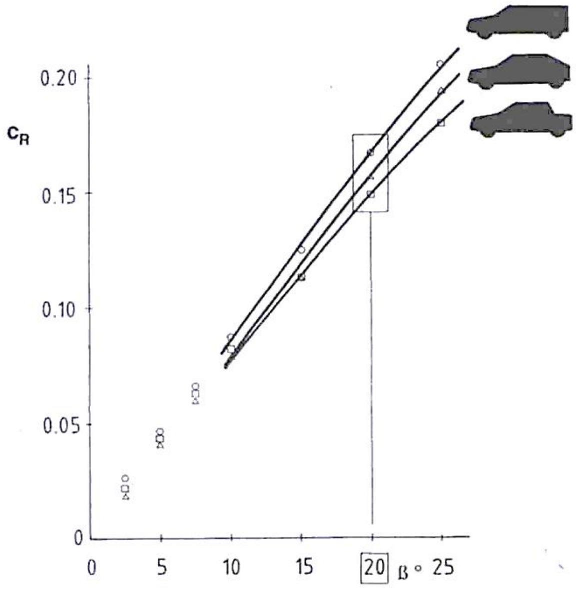

Fig. 2.14. Typical rolling moment coefficient, CR, variation in response to side winds for different vehicle shapes (Hucho, 1986).

2.9 Fundamentals of Applied CFD

The following sub-sections describe the most important aspects of Computational Fluid Dynamics (CFD) which are relevant to the simulations which will be carried out in later chapters.

2.9.1 CFD Overview

CFD is widely used to model fluid flow systems in many engineering applications. Fig. 2.15 shows the three main steps used to generate a CFD model. Firstly, in the pre-processing stage the computational domain including geometrical details (e.g. a vehicle) are defined. Then the domain is discretised, typically into millions of cells, to produce a mesh from which to compute the flow field. Pre-processing is complete once suitable boundary conditions have been assigned. This step involves selecting appropriate physical models to represent various flow phenomena such as turbulence, heat transfer and radiation etc. Relevant solution algorithms and solver settings are also specified based on the assumptions in the model set up (e.g. incompressible, steady state etc.). In the second (solver) stage the governing equations relating to the problem of interest are solved. Finally, the third stage in the CFD process is post-processing which involves data analysis to reveal insights into the solution using a combination of qualitative and quantitative approaches.

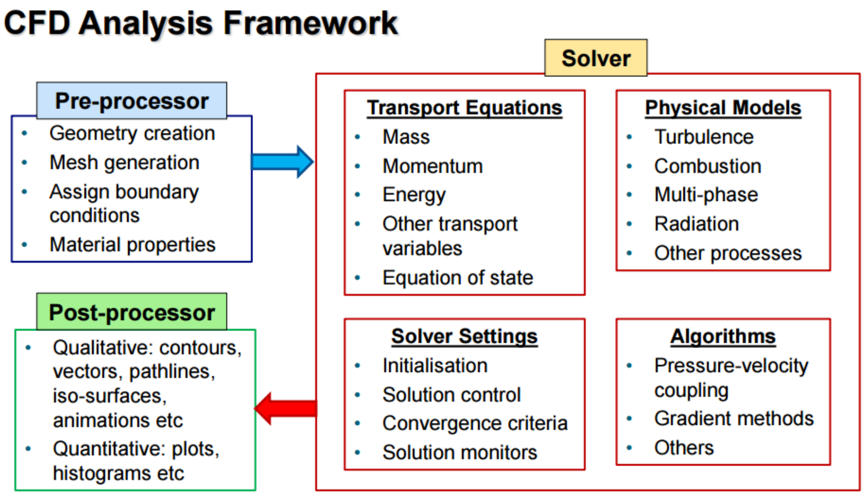

CFD Analysis Framework

Pre-processor
- Geometry creation
- Mesh generation
- Assign boundary conditions
- Material properties

Solver

Transport Equations
- Mass
- Momentum
- Energy
- Other transport variables
- Equation of state

Physical Models
- Turbulence
- Combustion
- Multi-phase
- Radiation
- Other processes

Solver Settings
- Initialisation
- Solution control
- Convergence criteria
- Solution monitors

Algorithms
- Pressure-velocity coupling
- Gradient methods
- Others

Post-processor
- Qualitative: contours, vectors, pathlines, iso-surfaces, animations etc
- Quantitative: plots, histograms etc

Fig. 2.15. CFD Analysis Framework (Tu et al., 2018).

2.9.2 **Conservation Laws and the Navier-Stokes Equations**

Fluid flow problems can be described mathematically by the three conservation laws, namely, the conservation of mass, momentum and energy (Tu et al., 2018, Fox et al., 2010). The conservation of mass is given by:

$$\frac{\partial \rho}{\partial t} + \nabla . \rho \vec{V} = 0 \tag{2.20}$$

where ρ, t and V are the fluid density, time and the fluid velocity vector defined as $\vec{V} = ui + vj + wk$, where u, v and w are the fluid velocities in the three coordinate directions. The momentum equations in three-dimensions are given as:

$$\frac{\partial \rho u}{\partial t} + \nabla . \rho u \vec{V} = \rho g_x + \frac{\partial \sigma_{xx}}{\partial x} + \frac{\partial \tau_{yx}}{\partial y} + \frac{\partial \tau_{zx}}{\partial z} \tag{2.21}$$

$$\frac{\partial \rho v}{\partial t} + \nabla . \rho v \vec{V} = \rho g_y + \frac{\partial \tau_{xy}}{\partial x} + \frac{\partial \sigma_{yy}}{\partial y} + \frac{\partial \tau_{zy}}{\partial z} \tag{2.22}$$

$$\frac{\partial \rho w}{\partial t} + \nabla . \rho w \vec{V} = \rho g_z + \frac{\partial \tau_{xz}}{\partial x} + \frac{\partial \tau_{yz}}{\partial y} + \frac{\partial \sigma_{zz}}{\partial z} \tag{2.23}$$

where σ_{xx}, τ_{yx} and τ_{zx} represent the viscous stress tensor in the x direction, σ_{yy}, τ_{xy} and τ_{zy} are the viscous stress tensors in the y direction and τ_{xz}, τ_{yz} and σ_{zz} are those in the z direction. Furthermore, g_x, g_y and g_z are the gravitational components in the x, y and z directions, respectively. The individual viscous stress tensors are given by the expressions:

$$\tau_{xy} = \tau_{yx} = \mu \left(\frac{\partial v}{\partial x} + \frac{\partial u}{\partial y} \right) \tag{2.24}$$

$$\tau_{yz} = \tau_{zy} = \mu \left(\frac{\partial w}{\partial y} + \frac{\partial v}{\partial z} \right) \tag{2.25}$$

$$\tau_{yz} = \tau_{zy} = \mu \left(\frac{\partial w}{\partial y} + \frac{\partial v}{\partial z} \right) \tag{2.26}$$

$$\sigma_{xx} = -p - \frac{2}{3} \mu \nabla . \vec{V} + 2\mu \frac{\partial u}{\partial x} \tag{2.27}$$

$$\sigma_{yy} = -p - \frac{2}{3} \mu \nabla . \vec{V} + 2\mu \frac{\partial v}{\partial y} \tag{2.28}$$

$$\sigma_{zz} = -p - \frac{2}{3} \mu \nabla . \vec{V} + 2\mu \frac{\partial w}{\partial z} \tag{2.29}$$

where μ is the dynamic viscosity and p is the static pressure. Combining equations (2.21)-(2.23) with equations (2.24)-(2.29) produces a different form of the momentum equations:

$$\frac{\partial \rho u}{\partial t} + \nabla . \rho u \vec{V} = \rho g_x - \frac{\partial p}{\partial x} + \mu \left(\frac{\partial^2 u}{\partial x^2} + \frac{\partial^2 u}{\partial y^2} + \frac{\partial^2 u}{\partial z^2} \right) \tag{2.30}$$

$$\frac{\partial \rho v}{\partial t} + \nabla . \rho v \vec{V} = \rho g_y - \frac{\partial p}{\partial y} + \mu \left(\frac{\partial^2 v}{\partial x^2} + \frac{\partial^2 v}{\partial y^2} + \frac{\partial^2 v}{\partial z^2} \right) \tag{2.31}$$

$$\frac{\partial \rho w}{\partial t} + \nabla . \rho w \vec{V} = \rho g_z - \frac{\partial p}{\partial z} + \mu \left(\frac{\partial^2 w}{\partial x^2} + \frac{\partial^2 w}{\partial y^2} + \frac{\partial^2 w}{\partial z^2} \right) \tag{2.32}$$

These four equations have four unknown variables, u, v, w and p which can be solved numerically without additional approximations, and in simple flow cases they can even be solved analytically. The conservation laws must be satisfied in commercial CFD codes to ensure that simulations converge and give physically realistic solutions. When CFD codes are implemented, it is convenient to use the general set of transport equations, which can be adapted to represent all relevant equations for the problem being solved. The similarity between the conservation laws above and the generic form below is clear to see:

$$\underbrace{\frac{\partial \rho \emptyset}{\partial t}}_{1} + \underbrace{\nabla . \rho \emptyset \vec{V}}_{2} = \underbrace{\nabla . (\Gamma \nabla \emptyset)}_{3} + \underbrace{S_{\emptyset}}_{4} \tag{2.33}$$

where ϕ is the fluid property of interest. The physical Interpretation for each term in Eq.(2.33) is as follows:

1- Rate of increase of $\emptyset$ of fluid element.
2- Net rate of flow of $\emptyset$ out of fluid element.
3- Rate of increase of $\emptyset$ due to diffusion.
4- Rate of increase of $\emptyset$ due to source terms.

Where $\vec{V}$ is the velocity vector, Γ is the diffusion coefficient and $S_{\emptyset}$ is the source term. Table 2.1 provides the values of Γ and $S_{\emptyset}$ to generate the continuity, momentum, energy equations and it can be extended to other transport equations such as species transport and turbulence.

Table 2.1. the values of Γ and $S_{\emptyset}$.

Equation	$\emptyset$	Γ	$S_{\emptyset}$
conservation of mass	1	0	0
momentum equations in the x direction	u	μ	$-\frac{\partial p}{\partial x}+\rho g_x$
momentum equations in the y direction	v	μ	$-\frac{\partial p}{\partial y}+\rho g_y$
momentum equations in the z direction	w	μ	$-\frac{\partial p}{\partial z}+\rho g_z$
The energy equations	T	K	$\rho\dot{q}+\Phi$

For the aerodynamics simulations carried out later in this thesis, the energy equation is not required because it is an isothermal problem. Another assumption will be that the aerodynamic flows are steady so the time dependent terms disappear from the continuity and momentum equations described above, making them easier to solve numerically.

2.9.3 **Discretisation and Pressure-Velocity Schemes**

For most practical cases in fluid dynamics, finding of an analytical solution to the governing equations is not possible so the PDEs must be changed to a system of algebraic equations. This process is known as discretisation. There are different of methods of discretisation such as Finite Difference, Finite volume and Finite Element approaches.

2.9.3.1 **Finite difference method**

For the Finite Difference approach, the system of PDEs can be approximated to a set of algebraic equations by rewriting the partial derivatives as differences using a Taylor's series or by using a piecewise polynomial function (Tu et al., 2018). Whichever method is used, the approximation requires the solution domain to be discretised into a grid of points named "nodes" at which discrete values of the solution exist. This method was used in early CFD codes but is rarely implemented nowadays.

2.9.3.2 **Finite element method**

In this method of discretisation the domain is also divided into small discrete elements. The main feature of this method is the representation of the dependent variable (such as pressure, temperature, velocity) throughout the flow domain by using a piecewise polynomial function (Hirsch, 2007, Patankar, 1980). This polynomial is used to interpolate and represent the value of the dependent variable at any point in the domain as a function of the distance from this point to the element's nodes. By substituting this polynomial function in PDE's, an algebraic set of equations can be obtained for just the value of the variable at these nodes. With this method, the approximation of PDE's can be obtained by replacing the dependent variable (solution) by a polynomial function rather than replacing the partial derivatives as finite differences.

2.9.3.3 Finite volume Method

In the finite volume method (FVM), the flow domain is divided into small elements named control volumes. Next, the governing PDE's are integrated over each control volume to cancel the derivative so that the algebraic set of equations can be derived in terms of independent variables (Patankar, 1980). This method is based on integration over each control volume, therefore it ensures the local conservation of all governing equations such as mass, momentum and energy. This local conservation ensures global conservation for the whole flow domain for any mesh structure. FVM is the basis for the commercial CFD code, ANSYS Fluent which will be used in this thesis.

2.9.3.4 Pressure-velocity coupling schemes

Once FVM-based discretisation is applied to a computational domain, it is important to link the pressure and velocity fields using a pressure-velocity coupling scheme. To do this, once the system of algebraic equations representing the governing PDE's is obtained (in terms of independent variables such as temperature, pressure and velocity) there are two general approaches: coupled and segregated. A coupled solver will solve the algebraic equations for velocity and pressure simultaneously. This approach is often used for compressible flow cases. Alternatively, segregated solvers employ a sequential approach to solve momentum equations, followed by the continuity equation (pressure correction) for each iteration. This approach is typically used for incompressible flow cases such as the ones considered in later chapters.

For incompressible flows, the Semi-Implicit Method for Pressure Linked Equations (SIMPLE) method is the most popular example of a pressure-velocity coupling algorithm which uses the guess-and-correct technique (Patankar and Spalding, 1983). The pressure field is guessed and denoted by p^*. This is then used in the momentum equation to solve for velocities, namely: u^*, v^* and w^*. As these velocities are based on a guess, the continuity equation is then used to calculate new and more accurate values of pressure, p_{new} i.e. a pressure correction. The newly corrected pressure values now ensure that the velocity field agrees more closely to the continuity equation (Anderson John, 1995). The SIMPLE technique is prone to divergence as with any other iterative technique so the under-relaxation factor, α, is involved in the pressure correction equation:

$$P_{new} = p^* + \alpha p' \tag{2.34}$$

where $0 \leq \alpha \leq 1$. When the solver experiences divergence lowering the value for α is recommended to decrease the change in pressure per iterative step so the probability of divergence decreases. For the specific value of $\alpha = 1$, the method reduces to a conventional method.

2.10 Meshing and Boundary Conditions

The following sub-sections describe the important aspects of meshing methods (i.e. the application of discretisation) and boundary conditions.

2.10.1 Mesh methods

The purpose of mesh generation is to discretise the solution domain to break it into small elements or control volumes. The size and type of the grid elements can impact the quality of CFD results. In simple cases of flow through pipes, for example, high-quality Cartesian meshes can easily be produced. In contrast, for more complex 3D problems, achieving high-quality meshes needs more effort and time. There are many different strategies to deal with complex geometries but three common ones are:

1. Body-fitted
2. Block-structured
3. Unstructured

In body-fitted strategies the flow domain is converted onto a simple shape and then simple matrices are applied to produce the mesh structure. Fig. 2.16 illustrates a body-fitted mesh and a corresponding computational domain. The body-fitted approach has a major drawback which is, in a highly complex domain, it can produce degenerate cells in the grid often leading to unstable behaviour. Therefore, it is only suitable for moderately complex geometries.

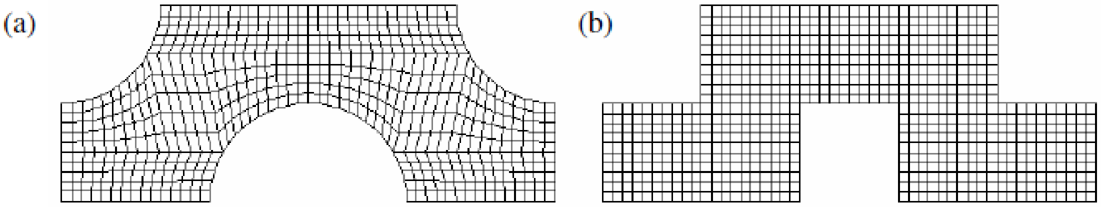

Fig. 2.16. (a) a body-fitted grid and (b) the corresponding computational grid.

Alternatively, block-structured meshes rely on the domain being decomposed and divided into different sub-blocks with each one meshed separately. This method allows the mesh density to be controlled so that it is finer around areas of interest (e.g. in the wake of a bluff body). An example of this approach is shown in Fig. 2.17.

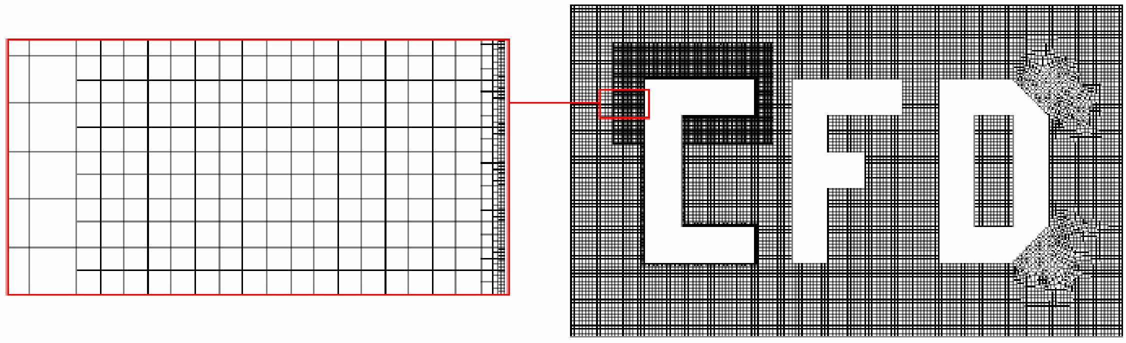

Fig. 2.17. Schematic of a block-structured grid including cell refinement (Gilkeson, 2009).

Another common meshing technique is the unstructured method which has flexibility especially for complex geometries. Cell sizes are able to change very easily to deal with complicated shapes with large and small features. Fig. 2.18 shows a typical unstructured mesh with refinement around a 2D cylinder. This method generally requires less effort and time to implement, compared with the other methods already outlined above.

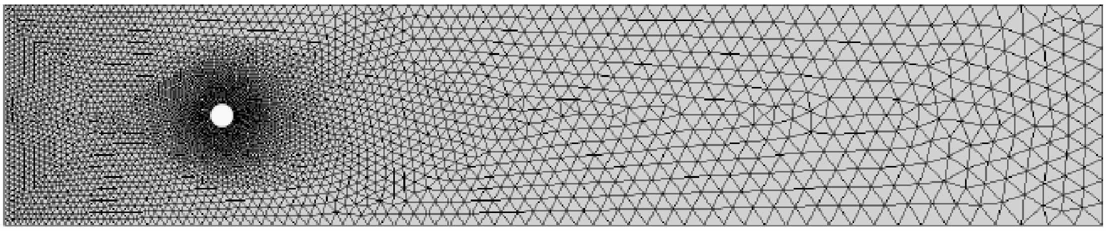

Fig. 2.18. Illustration of an unstructured triangular mesh (Gilkeson, 2009).

2.10.2 **Mesh Quality**

For CFD solutions to converge properly, the quality of the mesh in each cell in the solution domain is crucial; the better the quality, the more likely a solution is to converge. Generally, there are a number of different cell quality criteria which are used in commercial CFD codes such as ANSYS Mesh and ICEM (which will be used later in this study). Typical quality criteria are:

- Aspect-ratio - ratio of the maximum and minimum edge length, per cell.
- Equiangle skew – a measure of cell distortion based on internal angles.
- Equisize skew – assessment of distortion from cell edge lengths.
- Volume - compares cell volumes.

High levels of "skewness" of the elements in a mesh has a strong effect on accuracy and solution stability, so the measurement of skewness is crucial. Cell skewness is defined as the difference between the shape of any given cell and the shape of an ideal equilateral cell. The Equiangle skew criteria is a common measure of skewness level and it is given by:

$$Q_{SK} = max\left(\frac{\theta_{max} - \theta_{eq}}{180 - \theta_{eq}}, \frac{\theta_{eq} - \theta_{min}}{\theta_{eq}}\right) \tag{2.35}$$

Where θ_{max} and θ_{min} are the maximum and minimum internal angles of a given cell respectively, and θ_{eq} is the angle which corresponds to a perfect cell which has no distortion i.e. θ_{eq} = 60º for triangular and tetrahedral elements and θ_{eq}= 90º for quadrilateral and hexahedral elements. Generally, the maximum and average value of skewness in a mesh should not exceed 0.95 and 0.33, respectively (ANSYS). When the maximum skewness reaches 0.95 or greater, the solution can experience difficulties in convergence. Sometimes these difficulties can be alleviated by changing the solver controls, such as reducing under-relaxation factors, however, often the mesh quality must be improved. Table 2.2 shows the different classifications of cell quality based on the skewness criterion.

Table 2.2. *Classification of cell quality* (ANSYS, 2017)

Quality	Classification
$Q_{SK} = 0.00$	Perfect
$0.00 < Q_{SK} < 0.25$	Excellent
$0.25 < Q_{SK} < 0.50$	Good
$0.50 < Q_{SK} < 0.75$	Fair
$0.75 < Q_{SK} < 0.90$	Poor
$0.90 < Q_{SK} < 1.00$	Very Poor
$Q_{SK} = 1.00$	Degenerate

Another important quality criterion is the cell aspect ratio which is a measure of the level of stretching of mesh cells. Generally, inside boundary layers, the aspect ratios of quadrilateral/hexahedral/wedge cells should not exceed 10:1. On the other hand, away from walls where flow gradients are generally lower, the aspect ratios should not exceed 5:1.

2.10.3 **Boundary Conditions**

Boundary conditions are very important because they determine the flow conditions in a solution domain and they are an essential part of the CFD calculation procedure. The main types of boundary conditions available in commercial CFD solvers such as ANSYS Fluent are:

- Walls
- Symmetry
- Inlets
- Outlets

Walls are one of the most common boundary types. Each wall in a solution domain can be assigned a no-slip condition, or full-slip and can be defined as stationary or moving. In the case of stationary no-slip walls, the cells at the wall surface are assigned a velocity of zero. On the other hand, in the case of full-slip, zero-shear conditions are applied on a surface, so the development of the boundary layer will be prevented. This is equivalent to a symmetry condition which prevents fluid crossing the boundary surface. Symmetry or full-slip wall conditions are useful in applying to side walls and the ceiling of the domain for external aerodynamics because it ensures that unrealistic boundary layers do not form at the domain extremities. In the case of moving walls, the velocity of cells attached to the surface have a non-zero value. The moving wall type is needed for simulations of real vehicles which have a moving road (translation) and rotating wheels (rotation).

Both inlet and outlet boundaries are needed to specify the free-stream velocity, mass flow rate or pressure. For simulations of road vehicle aerodynamics, the velocity-inlet and pressure-outlet types are used. As their names suggest, velocity inlets require the velocity of the free-stream to be prescribed and for pressure outlets, the static pressure (usually atmospheric pressure) is set. In cases of wind tunnel simulations or free-air simulations, the position of inlet and outlet boundaries is significant. Usually, the inlet must be placed sufficiently upstream of the object (e.g. a vehicle) to allow the flow to be fully developed. Similarly, the outlet must be located far enough downstream of it to allow turbulent wakes to be fully developed, especially in the case of bluff body aerodynamics. (Gilkeson, 2009) found that inlets placed $5L$ upstream of a bluff vehicle of length L and outlets located $20L$ downstream of the vehicle were sufficient to capture the flow field accurately.

2.11 Turbulence Modelling

In laminar flow regimes, the Navier–Stokes equations can completely describe flow behaviour. In such cases, these equations can be solved numerically without additional approximations, and they even be solved analytically in some cases. On the other hand, in turbulent flow regimes, due to fluctuations in flow variables (e.g. velocity, pressure etc), additional approximations and assumptions are required to solve the Navier–Stokes equations and to describe the flow characteristics (Versteeg and Malalasekera, 2007). In order to deal with the random nature of turbulent flow, fluid properties are defined as the summation of two components, namely: (i) the mean values ($\bar{u}$, $\bar{v}$, $\bar{w}$ and $\bar{p}$) and (ii) the fluctuations ($\grave{u}$, $\grave{v}$, $\grave{w}$ and $\grave{p}$). They are mathematically described as:

$$u = \bar{u} + \grave{u} \tag{2.36}$$

$$v = \bar{v} + \grave{v} \tag{2.37}$$

$$w = \bar{w} + \grave{w} \tag{2.38}$$

$$p = \bar{p} + \grave{p} \tag{2.39}$$

$$\vec{\boldsymbol{V}} = \bar{\boldsymbol{V}} + \grave{\boldsymbol{V}} \tag{2.40}$$

where u, v and w are the fluid velocity in the x, y and z directions, p is the static pressure and $\vec{\boldsymbol{V}}$ is the fluid velocity vector. Furthermore, the definition of the mean $\bar{\varphi}$ of a property can be time-averaged if the temporal variation, $\varphi(t)$, is known:

$$\bar{\varphi} = \frac{1}{\Delta t}\int_0^{\Delta t} \varphi(t)dt \tag{2.41}$$

Fig. 2.19shows a typical time history the velocity of a fluid measured at one point for both laminar and turbulent flow. Note that in a real fluid, turbulent fluctuations vary in all directions.

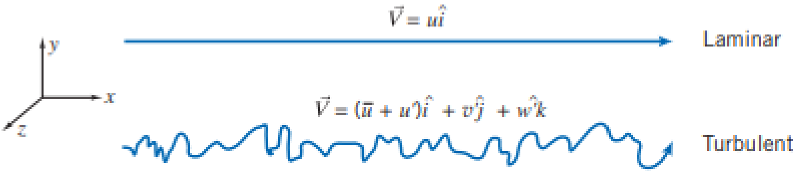

Fig. 2.19. Particle pathlines in 1D laminar and 3D turbulent flows.

In turbulent flow problems, the structure experiences rotational flow (turbulent eddies) which is caused by mixing. The range of size of these turbulent eddies is very wide, from large eddies as large as metres in size down to microscopic eddies. The largest eddies can extract energy from the main flow by interaction with it. Large eddies stretch and produce smaller eddies which in turn produce even smaller eddies. The transfer of kinetic energy from large to smaller and smaller eddies is a process known as the energy cascade which is visualised in Fig. 2.20. The kinetic energy of the smallest turbulent eddies dissipate and this is converted into thermal internal energy. Considering the energy cascade as a whole the kinetic energy of the largest eddies cascades down through to the smallest sizes. This dissipation results in energy losses.

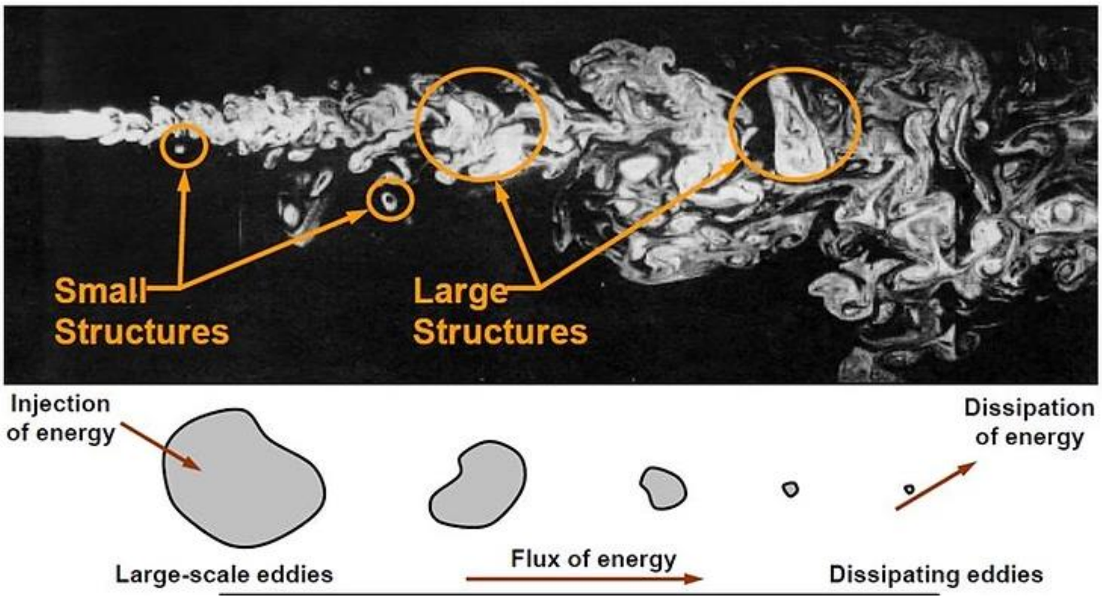

Fig. 2.20. Visualisation of a turbulent eddies.

Generally, there are two ways to solve the Navier-Stokes equations. They can be solved directly by taking account of the full spectrum of turbulent eddy sizes from large to micro scales as well as the full spectrum of time scales, or they can be modelled using a RANS approach which accounts for the mean flow field and gives a steady-state picture of the flow physics. With RANS, only the largest turbulent scales are resolved which makes it a computationally cheaper method compared to Large Eddy Simulation (LES) or Direct Numerical Simulation (DNS). With RANS, wall functions are often used (for certain turbulence models) to enable modelling of near-wall turbulence. Although DNS is considered to be a powerful research tool which can provide a deep understanding of fundamental flow problems (Hirsch, 2007), the drawback of this method is that the mesh density must be much smaller than the smallest eddies and the temporal resolution must be sufficiently small to capture all eddy timescales. The sheer computational demand required to complete DNS simulations of the external aerodynamics of a road vehicle means that this approach is completely out of reach and it will be for decades (Spalart, 2000). Similarly, LES has a high computational demand but not as great as DNS. There are studies of LES around bluff bodies (Krajnović and Davidson, 2005, Choi et al., 2014) which reveal insights into the aerodynamics (more on this in Chapter 3).

2.11.1 **Reynolds averaged Navier-Stokes equations**

The sheer computational demand required for the direct solution of the time-dependent governing Navier-Stokes equations (2.20) and (2.30)-(2.32) in turbulent flow problems means that this approach is completely out of reach. Therefore, time-averaging the properties of the flow, for example mean velocities, mean pressure etc, avoids the requirement to model the lifetime of each and every eddy. For engineering applications, understanding the mean flow properties is sufficient without the need to capture turbulent fluctuations (Versteeg and Malalasekera, 2007). The Reynolds Averaged Navier-Stokes equations, are a form of the Navier-Stokes equations which take advantage of the averaging process without the need to consider turbulent fluctuations. Therefore, the RANS equations and very important because they allow solutions of flow fields to be obtained more easily.

To derive the RANS equations, it is necessary to substitute the generic form of the flow property variable from equation (2.41) into the time-dependent continuity and momentum equations (2.20) and (2.30)-(2.32). Therefore:

$$\frac{\partial \rho}{\partial t} + \nabla . \rho \overline{\boldsymbol{V}} = 0 \tag{2.42}$$

$$\begin{aligned}\frac{\partial \rho \bar{u}}{\partial t} + \nabla . \rho \bar{u} \overline{\boldsymbol{V}} = \rho g_x - \frac{\partial \bar{p}}{\partial x} + \mu \left(\frac{\partial^2 \bar{u}}{\partial x^2} + \frac{\partial^2 \bar{u}}{\partial y^2} + \frac{\partial^2 \bar{u}}{\partial z^2} \right) \\ + \left[- \frac{\partial \left(\rho \overline{\grave{u}^2} \right)}{\partial x} - \frac{\partial \left(\rho \overline{\grave{u}\grave{v}} \right)}{\partial y} - \frac{\partial \left(\rho \overline{\grave{u}\grave{w}} \right)}{\partial z} \right]\end{aligned} \tag{2.43}$$

$$\begin{aligned}\frac{\partial \rho \bar{v}}{\partial t} + \nabla . \rho \bar{v} \overline{\boldsymbol{V}} = \rho g_y - \frac{\partial \bar{p}}{\partial y} + \mu \left(\frac{\partial^2 \bar{v}}{\partial x^2} + \frac{\partial^2 \bar{v}}{\partial y^2} + \frac{\partial^2 \bar{v}}{\partial z^2} \right) \\ + \left[- \frac{\partial \left(\rho \overline{\grave{u}\grave{v}} \right)}{\partial x} - \frac{\partial \left(\rho \overline{\grave{v}^2} \right)}{\partial y} - \frac{\partial \left(\rho \overline{\grave{v}\grave{w}} \right)}{\partial z} \right]\end{aligned} \tag{2.44}$$

$$\begin{aligned}\frac{\partial \rho \bar{w}}{\partial t} + \nabla . \rho \bar{w} \overline{\boldsymbol{V}} = \rho g_z - \frac{\partial \bar{p}}{\partial z} + \mu \left(\frac{\partial^2 \bar{w}}{\partial x^2} + \frac{\partial^2 \bar{w}}{\partial y^2} + \frac{\partial^2 \bar{w}}{\partial z^2} \right) \\ + \left[- \frac{\partial \left(\rho \overline{\grave{u}\grave{w}} \right)}{\partial x} - \frac{\partial \left(\rho \overline{\grave{v}\grave{w}} \right)}{\partial y} - \frac{\partial \left(\rho \overline{\grave{w}^2} \right)}{\partial z} \right]\end{aligned} \tag{2.45}$$

Equations (2.43)-(2.44) are the turbulent, compressible form of the RANS equations which are widely used in commercial CFD packages such as ANSYS Fluent (as will be used in later chapters). These equations include six extra unknowns which are named the Reynolds stresses which are given by:

$$\tau_{xy} = \tau_{yx} = -\rho\overline{\grave{u}\grave{v}} \tag{2.46}$$

$$\tau_{yz} = \tau_{zy} = -\rho\overline{\grave{v}\grave{w}} \tag{2.47}$$

$$\tau_{yz} = \tau_{zy} = -\rho\overline{\grave{u}\grave{w}} \tag{2.48}$$

$$\sigma_{xx} = -\rho\overline{\grave{u}}^{2} \tag{2.49}$$

$$\sigma_{yy} = -\rho\overline{\grave{v}}^{2} \tag{2.50}$$

$$\sigma_{zz} = -\rho\overline{\grave{w}^{2}} \tag{2.51}$$

It is important to be able to deal with these Reynolds stress terms and turbulence models have been designed to do this. Critically, turbulence models have been developed to predict the Reynolds stresses terms in order to close the RANS equations shown by equations (2.42)-(2.51); this is known as turbulence closure and it is essential to be able to obtain meaningful CFD solutions (Versteeg and Malalasekera, 2007). Different approaches to closure are described in the next section.

2.11.2 **Eddy viscosity**

The RANS method itself computes the mean, time-average of flow variables avoiding the details of the fluctuations by solving the continuity and the Reynolds equations. Turbulence models take account of turbulence effects on the mean flow by calculating the Reynolds stresses in equations (2.46)-(2.51). There are different turbulence models including: mixing length models, the Spalart-Allmaras model, k-ε models, k-ω variants and the Reynolds Stress Model (Storms et al., Tu et al., 2013). The main differences between these models is how to calculate the Reynolds stresses. They are based on replacing the Reynolds stress terms by viscous stresses of the mean flow, and critically, these substitutions are expressed in terms of mean values and not instantaneous ones. Boussinesq proposed in 1877 that the Reynolds stress is proportional to the main rates of deformation as described mathematically in the equations below:

$$\tau_{xy} = \tau_{yx} = -\rho\overline{\grave{u}\grave{v}} = \mu_t\left(\frac{\partial\bar{v}}{\partial x} + \frac{\partial\bar{u}}{\partial y}\right) \tag{2.52}$$

$$\tau_{xz} = \tau_{xy} = -\rho\overline{\grave{u}\grave{w}} = \mu_t\left(\frac{\partial\overline{w}}{\partial x} + \frac{\partial\overline{u}}{\partial z}\right) \tag{2.53}$$

$$\tau_{yz} = \tau_{zy} = -\rho\overline{\grave{v}\grave{w}} = \mu_t\left(\frac{\partial\overline{w}}{\partial y} + \frac{\partial\overline{v}}{\partial z}\right) \tag{2.54}$$

$$\sigma_{xx} = -\rho\overline{\grave{u}^2} = 2\mu_t\left(\frac{\partial\overline{u}}{\partial x}\right) \tag{2.55}$$

$$\sigma_{yy} = -\rho\overline{\grave{v}^2} = 2\mu_t\left(\frac{\partial\overline{v}}{\partial y}\right) \tag{2.56}$$

$$\sigma_{zz} = -\rho\overline{\grave{w}^2} = 2\mu_t\left(\frac{\partial\overline{w}}{\partial z}\right) \tag{2.57}$$

where μ_t is turbulent or eddy viscosity.

The Mixing length (zero equation) model, represents a solution to the closure problem. It introduces an eddy viscosity which describes momentum transfer within a fluid by turbulent Reynolds stresses. The effects of convection and diffusion of turbulent properties in the flow are neglected so the influences of turbulence on mean flow can be expressed in simple algebraic formulae for eddy viscosity, μ_t , as a function of position. However, experimental observations show that turbulence usually adjusts itself to local conditions. Therefore, in other models, such as the k-ε model, this takes into account the effects of convection and diffusion in some other turbulent quantities such as the turbulent kinetic energy or the dissipation rate. This is achieved by solving additional transport equations for those quantities (Versteeg and Malalasekera, 2007).

2.11.3 **RANS models**

Practically, there are two major problems when RANS is used. Firstly, the RANS result can be strongly dependent on choice of turbulence model. Secondly, by its very nature, RANS cannot be used to characterise unsteady flow phenomena such as when massive separation flow occurs, for example. Therefore, RANS simulations should ideally be validated with a wind tunnel test or another means of validation (Tsubokura et al., 2009) to give confidence in the results.

CFD has become an increasingly important investigation tool for practical aerodynamic analysis of bluff bodies such as HGVs since the end of the 1980's (Choi et al., 2014, Hucho and Sovran, 1993). Some of the earliest commercial CFD software commonly used the RANS approach as a method for analysing vehicle aerodynamics (Tsubokura et al., 2009). This represented the state-of-the-art at the time and it was only feasible because of the computational resources available; more advanced methods were generally unfeasible.

Today, the RANS approach is still popular in research and industry although the models used have improved significantly.

The simulation of flow structures around HGVs using steady-state RANS is generally good, however, accuracy cannot be assured in the base region behind such vehicles because RANS cannot simulate full details of the near-wake structure. Despite this, in the case of bluff-body aerodynamics, the overall drag has been shown to be generally in good agreement with experiments due accurate computation of the total pressure in the base region (Roy et al., 2006a). In this study, experimental analysis showed that the time averaged flow structure in the wake included a pair of counter-rotating vortices and a recirculation bubble; RANS simulations are capable of giving good qualitative agreement with these flow structures (Roy et al., 2006a). These important characteristics coupled with the relatively good computational efficiency are the rationale for using the RANS approach in this thesis. Because this work concerns external flow, the following three turbulence models, which are all suitable for this type of application, are presented. Other models do exist, but they are beyond the scope of this work.

2.11.4 ***k-ε*** **model**

The *k-ε* model is one of the RANS types which invokes two extra transport equations. The standard two-equation *k-ε* model (SKE) is one of the oldest turbulence models, and so it has been extensively validated through its long history. The sophistication of the SKE is based on taking into account the effects of convection and diffusion of two turbulent properties, namely: the turbulence energy, *k*, and the dissipation rate of turbulence, *ε*, of the mean flow. These are given by:

$$k = \frac{1}{2}\left(\overline{\acute{u}^2} + \overline{\acute{v}^2} + \overline{\acute{w}^2}\right) \tag{2.58}$$

$$\varepsilon = 2\frac{\mu}{\rho}\overline{\acute{e}_{ij}.\acute{e}_{ij}} \tag{2.59}$$

$$\overline{\acute{e}_{ij}.\acute{e}_{ij}} = \left(\overline{\acute{e}_{xx}}^2 + \overline{\acute{e}_{yy}}^2 + \overline{\acute{e}_{zz}}^2 + 2\overline{\acute{e}_{xy}}^2 + 2\overline{\acute{e}_{xz}}^2 + 2\overline{\acute{e}_{yz}}^2\right) \tag{2.60}$$

$$\acute{e}_{xx} = \frac{\partial \acute{u}}{\partial x} \tag{2.61}$$

$$\acute{e}_{yy} = \frac{\partial \acute{v}}{\partial y} \tag{2.62}$$

$$e'_{zz} = \frac{\partial \acute{w}}{\partial z} \tag{2.63}$$

$$e'_{xy} = \frac{1}{2}\left(\frac{\partial \acute{u}}{\partial y} + \frac{\partial \acute{v}}{\partial x}\right) \tag{2.64}$$

$$e'_{xz} = \frac{1}{2}\left(\frac{\partial \acute{u}}{\partial z} + \frac{\partial \acute{w}}{\partial x}\right) \tag{2.65}$$

$$e'_{yz} = \frac{1}{2}\left(\frac{\partial \acute{v}}{\partial z} + \frac{\partial \acute{w}}{\partial y}\right) \tag{2.66}$$

The SKE solves transport equations for the turbulent energy, k, and the dissipation rate of turbulence, ε, (Launder and Spalding, 1983). These transport equations (Versteeg and Malalasekera, 2007) are given by:

$$\frac{\partial(\rho k)}{\partial t} + \nabla.(\rho k\overline{\boldsymbol{V}}) = \nabla.\left(\frac{\mu_t}{\sigma_k}\nabla k\right) + 2\mu_t E_{ij}.E_{ij} - \rho\varepsilon \tag{2.67}$$

$$\frac{\partial(\rho\varepsilon)}{\partial t} + \nabla.(\rho\varepsilon\overline{\boldsymbol{V}}) = \nabla\cdot\left(\frac{\mu_t}{\sigma_\varepsilon}\,\nabla\varepsilon\right) + \ C_{1\varepsilon}\frac{\varepsilon}{\kappa}2\mu_T E_{ij}.E_{ij} - \ C_{\varepsilon 2}\,\rho\frac{\varepsilon^2}{\kappa} \tag{2.68}$$

$$\mu_t = \rho C_\mu \frac{k^2}{\varepsilon} \tag{2.69}$$

where:

$C_\mu = 0.09; \sigma_\kappa = 1.0; \sigma_\varepsilon = 1.3\ \ C_{1\varepsilon} = 1.44; C_{2\varepsilon} = 1.92$

The SKE is used across a wide range of industries. It exhibits good performance in internal flows because SKE has high accuracy in predicting boundary layers, thin layers and duct flows (Tu et al., 2018). On the other hand, the SKE is unsuitable when flow separation occurs. The SKE was modified to use in higher Reynolds number applications through the creation of a new model called the realizable k-ε model (RKE). This modification is made by redefining the model constants for the ε equation (Versteeg and Malalasekera, 2007), namely:

$$\mu_t = \rho C_\mu f_\mu \frac{k^2}{\varepsilon} \tag{2.70}$$

Where f_μ is wall-damping function which is given by:

$$f_\mu = \left[1 - eep(-0.0165Re_y)\right]^2 \left(1 + \frac{20.5}{Re_t}\right) \tag{2.71}$$

$$Re_t = \frac{k^2}{\varepsilon \nu} \tag{2.72}$$

$$Re_y = k^{1/2} y/\nu \tag{2.73}$$

Where ν is kinematic viscosity. these changes make the RKE suitable for a wider range of cases including the backward-facing step and rotating homogeneous shear flows (Shih et al., 1994). The RKE had success in the design the JCB Dieselmax which set a land speed record in 2006 (Lock, 2007).

2.11.5 ***k*-*ω* Model**

The *k*-*ω* (KO) model is another of the RANS types which invokes two extra transport equations, an equation for the turbulent kinetic energy, *k*, and another for the specific rate of dissipation, *ω* (Wilcox, 1998) where:

$$\omega = \frac{\varepsilon}{k} \tag{2.74}$$

The two transport equations for the KO model is shown below:

$$\begin{aligned} &\frac{\partial(\rho k)}{\partial t} + \nabla.(\rho k \overline{\boldsymbol{V}}) \\ &\qquad = \nabla.\left(\left(\mu + \frac{\mu_t}{\sigma_k}\right)\nabla k\right) + \left(2\mu_t S_{ij}.S_{ij} - \frac{2}{3}\rho k \frac{\partial U_i}{\partial x_j}\delta_{ij}\right) \\ &\qquad - \beta^* \rho k \omega \end{aligned} \tag{2.75}$$

$$\begin{aligned} &\frac{\partial(\rho \omega)}{\partial t} + \nabla.(\rho \omega \overline{\boldsymbol{V}}) \\ &\qquad = \nabla.\left(\left(\mu + \frac{\mu_t}{\sigma_\omega}\right)\nabla \omega\right) + \gamma_1\left(2\rho S_{ij}.S_{ij} - \frac{2}{3}\rho \omega \frac{\partial U_i}{\partial x_j}\delta_{ij}\right) \\ &\qquad - \beta_1 \rho \omega^2 \end{aligned} \tag{2.76}$$

and where the eddy viscosity:

$$\mu_t = \rho \frac{k}{\omega} \tag{2.77}$$

and

$$\sigma_k = 2.00;\ \sigma_\omega = 2.00;\ \gamma_1 = 0.553;\ \beta_1 = 0.075;\ \beta^* = 0.09$$

Following the development of the KO model, a modified one was proposed by combining both KO, and SKE models to formulate a new model known as Menter's Shear Stress Transport *k-ω* (SSTKO) turbulence model (Menter, 1994). The SSTKO takes advantage of both the KO and SKE models by using the KO in near-wall regions where adverse pressure gradients commonly occur and the SKE model in the free-stream (Versteeg and Malalasekera, 2007). Roy et al., (2006) compared the SSTKO with experimental data for the flow past a HGV shape and found good agreement between the predicted drag and the results of wind tunnel experiments; this will be discussed in later chapters.

2.11.6 **Spalart Allmaras model**

The Spalart Allmaras (SA) model (Spalart and Allmaras, 1992) invokes only one extra transport equation for the kinematic eddy viscosity parameter $\tilde{\nu}$ (Versteeg and Malalasekera, 2007), which is given by:

$$\begin{aligned}\frac{\partial(\rho\tilde{\nu})}{\partial t} &+ \nabla.(\rho\tilde{\nu}\overline{\boldsymbol{V}}) \\ &= \frac{1}{\sigma_v}\nabla.\left((\mu_t + \rho\tilde{\nu})\nabla\tilde{\nu}\right) + C_{b2}\rho\frac{\partial\tilde{\nu}}{\partial x_k}\frac{\partial\tilde{\nu}}{\partial x_k} + C_{b1}\rho\tilde{\nu}\widetilde{\Omega} \\ &- C_{w1}\rho\left(\frac{\tilde{\nu}}{ky}\right)^2 f_w\end{aligned} \tag{2.78}$$

where:

$$\widetilde{\Omega} = \Omega + \left(\frac{\tilde{\nu}}{(ky)^2}f_{v2}\right) \tag{2.79}$$

Where f_w and f_{v2} are wall damping functions and the model constants are given:

$$\sigma_v = \frac{2}{3};\ k = 0.4187;\ C_{b1} = 0.1355;\ C_{b2} = 0.622;\ C_{w1} = C_{b1} + k^2\frac{1 + C_{b2}}{\sigma_v}$$

The SA model was created specifically for aerospace applications to simulate attached external flows because of its ability to predict adverse pressure gradients in boundary layers. However, its applicability is widening and it has shown good performance in aerodynamic studies of bluff road vehicles (Gilkeson et al., 2006, Maddox et al., 2004).

2.12 **Error and Uncertainty**

When running CFD simulations, it is crucial to follow the correct quality control procedures to ensure maximum accuracy. Such measures were introduced in the 1980's in the nuclear industry (Mehta, 1998) before industry-standard guidelines were published (Babuska and Oden, 2004). This led to widely recognised Verification and Validation (V&V) procedures published by the European Research Community on Flow, Turbulence and Combustion (Casey and Wintergerste, 2000), the American Institute for Aeronautics and Astronautics (Aeronautics and Astronautics, 1998, Oberkampf and Trucano, 2002) and the American Society of Mechanical Engineers (Engineers, 2009). The key aspects in all of these works of V&V are that errors are recognisable deficiencies in simulations which are not due to lack of knowledge, whereas uncertainties are potential deficiencies caused through lack of knowledge. Furthermore, validation can be described as "solving the right governing equations" and verification as "solving the governing equations right" (Roache, 1994). The quality of V&V and thus CFD simulations depends strongly on the control of errors and uncertainties. These will be outlined below.

There are three main groups of errors associated with CFD (Versteeg and Malalasekera 2007):

1. Coding errors.
2. User errors
3. Numerical errors, which include round-off error, convergence error and discretisation error

Human mistakes cause coding errors and user errors. Coding errors inevitably occur during code development and so there is emphasis on validation to approve a given code (e.g. ANSYS Fluent) to minimise these issues. Commercial code vendors invest a great deal of time to minimise coding errors. On the other hand, user errors occur due to human mistakes when actually using the CFD codes themselves, for example, when defining the dimension of the problem and details of the solution domain or when defining turbulence models and boundaries conditions; these errors can be reduced with practice.

Numerical errors are much better defined and easier to control (Casey and Wintergerste, 2000, Oberkampf and Trucano, 2002, Aeronautics and Astronautics, 1998, Engineers, 2009). The first type of numerical error is round-off error and this depends on how many significant figures are used by the CFD solver. Typically, users of commercial software have a choice between single-precision (8 significant figures) and double precision (16 significant figures). If more significant figures are used during CFD calculations, the round-off error reduces. ‘Rounding off’ problems arise when adding a very small number to a very large number. Tu et al., (2008) give the following example to illustrate the impact of round-off error when using single-precision:

A = 8888888 – 8888887 + 0.3333341

A = 1 + 0.3333341

A = 1.333334 (correct result).

B = 8888888 + 0.3333341 – 8888887

B = 8888888 – 8888887

B = 1.000000 (incorrect by 25%).

The reason why A ≠ B is because of the round-off error, specifically, when adding a very large number to a smaller one in the first part of the calculation of B, this is rounded to the nearest integer, giving the wrong result. Round-off error can grow rapidly and swamp the solution iteratively, especially when a given CFD solution contains millions of cells. Therefore, choosing to use double-precision solvers is an easy way to drastically minimise the effect of round-off error.

Another common numerical error is convergence error. This occurs when flow solutions are not run for enough iterations and they are stopped before the solution is properly converged (convergence point). The convergence point can be reached by increasing the number of iterations until there is no tangible difference in the solution from one iteration to the next. Usually, CFD solutions are considered to be converged when the residual levels drop by three to five orders of magnitude (Versteeg and Malalasekera 2007), however, it is very important to assess this on a case-by-case basis which requires careful judgement by the CFD user. To illustrate the problem of convergence error, Fig. 2.21 shows how the solution of the flow over a backward-facing step is changed dramatically with increasingly fine converge level tolerance (Gilkeson, 2009).

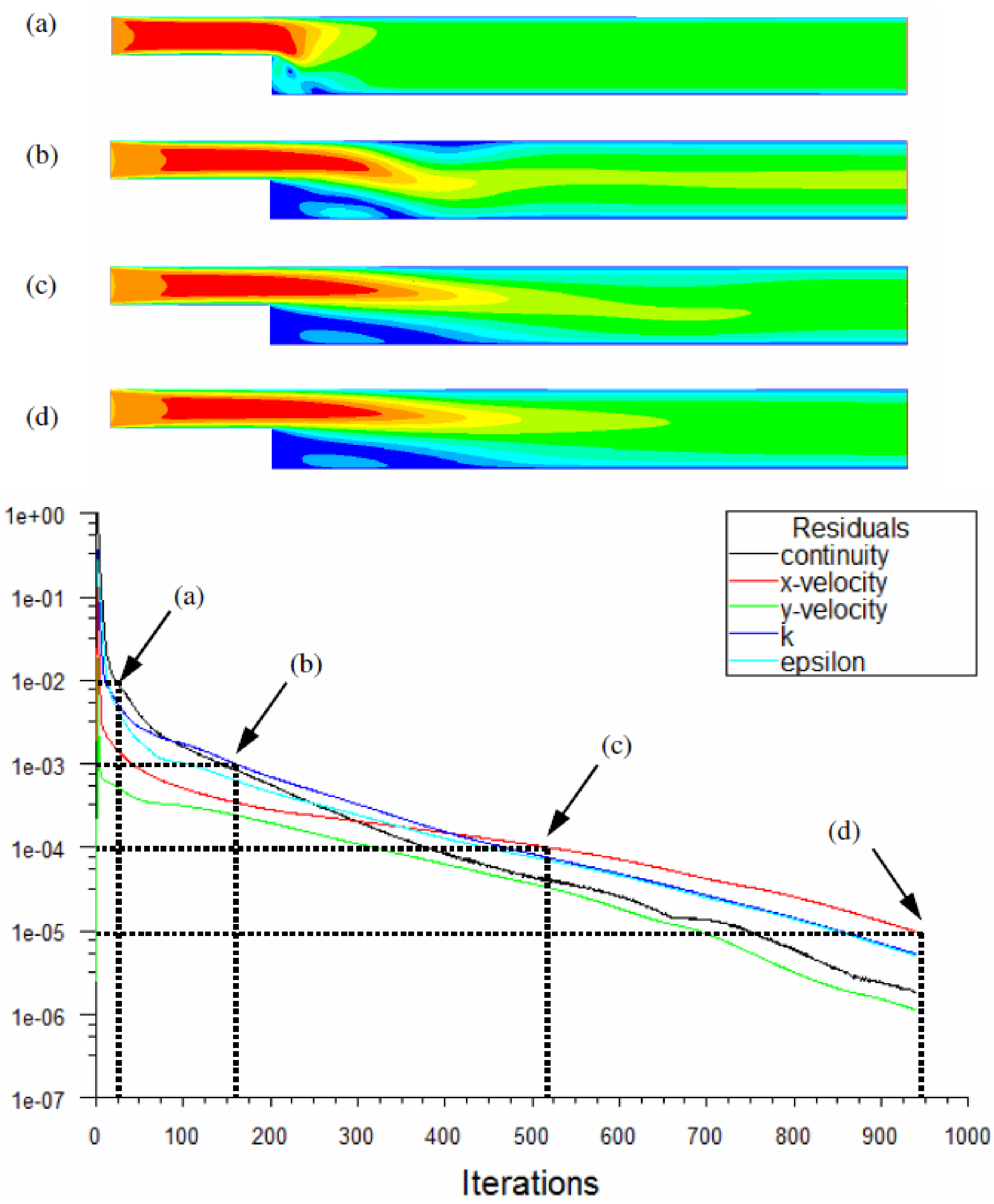

Fig. 2.21. Illustration of a converging flow solution for the backward-facing step (Gilkeson, 2009)

Of all the numerical error sources, discretisation error is one of the most challenging ones to define and minimise. The process of discretising the continuous governing equations of fluid flow inevitably leads to discresitation error. This type of error is impacted by the iterative processes employed by numerical solver methods and other factors such as numerical diffusion which depends on cell shape. The only way to minimise discretisation error is to conduct rigorous mesh independence studies and select a mesh which gives sufficient accuracy for the given application. In order to establish a uniform method for verifying CFD results, the Grid Convergence Index (GCI) was proposed and is widely used by Roache (1994) (Vinchurkar and Longest, 2008, Hefny and Ooka, 2009). It is given by:

$$GCI_{FINE-GRID} = \frac{F_s|e|}{(r^p - 1)} \tag{2.80}$$

where F_s is the factor of safety (this is set to 1.25 for rigorous studies or 3.00 for conservative ones), *e* is the error computed between solutions which is given by:

$$e = \frac{(f_2 - f_1)}{f_1} \tag{2.81}$$

where $f_1$and f_2 are calculated solutions on the fine and coarse grids (meshes) respectively, and *r* is the grid refinement ratio, given by:

$$r = \frac{h_2}{h_1} \tag{2.82}$$

where h_1 and h_2 are the fine and coarse grid (Hyams et al.) spacing sizes (or number of elements). Also, p is the order of discretization which is 1 for first order simulations and 2 for second order ones. To apply this method in practice, the same value of *r* should be used between each successive mesh refinement for consistency. The solution values (f_1 and f_2) can be anything in a given set of solutions, for example, drag coefficients or the position of a separation point; it is up to the user to decide on which are the most appropriate solutions to use. This method has been used successfully in vehicle aerodynamics simulations (Gilkeson et al., 2013).

2.13 **Design Optimisation**

In this section, a short review of design optimisation is presented, this is not an exhaustive review but it covers the methods and algorithms used in Chapter 6 of this thesis. Optimisation is a way of finding the optimum design or operation of a system under certain constraints (Thévenin and Janiga, 2008). Mathematically, it is often defined as finding the minimum of a solution (e.g. minimum aerodynamic drag), $min(f(x))$, where *x* is an input to the system or a determined design variable (e.g. dimension of a car body) and $f(x)$ is an objective function such as the cost of a project, force acting on a car, weight of an object etc. In the context of design optimisation, the problem can be summarised by the objective function:

$$min(f(x)) \tag{2.83}$$

where the design space is governed by:

$$x^{lower} \leq x \leq x^{upper} \tag{2.84}$$

where, x^{lower} and x^{upper} represent the lower and the upper limit for each of the design variables. It is also possible to have inequality constraints, $g(x)$, which effectively reduces the size of the design space, however this is not used in the current work.

2.13.1 **Design of experiments**

After deciding which input parameters are of interest, i.e. the design variables, the objective function will be derived as functions of these design variables. The number of these variables is equal to the number of degrees of freedom in the design space. Having too many design variables leads to the "curse of dimensionality" which means that the design space is so large that it is very difficult to accurately sample it (Forrester et al., 2008). The number of designs evaluated for a given problem are determined by a design of experiments (DoE). A DoE is effectively a distribution of points in a design space, with each point having a unique combination of design variables i.e. an individual design. Fig. 2.22 shows typical classical approaches to DoE's (Veldhuis et al., 2016).

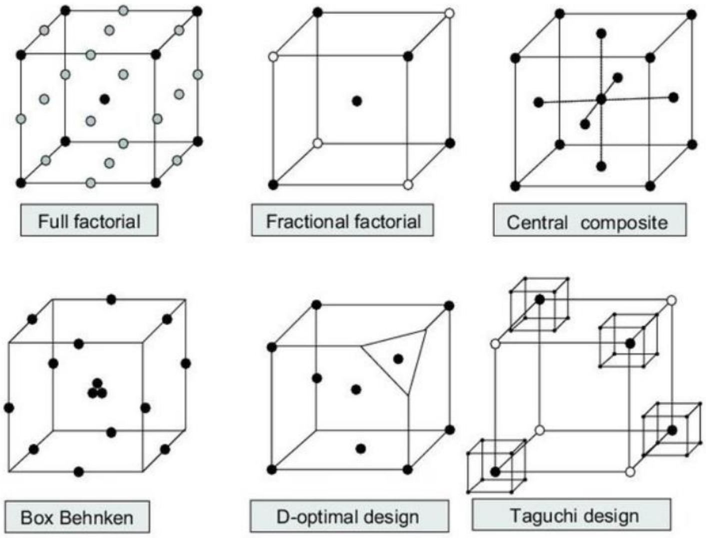

Fig. 2.22. Illustration showing different classic approaches to DoE's (Veldhuis et al., 2016).

The different classical DoE methods include densely populated ones such as full factorial and central composite designs and less populated ones including the fractional factorial (Veldhuis et al, 2016). Other types of DoE exist such as the Latin Hypercube (LH) and Optimal Latin Hypercube (OLH), (Narayanan et al., 2007). One of the issues with the OLH is that the point distribution does not extend to the corners or the edges of the design space which is a problem in physically constrained problems (Gilkeson et al., 2013). Due to the size restrictions of HGVs, the design optimisation problem in this thesis will be constrained (especially in height and width), therefore, the full factorial approach is used later in this work; such a method gives a uniform distribution of points including the edges and corners of the design space and it can be more easily implemented than other methods. After choosing the number and distribution of DoE points in the design space, the values of the objective function of the system (e.g. aerodynamic drag) should be found by experimental or by numerical means; in the present study, CFD is used.

2.13.2 **Metamodels**

Once the values of the design variables (inputs) and their corresponding objective function values (outputs) are known, a mathematical relationship between them, a metamodel, can be obtained to describe the behaviour of the system as a whole. The accuracy of a given metamodel in describing the response of a system depends on the number and distribution of DoE points, as well as the number of dimensions (Queipo et al., 2005). Fig. 2.23 shows a typical metamodel illustrating how the aerodynamic drag coefficient of a bluff road vehicle varies as a function of three design variables (Gilkeson et al., 2013).

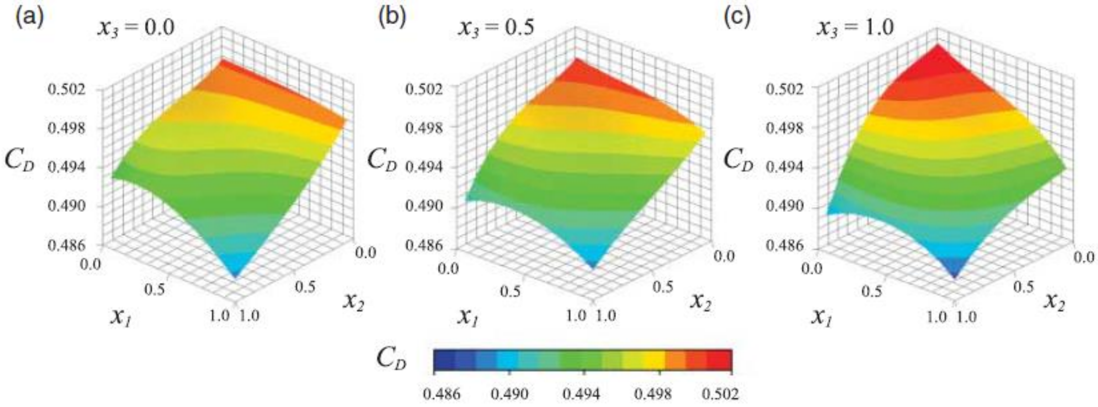

Fig. 2.23. Illustration a four dimensional metamodel with three design variables and one objective function, C_D (Gilkeson et al, 2013).

After a metamodel has been created, optimisation methods are required to find the global minimum of the objective function on the metamodel surface. The benefit of building a metamodel using a DoE approach is that if the metamodel is accurate (i.e. it has sufficient data points) it is possible to avoid doing more CFD simulations (Forrester et al., 2008, Viana and Haftka, 2008). There are various mathematical and statistical techniques and methods used to build metamodels. In particular, there are two distinct types: interpolation-based and approximation-based methods (Forrester et al., 2008). The main difference between these is that interpolation-based methods require the metamodel to pass directly through objective function data points. Examples of interpolation-based metamodels are kriging and radial basis functions (Queipo et al., 2005, Forrester et al., 2008). In contrast, in approximation-based approaches, the metamodel doesn't need to pass directly through the data points (analogous to a line of fit to a cloud of data). This feature gives approximation-based methods more flexibility to deal with noisy data points which is a common problem in CFD (Gilkeson et al., 2014). A more thorough review of metamodels is beyond the scope of this thesis, however, for the reasons outlined above, a common approximation-based method, the Moving Least Squares method (MLS) is used later in this work (Toropov et al., 2005). In MLS, an approximation function, $\hat{f}(x)$, based on N DoE points (inputs) and the values of the objective function (outputs), f_i, are given by:

$$\hat{f}(x) = \sum_{i=1}^{N} w_i f_i \tag{2.85}$$

where w_i is a weight assigned to each point which is represented by a Gaussian weight decay function, namely:

$$w_i = \exp(-\theta r_i^2) \tag{2.86}$$

were r_i is the Euclidean distance from the metamodel approximation and the objective function value i.e. $r_i = |x - x_i|$ and θ is the closeness of fit parameter.

2.13.3 **Optimisation Techniques**

The next step in the optimisation process is to search the metamodel for the global minimum. There are several different methods of optimization. There can be classified in two type global and local search methods. The Sequential Quadratic programming (SQP) method is example of local research type. It required an initial good guess of the solution. On the other hand, Genetic Algorithms (GAs) is global research methods witch is does required started point to research. The Both global and local search methods are used to fulfil this step.

2.13.3.1 **Genetic Algorithm**

GAs are commonly used because they can effectively scan the whole of a typical design space to find suitable candidate(s) for the global minimum. The three stages in implementing the GA can be summarised as:

1. Initialization
2. Creating the Next Generation (selection, crossover and mutation)
3. Termination

The initialisation stage involves generating a seed by randomly choosing the number of potential candidates of the position of the minimum value of an objective function; these are called chromosomes. For example, in the case of a three design variable optimisation problem, each chromosome represents the value of every design variable D_1, D_2 and D_3. The chromosomes stores the solution which it represents in different ways depending on the nature of the problem, such as: binary, real number, vector of a real number etc. Each chromosome consists of a unique combination of genes. Fig. 2.24 and Fig. 2.25 show how chromosomes are made up of genes for binary and vector-based systems, respectively.

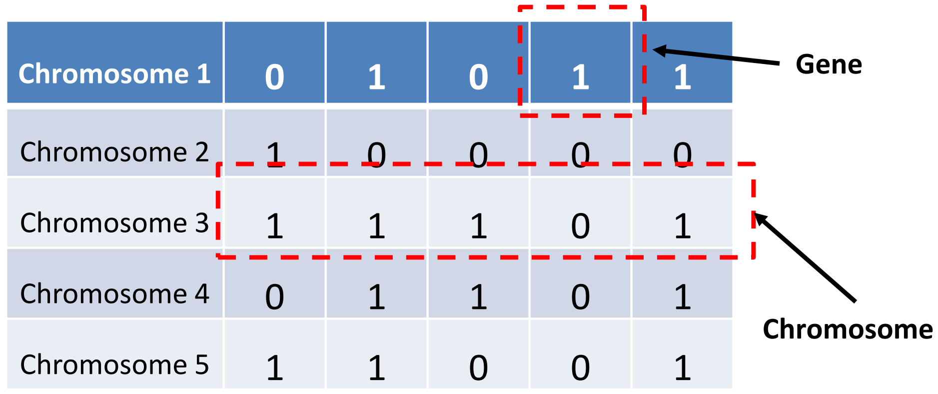

Chromosome 1	**0**	**1**	**0**	**1**	**1**
Chromosome 2	1	0	0	0	0
Chromosome 3	1	1	1	0	1
Chromosome 4	0	1	1	0	1
Chromosome 5	1	1	0	0	1

Fig. 2.24. Example of a binary chromosome representation.

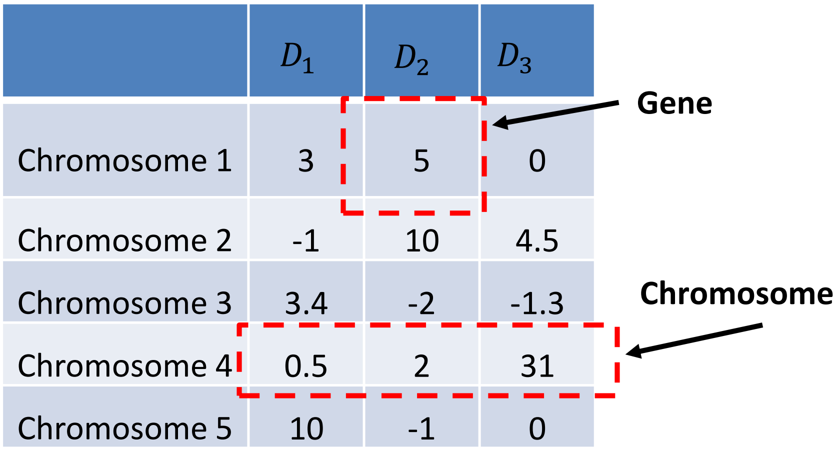

	D_1	D_2	D_3
Chromosome 1	3	5	0
Chromosome 2	-1	10	4.5
Chromosome 3	3.4	-2	-1.3
Chromosome 4	0.5	2	31
Chromosome 5	10	-1	0

Fig. 2.25. Example of a vector of real number type chromosome representation.

The group of initial chromosomes are together called the initial population. All subsequent processes depend on these chromosomes including the next generation (Holland, 1992). An overview of the entire GA process is shown in Fig. 2.26.

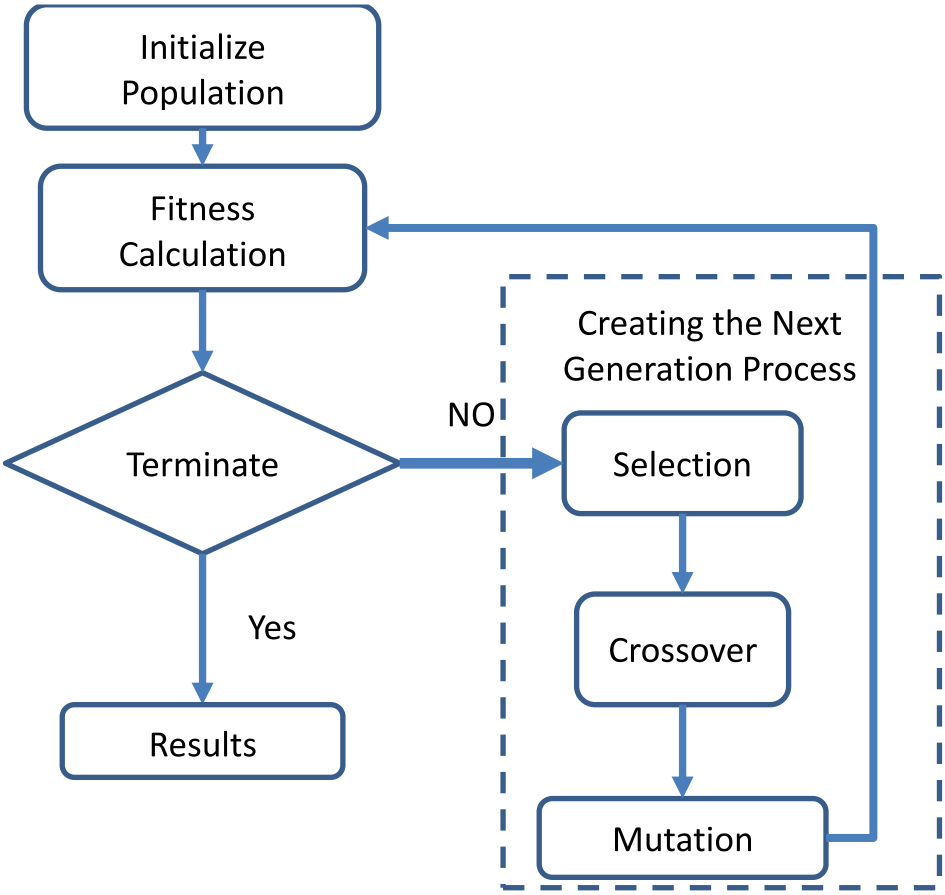

Fig. 2.26. Illustration the steps involved in the genetic algorithm.

In step (2), creating the next generation, the GA uses the current population to create a new solution, made up from 'child' chromosomes, to generate an enhanced next generation. Before this is done, firstly a fitness calculation is made on the initial population to identify candidate 'parent' chromosomes. Because of the random nature of GAs, the fitness function assesses the entire initial population (from step (1)) to find the best solutions from them to select a suitable group of individuals, called parents, who contribute their genes to children. The fitness function is related to the value of an objective function and typically, as the fitness function increases, the objective function decreases. The algorithm usually selects individuals that have better fitness values as parents (Holland, 1992). It is important to appreciate that the size of chromosome populations always remains unchanged from one generation to next.

There are three different sub-processes to step (2) in order to identify the next generation:

a) Selection process: selecting the elite chromosomes in the current generation which have the best fitness values too form the next generation.

b) Crossover process: creating new child chromosomes by combining a pair of elite parent chromosomes, see Fig. 2.27.

c) Mutation process: introducing small random changes, or mutations, to a single gene, see Fig. 2.28.

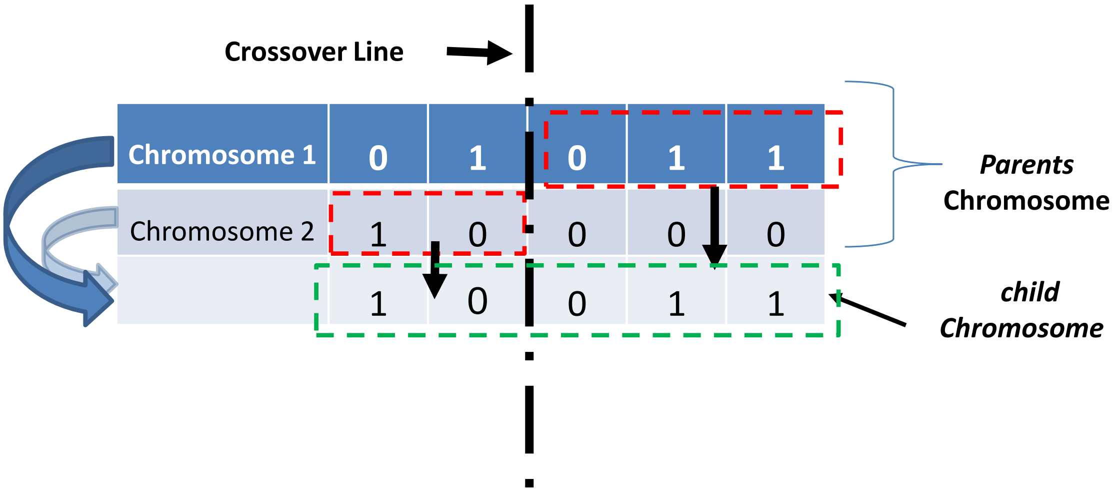

Fig. 2.27. Example of the crossover process on binary chromosomes.

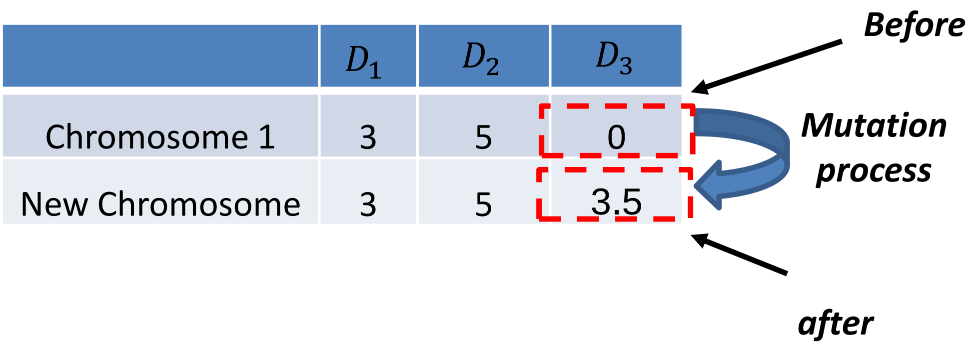

Fig. 2.28. Example of the mutation process on a gene in chromosomes represented by real number vectors.

The crossover and mutation processes are not always performed when generating a new population; these processes are dependent on crossover and mutation probabilities. Typically, the crossover probability is high at about 80% whereas the mutation probability is very low about at 3%. The mutation process is important because it prevents the search falling into a local optimum and it thereby extends the search space. Higher mutation probabilities can cause the search to degrade to a random one which undermines the purpose of the GA (Holland, 1992).

The last step, step (3), is termination. There exist different criteria to stop searching. A search is stopped when a maximum number of generations or a maximum time limit is reached. However, typically, the GA detects if there is no change in the best fitness value for a given time in seconds (stall time limit), or for a specified number of generations (stall generation limit). A candidate is then put forward for the global optimum.

Despite the strength of the GA method, it is only suitable for finding the approximate location of the global minimum and not necessarily the absolute optimum value. Therefore, any design proposed by a GA needs to be confirmed by using local gradient-based search methods. Local optimisation search methods require an initial ‘good’ guess of the solution, so the GA result is used as a starting location. At this point, the local (and hopefully global) optimum will have been found. The design variables (inputs) for this candidate can then be assessed using the simulation method, such as CFD, to see if the final result matches the metamodel prediction. A new metamodel will need to be built from the extra data point(s) and only when the CFD and metamodel predictions are very close, will the optimum result have been found. Many different local optimisation methods and the GA are embedded within the MATLAB Optimisation Toolbox, which is used later in this study.

Chapter 3 : Review of Aerodynamics and Stability of Heavy Goods Vehicles

Following the review of fluid mechanics principles and the key aspects of CFD and design optimisation in the previous chapter, the following chapter reviews bluff body aerodynamics including a summary of strategies for reducing the aerodynamic drag force on HGVs. It is widely known that the main flow features surround such vehicles are three dimensional and unsteady in nature (Choi et al., 2014). The flow around HGV's has these features because of two reasons. Firstly, HGVs are bluff bodies which produce extensive flow separation from many parts of their surfaces. Secondly, the flow structure is further complicated by the ground, in turn affecting the aerodynamic forces and flow features (Choi et al., 2014). In order to appreciate these aspects, it is important to clarify understanding of the complex flow structures around HGVs and similar vehicles; this is the purpose of this chapter.

3.1 Flow around simplified three-dimensional vehicles.

Aerodynamic flows around vehicles in general, such as aeroplanes, ships and road vehicles are broadly similar, however, in the case of road vehicles they are usually bluff bodies and so the resulting flow field is dominated by massive flow separation leading to significant drag forces (Choi, et al., 2014). In the field of road vehicle aerodynamics two models which are widely used to study the aerodynamic performance of real HGVs are: (i) the Ahmed and (ii) the GM model (Choi, et al., 2014, Hucho, 1986). The only difference between the two is that the Ahmed model has a slanted end edge, see Fig. 3.1.

Fig. 3.1. a) Ahmed model and b) the GM model (Choi et al, 2014).

The flow around the Ahmed model contains three common features including:

1. A separation bubble on the slanted surface;
2. A pair of counter-rotating longitudinal vortices;
3. Another recirculation bubble behind the vertical base.

These flow features, shown in Fig. 3.2, are the main reason for relatively large drag forces (e.g. compared to an aeroplane) and the drag force strongly depends on the slant angle, α (Hucho, 1986).

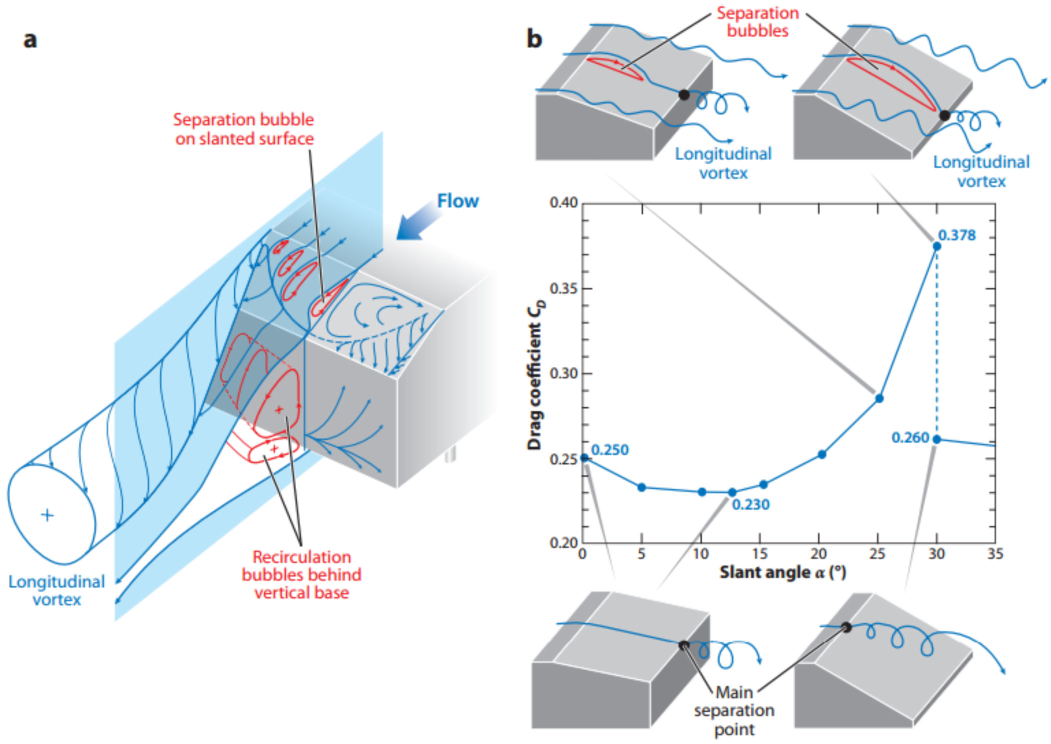

Fig. 3.2. Aerodynamics of the Ahmed model: a) the flow structure b) the drag coefficient (Choi, et al., 2014).

In a time-averaged sense, when the slant angle is in the range $0^{\circ} \leq \alpha \leq 12.5^{\circ}$, the drag coefficient decreases, from 0.25 to approximately 0.23 and flow separation appears only at the end of the edge, showing in Fig. 3.2 (Choi, et al., 2014). However, when the slant angle is large and in the range of $12.5^{\circ} \leq \alpha \leq 30^{\circ}$, the drag coefficient increases by approximately 65% from 0.230 to 0.378. This drag rise is partly due to flow separation occurring immediately downstream of the front edge of the sloped area. In addition, small recirculation bubbles are created in the same area and the size of these bubbles increases with the slant angle. Moreover, a pair of counter-rotating longitudinal vortices appear around the two side edges of the slope area, and their strength increases as the angle of the slope area increases. When $\alpha = 30^\circ$ there are two possible regimes. Firstly, a high-drag regime where the longitudinal vortices have maximum strength and the extent of flow separation reaches the maximum. Secondly, the low-drag regime, where the longitudinal vortices and recirculation bubble can disappear and the flow separates completely from the slant area so the drag decreases dramatically (Hucho and Sovran, 1993).

It is important to appreciate that there can be a strong relationship between unsteady flow features and drag generation mechanisms (Thacker et al., 2010). The recirculation bubbles behind the vertical base region are intermittently shed and the separation region on the slanted surface is highly unsteady; it can instantaneously fully separate, even at $\alpha = 25^\circ$. Thacker et al. (2010) also reported a slight drag coefficient change with change of Reynolds number (Fig. 3.3), which relates to the change in flow structure.

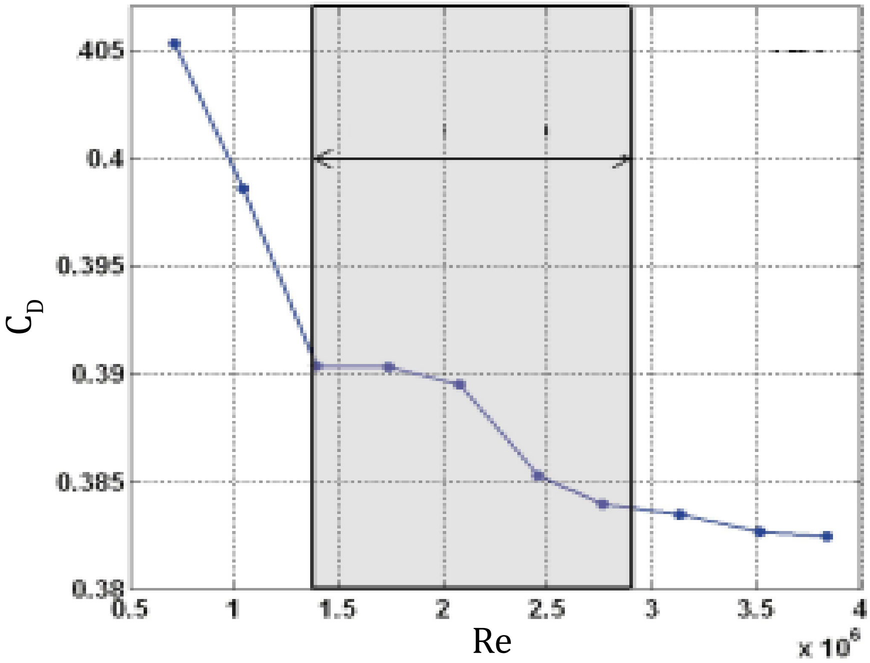

Fig. 3.3. Drag coefficient of the Ahmed model versus Reynolds number (Thacker et al. 2010).

The GM model is another important model used in aerodynamic studies. The only difference between the Ahmed model and the GM model is the sloped surface at the back end of the GM model is completely removed i.e. α = 0°. The flow around this model is similar to flow around Ahmed's model with a large recirculation bubble appearing behind the base (Choi, et al., 2014). As we can see from Fig. 3.4 and Fig. 3.5 the CFD results computed using Large

Eddy Simulation (LES), the near-wake experiences a high level of unsteadiness and it contains a large number of small-scale vortices. The shear layer region continuously generates strong small-scale vortices, giving high turbulence intensities (Lee and Choi, 2009).

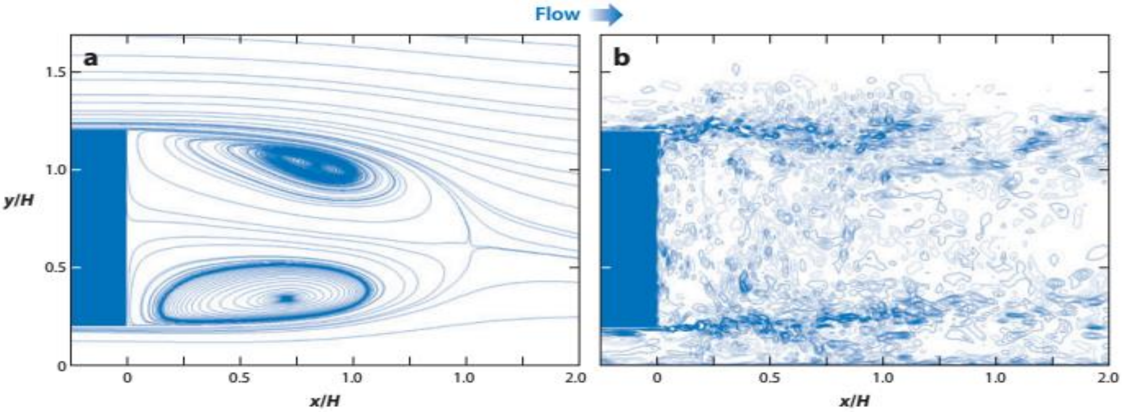

Fig. 3.4. Side view of the flow structure in the near wake behind the GM model on the vertical plane of symmetry: a) time-averaged streamlines and b) contours of the instantaneous spanwise vorticity (Choi, et al., 2014; Lee & Choi 2009).

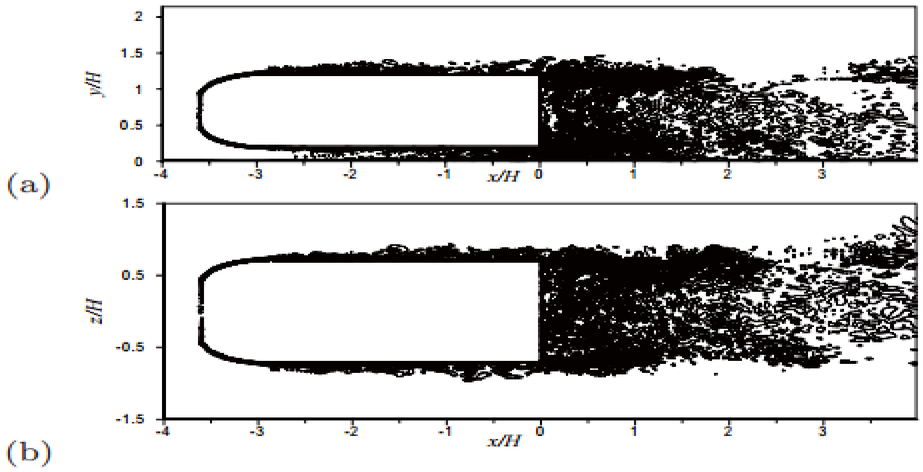

Fig. 3.5. Instantaneous vorticity contours around GM model: a) spanwise vorticity in the symmetrical plane and b) transverse vorticity in the horizontal plane (Lee & Choi 2009).

3.2 Flow features around real ground vehicles

3.2.1 Flow around a bus

We can use the GM model to analyse the flow around buses. It is clear that there is a noticeable similarity between the geometric shape of such vehicles and of the GM model. Aerodynamically, the flow separates at the front lateral and roof edges and then reattaches so the separation bubble appears. There are two parameters which are used to explain the behaviour of the aerodynamic performance for buses: the Reynolds number and the front-edge roundness, given as:

$$\text{Roundness} = {}^{r}\!/_{\sqrt{A}} \tag{3.1}$$

where the r is the radius of the front edge and the A is the area of the cross section of the bus. As the Reynolds number increases, the drag force decreases significantly before the drag force stays constant and the separation bubble disappears (Choi et al., 2014, Krajnović and Davidson, 2005). As a result, the value of the front-edge roundness of buses should reach more than 0.125 to avoid high drag due to flow separation.

Krajnovic and Davidson (2005) investigated the flow structure around a bus shaped model vehicle at the Reynolds number of 0.21×10^6 in zero yaw conditions and they discovered a new smaller-scale flow structure which was revealed by using LES. In their study, it is clear that the difference between the instantaneous flow field and the time-averaged one is significant. Fig. 3.6 and Fig. 3.7 show the features of flow separation at the front lateral and roof edges. As can be seen, the hairpin vortices are formed in these separation regions and these vortices are aligned so that their axes are parallel with the separation lines. The two ends of hairpin vortices are attached to the surface. These vortices are broken down soon after they are generated. In a time-averaged visualisation, the vortices are formed on each side and on the roof, revealing the separation lines, see Fig. 3.7.

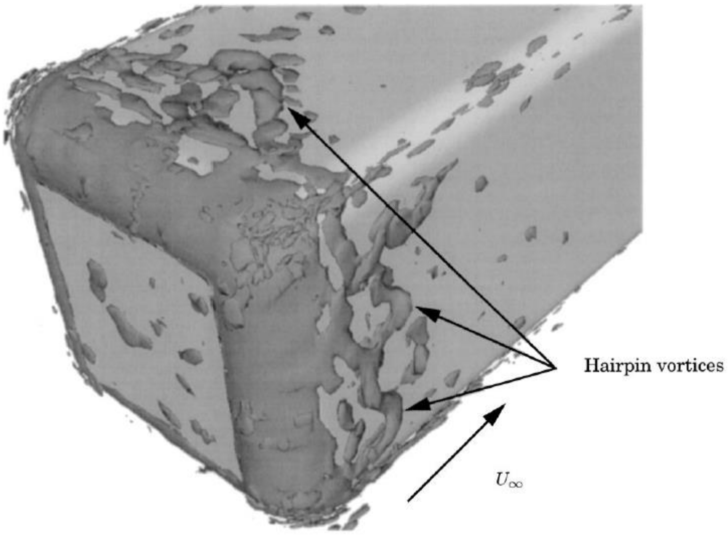

Fig. 3.6. Instantaneous visualisation of the isosurface of instantaneous second invariant of the velocity gradient around the GM model (Krajnovic and Davidson 2005).

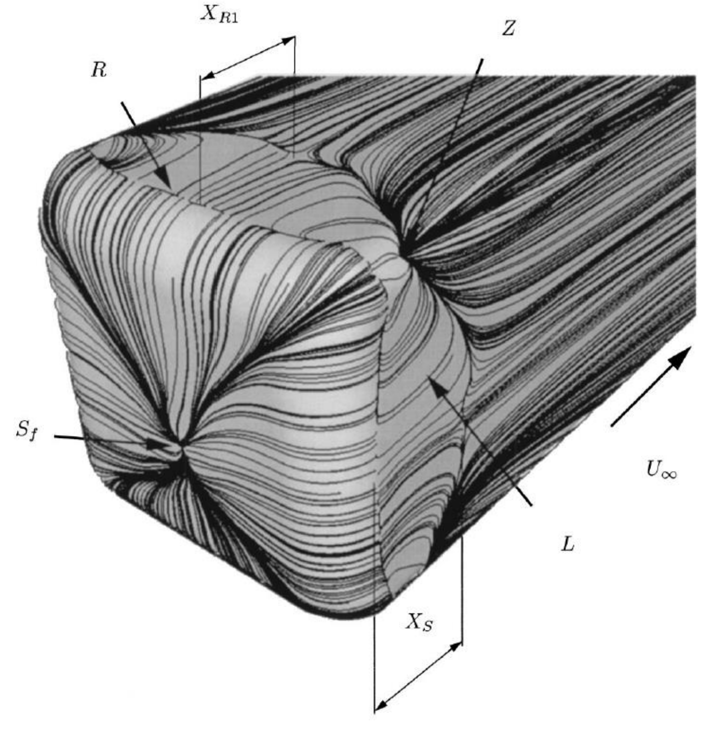

Fig. 3.7. View of the front face of the GM model showing time-averaged trace lines on the surface of the body showing the roof vortex ,(R) the lateral vortex (L) and the stagnation point (S_f). (Krajnovic and Davidson 2005).

Fig. 3.8 shows the time-averaged flow structure around the rear part of the body. As can be seen in the upper right hand corner, two trailing vortices U_p and U_s and one very thin separation bubble C_u are visible. Fig. 3.9 shows a transverse slice through these vortices which are parallel to the surface of the body in the longitudinal axis. Similarly, a strong trailing vortex (denoted by T in Fig. 3.8) extends from the lower edges. As this flow structure is analysed it can be seen that the vortex increases in size and then reduces again, moving downstream, Fig. 3.10. All of these flow features show how complex the flow field can be around bodies such as these.

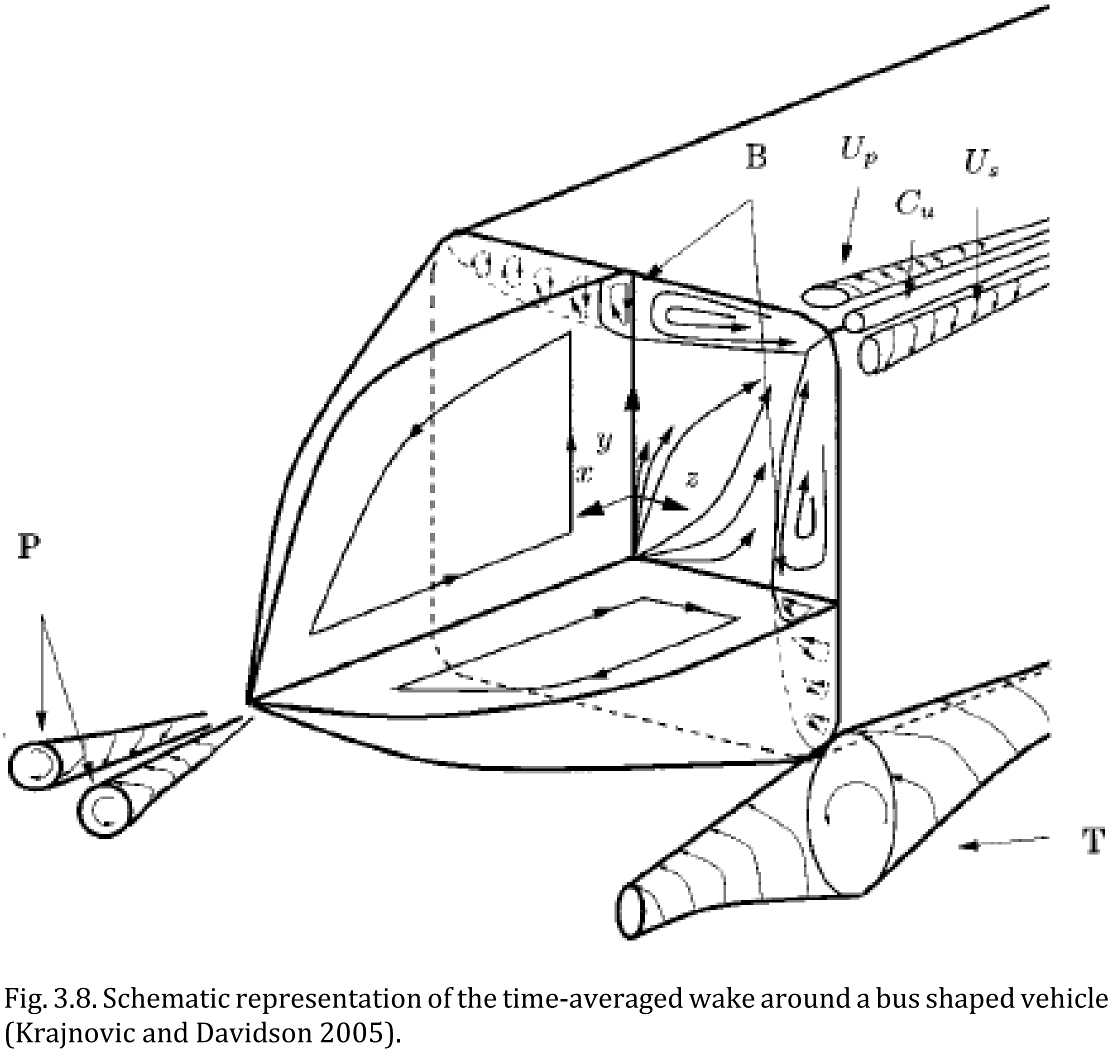

Fig. 3.8. Schematic representation of the time-averaged wake around a bus shaped vehicle (Krajnovic and Davidson 2005).

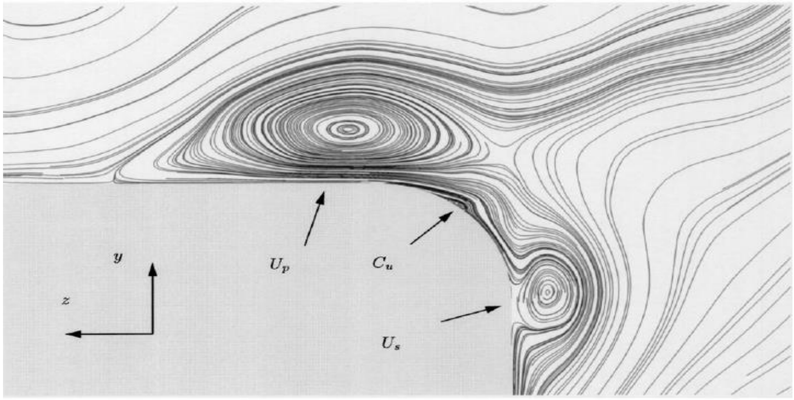

Fig. 3.9. Transverse view looking from behind the GM body showing time-averaged streamlines, sliced through the upper-right trailing vortices. Note that the rotation of vortices U_p and U_s are counter clockwise and clockwise, respectively (Krajnovic and Davidson 2005).

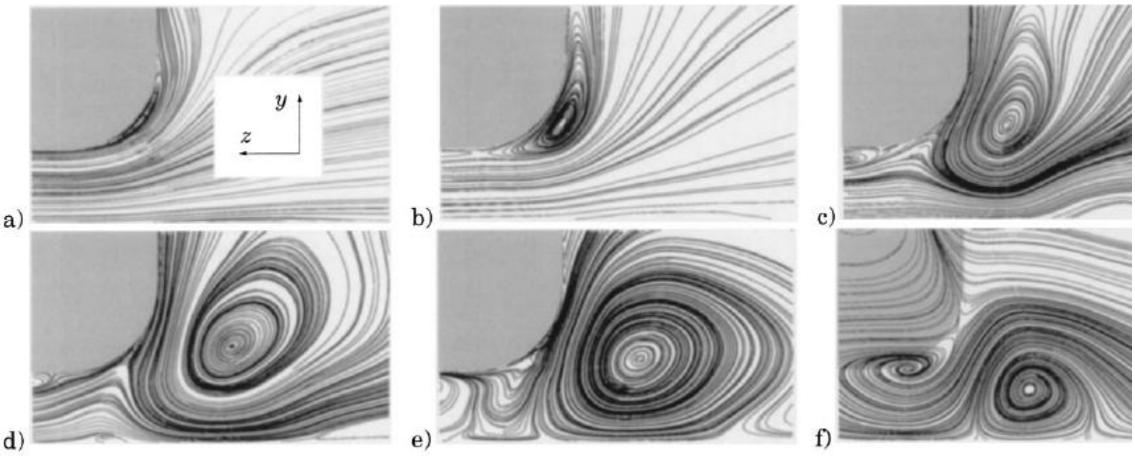

Fig. 3.10. Time-averaged streamlines projected onto planes: a) x=-3.36H, b) x=-2.88H, c) x=-1.68H, d) x=-0.48H, e) x=0, and f) x=0.32H. Note that the direction of the rotation of this vortex, *T*, is counter clockwise. View from behind of the lower-right edge of the body (Krajnovic and Davidson 2005).

3.2.2 Flow around tractor-trailer vehicles

The main features of the flow structure around a tractor-trailer include: the stagnation region at the front of the tractor, flow separation at the rear edge of the tractor, two counter rotating vortices in the separation gap between the tractor and the trailer and a long wake behind the trailer unit. Some or all of these flow features can be replicated using numerous simplified models to study the flow around tractor-trailer type vehicles. The simplified models are the ground transportation system (GTS) and the generic conventional model (GCM), see Fig. 3.11. Note that the standard GTS model has no gap, no wheels and no undercarriage, whereas the standard GCM model is more complex and includes these features. Both models have more developed versions to add realism which leads to the modified ground transportation system model (M-GTS) and the modified generic conventional model (M-GCM).

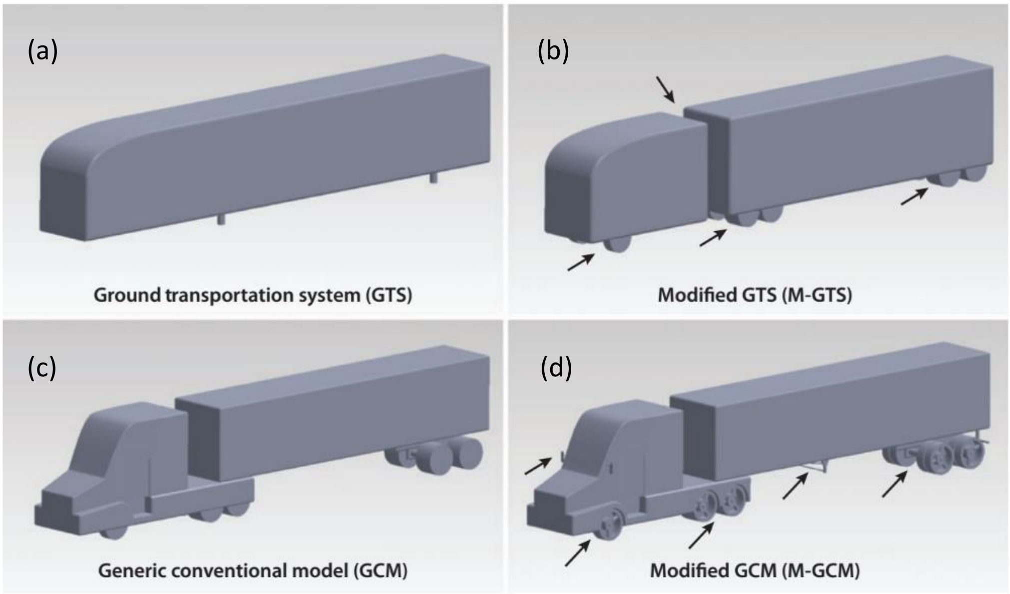

Fig. 3.11. Simplified tractor-trailer models: a) GTS, b) M-GTS, c) GCM and d) M-GCM (Choi, et al., 2014).

Lo and Kontis (2017) conducted an experimental study to investigate the flow structure around a European-type tractor-trailer vehicle at a Reynolds number of 6×10^5 in zero yaw conditions using a 1:20 scale model. This is designed based on some common UK HGVs with articulated lorries, see Fig. 3.12.

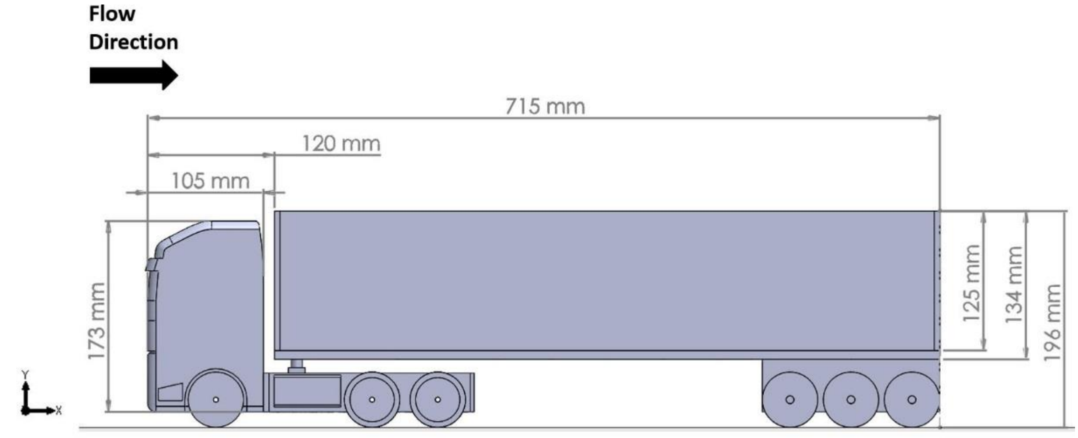

(a) Side View

(b) Top View

Fig. 3.12. A 1:20 scale articulated HGV model viewed from a) side and b) top (Lo and Kontis, 2017).

Experimental results from this study are presented in Fig. 3.13a which shows the overall flow structure over the HGV. Of particular interest is the stagnation region (ST) at the front of the model and massive flow separation at the rear end (SP) which produces an upper shear layer (SL_U) (Lo and Kontis, 2017). The authors of this study also carried out some CFD analysis, Fig. 3.14, and there are clear similarities with the flow features already mentioned from the experimental work, Fig. 3.13. Another observation was a clear acceleration region over the curved roof of the cab unit before hitting the sharp edge of the trailer's roof creating a secondary stagnation region (ST_2) which in turn induces separated flow and a recirculating bubble (SB) on the front portion of the trailer's roof. In the experiments, Fig. 3.13c shows a large recirculation bubble (VC) behind the vertical base, in addition to two shear layers (SL_U) and (SL_L) coming from the upper and lower sections of the trailer, respectively.

As with Krajnovic and Davidson (2005), Lo and Kontis (2017) found that there is a significant difference between the instantaneous flow field and the time-averaged one, especially in the recirculation region behind the vertical base. In a time-averaged visualisation, one vortex was found in the recirculation region Fig. 3.13 and Fig. 3.14. On the other hand, Lo and Kontis (2017) found two vortices in the same region.

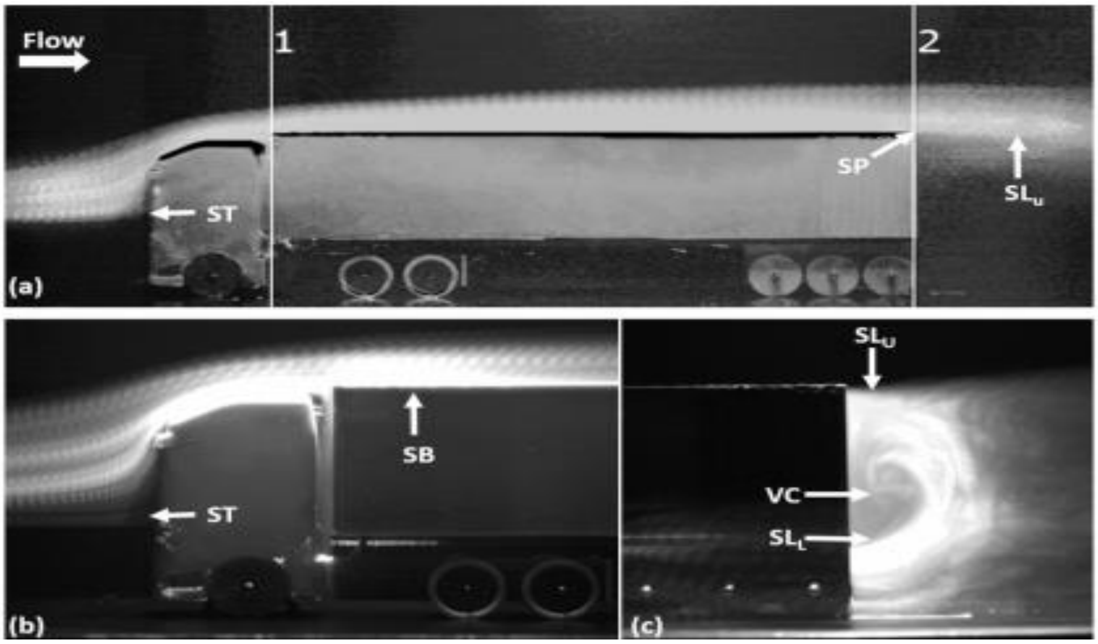

Fig. 3.13. Experimental flow structure over an HGV showing a) Overall flow pattern, b) front region and c) base region (Lo and Kontis, 2017).

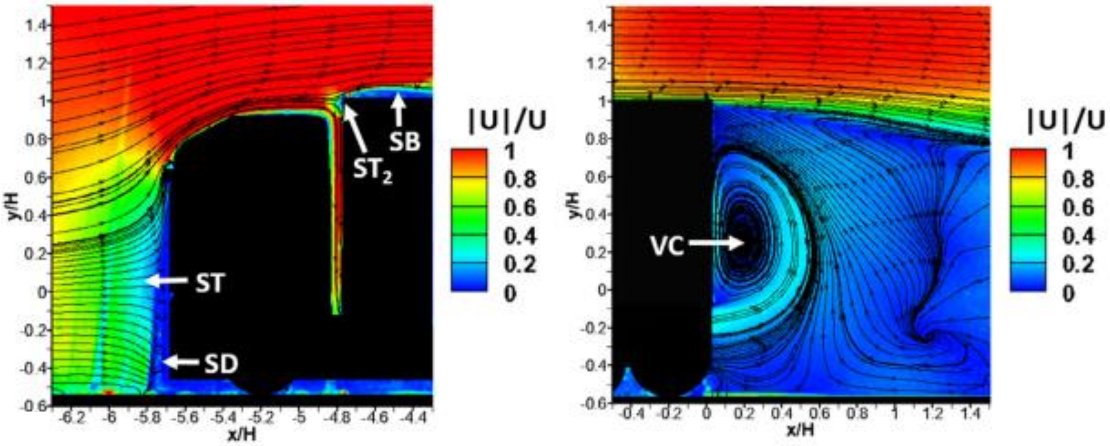

Fig. 3.14. CFD visualised velocity contours over the front and rear part of the HGV (Lo and Kontis, 2017).

Moving on from the overall flow field, the airflow through the gap between tractor and trailer units has been shown to have an important effect on the net drag force (Choi et al., 2014, Hyams et al., 2011). The configuration is effectively represented by two buses, one following the other. The effect depends on the gap size and yaw angle. For example, Fig. 3.15 shows that when the gap clearance is between $0.1 \leq G/\sqrt{A} \leq 0.5$, where G is the gap distance and A is the frontal area of the vehicle, experimentally, the drag will be relatively low. The flow structure inside the gap consists of two counter-rotating vortices as can be seen in Fig. 3.15b (Choi, et al., 2014).

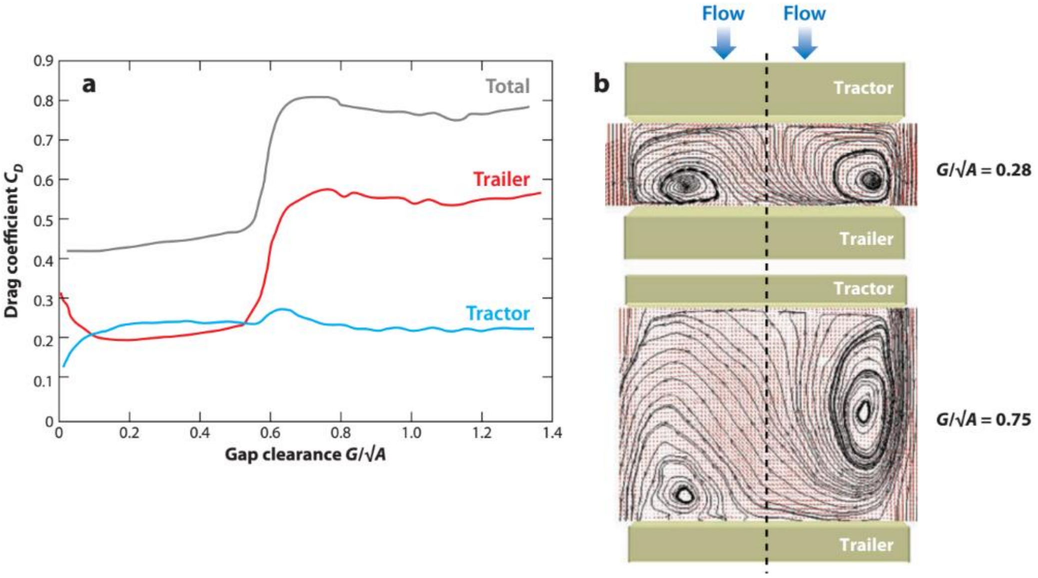

Fig. 3.15 a) The drag coefficients as a function of gap clearance, b) top view of the time-averaged flow structure in the gap between tractor and trailer (Choi, et al., 2014).

The behavior of the vehicle's drag is related to the flow structure in the gap, as this gap increases. When the gap clearance is between $0.1 \leq G/\sqrt{A} \leq 0.5$ the drag is low because the flow inside the gap consists of two steady symmetric counter-rotating vortices so a low-pressure region at the front face of the trailer exists and the trailer experiences comparatively low drag. Moreover, when the gap increases to $G/\sqrt{A} \geq 0.5$, the two vortices break down and the flow becomes unsteady with extensive flow separation at the rear edge of the tractor and an increase in the pressure at front face of trailer occurs, thereby increasing drag. At low yaw angles, the relationship between gap clearance and the drag is strong. In contrast, at high yaw angles, this relationship becomes weak because the flow passes through the side of the gap, dominating the flow structure there which increases the pressure on the front face of the trailer so its drag rises (Choi, et al., 2014).

Moving further downstream, the flow structure of a typical tractor-trailer has a significant and elongated wake zone behind the trailer. The wake structure, from time-averaged analysis, consists of two large recirculation bubbles, similar to the wake structure of the GTS model, (Ortega et al., 2004; Roy et al., 2006) (Fig. 3.16). Ortega (2004) found using unsteady

CFD analysis that separation shear layers extend from the rear edges of the trailer, which roll up into vortex rings before they mix with the wake in the base region (Ortega et al., 2004).

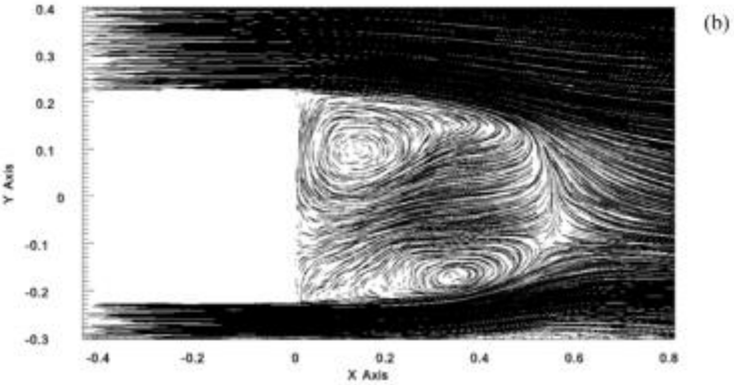

Fig. 3.16. Time-averaged velocity fields in vertical symmetric plane (Ortega et al., 2004).

The flow structure around a tractor-trailer can also be influenced by a crosswind, causing a flow separation region at the front lateral edge of the tractor (A-pillar vortex) and a separation bubble, as revealed from Detached Eddy Simulation (DES), see Fig. 3.17 and Fig. 3.18 (Maddox et al., 2004). In addition, the aforementioned crosswind effect of flow in the gap increasing the pressure on the front face of the trailer (Choi, et al., 2014) also occurs, contributing to a drag rise (Maddox et al. 2004). Moreover, the crosswind causes flow separation at the leeward side edge of the trailer so the side force on the vehicle increases significantly, influencing the stability of the vehicle.

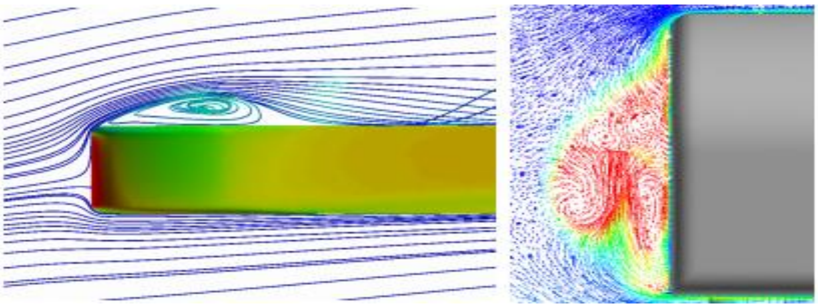

Fig. 3.17 Streamline and velocity vectors from DES prediction of the flow at a 10^{o} yaw angle. GTS surface coloured by pressure in the left frame, velocity vectors coloured by the eddy viscosity ratio in the right frame (Maddox et al., 2004).

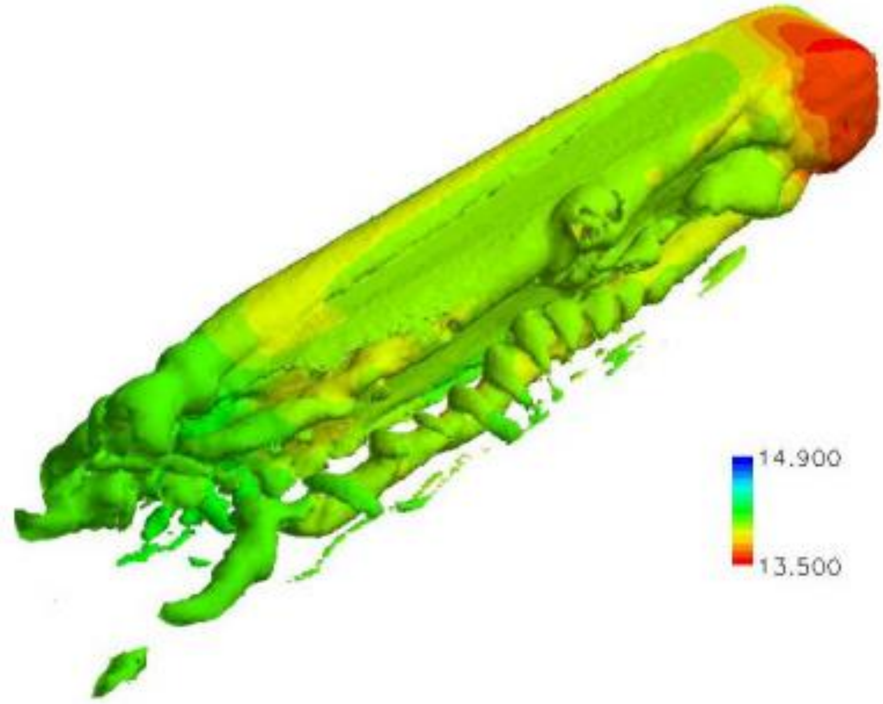

Fig. 3.18 Instantaneous vorticity isosurfces coloured by pressure from DES results at a 10^0 yaw angle (Maddox et al. 2004).

Ground effect is another important aspect of the aerodynamic performance and flow structure of tractor-trailer units/HGVs. Many studies explain that increasing ground proximity affects the flow structure leading to a rise in the aerodynamic drag force (see e.g. Choi, et al., 2014; Storms et al. 2004). However, ground proximity is largely a fixed parameter for HGVs and the focus of this thesis is the contouring of the upper region of such vehicles. Therefore, ground effect is not explored in any further detail here.

3.3 Review of flow control and drag-reduction devices for heavy vehicles

In this section, various types of drag-reduction devices used with HGVs or similar vehicles will be considered. These devices are generally classified in relation to their location, typically on the forebody, base, and underbody. More recently, over-body drag reduction has been used so a short review of the limited literature in this area is also described.

3.3.1 **Forebody drag reduction devices**

Forebody drag reduction devices are widely used with tractor-trailer vehicles to enhance their aerodynamic performance. Typically, these are located immediately in front of tractor units and in the gap between the tractor and trailer. These devices are very important because about 45% of the total drag force is generated in the front part of tractor-trailer, including 25% at the nose of the tractor and 20% in the gap, see Fig. 3.19 (Wood, 2006). It has been shown that by making the all corners/edges of the front face of the tractor smoother and by using a small fairing on the roof of the tractor unit itself, fuel savings of roughly 20% can be realised for tractor-trailers (Choi et al., 2014).

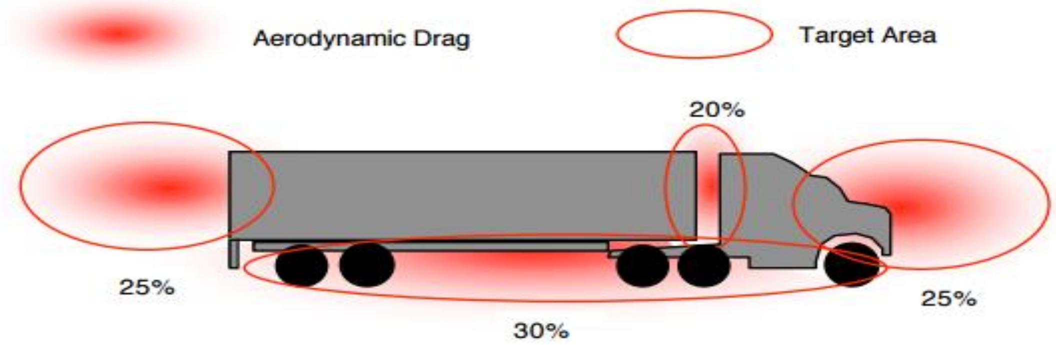

Fig. 3.19. Aerodynamic drag distribution for a tractor-trailer (Wood, 2006).

Generally, there are various strategies for minimising forebody drag. Careful control of the flow around the front face of the tractor, making it more streamlined, can be effective. Fig. 3.20 shows an array of devices located on the tractor, including a vertical fence (Allan, 1981, Choi et al., 2014), a cab deflector (Malviya et al. 2009; Choi et al., 2014), moving surface boundary-layer control (Malviya et al. 2009; Choi et al., 2014), and a front spoiler (Hyams et al., 2011; Choi et al., 2014). The front spoiler reduces drag by decreasing the flow velocity in the underbody region, whereas the other devices mentioned above enable better airflow over the tractor, minimising stagnation on the front of the trailer unit.

Another key strategy is to control the airflow in the gap between typical tractor-trailer units. There are many devices which use this strategy, including gap enclosure (Allan 1981; Choi et al., 2014), cab side extenders (Storms et al., 2004, Hyams et al., 2011, Choi et al., 2014), trailer splitter plates (Hyams et al. 2011; Mohamed-Kassim & Filippone, 2010; Choi et al., 2014), cross-flow vortex trap devices, tractor splitter plates, and base bleeding (Ortega et al., 2009, Choi et al., 2014), see Fig. 3.20.

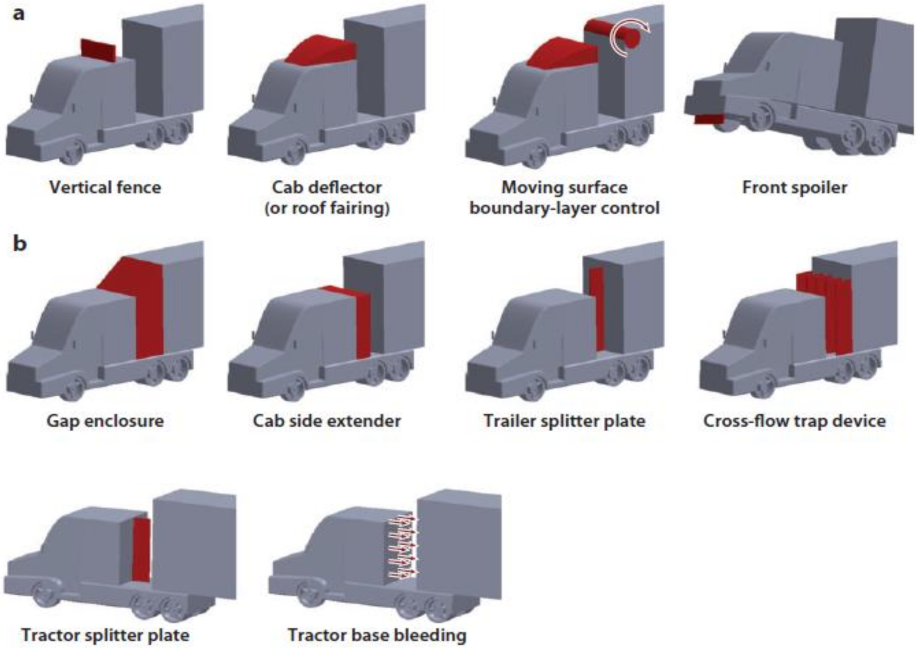

Fig. 3.20. Typical forebody drag reduction devices: a) forebody flow control, b) Gap flow control. (Choi, et al., 2014).

Using side extender devices to control the gap flow is also very common. These devices reduce the drag force by delaying flow separation. In contrast, base bleeding devices are less popular because they cost more money to implement and operate, however, they have a significant effect on drag with drag reduction of up to $\Delta C_D = 0.146$ realised (Ortega et al., 2009; Choi et al., 2014).

All these devices are strongly affected by crosswinds, so their aerodynamic performance depends on the angle between the direction of the vehicle and the oncoming wind, β, also known as the yaw angle. As can be seen in Fig. 3.21, the drag reduction of cab deflector and tractor splitter plate devices decreases with the yaw angle whereas the drag reduction of the gap enclosure improves. It is clear that a promising solution is to use side extenders which can reduce the drag by between ~28% and 42%, depending on the yaw angle. It should be noted that the benefit of side extenders depends on their length; interestingly, the details of the drag reduction mechanisms are still not clear (Choi et al., 2014).

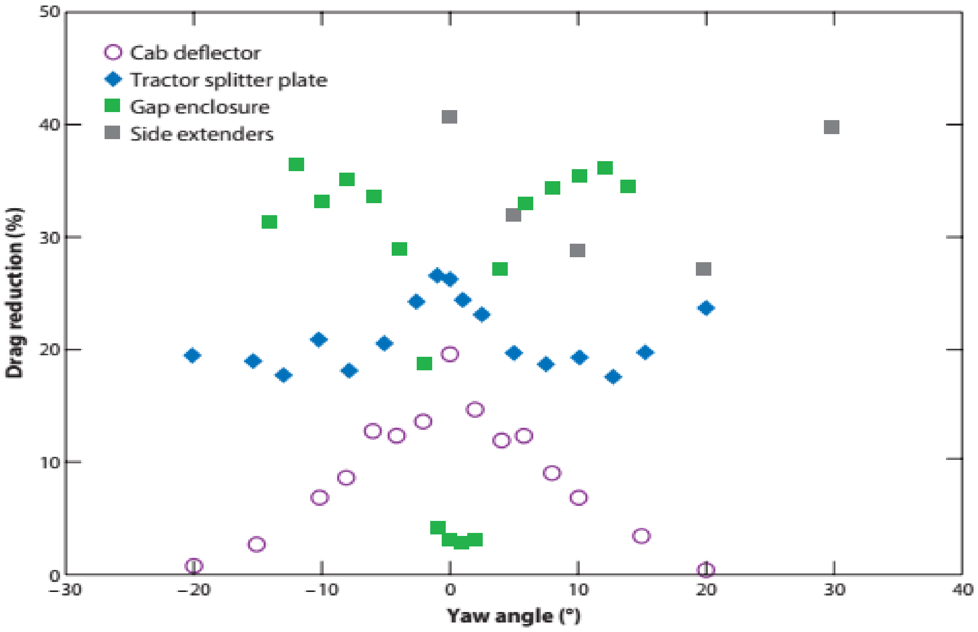

Fig. 3.21. The drag reduction of various devices as function of the yaw angle (Choi, et al., 2014).

3.3.2 Base drag reduction devices

Another broad category of drag reduction devices relates to those influencing the base region. It is widely acknowledged that the drag generated in the base of most HGVs is large because the end edges are typically sharp with an abrupt end of the trailer unit (Hucho and Sovran, 1993). For example, Wood (2006) found that around 25% of the drag is due to energy losses in the base region. More recently, there have been many research studies focusing on the understanding of unsteady vortical flow structures in the wake behind HGV-type vehicles with an aim being to help to design new passive or active drag reduction devices. Choi et al., (2014) concluded that a good understanding of these unsteady flow phenomena are needed to come up with effective design solutions (Choi et al., 2014).

In general, there are two broad bluff body shapes representing the tail end of road vehicles, namely: fast-back and square-back types. Base drag reduction devices for fast-back vehicles are associated with the Ahmed body model (Ahmed et al., 1984) and Fig. 3.22(a) shows a selection of these. As mentioned before, the separation bubble and a pair of vortices are the dominant features within the flow structure for the Ahmed model and they are largely responsible for the pressure drag. Therefore, there are two primary strategies used to reduce the drag force on such vehicles. One strategy is to exclude and prevent the separation bubble by making the flow fully attached on the slanted surface. There are various methods suitable for achieving this. One of these is to install a group of small objects (such as vortex generators) on the top of the slanted area, or slightly upstream of the slant. This serves to generate coherent stream-wise vortices that promote high-momentum flow near the wall, thereby preventing the separation bubble (Pujals et al., 2010). Another method used is to make the edge between the roof and the slanted surface more rounded so the flow on the slant area remains fully attached for longer (Choi, et al., 2014).

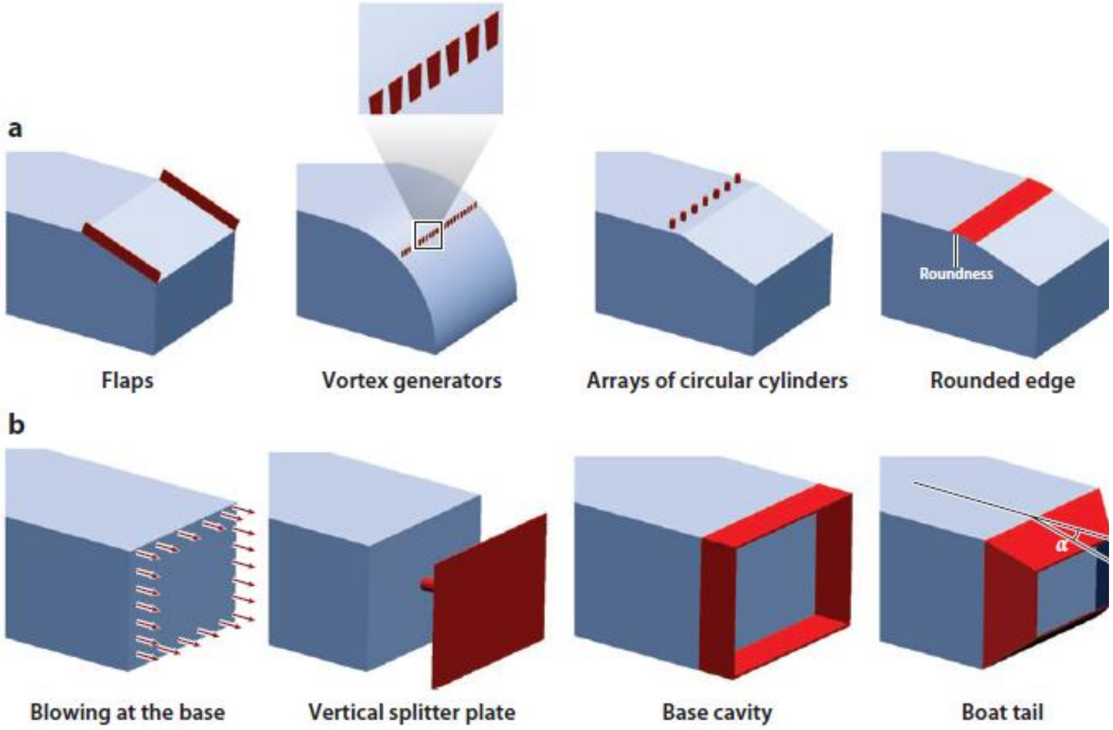

Fig. 3.22. Base region drag reduction devices: a) Fast-back. b) Square-back (Choi, et al., 2014).

An alternative strategy is to reduce the strength of the longitudinal vortices (Choi, et al., 2014) by inducing fully separated flow from the transverse edge at the point where the roof and slanted surfaces meet; the resulting flow field is similar to that of the low-drag regime at the critical slant angle $\alpha = 30^\circ$ (recall section 3.1). An example of a device which uses this strategy are flaps as shown in Fig. 3.22(a). These flaps interrupt the flow reattachment to the slanted surface which would normally occur due to the trailing vortices; by making the flow fully separate, the formation of these longitudinal vortices is prevented (Beaudoin and Aider, 2008). Another method is to insert vortex generators on the slanted surface at the main separation point. If they are carefully positioned, these vortex generators can instigate early separation and a very large recirculation bubble which dominates the flow field and prevents the longitudinal vortices from forming, which can lead to an overall drag decrease (Aider et al., 2010).

Base drag reduction devices for square-back vehicles are associated with the GM model and Fig. 3.22(b) shows typical solutions which are suitable for these vehicles (such as HGVs). As previously mentioned, attributes of the flow field of the GM model are dominated by large recirculation bubbles and flow separation at the base, leading to high pressure drag. Therefore, typical strategies for reducing the drag force in this case is to reduce the size of the recirculation bubbles and/or by shifting them away from the base (Choi, et al., 2014; Hucho, 1986). Numerically, (Littlewood and Passmore, 2012) investigated a blowing system at the base, finding that the drag can be reduced by up to 50% compared with the baseline. Although active blowing at the base has a significant beneficial effect on reducing aerodynamic drag, they are not widely used because the installation and operating costs are prohibitive (Englar, 2001). Vertical splitter plates are also effective but they are totally impractical because of their size, see Fig. 3.22(b). Related to this, (Gilliéron and Kourta, 2010) investigated by experiments the concept of vertical splitter plates, finding that the drag can be reduced by up to 45% compared with the baseline; again, this is not a very practical design.

In practice, base cavities and boat tails are the most promising design solutions. Both rely on delaying base flow separation and pushing the recirculation bubble away from the vehicle and/or reducing its size (Khalighi et al., 2001), see Fig. 3.23. Fig. 3.23 illustrates this effect by showing the change in the structure of the wake at the base of a typical bluff body, before and after installation of cavities (middle row of images) and boat tails (bottom row of images). Clearly, the size of the recirculation bubble is reducing, and, in the case of the cavity, these recirculation regions are being pushed downstream from the vehicle. The size of the separated flow region for the boat tail design is noticeably smaller because the cross-section at the base has reduced.

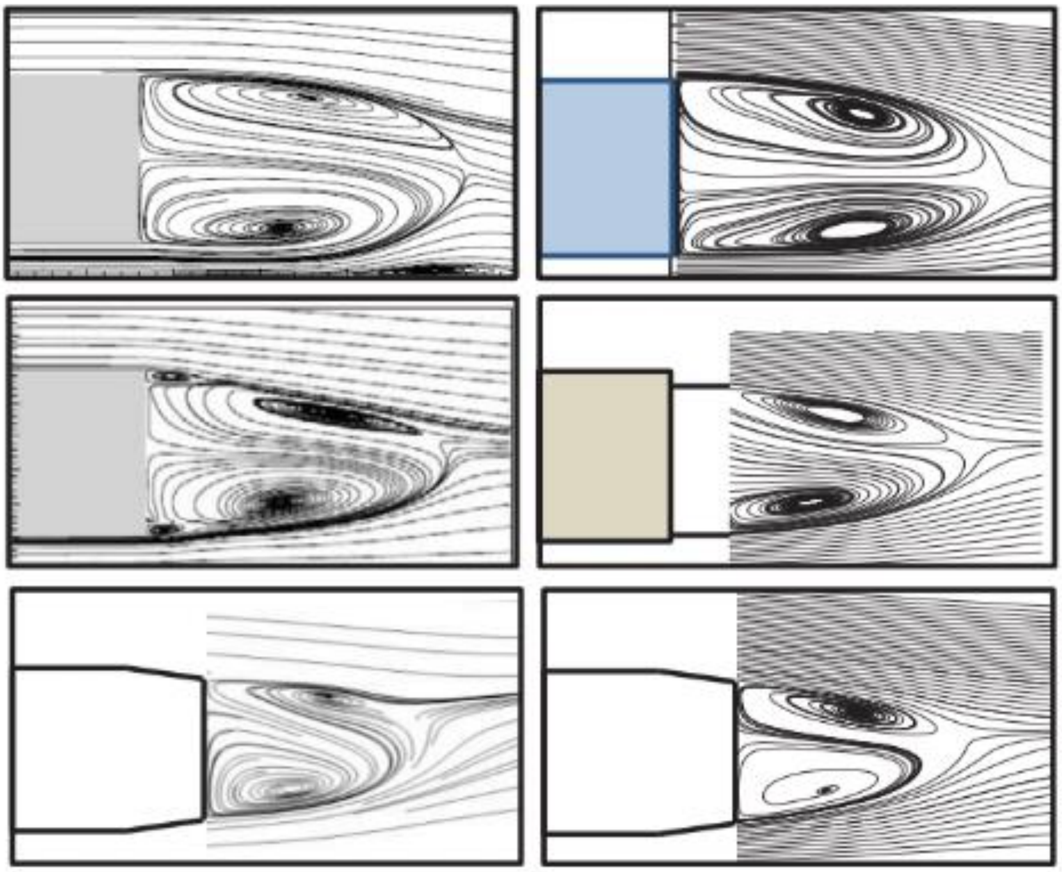

Fig. 3.23. Side illustrations showing streamlines on the symmetry plane at the base of a bluff vehicle, (left) CFD simulation results, (right) PIV measurements: (top) square-back, (middle) cavity device and (bottom) boattail device (Khalighi et al., 2001).

Khalighi et al. (2001) found that the drag can be reduced by about 18% and 30% by using the cavity and the boat-tail, respectively. Interestingly, a boat tail with a cavity has more drag reduction than a solid boat tail which (Balkanyi et al., 2002) verified experimentally, observing a reduction of about 50%. The effectiveness of a boat tail design is a function of its length and slant angle, α (Wong and Mair, 1983, Yi et al., 2007). For example, Yi et al., (2007) investigated the effectiveness of a boat tail experimentally as a function of α. As shown in Fig. 3.25, he highlighted under what conditions the flow is fully attached, separated, where it is reattaches and where the separation bubble can occur. Fig. 3.24 shows this relationship which is characterized by four different regions. In the first region ($0^{o} \leq \alpha \leq 5^{o}$) the flow is fully attached to the slant surface. As the slant angle increases further ($5^{o} \leq \alpha \leq 1\ 5^{o}$), flow separation initiates from the front edge of the sloped area and a corresponding small separation bubble is created in the same area. This separation bubble increases in size with the slant angle, however, massive separation is delayed by strong near-wall momentum so the drag continues to decrease significantly until it reaches a minimum at 15˚. In the third region ($16^{o} \leq \alpha \leq 19^{o}$), beside the separation bubble, a pair of counter-rotating longitudinal vortices appear and their strength increases as the angle of the slope area rises which leads to a dramatic increase in overall drag. In the forth region ($\alpha \geq 20^{o}$), the drag reaches the maximum which is equal to the drag of the base vehicle without the boat tail i.e. the flow has fully separated from the leading edge of the boat tail (Choi et al., 2014, Yi et al., 2007), see Fig. 3.24 and Fig. 3.25. Note that some of these flow features can be determined from the on-surface oil flow images from the wind tunnel experiments shown in Fig. 3.25; the relationship between Fig. 3.24 and Fig. 3.25 is clear to see.

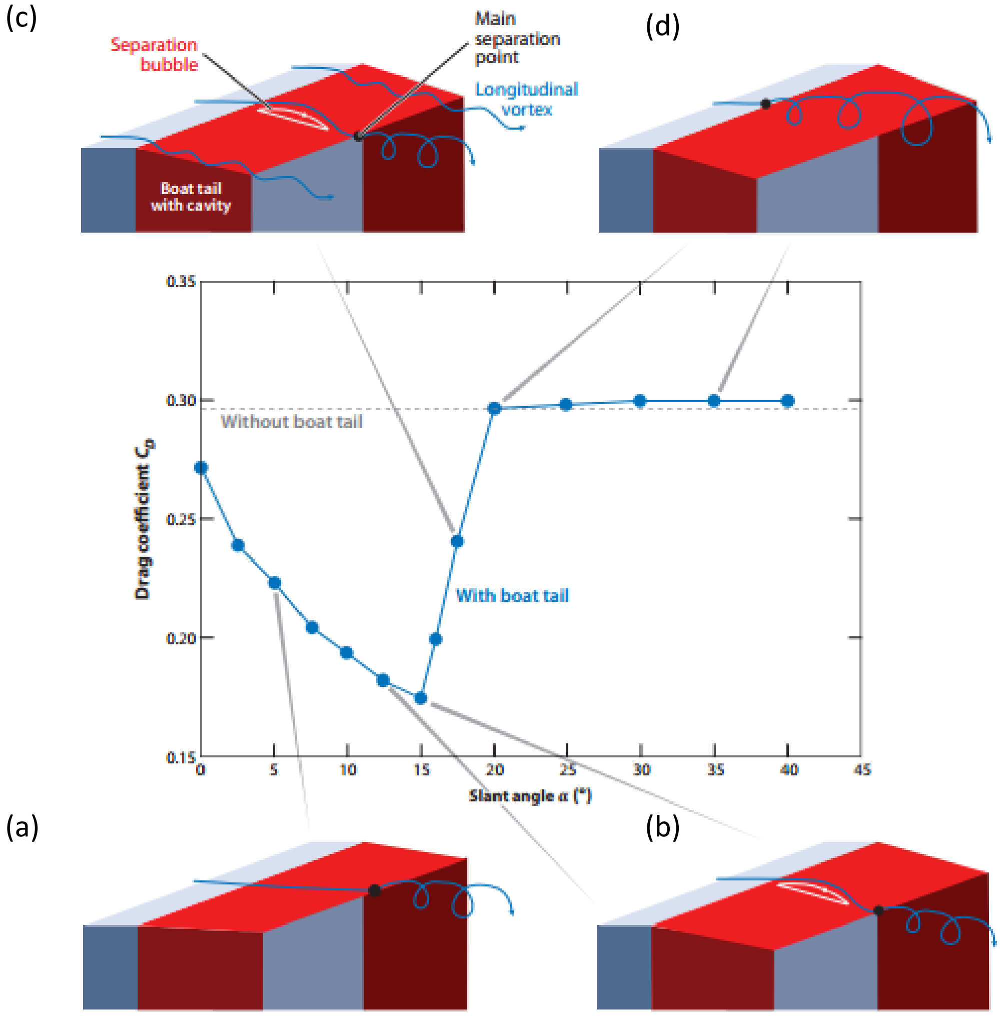

Fig. 3.24. Drag coefficient of the GM model using the boat tail as function of the slant angle, α .Labels a), b), c) and d) relate to Fig. 3.25 (Choi et al., 2014, Yi et al., 2007).

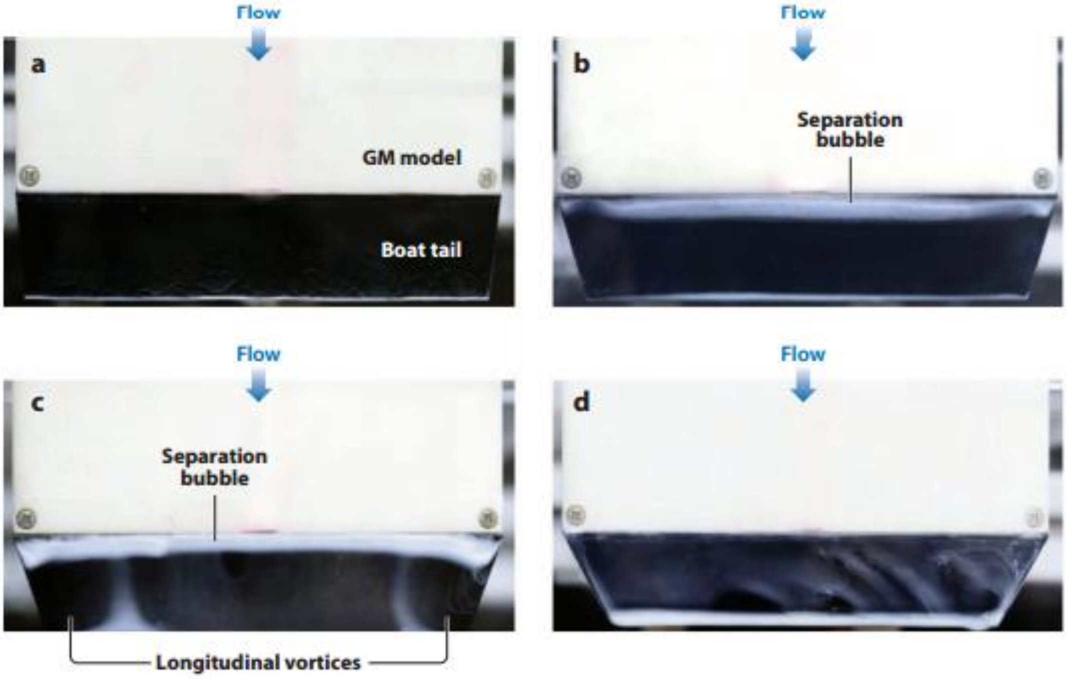

Fig. 3.25. Oil-flow visualisation on the upper plate of a boat tail attached to the GM model at *Re* =1.75 ×10^5 : a) α=5˚, b) 15˚, c) 17.5˚ and d) 25˚(Choi et al., 2014, Yi et al., 2007).

3.3.3 Underbody drag reduction devices

The third general class of drag reduction device is the underbody type. According to Wood (2006), a significant drag source is from the underbody region, which generates about 30% of the total drag. Fig. 3.26 shows a small selection of devices suitable for underbody drag reduction. These include undercarriage straight skirts, belly boxes, and undercarriage wedge skirts. The purpose of these is to decrease the drag by shielding flow from entering under the body of typical HGVs through the side of the trailer unit. As underbody devices are not the focus of this research, this will not be explored any further.

A summary for the three types of drag-reduction devices used in heavy vehicles aforementioned above is presented in Table 3.1.

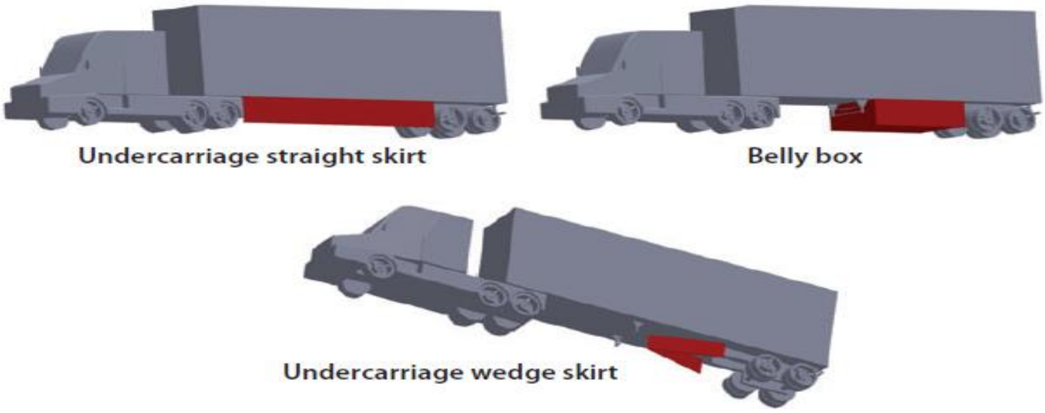

Fig. 3.26. A selection of typical underbody devices (Choi, et al., 2014).

Table 3.1 Summary of the literature review for the three types of drag-reduction devices used in heavy vehicles.

	Reference	Baseline	Device	C_d Baseline	C_d	Drag Reduction
1	(Malviya et al., 2009)	Tractor-trailer	Cap roof fairing	0.9 (Exp)	0.78 (CFD)	13.33%
2	(Malviya et al., 2009)	Tractor-trailer	Moving Surface Boundary Layer Control (MSBC) system	0.9 (Exp)	0.79 (CFD)	12.22%
3	(Malviya et al., 2009)	Tractor-trailer	Both (Cap roof fairing + MSBC)	0.9 (Exp)	0.70 (CFD)	22.22%
4	(Littlewood & Passmore, 2012)	Square Back (SB)	steady blowing	/	/	(3%-12%) (Exp)
5	(Gillieron & Kourta, 2009)	Ahmed Model (0°)	vertical splitter plates	0.305 (Exp)	/	(-1%-12%) (Exp)
6	(Gillieron & Kourta, 2009)	Ahmed Model (25°)	vertical splitter plates	0.448 (Exp)	/	(-8%-45%) (Exp)
7	(Beaudoin & Aider, 2008)	Ahmed Model (30°)	flaps fixed on edges	(0.365-0.355-0.351) (Exp)	/	To 25% (Exp)
8	(Krishnani & Zhou, 2009)	Sport utility vehicle (SUV)	Upper And Lower Flat Tail Plates	0.29829 (CFD)	0.27151 (CFD)	8.98% (CFD)
9	(Khalighi. et al., 2001)	Square Back (SB)	Cavity	0.300 (Exp)	0.240 (Exp)	20% (Exp)
10	(Verzicco et al., 2002)	Square Back (SB)	Cavity	0.300 (Exp)	0.279 (CFD)	7%
11	(Verzicco et al., 2002)	Square Back (SB)	boat-tail	0.300 (Exp)	0.23 (Exp)	23.33% (Exp)
12	(Wahba et al., 2012)	Square Back (SB)	Lateral guide vanes	0.995 (Expl)	/	Up to 18% (CFD)
13	(Wahba et al., 2012)	SUV	Lateral guide vanes	0.57 (Exp)	/	Up to 18% (CFD)
14	(Mosaddeghi et al, 2015)	Tractor-trailer	Cab vane +deflector+ base flap	/	/	41% (CFD)
15	(Ortega & Salari, 2004)	Tractor-trailer	Wedge-shaped skirt+ curved base flaps	/	/	20%
16	(Aider & Beaudoin, 2010)	modified Ahmed model	Vortex generators	/	/	12%
17	(Pujals et al. 2010))	Ahmed Model (25°)	Coherent streamwise streaks	/	/	10%
18	(Holt J. et al., 2015)	LGV	Roof Curvature			Up to 12.5% (Experimental)

3.3.4 **Effect of roof curvature**

As already briefly described in Chapter 1, roof curvature or over-body design is a relatively new passive flow control method and is often used with other drag reducing devices to improve the aerodynamics of HGVs. The practical use of roof curvature on fleets of HGVs has been shown to produce significant reduction in fuel consumption (Holt et al., 2015). Indeed there is a wide variety of over-body solutions on HGVs operating throughout the UK transport industry and various solutions have been used for about the past 10 years, see Fig. 3.27.

Fig. 3.27. Examples showing contemporary curved roof sections of HGV compared to the Labatt's streamliner from 1947 (Cooper, 2004, De Boer et al., 2016).

Despite their prevalence, to the authors' knowledge, there is no publicly available CFD or wind tunnel data to quantify performance benefits or to offer design guidance (e.g. the amount of curvature required, position of maximum camber etc.) (Holt et al., 2015). This is not a new idea because the Labatt's streamliner, a fire engine, showed an early iteration of this streamlining concept in 1947 as detailed in the review by Cooper (2004). This vehicle is shown in the upper right of Fig. 3.27 and the similarities between it and present day solutions is clear.

The only notable academic study for quantifying the effect of roof curvature on bluff vehicle aerodynamics is the study by Holt et al., (2015) who used a 1/8th scale model of a light goods vehicle (LGV), based on the Mercedes Sprinter, see Fig. 3.28.

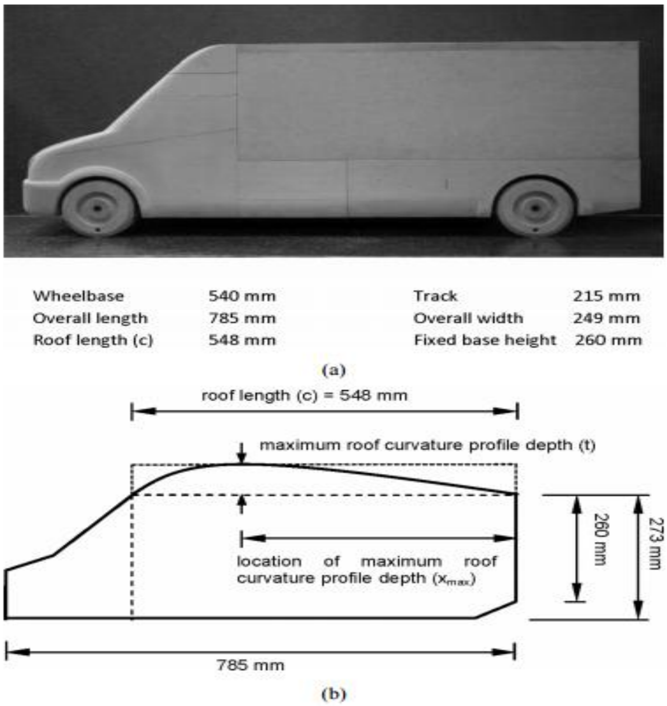

Fig. 3.28. View of a) baseline LGV wind tunnel model based on the Mercedes Sprinter and b) schematic arrangement of the modular vehicle configuration highlighting key roof profile parameters (Holt et al., 2015).

They carried out a series of measurements of drag force at different yaw angles, $-6° \leq \beta \leq 16°$, for six different curved roof profiles. Moreover, they investigated the effect of changing two parameters of roof curvature, namely the magnitude and position of the maximum roof profile depth, in crosswind conditions. A summary of their main findings, including images of the configurations tested are shown in Fig. 3.29.

No.		*Roof profile* *(NACA 4- and 5-digit series notation)*	*Max roof curvature profile depth (t/c)* (%) *and* *t* (mm)	*Location of roof max roof curvature profile depth forward of base (x/c)*	*Reference area* A (m^2)	*Surface inclination angle at roof trailing edge* (deg)
1		2413	8.3% 45.6 mm	65.8%	0.0761	11
2		2408	5.9% 32.4 mm	64.9%	0.0728	8
3		2404	4.0% 21.7 mm	63.5%	0.0701	5
4		4705	5.9% 32.5 mm	74.8%	0.0728	7
5		22009	6.0% 32.9 mm	88%	0.0729	7
6		4 digit Series Camber line	5.9% 32.2 mm	47.4%	0.0728	12

Fig. 3.29. Summary of wind tunnel model configurations and key performance data for the LGV (Holt et al., 2015).

They found that roof curvature is seen to reduce the drag coefficient in every case and this was repeated for all yaw angles tested, see Fig. 3.30 and Fig. 3.31.

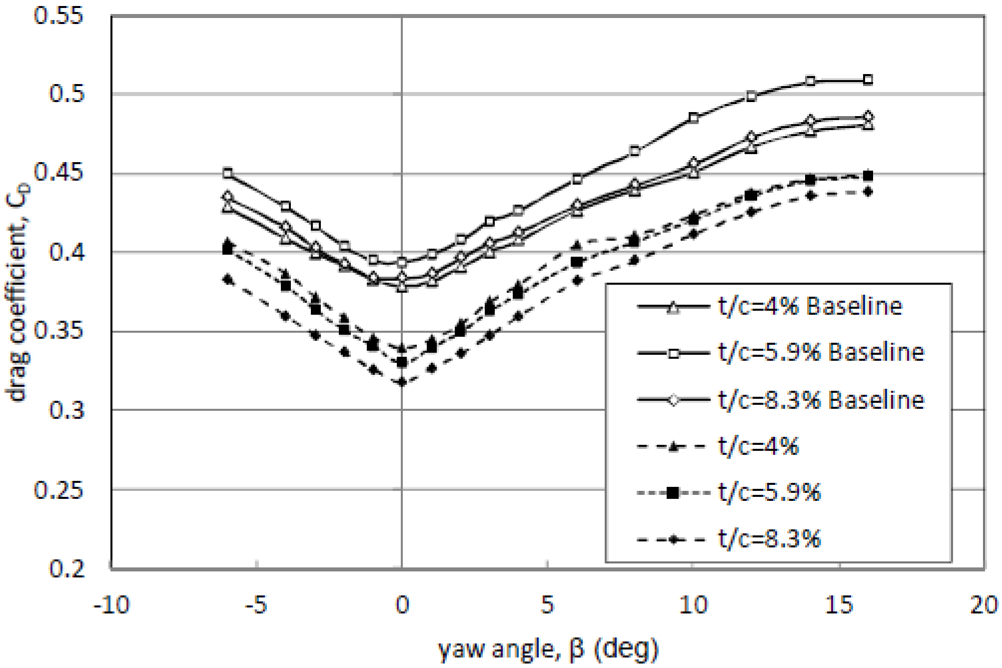

Fig. 3.30. Variation of the drag coefficient as function of yaw angle for different roof depths (for a constant longitudinal position). Dashed lines show curved roof designs; solid lines show baseline configurations (flat roof) with equivalent depths (Holt et al., 2015).

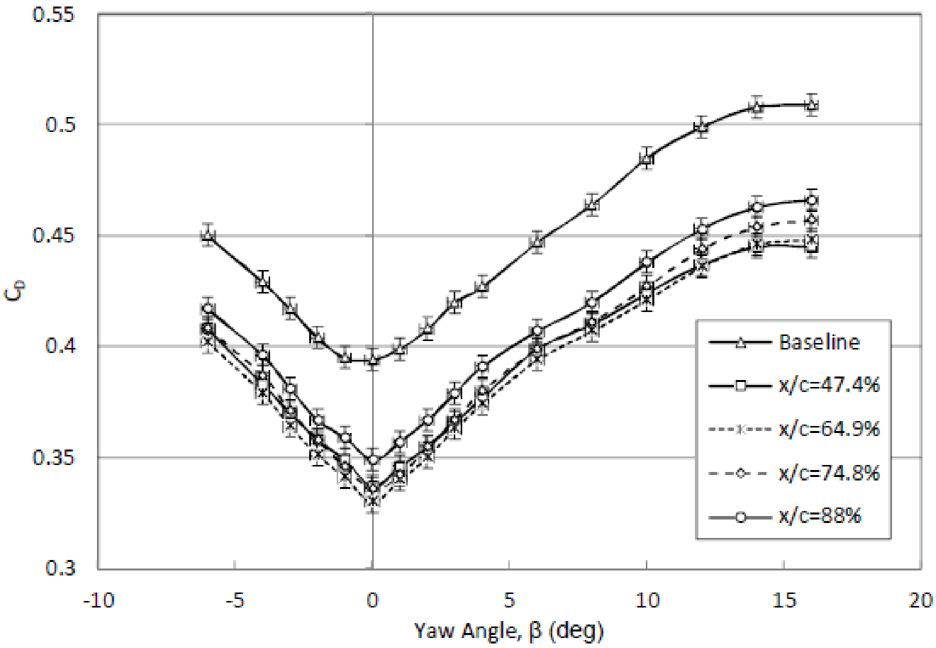

Fig. 3.31. Variation of the drag coefficient as function of yaw angle for different longitudinal locations of maximum roof depth (for constant depth). Dashed lines show curved roof designs; solid lines show baseline configurations (flat roof) with equivalent depths (Holt et al., 2015).

They investigated the difference in drag, ΔC_d, between the curved roof models and the equivalent baseline model (flat roof) with the same overall height, as a function of yaw angle, see Fig. 3.32 and Fig. 3.33.

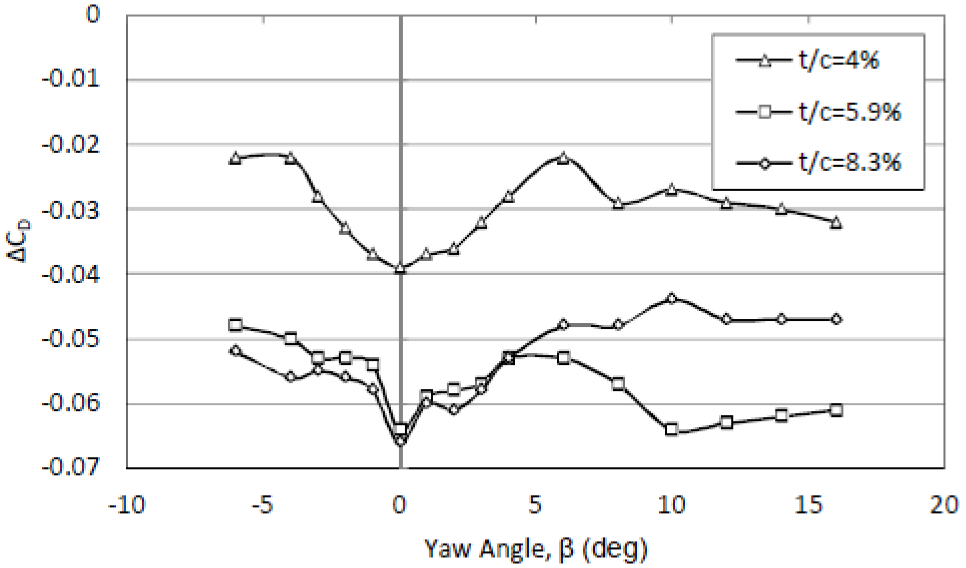

Fig. 3.32. The effect of roof curvature (t/c) on the change in drag coefficient, relative to the flat roof baseline, as a function of yaw angle (Holt et al., 2015).

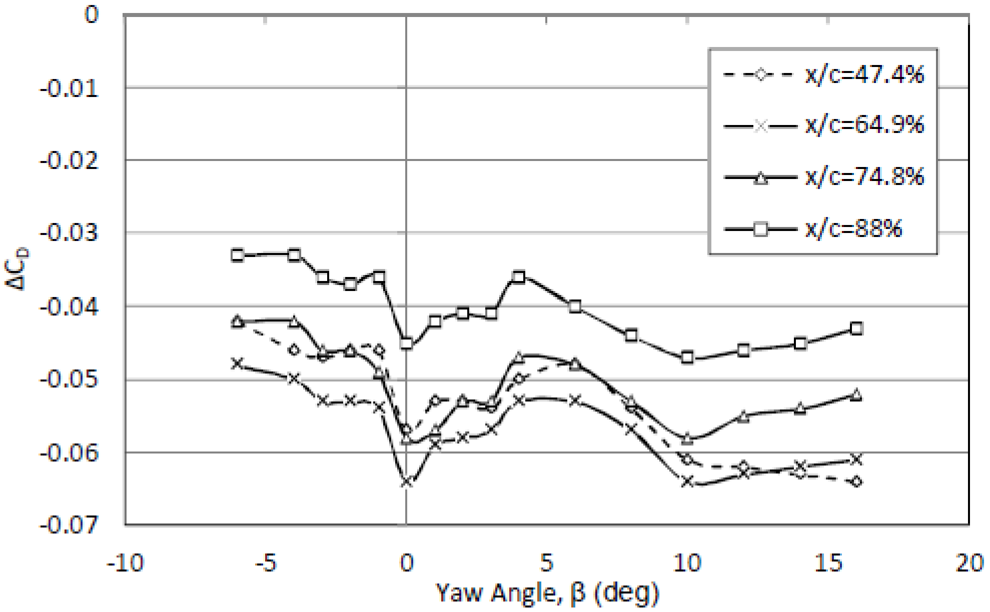

Fig. 3.33. The effect of changing the axial location (x/c) of the maximum roof curvature profile depth on the change in drag coefficient, relative to the flat roof baseline, as a function of yaw angle (Holt et al., 2015).

Two trends in ΔC_D were identified, one occurring for small yaw angles and one at large angles, for all configurations. At low angles of yaw, $-6^{\circ} \leq \beta \leq 6^{\circ}$, the strength of a weak longitudinal vortex develops on the windward upper surface of the roof and it weakens as it moves downstream over the model. At high angles of yaw ($\beta \geq 6^{\circ}$), the strength of this longitudinal vortex is stronger, see Fig. 3.34 . In experiments, it was observed that that vortex formed close to the maximum height of the vehicle (indicated by the solid arrows in Fig. 3.34b) before it left the roof surface (indicated by dashed lines).

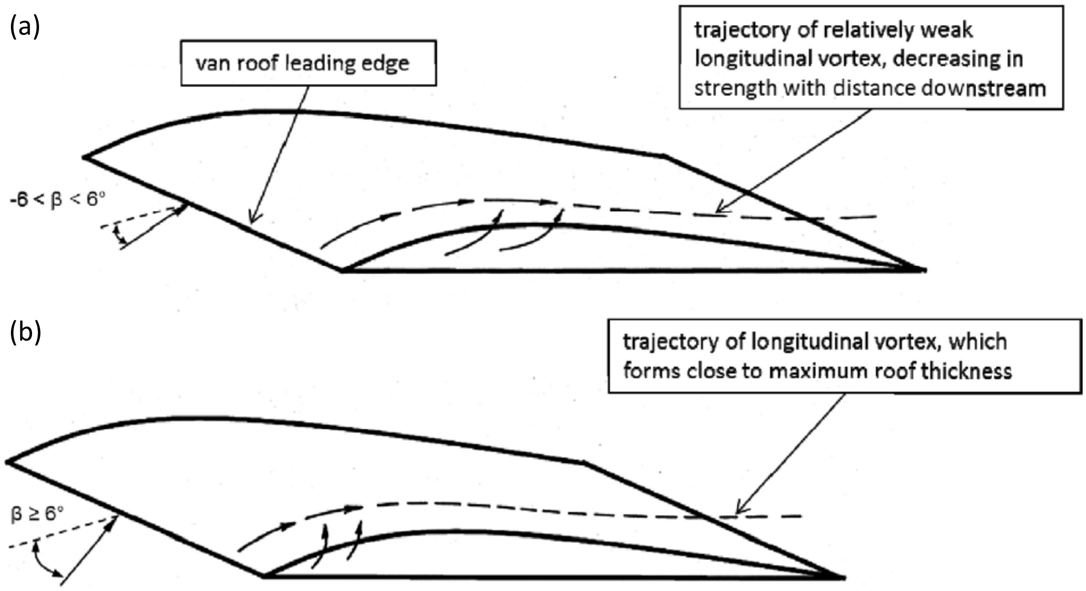

Fig. 3.34. General flow structure details on the top surface of an LGV at (a) small angles of yaw, $-6^{\circ} \leq \beta \leq +6^{\circ}$ and (b) at larger angles ($\beta \geq 6^{\circ}$) (Holt et al.,2015).

The authors could not identify how differences in the flow structure on the roof can account for the significant changes in the behavior of ΔC_D because the investigation of flow structure required advanced measurement techniques and/or high accuracy numerical simulations, which were beyond the scope of their study. Therefore, there is scope for simulating modified curved roof LGV designs using numerical methods, which could give important insights and account for the significant difference in the behavior of ΔC_D, as seen by Holt et al., (2015).

However, their work does show that over-body curvature can reduce the drag coefficient of a (small) bluff vehicle by up to 12.5% and that the best longitudinal location of the maximum roof curvature (i.e. maximum vehicle height) is 65% of the roof length (measured from the base of the van in the upstream direction). One caveat is that the optimal size of the maximum depth cannot be ascertained from such a limited dataset. Therefore, aerodynamic shape optimisation requires more experimental investigation and/or numerical simulations, to develop design solutions for HGVs, which is the purpose of this study.

3.4 Gaps In knowledge and the goals of the research

As already described, in recent years, roof curvature or over-body shape has been used extensively in practice for HGVs on the UK road network. However, the wind tunnel testing by Holt et al., (2015) is, to the author's knowledge, the only known example in the literature of a systematic investigation of roof curvature for bluff road vehicles. Despite the large number of different curved roof shapes seen on HGVs in the UK in recent years, there is no clear indication of which design may offer the best results for a generic HGV.

Therefore, the main focus of this PhD is to explore HGV roof curvature using aerodynamic shape optimisation. The purpose will be to minimise aerodynamic drag without negatively impacting the static stability of a generic HGV in both yaw and roll. The impact of dynamic stability would require the use of transient simulations which is beyond the scope of this work, therefore only static stability will be considered.

The goals of this research, which are closely related to the main objectives in Section 1.5, are:

1- Develop an accurate and reliable simulation approach to evaluate the aerodynamic forces and moments of HGVs. This will involve validation using a generic test case, the GTS model, to compare numerical results generated by ANSYS Fluent with known experimental data.
2- Explore potential design parameters which can positively influence the aerodynamic behaviour of HGVs.
3- Formulate a design optimisation problem with design objectives of minimising drag and maximising stability.
4- To use the optimisation results to propose design guidance for UK HGVs.

These goals are satisfied in the proceeding Chapters of this thesis.

Chapter 4 Computational Method: Verification and Validation

Since the aim of this research is to investigate the aerodynamic characteristics of HGV's, it is necessary to conduct CFD simulations of relevant vehicle shapes. The vehicle used in this chapter is the ground transportation system (GTS) model which was described in the literature review. This vehicle shape is representative of a generic HGV and it is similar to those used in the UK. Previously published experimental data also make it suitable for validating the CFD method used in later chapters, following a detailed verification study. This chapter shows the development of the computational method employed.

4.1 Ground Transportation System (GTS)

CFD simulations are used to simulate the aerodynamic flow structure around the GTS model. The GTS is the name for a simplified tractor-trailer model where the tractor and trailer are combined into one continuous shape, without a towing gap between them. The geometry is based on a 1:8 scale wind tunnel model of the vehicle, which was mounted on four posts, 0.0778m above a ground board (Roy et al., 2006a). The dimensions of the model are shown in Fig. 4.1.

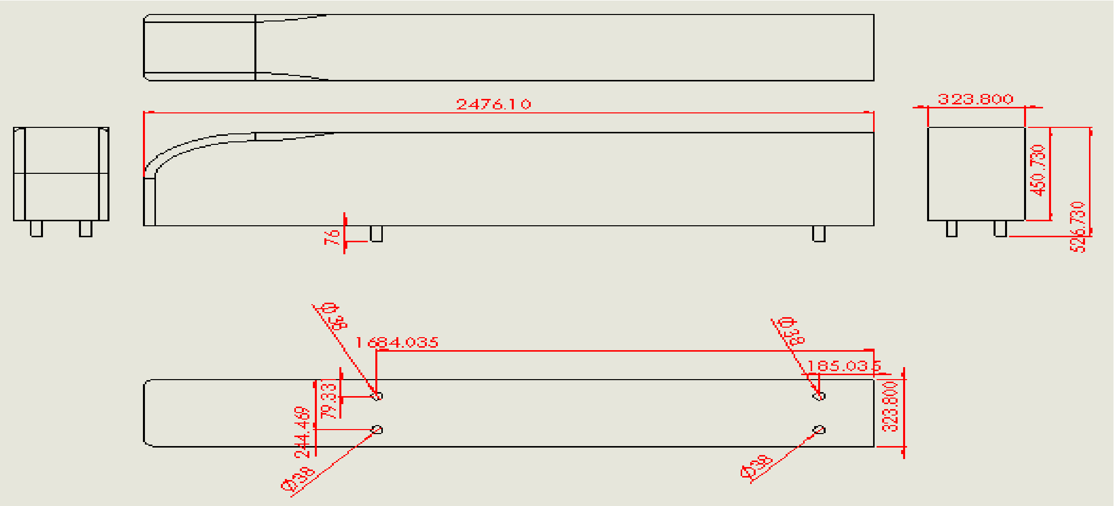

Fig. 4.1. Main dimensions of the Ground Transportation System (GTS) Model.

4.2 Solution domain and boundary conditions

A CAD model of the GTS model was produced using Solidworks (2015) before being imported to ANSYS Design Modeler (Version 19.1) to generate the solution domain. Fig. 4.2 shows where the GTS model is located within the computational domain which is 3.05m wide, 2.13m high (Storms et al., 2001) and the length is 52.48m. The inlet of the domain is located 5L upstream of the model where L is the length of the GTS model and the outlet is located 15L downstream of it to allow full development of the flow, including the turbulent wake.

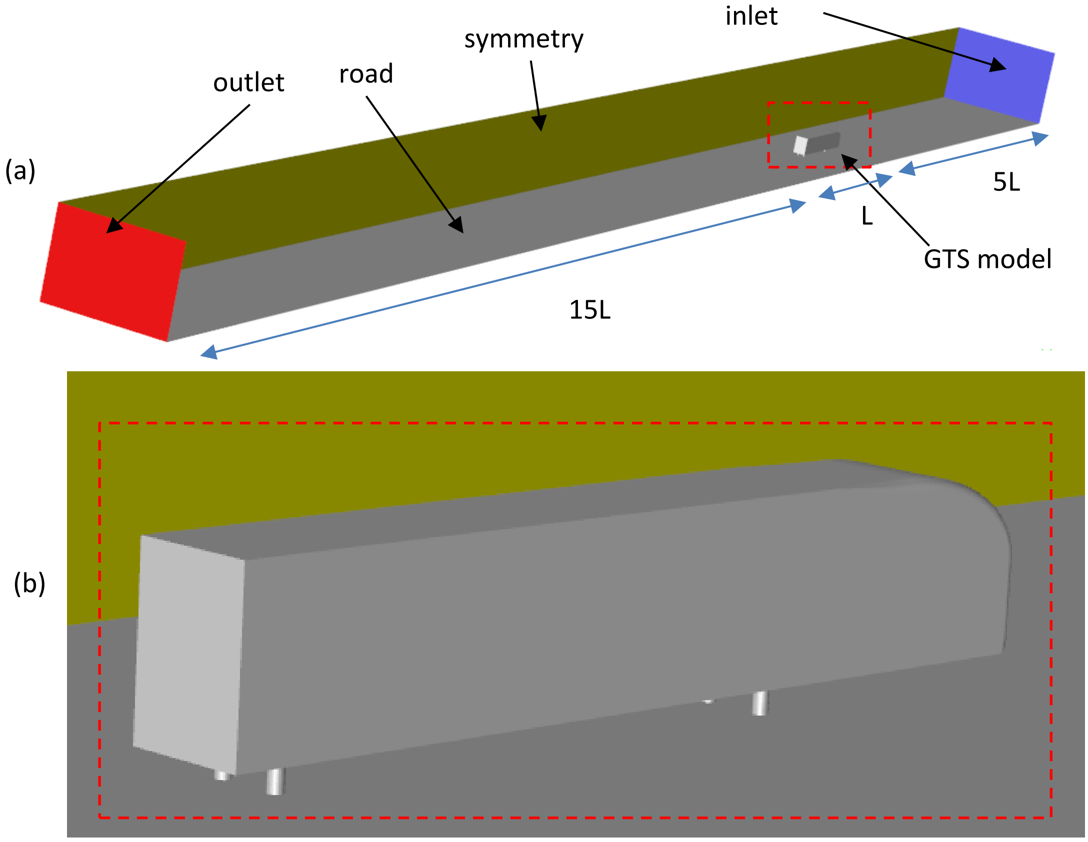

Fig. 4.2. View of (a) the entire computational domain and (b) close-up of the GTS model.

The free-stream velocity within the working section of the wind tunnel is 90 m/s leading to a high Reynolds number of two million. Therefore, a uniform velocity inlet to the domain is used with a velocity of 90 m/s. The inlet turbulence parameters used are the turbulence intensity, I = 0.3% (Roy et al., 2006a), and the turbulent length scale, L_T = 0.173 m, where L_T = 0.07L (ANSYS User Guide, 2017) and L is the length of GTS model. On all the wall surfaces (ground plane and the GTS model) the no-slip condition is imposed. The outlet boundary condition is a pressure outlet with a constant atmospheric pressure of 0 Pa.

4.3 Turbulence models

The choice of turbulence model depends on the application and the expected flow features. In this study the Reynolds number is high with massive separation expected behind this bluff shape. Consequently, it is suitable to use the SST k-ω model (Menter, 1994) which was described in Chapter 3. However, two additional turbulence models are also considered, namely: the Spalart-Allmaras (SA) model (Spalart and Allmaras, 1992) and the standard k-ε model (SKE) (Launder and Spalding, 1983) with enhanced wall treatment. These three models are used to show the differences in results from solutions generated on different meshes. The same mesh structure can be used for the three turbulence models as they have the same mesh resolution requirements governed by the condition $y^+ \approx 1$, where y^+ is the dimensionless distance from wall and is used to guide the first cell height in the mesh. Therefore, this essential condition has an impact on the mesh structure, which follows in section 4.4. More details on the turbulence models, their mesh requirements and transport equations were provided in the previous chapter.

4.4 **Mesh generation**

Two types of mesh structure, a hybrid one and a fully structured approach were developed and tested. The hybrid mesh, a combination of structured and unstructured elements, was used because the unstructured cells are more compatible with curved surfaces such as those on the GTS model. Secondly, a structured mesh was developed using ICEM (version 19.1) to allow a comparison between these two mesh philosophies. As mentioned in chapter 3, structured meshes often need more time and effort to implement in addition to greater computer resource requirements. However, they can enhance simulation stability, reduce the overall number of elements in the grid and numerical diffusion is reduced because the cell faces are generally aligned with the flow which is impossible for an unstructured mesh.

This section explains the key aspects of the mesh structure and how it was developed for use in all later chapters. This allowed five different meshes to be produced with varying levels of refinement, for each mesh type. Eventually, one of these meshes is selected to conduct the simulations for the current investigation, in all later chapters.

4.4.1 **Hybrid mesh design**

The ANSYS Mesh tool in the ANSYS Workbench (version 17.2) platform was used to carry out hybrid discretisation of the solution domain around the GTS vehicle. The hybrid meshing strategy was used to explicitly control the mesh density in the domain with suitable refinements around the GTS body. Firstly, as can be seen in Fig. 4.3 there is a box created around the body of the vehicle (Car Box) so that structured hexahedral cells can be placed outside this box and unstructured tetrahedral cells can be used inside it. The unstructured cells are essential because of the curved surface of body of GTS model as well as the legs which connect it to the floor.

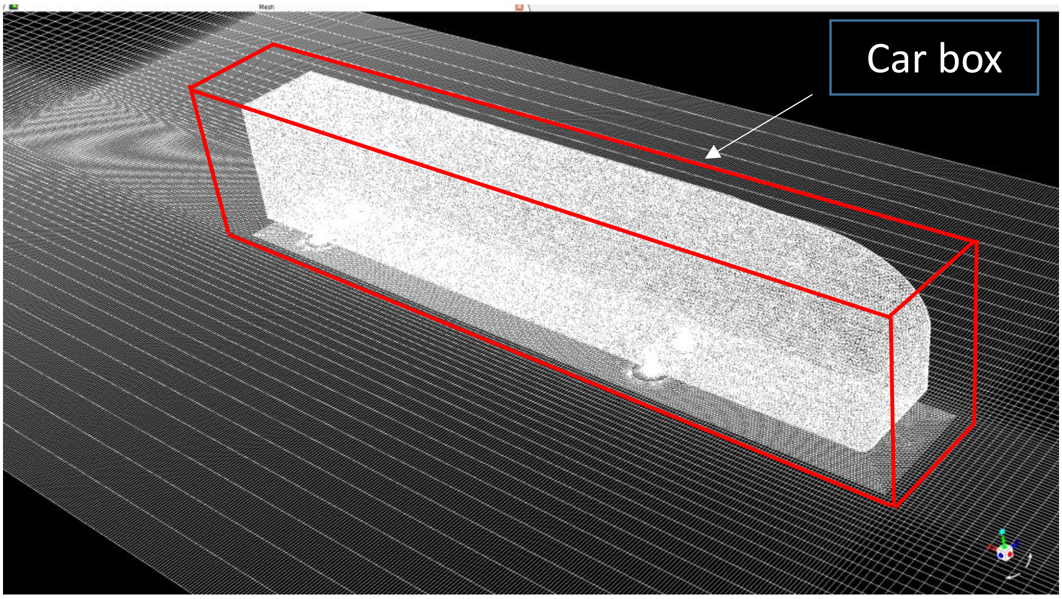

Fig. 4.3. Mesh structure around the GTS model, showing the Car Box region (red lines).

One volume and two face size controls were used to control the size of the elements inside the Car Box. The local grid spacing on the GTS body model was defined by using two face size controls, one on the legs of the model and another on the rest of the surfaces of the GTS model. These were essential because the size of the legs is very small as compared to the rest of the body. Next, inflation layers were used to capture the velocity gradients near the surface of the GTS model and the road (no-slip walls). More details on the inflation layer settings are provided in the next section. Furthermore, the hexahedral mesh used outside the Car Box was structured to have fine cells near the Car Box which gradually stretches to have coarse cells at the domain boundaries as can be seen in Fig. 4.4(a). A wake refinement region was also implemented, see Fig. 4.4(b) and (d).

Table 4.1. Key aspects of the mesh structure of Hybrid mesh.

	Inside car box controls			Outside car box controls edges (number of divisions)									
Refinement step	Face size of the legs (mm)	Face size for the rest of the surfaces (mm)	Volume size (mm)	In X-direction				In Y-direction			In Z-direction		
				X-Front	X-Car Box	X-Near Wake Box	X-Back	Y-Bottom	Y-Car Box	Y-Top	z-Left	Z-Car Box	z-Right
Extra fine	1.2	6	6	56	435	289	67	15	107	34	33	67	33
Finer	1.6	7.7	7.7	54	339	218	65	15	83	32	31	52	31
Fine	2	10	10	51	261	168	65	15	65	50	51	35	51
Normal	2.6	13	13	48	201	129	59	15	49	26	25	31	25
Coarse	3.38	16.9	16.9	45	154	99	56	15	38	24	23	24	23

This was facilitated by splitting the whole domain into sub-volumes and the edges meshed with various biases to control the mesh outside the Car Box. The edge sizing applied to all edges of the domain are presented in Table 4.1.

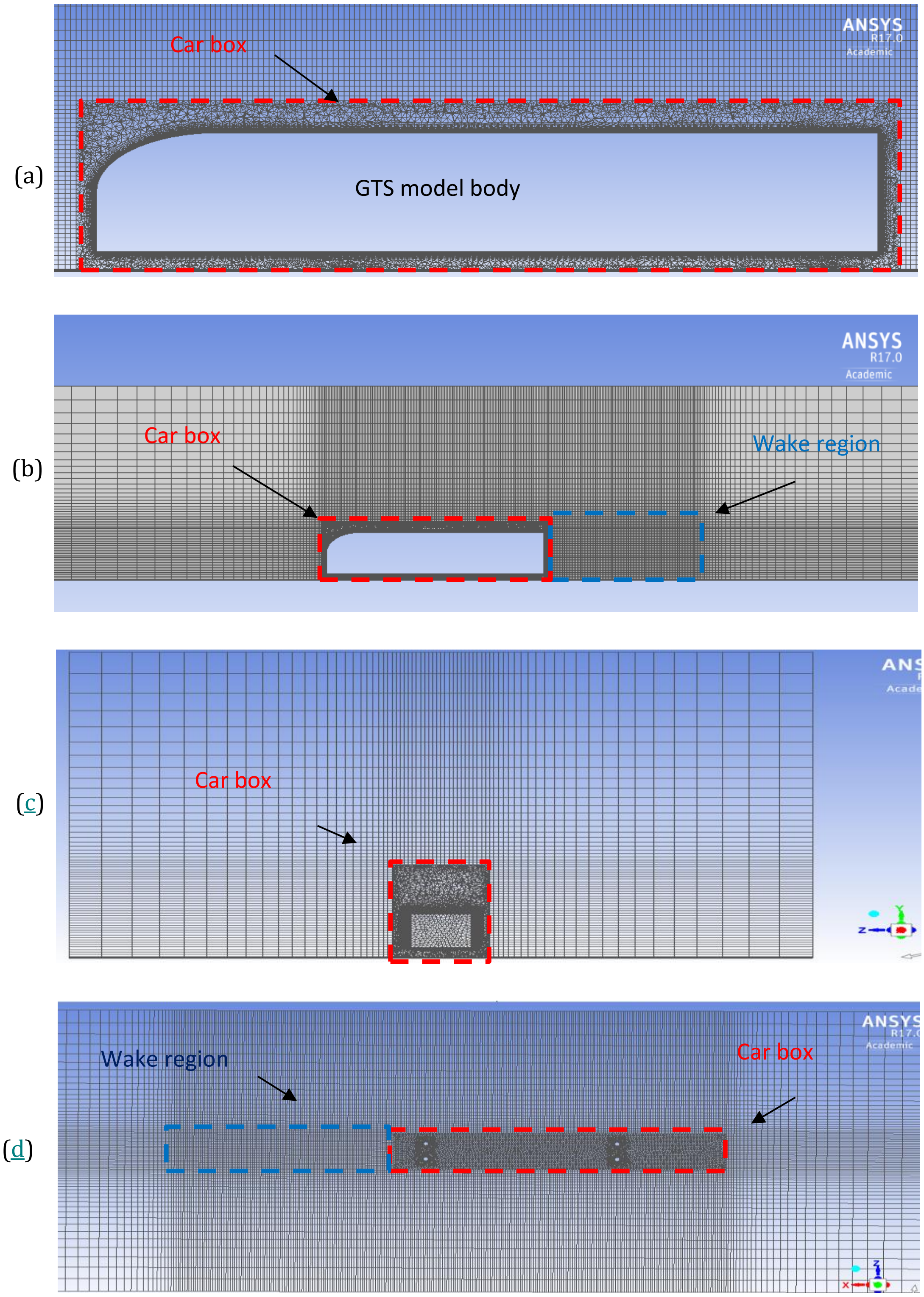

Fig. 4.4. Mesh structure around the GTS model from (a,b) the side, (c) the front and (d) the top.

4.4.1.1 **Inflation layers**

In addition to the overall mesh structure, adequately capturing the airflow gradients in the boundary layer required having sufficient cells near walls. This is achieved using stacked layers of prismatic cells which form an inflation layer. The number of cells in the inflation layer must be determined to ensure that the wall treatment is valid. Following a sensitivity study, an appropriate first cell height of 0.01mm was found in conjunction with 37 layers of cells and a cell height growth factor of 1.2. These details are shown in Table 4.2 and Fig. 4.5 shows a close-up view of the inflation layer near the GTS.

Table 4.2: Properties of the inflation layers used in the simulations

	Property	Selection
1	Inflation Option	First Layer Thickness
2	First Layer Height	0.01 mm
3	Maximum Layers	37
4	Growth Rate	1.2

Preliminary airflow simulations using the SST *k-ω* turbulence model are shown in Fig. 4.6. Here, a 10 mm face size was used on the GTS surfaces and the same size was used in the refinement Car Box around the GTS model (fine mesh). Fig. 4.6 shows that the average y^+ value measured at the surface of the model which was found to be 1.99 with the exception of the base and lower face of the vehicle (where flow separation occurs and y^+ is irrelevant). These values are in the correct range for the turbulence model used in the simulations and they are representative for all three turbulence models tested.

As can be seen in Fig. 4.7 the inflation layer mesh is deep enough to capture the entire boundary layer, even at the rear of the vehicle where the boundary layer has grown to its maximum height. The velocity contours shown in the top cells in the inflation layer match the free-stream velocity (red colours). It can clearly be seen that the inflation layer captures the entire boundary layer, all the way to the base of the vehicle.

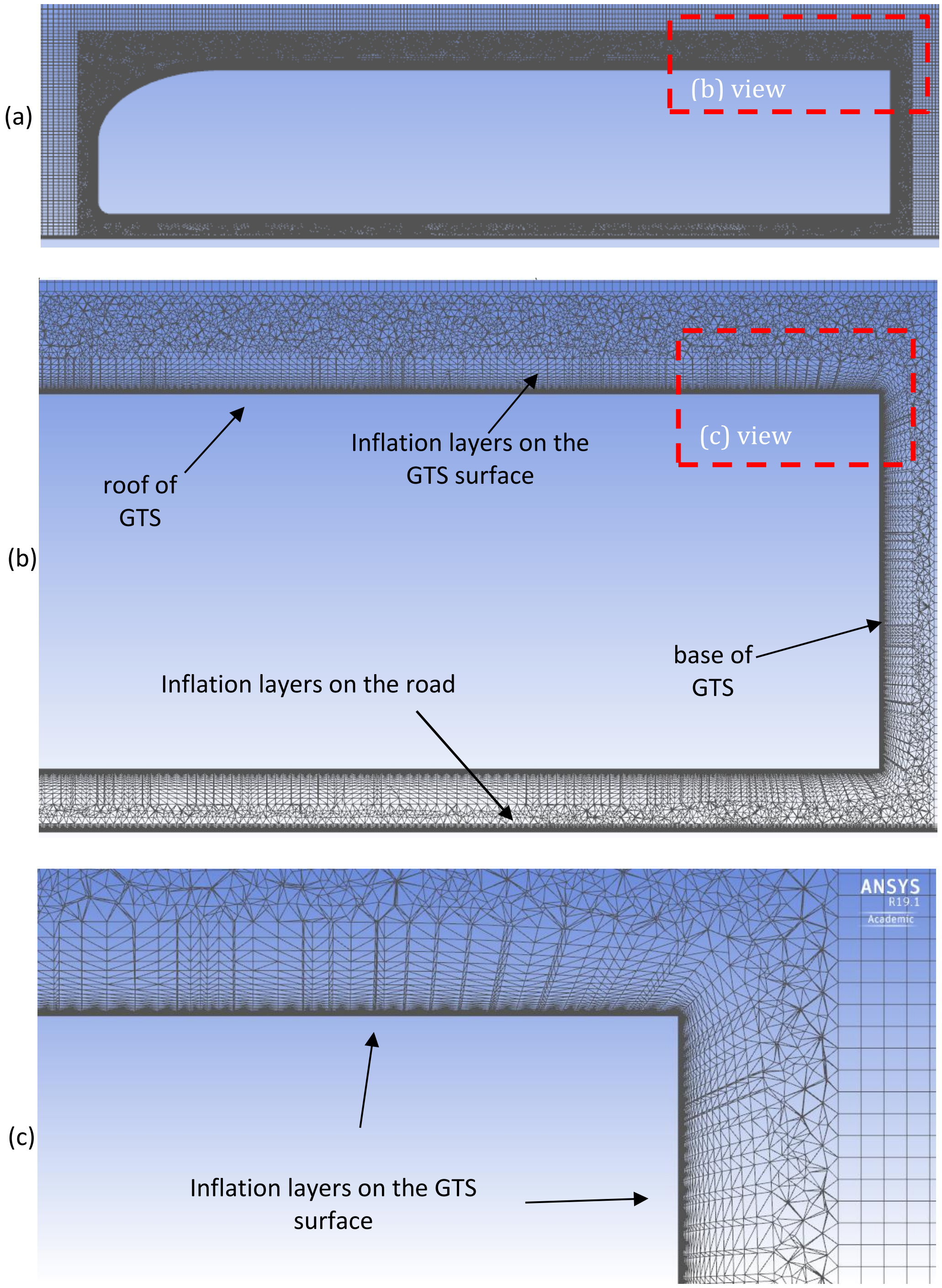

Fig. 4.5. Inflation layers around the GTS model from the side with three different levels of zoom: (a) overview (b) and (c) very close up views of the inflation layer.

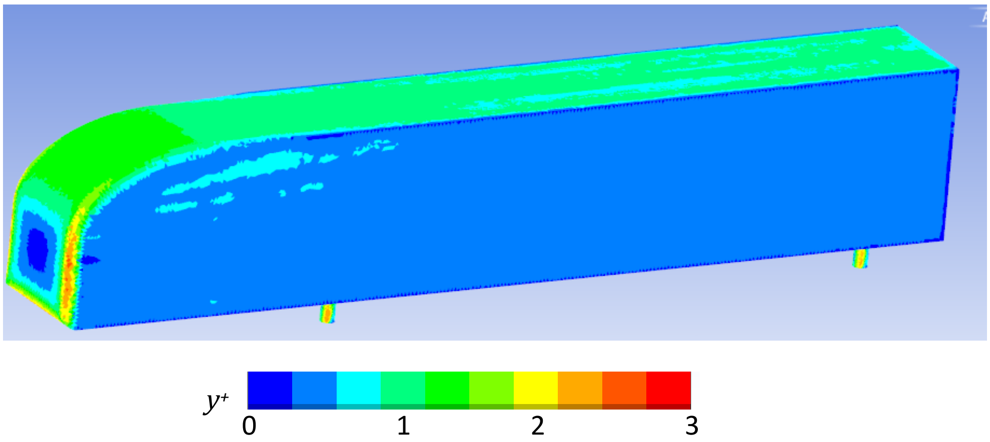

Fig. 4.6. Wall y^+ distribution on the GTS surfaces.

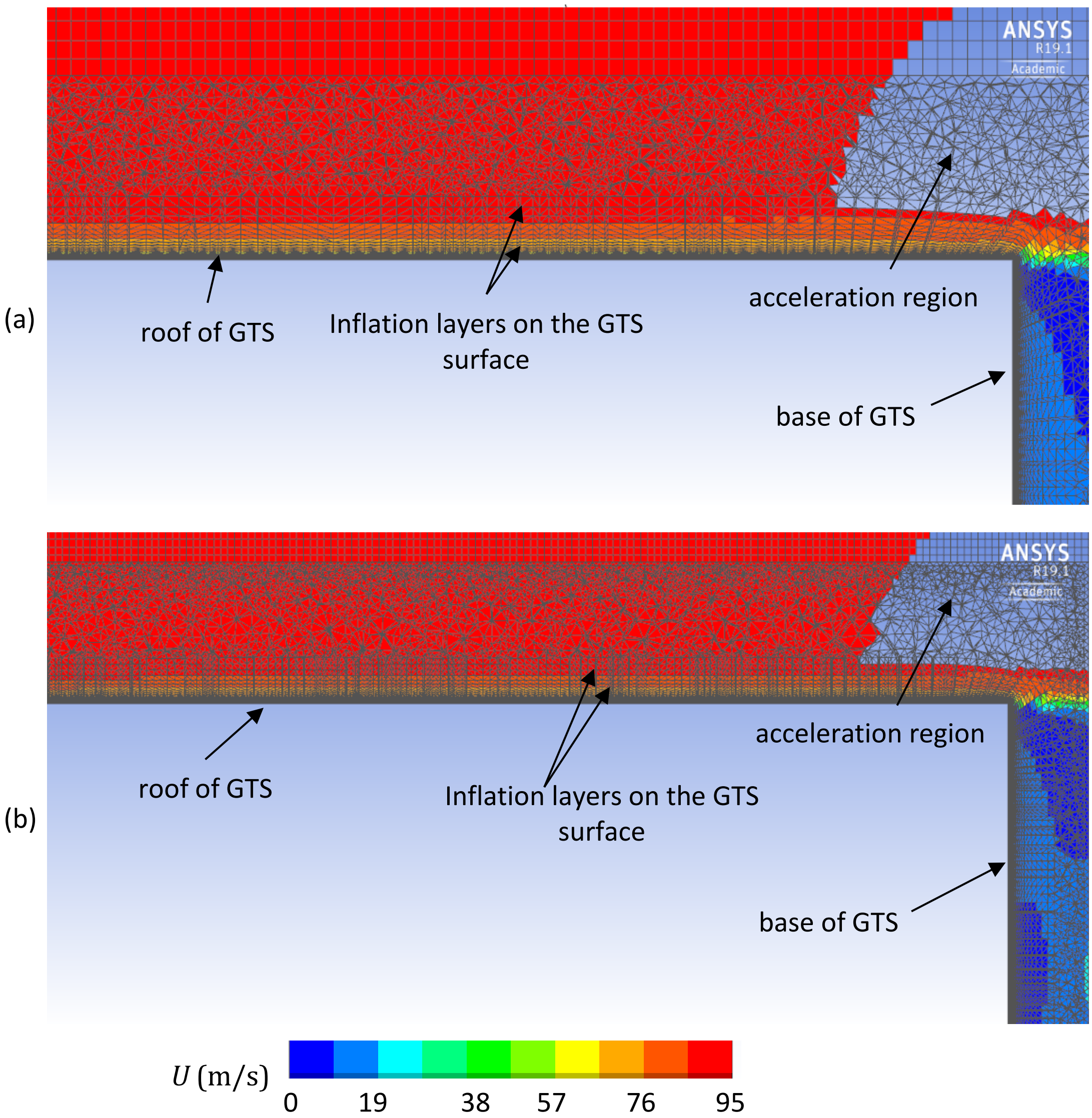

Fig. 4.7. Inflation layer mesh (grey lines) and velocity distribution on the symmetry plane when viewed from the side of the GTS at the rear for (a) 10mm and (b) 6mm surface meshes.

4.4.2 **Structured mesh design**

As an alternative to the hybrid approach, ANSYS ICEM (version 19.1) was used to design a structured and fully hexahedral mesh to discretise the solution domain. To obtain sufficient control over the mesh, the domain was split into 507 blocks as shown in Fig. 4.8. It can be seen that the solution domain is decomposed into various volumes with the edges used to control the mesh everywhere. The number of nodes for each of the major edges of the domain, for four different mesh densities, is shown in Table 4.3; a typical mesh structure is shown in Fig. 4.9.

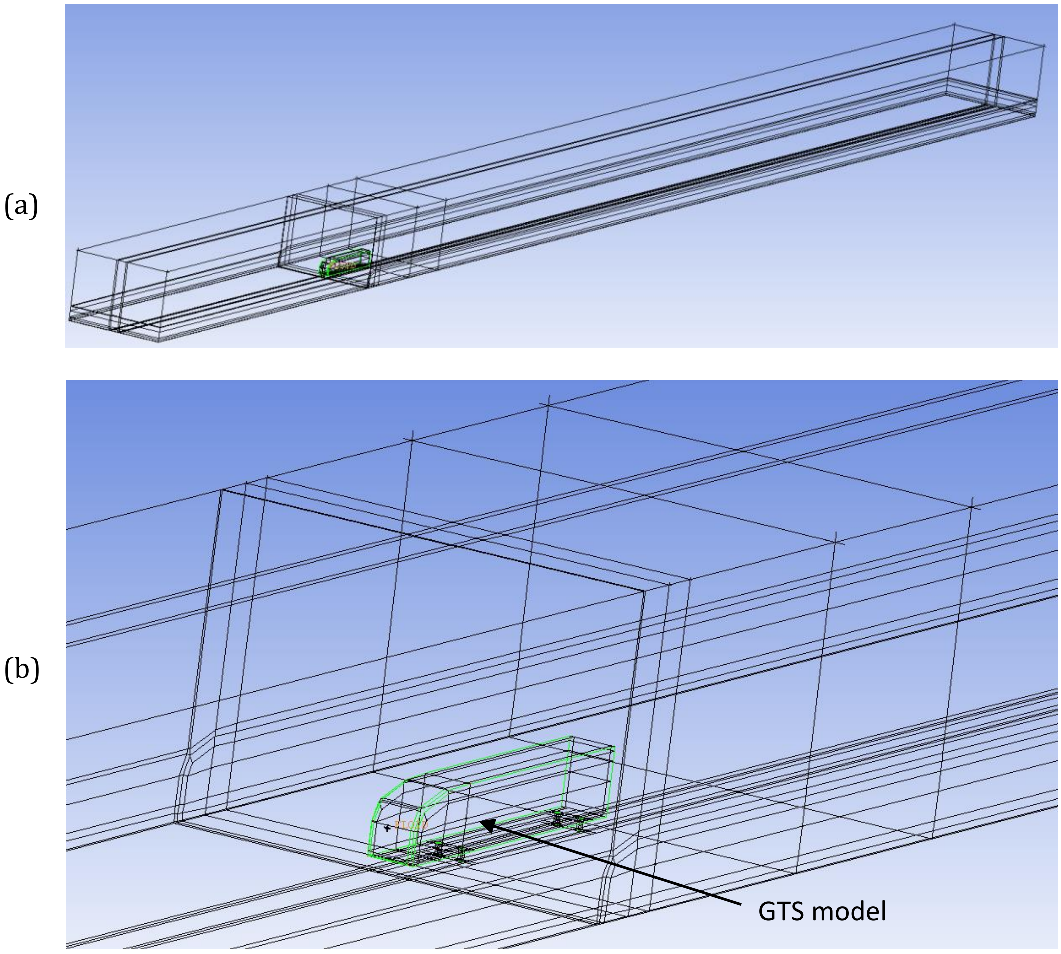

Fig. 4.8. View of the stencil lines in the block structured mesh (a) throughout the domain and (b) a close-up view near the GTS model.

Table 4.3: Key aspects of the mesh structure of structure mesh.

			Outside car box controls edges (number of divisions)						
			In X-direction			In Y-direction			In Z-direction
Refinement step	Number of elements	Volume size (mm)	X-Front	X-Near Wake Box	X-Back	Y-Bottom	Y-Top	z-Left	z-Right
Finer (7.7)	15.23	7.7	31	224	66	19	34	32	32
Fine (10.0)	8.68	10	29	173	63	19	31	29	29
Normal (13.0)	5.39	13	26	132	60	19	29	27	27
Coarse (16.9)	3.98	16.9	24	102	58	19	26	24	24

To control the mesh near the surface of the GTS model an O-Grid strategy was used to explicitly control the inflation layer around the GTS body as well as the legs, which is necessary due to these rounded surfaces. The first cell height is set to 0.01mm and the number of layers is equal to 37 with a cell height growth factor of 1.2 (these were retained from the previous sensitivity study carried out for the unstructured mesh, Section 4.4.1.1). As can be seen in, Fig. 4.10-Fig. 4.13, the inflation layer around the body of the vehicle expands away from the surface of the GTS model and some of the mesh lines continue to the outer boundaries of the domain.

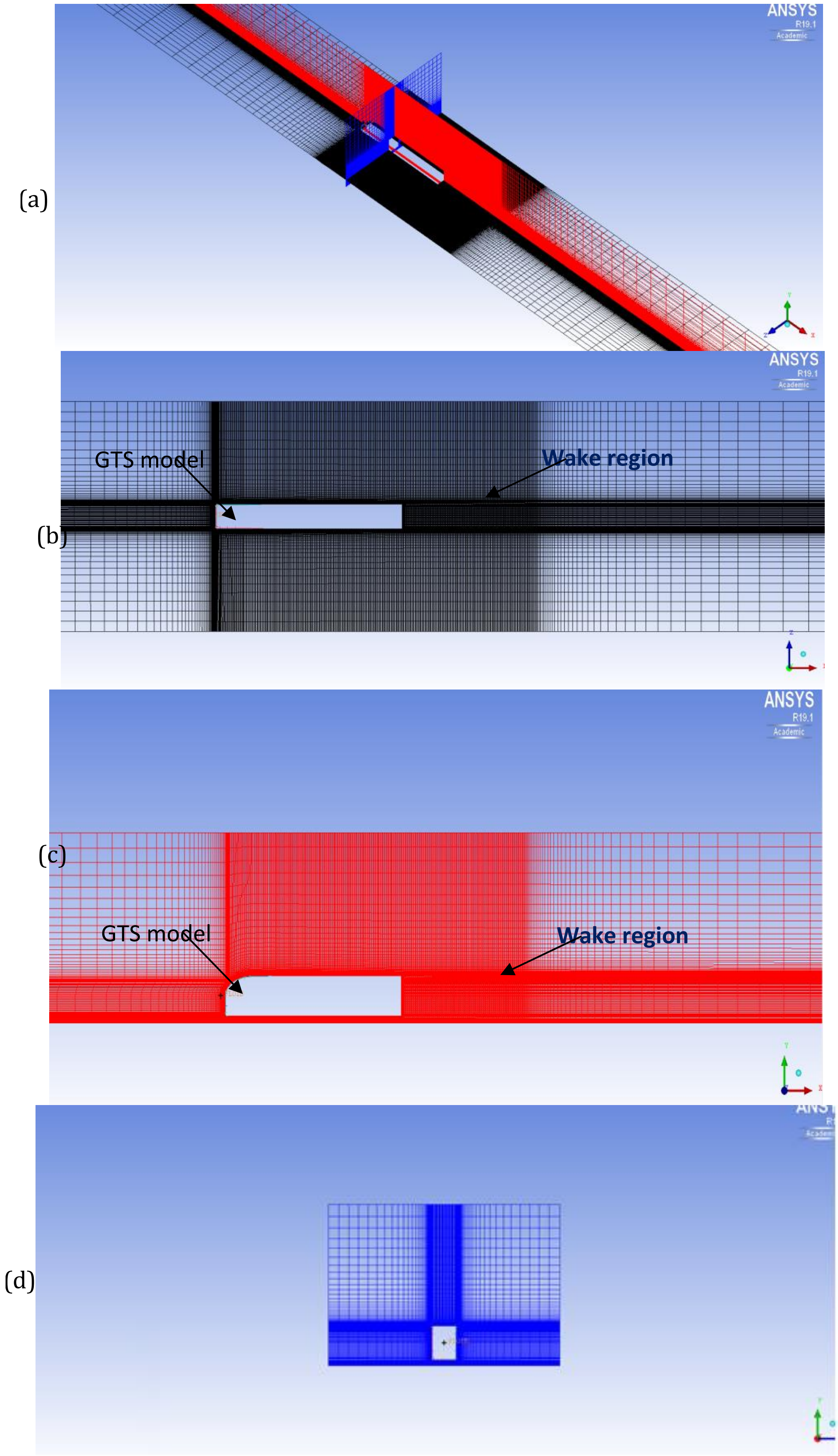

Fig. 4.9. Typical mesh structure around the GTS model from (a) isometric perspective, (b) the top, (c) the side and (d) the front.

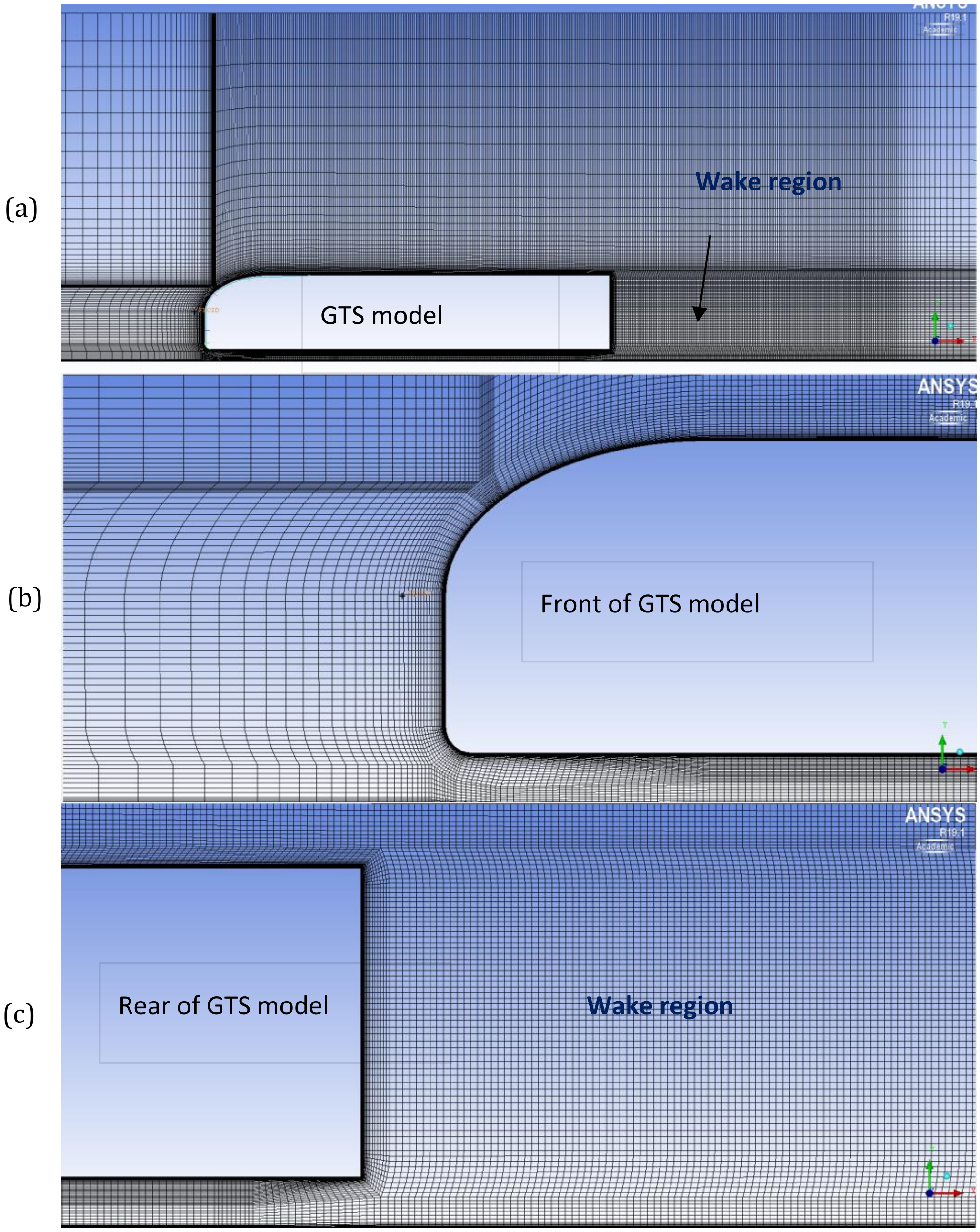

Fig. 4.10. Side views of a typical mesh structure around the GTS model (a) overview, (b) and (c) close-up views of the inflation layer

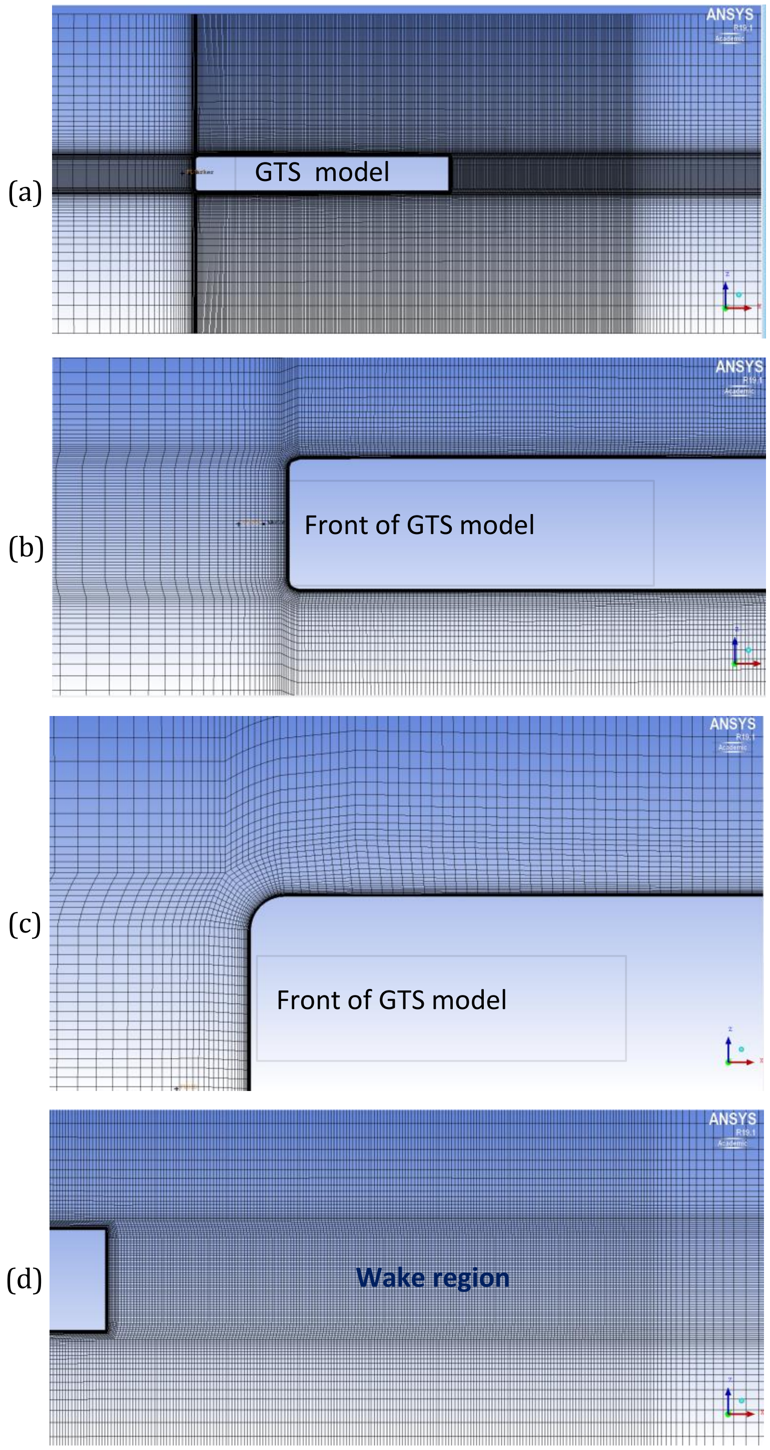

Fig. 4.11. Top views of a typical mesh structure around the GTS model (a) overview, (b), (c) and (d) close-up views of mesh details.

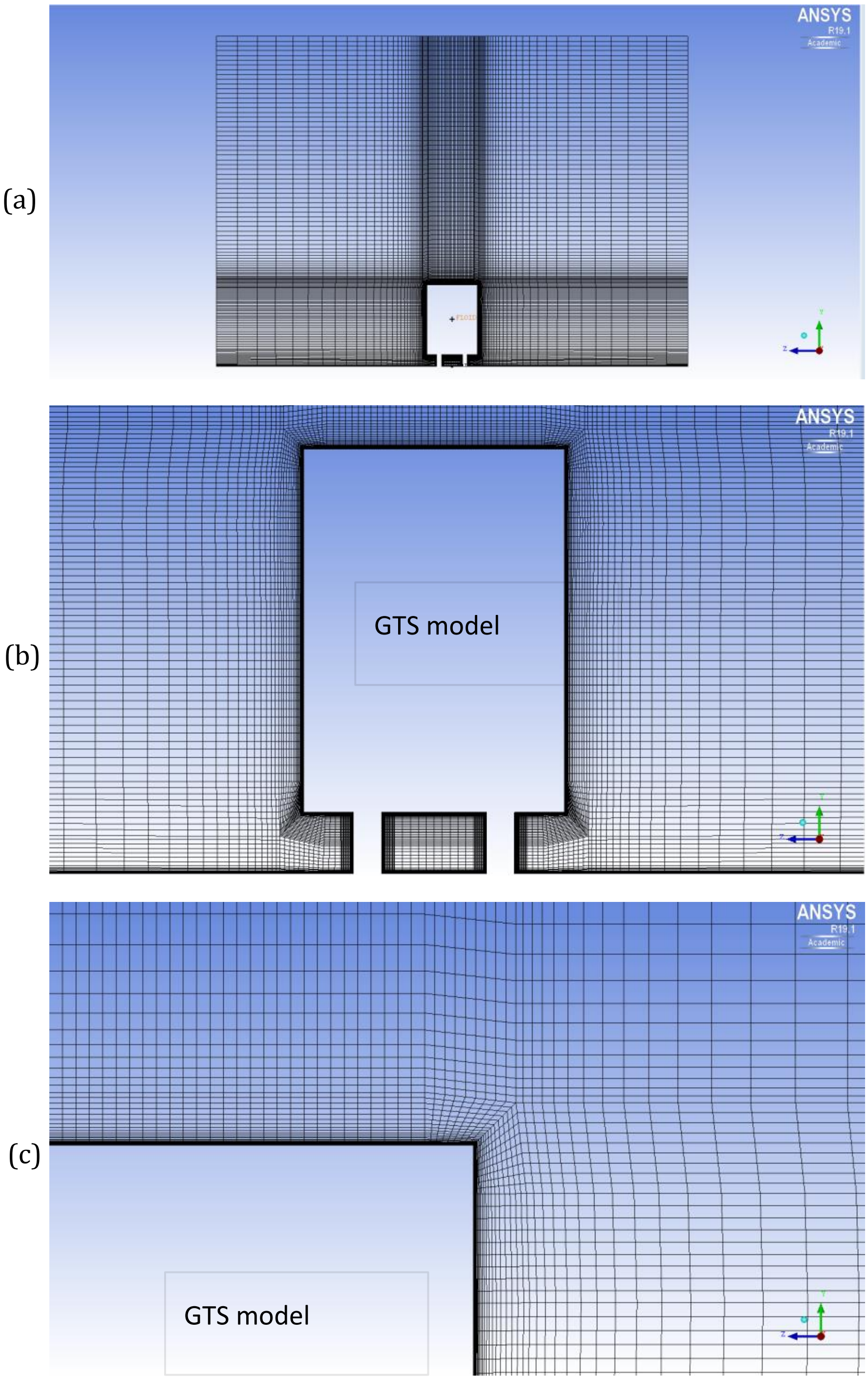

Fig. 4.12. From views of typical mesh structure around the GTS model (a) overview, (b) and (c) close-up views of the inflation layer.

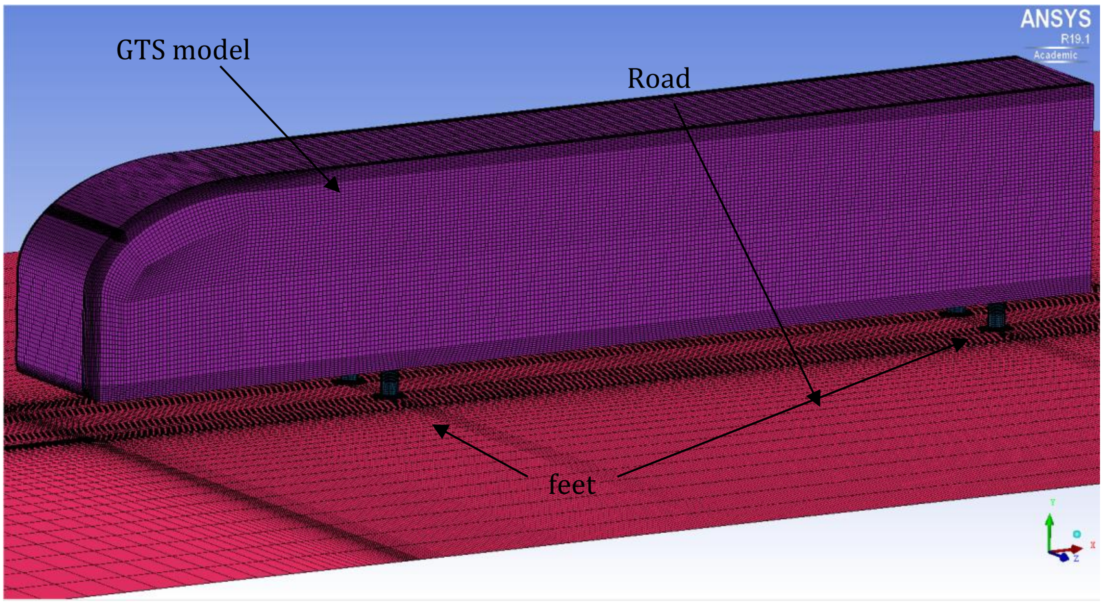

Fig. 4.13. Typical surface mesh on the body of the GTS model, road and feet.

Preliminary airflow simulations using the structured mesh and the SST *k-ω* turbulence model are shown in Fig. 4.14. Here, a 10 mm face size was used on the GTS (the "fine" mesh). Fig. 4.14 shows that the average y^+ value measured at surface of the model was found to be 1.12, not including the base and lower faces of the model (where flow separation occurs and y^+ is meaningless). These values are in the correct range for the turbulence model used in the simulations and they are representative for all three turbulence models tested. As can be seen in Fig. 4.15 the inflation layer mesh is deep enough to capture the entire boundary layer, even at the rear of the vehicle as was seen for the hybrid mesh structure. Again, the velocity contours shown in the top cells in the inflation layer match the free-stream velocity (red colours) and so it captures the entire boundary layer.

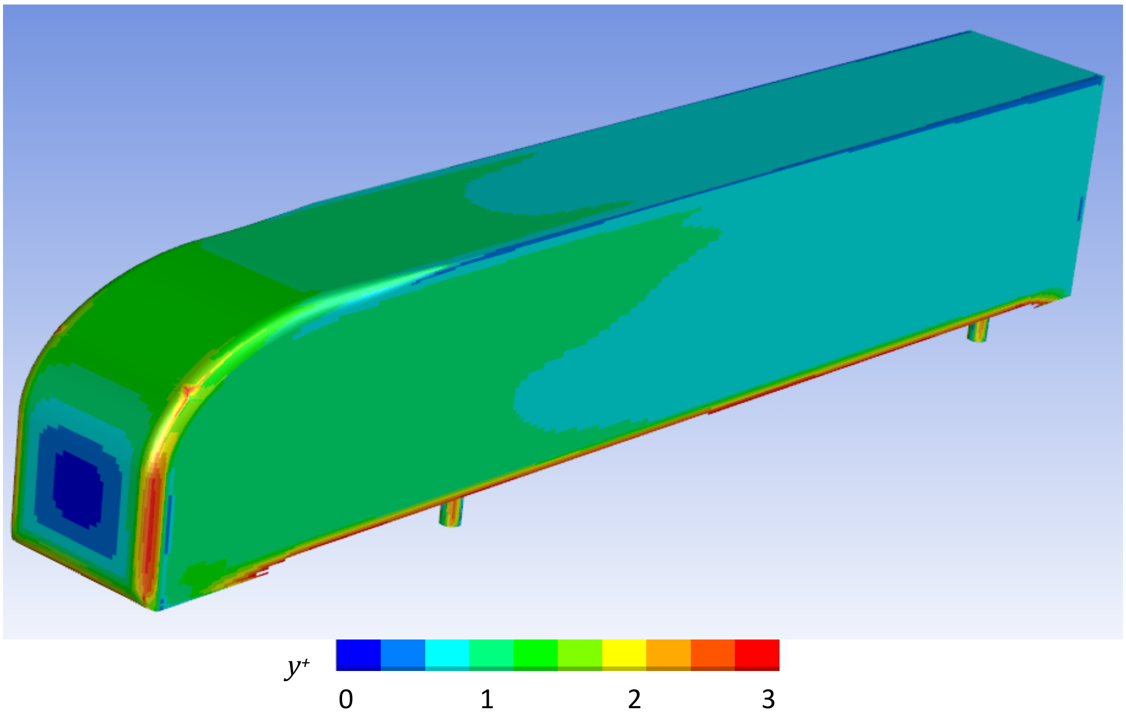

Fig. 4.14. Wall y^+ distribution on the GTS surfaces for the fine structured mesh results.

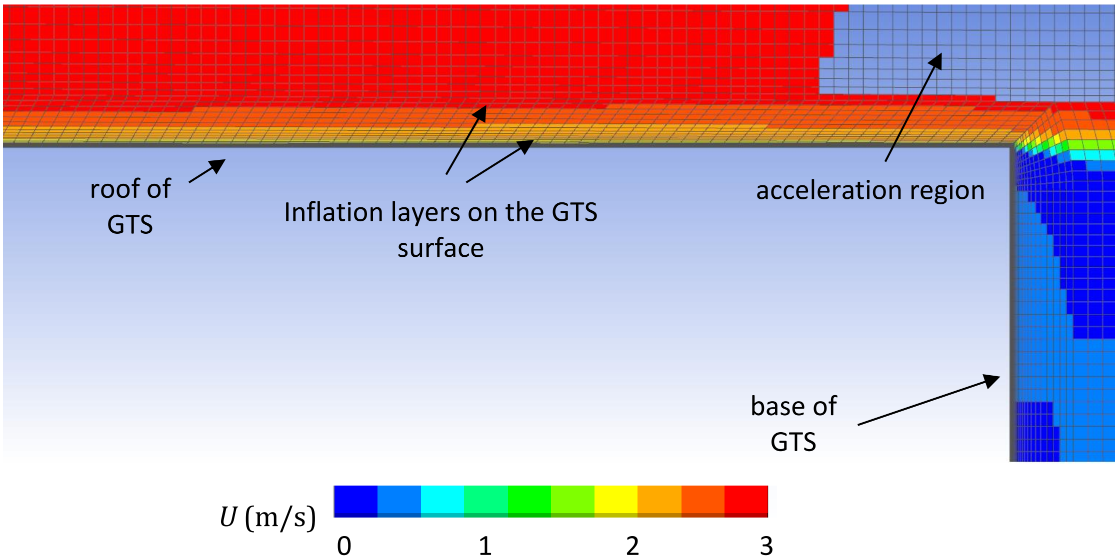

Fig. 4.15. Inflation layer mesh (grey lines) and velocity distribution on the symmetry plane when viewed from the side of the GTS at the rear with a surface mesh of 10mm.

4.4.3 **Mesh independence**

Using the two different types of grid described above (hybrid and structured), a mesh independence study was required to investigate the effect that the mesh size has on the simulation results. To do this, the element sizes in the whole domain were changed by a factor of 1.3. For the hybrid grid structure, this gave meshes designated: extra fine, finer, fine, normal and coarse, see Table 4.4, and for the structured meshes: finer, fine, normal and coarse, see Table 4.5. Three dimensional, isothermal, steady-state airflow simulations were computed on all mesh densities and types using the double precision solver, ANSYS Fluent (version 19.1). Second order simulations were run with the SIMPLE pressure-velocity coupling algorithm which is suitable for this problem. All simulations were run using the High Performance Computing resource, ARC3, with simulation times ranging from 1 to 15 hours for mesh sizes of approximately 4 million and 28 millions cells, respectively, using 16 processors and 3GB RAM per processor.

Table 4.4, 4.5 and Fig. 4.16 show that how the computed drag coefficient, C_D, varies with mesh density, for the three turbulence models chosen. These are compared to the study by Roy et al., (2006) which showed that the experimental drag coefficient for the GTS model is 0.250. Accordingly, the percentage difference between the CFD computations and the experimental value is expressed in terms of ΔC_D as shown in Table 4.4 and 4.5. Firstly, regarding the hybrid mesh results, it is clear that all turbulence models over-predict aerodynamic drag for all mesh densities, compared to the experimental value of Roy et al., (2006). The same is true for the structured mesh results. This can be seen on the data and Fig. 4.16; simulation results from structured meshes are noticeably more consistent than the hybrid ones.

Table 4.4: Drag coefficients for different mesh densities employing different turbulence models with the hybrid mesh design.

		Turbulence model					
		(SST k-ω)		(Spalart-Allmaras)		Standard (k-ε) Enhanced Wall Treatment	
mesh size (mm)	Cell count	C_D	ΔC_D (%)	C_D	ΔC_D (%)	C_D	ΔC_D (%)
Extra fine(6.0)	28,443,086	0.271	8.3%	0.366	46.5%	0.399	59.5%
Finer (7.7)	16,991,058	0.277	10.7%	0.370	47.9%	0.331	32.6%
Fine (10.0)	9,871,939	0.286	14.6%	0.375	50.0%	0.358	43.0%
Normal (13.0)	5,872,386	0.341	36.5%	0.385	53.8%	0.352	40.6%
Coarse (16.9)	3,501,277	0.360	43.9%	0.409	63.5%	0.369	47.5%

Table 4.5: Drag coefficients for different mesh densities employing different turbulence models with the fully structured mesh design.

		Turbulence model					
mesh size (mm)	Cell count	(SST k-ω)		(Spalart-Allmaras)		Standard (k-ε) Enhanced Wall Treatment	
		C_D	ΔC_D (%)	C_D	ΔC_D (%)	C_D	ΔC_D (%)
Finer (7.7)	15,232,740	0.2695	7.8%	0.3030	21.2%	0.3635	45.4%
Fine (10.0)	8,679,160	0.2878	15.1%	0.3079	23.2%	0.3659	46.4%
Normal (13.0)	5,393,112	0.2828	13.1%	0.3157	26.3%	0.3711	48.4%
Coarse (16.9)	3,976,846	0.2821	12.8%	0.3176	27.0%	0.3695	47.8%

For comparison, Roy et al., (2006) and Maddox et al., (2004) also carried out CFD simulations where the computed drag coefficient was found to be 0.298 and 0.279 using the (SST k-ω) using the SACCARA CFD code with 20 million elements and (DES) turbulence treatment using the Cobalt CFD code with 6 million elements, respectively. In the present study, the structured Finer (15.2 million elements) mesh results over-predict experimental drag by 7.8% using the SST k-ω model. However, the over-prediction is about 19.2% in the work by Roy et al., 2006 and 11.6% in the work by Maddox et al., 2004.

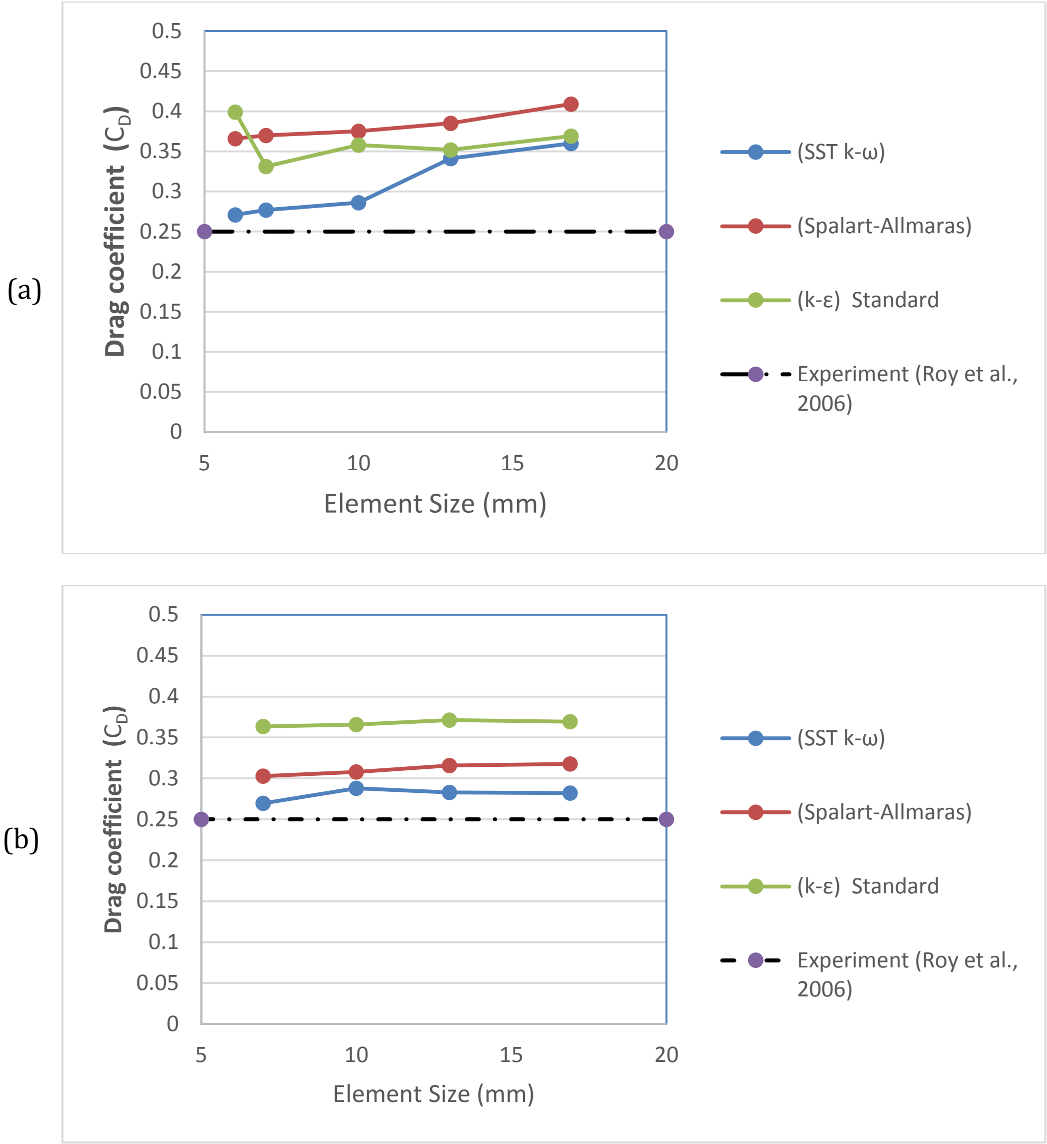

Fig. 4.16. Drag coefficients for different grid densities employing different turbulence models. (a) hybrid mesh (b) fully structured mesh.

To give an idea of the convergence criteria used in the results above, in the case of the fine hybrid mesh (10mm), a total of 6000 iterations were required for convergence. However, due to solution stability issues, the simulation was run for the first 1000 iterations using more stable 1st order discretisation schemes in conjunction with low under relaxation factors, before switching to 2nd order discretisation until the solution was converged, see Fig. 4.17(a). This process was typical for all hybrid mesh solutions. For all solutions computed on the fully structured mesh design, 1st order discretisation wasn't necessary nor was relaxation so the full simulation was run for about 5000 iterations using default under relaxation factors, except for pressure which was reduced from 0.30 to 0.25, see Fig. 4.17(b). A striking feature of Fig. 4.17 is that residual errors for continuity (mass balance) for hybrid and fully-structured mesh designs are about 2.8E-4 and 8.9E-07, respectively. This provides further evidence for how the accuracy of structured meshes is superior to hybrid/unstructured meshes, as previously discussed in the literature review.

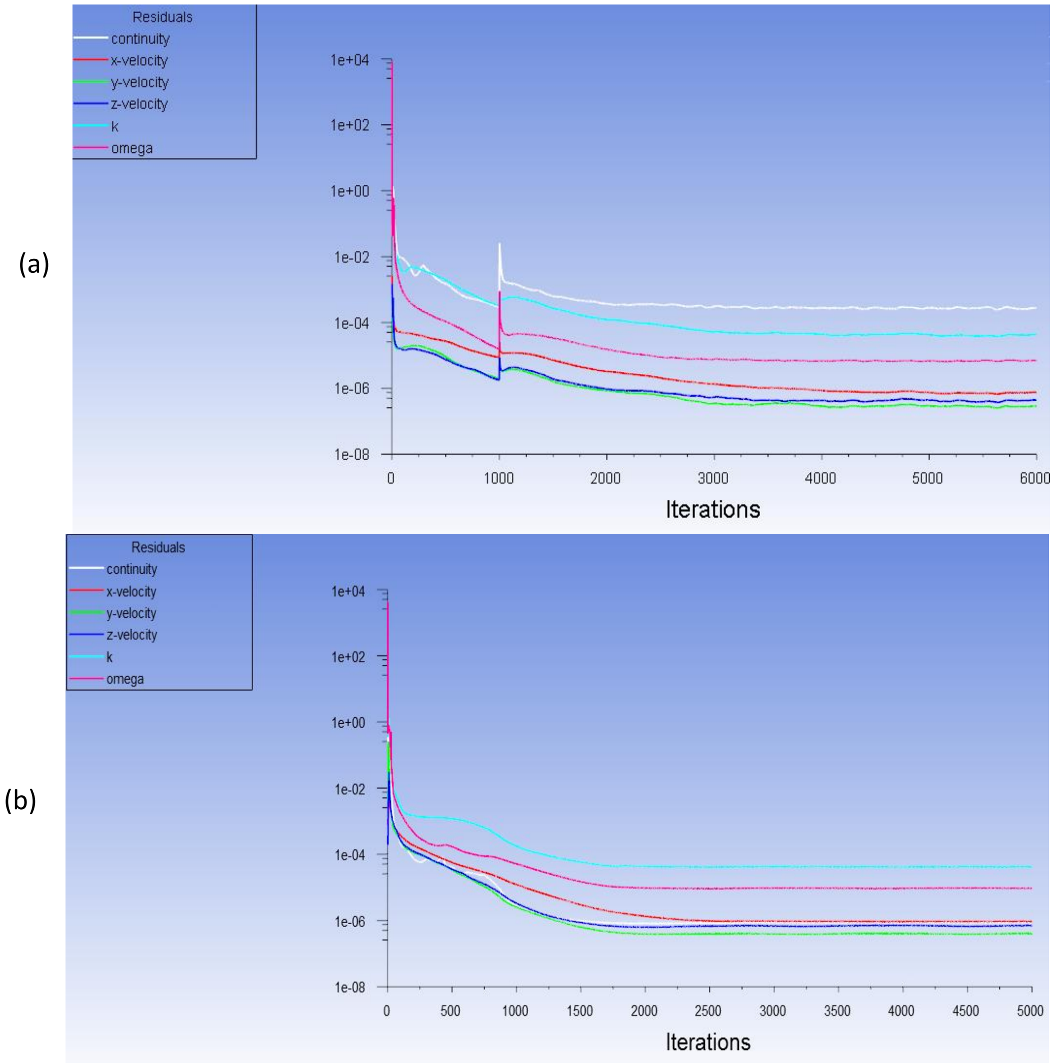

Fig. 4.17. Residual history for fine mesh (10mm) results for (a) hybrid and (b) structured meshes.

As well as the quantitative comparison shown in Table 4.4 and 4.5, results from the flow field are compared in different mesh densities and types, see Fig. 4.18-Fig. 4.21. It can be seen that the flow field is qualitatively very similar for simulation results computed on the different sizes and types of meshes. This is important ahead of the vehicle (Fig. 4.18 and Fig. 4.19) but it is especially important in the wake region behind the GTS because this is a critical region of the flow field and it has a significant impact on pressure drag. Fig. 4.20 and Fig. 4.21 show that the wake is formed between two shear layers from the top and bottom of the GTS.

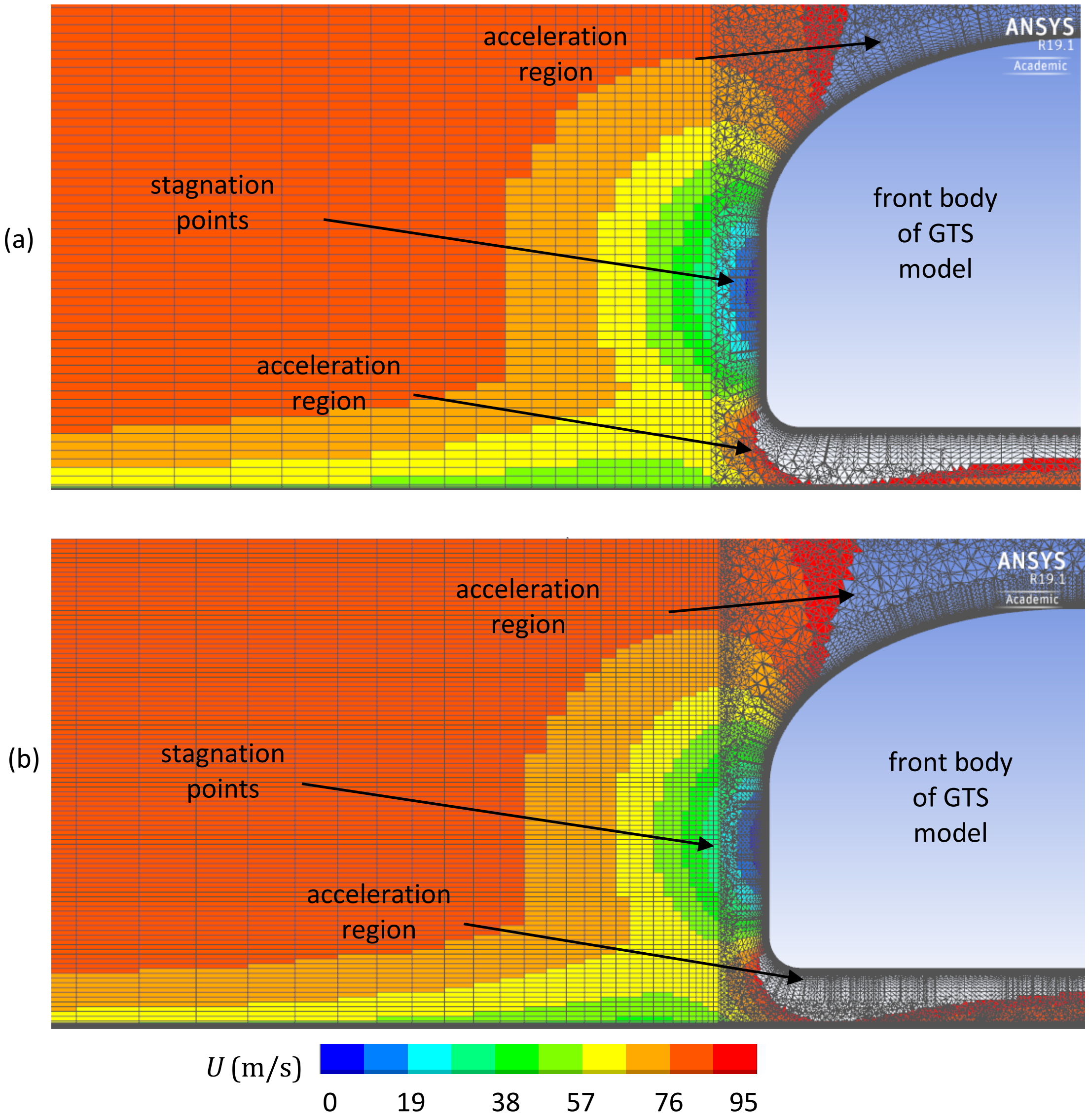

Fig. 4.18. Velocity magnitude contours on the symmetry plane immediately in front of the GTS for (a) 10mm mesh and (b) 6mm hybrid mesh structure (contours with no colour denote velocities higher than value of 95 m/s due to local acceleration).

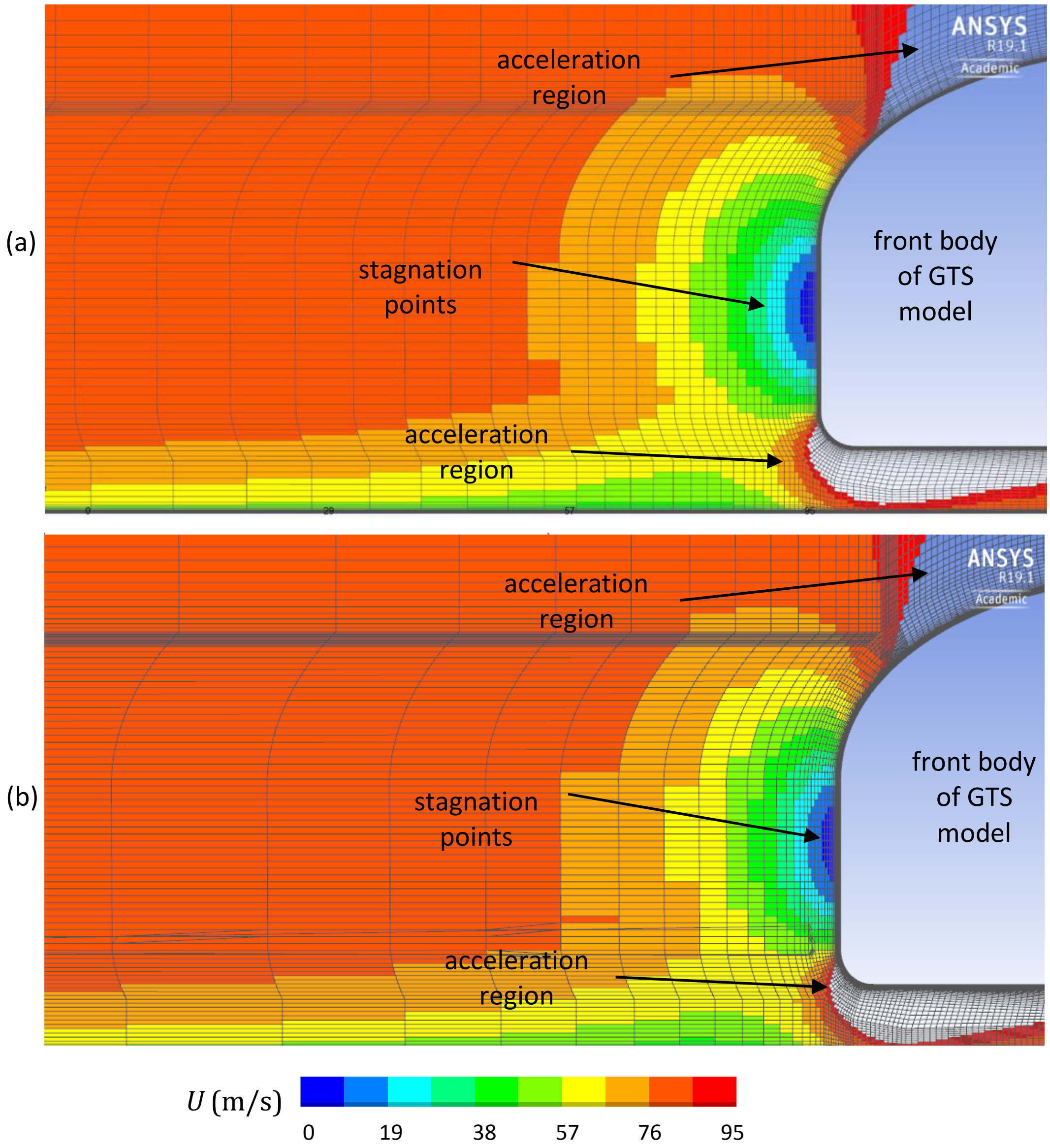

Fig. 4.19. Velocity magnitude contours on the symmetry plane immediately in front of the GTS for (a) 10mm mesh and (b) 7.7mm fully-structured meshes (contours with no colour denote velocities higher than the value of 95 m/s due to local acceleration).

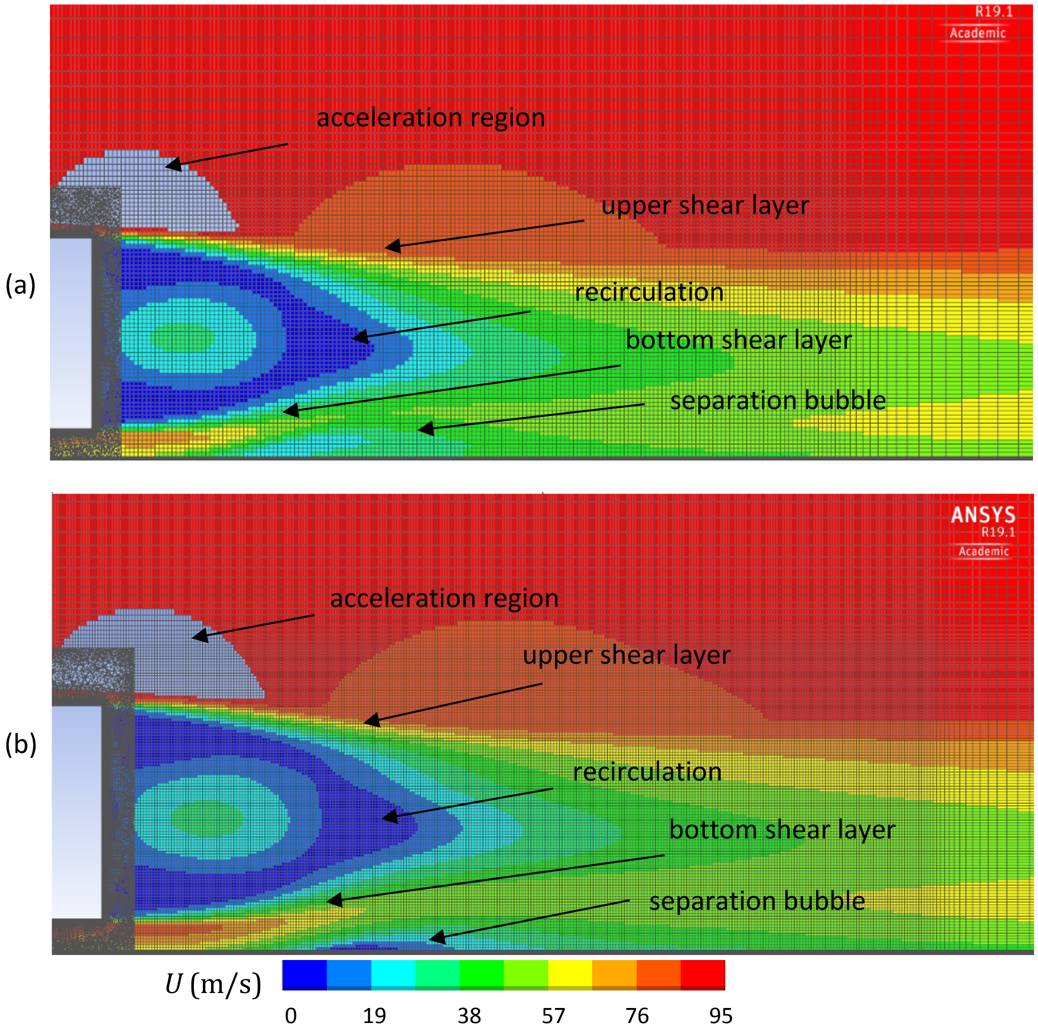

Fig. 4.20. Velocity magnitude contours on the symmetry plane in the wake of the GTS for (a) 10mm mesh and (b) 6mm hybrid mesh structure (contours with no colour denote velocities higher than the value of 95 m/s due to local acceleration).

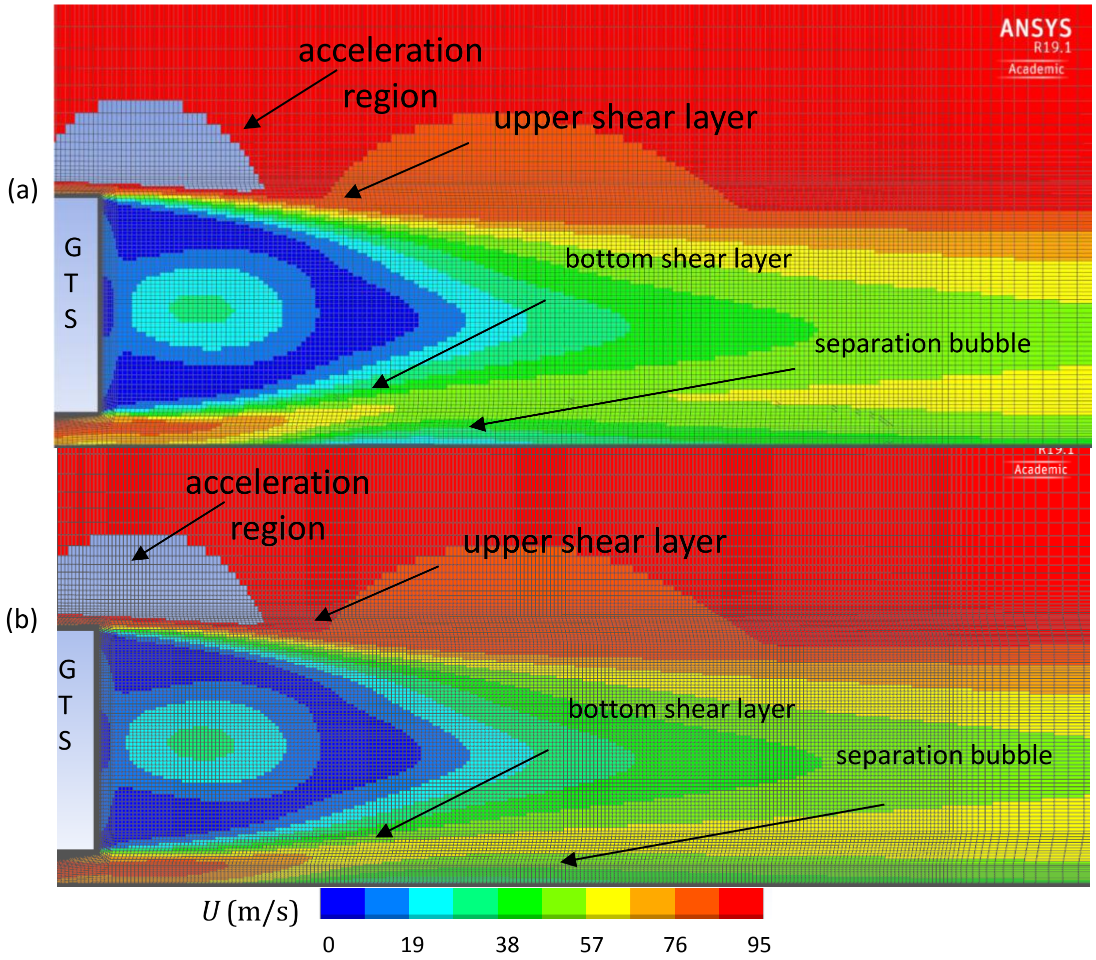

Fig. 4.21. Velocity magnitude contours on the symmetry plane in the wake of the GTS for (a) 10mm mesh and (b) 7.7mm one.

As a result of this mesh independence study, a decision was taken to complete further analysis on the result from the SST k-ω turbulence model computed on the Fine, fully structured mesh which contains approximately 8.7 million cells. This gives a good result in a reasonable simulation time. Obviously, choosing the Finer mesh gives even better results as shown above, however, the significant extra computational expense from almost double the cell count, makes this unfeasible for running optimisation simulations in later chapters. In any case, the Fine mesh result is still accurate and is considered to be mesh independent going forward.

4.5 Validation

4.5.1 Validation: aerodynamic drag comparisons

Table 4.6 summarises the comparison of C_D between the mesh-independent CFD result described above (second column) and five results from the work of both Roy et al., (2006) and Maddox et al. (2004), including experimental data. It can be seen that the prediction of

C_D in the present study is a fairly close match to the experimental result and much closer than the RANS CFD results of (Roy et al., 2006a) and Maddox et al. (2004) i.e. Spalart Allmaras and SST k-ω models. The accuracy of the DES model employed by Maddox et al. (2004) is higher than their RANS model results which was expected for this bluff body where massive flow separation is expected. However, their good DES result (compared to their RANS) could be a feature of the relatively coarse unstructured grid they used.

Table 4.6: Drag coefficient comparisons

	(Present study) Fluent CFD code 8 million elements, fine mesh (10mm)	(Roy et al., 2006) SACCARA CFD code 20 million elements			(Maddox et al., 2004) Cobalt code CFD 6 million elements	
Turbulence model	SST k-ω	Exp.	SST k-ω	Spalart Allmaras	DES	Spalart Allmaras
C_D	0.2878	0.250	0.298	0.413	0.279	0.370

4.5.2 **Validation: Flow field comparisons**

In addition to the overall drag coefficient, it is important to compare the flow field between the experimental data and the CFD results. Fig. 4.22 shows experimental data of the normalised streamwise velocity contours using the PIV method (Roy et al., 2006).

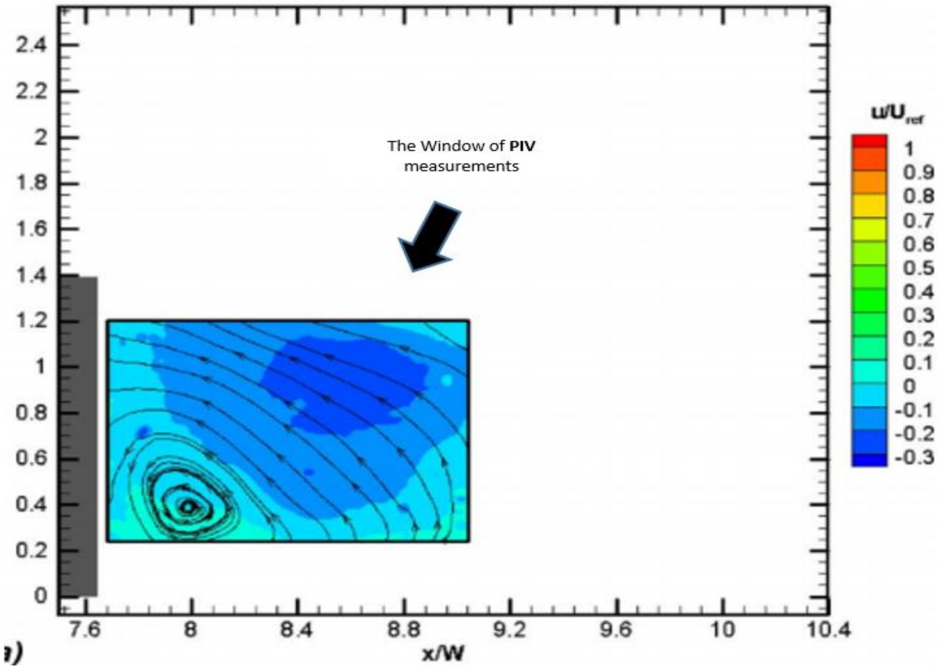

Fig. 4.22. Experimental 2D streamlines and contours of streamwise velocity projected onto the symmetry plane and displayed in the near wake region (Roy et al., 2006a).

It is evident that there is a region of flow opposing the streamwise velocity shown with negative velocities (blue region). Furthermore, a counter-clockwise vortex is revealed in the bottom left of the measurement window. Analysis of the CFD results obtained from both the hybrid and fully-structured mesh designs shows good qualitative agreement as shown in Fig. 4.23. In both cases, the recirculating vortex is present and it is rotating in the correct sense. Furthermore, the negative velocity region, which indicated flow opposing the free-stream direction, is also present in approximately the same location as the experimental results. Although the amount of experimental data is comparatively small, the similarities to CFD results adds further confidence in these results.

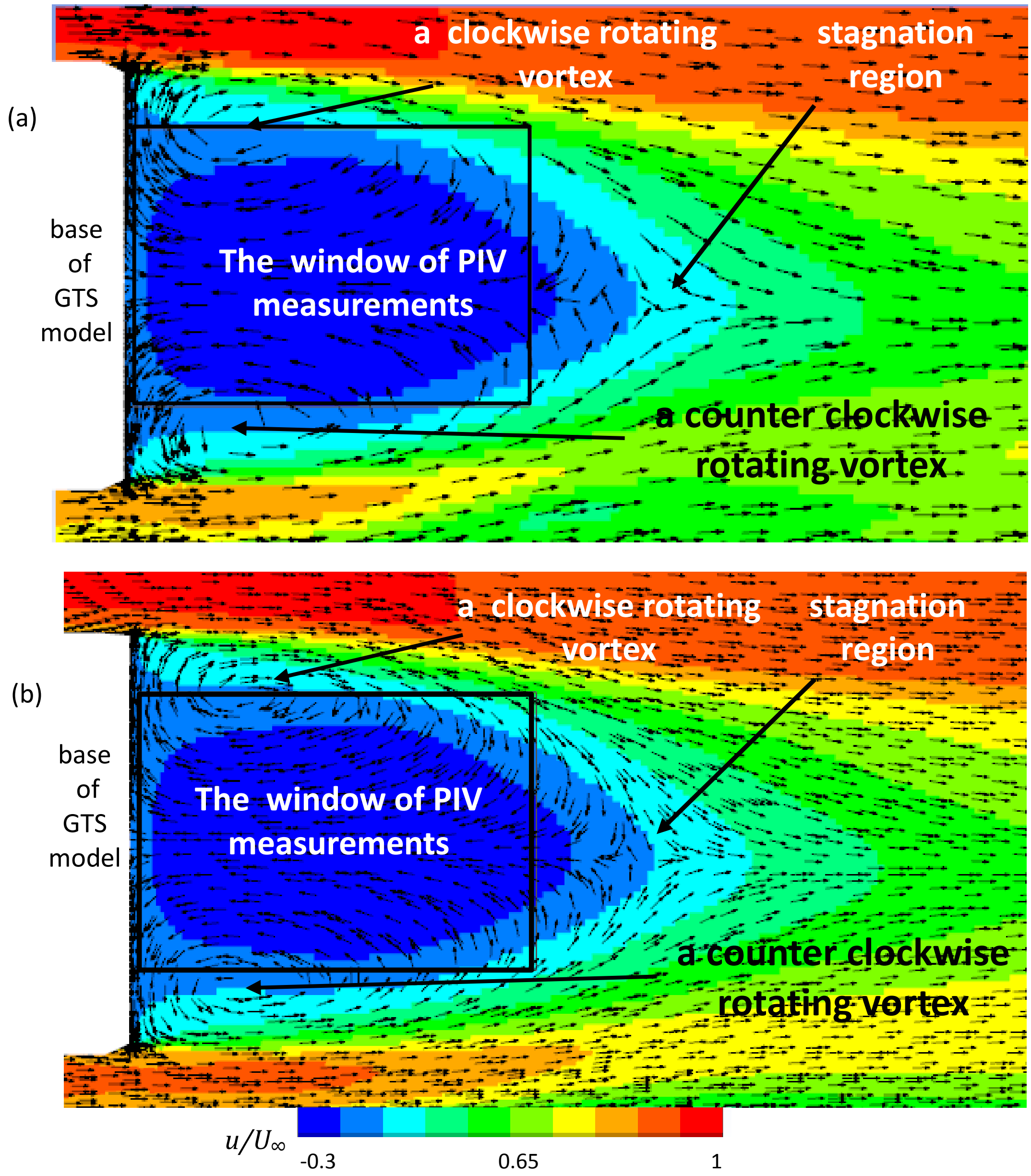

Fig. 4.23. Contours of the horizontal velocity component with overlaid velocity vectors projected on the symmetry plane and in the near-wake regions for (a) fine (10mm) hybrid mesh and (b) fine fully-structured mesh. Positive values correspond to the free-stream direction whereas negative values oppose it.

4.5.3 **Validation: pressure distributions**

A further means of validation is to compare the surface pressure from experimental data with the CFD results. In this section, only the CFD results obtained from the Fine fully-structured mesh are considered as these are considered mesh independent as already shown. Fig. 4.24-Fig. 4.31 compare the simulation results of the GTS model surface pressure coefficients to the experimental ones on the forebody, base, top and bottom. Note that for comparison, the simulation results from Roy et al., (2006) (same turbulence model) are shown. The close agreement of the drag coefficient described in section 4.4.3 (compared to experiments) can be explained by the pressure distributions shown.

Fig. 4.24 shows the pressure distribution on the front of the GTS on the symmetry plane (z = 0) as a function of the vertical coordinate i.e. top to bottom of the front face. This pressure distribution clearly shows the stagnation region (C_p = 1) on front face of the GTS which is concentrated on the lower half of the vehicle, coinciding with the vertical face. Near the top of the vehicle, it has a curved surface which blends into the flat roof section and this leads to local acceleration with a drop in pressure at the top of the vehicle. The results from the present study agree well with both experimental and simulation results from (Roy et al., 2006a).

Fig. 4.26-Fig. 4.28 show the vertical surface pressure distributions on the trailer base face in three spanwise locations. Fig. 4.26 shows the centreline distribution (z/w = 0.0), Fig. 4.27 shows the distribution which is just less than half way between the centreline and the outermost edge of the trailer unit (z/w = 0.2206) and Fig. 4.28 shows the distribution which is close to the outermost edge of the trailer (z/w = 0.4412); note that the trailer edge is at z/w = 0.5, see Fig. 4.25 to understand the orientation of these lines.

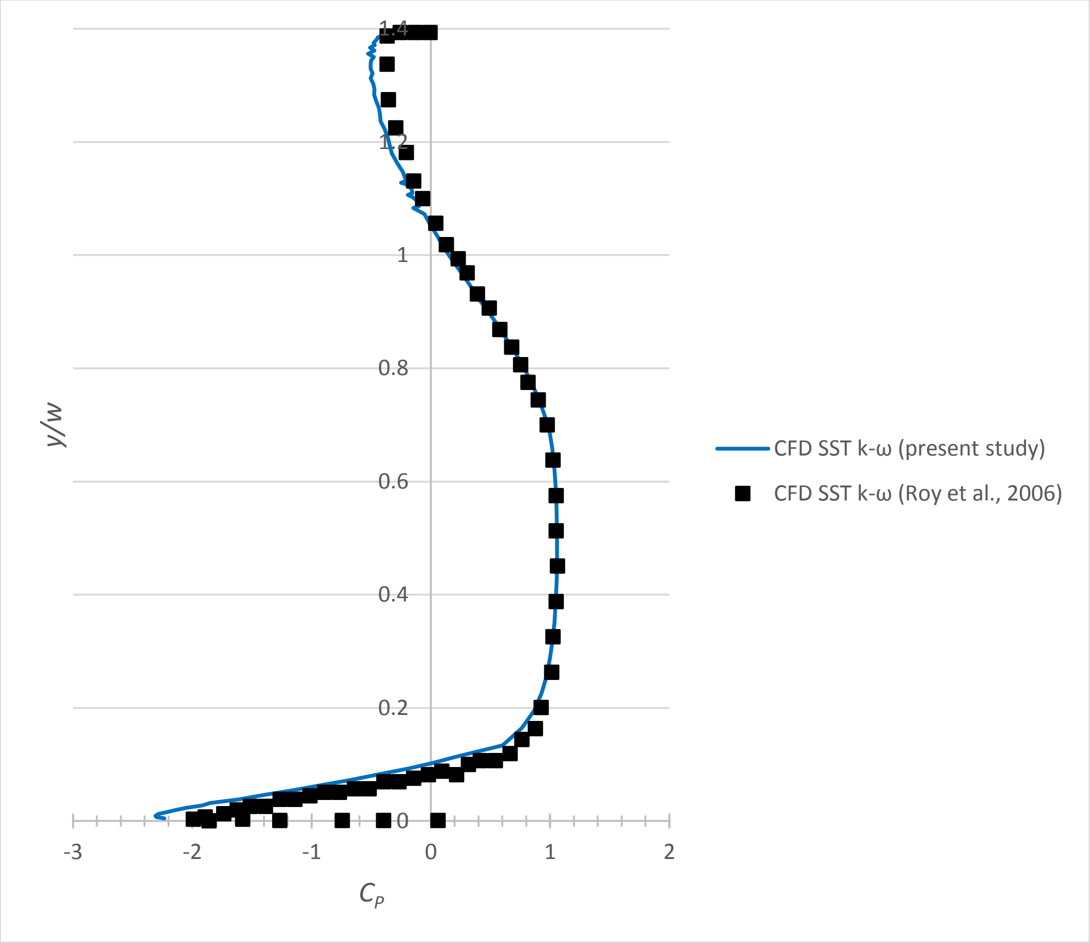

Fig. 4.24. Centreline surface pressure distributions on the GTS forebody region showing a comparison between the results from the fine, fully-structured mesh and simulation data from Roy et al., (2006).

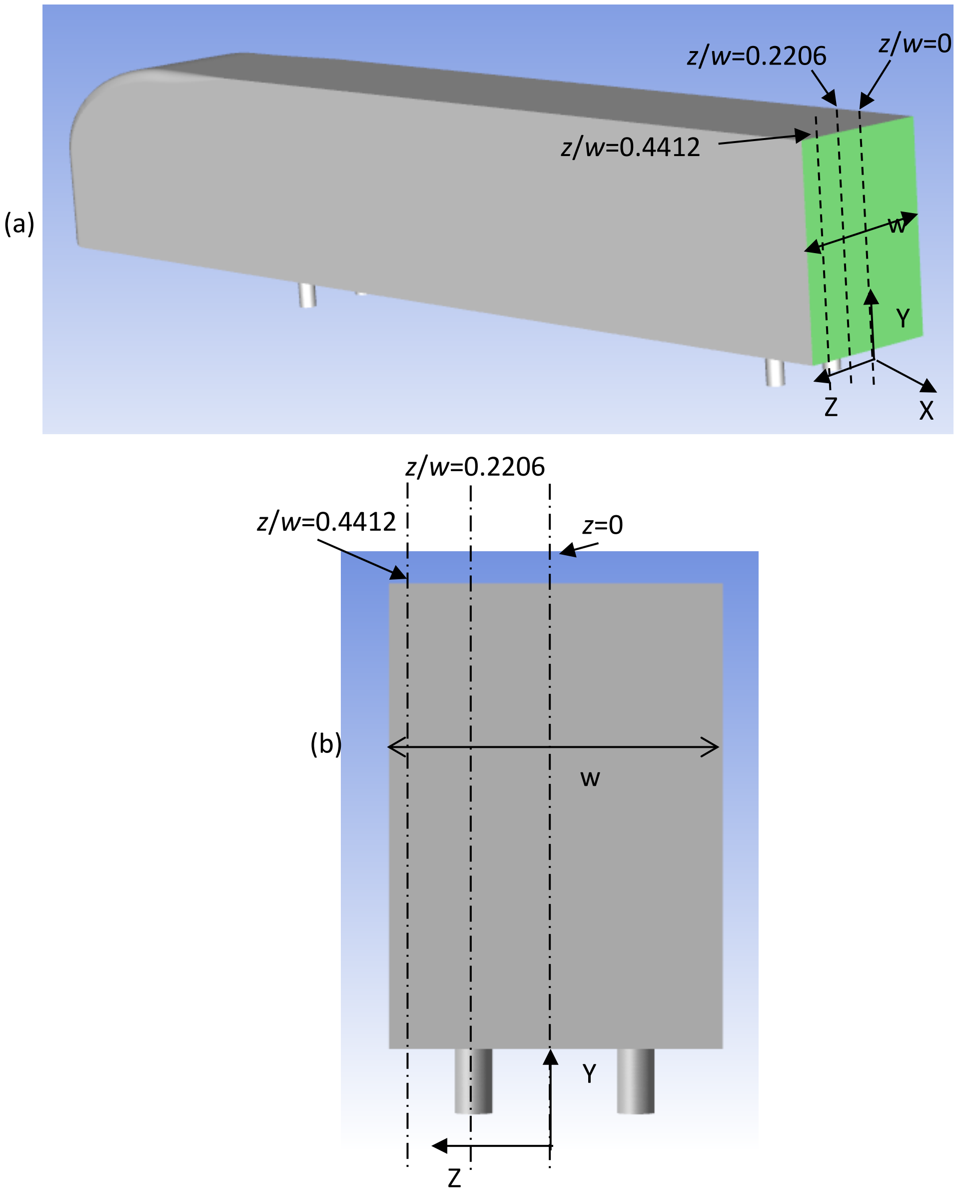

Fig. 4.25. Illustration showing location of the three spanwise lines on the trailer base face of the GTS model, (a) isometric view, (b) rear view.

It can be seen that although there are discrepancies between these experimental pressure profiles and the CFD simulations in the present study, they do provide reasonably good qualitative agreement overall with a similar range of pressure coefficients in this base region. In particular, there is close agreement at the lowest region between experiments and the CFD simulations from the present study. There is a small but clear improvement on the equivalent simulation results by Roy et al. (2006). The improvements are even more obvious for the outermost vertical pressure distribution (Fig. 4.26) where it can be seen that the CFD results in the present study generally follow the experimental measurements for the bottom half of the vehicle, whereas the pressures are notably under-predicted in the simulation results by Roy et al., (2006). This would suggest that the simulations presented in this chapter are better able to capture the flow physics in this region of the flow where gradients are generally high (close to the shear layer).

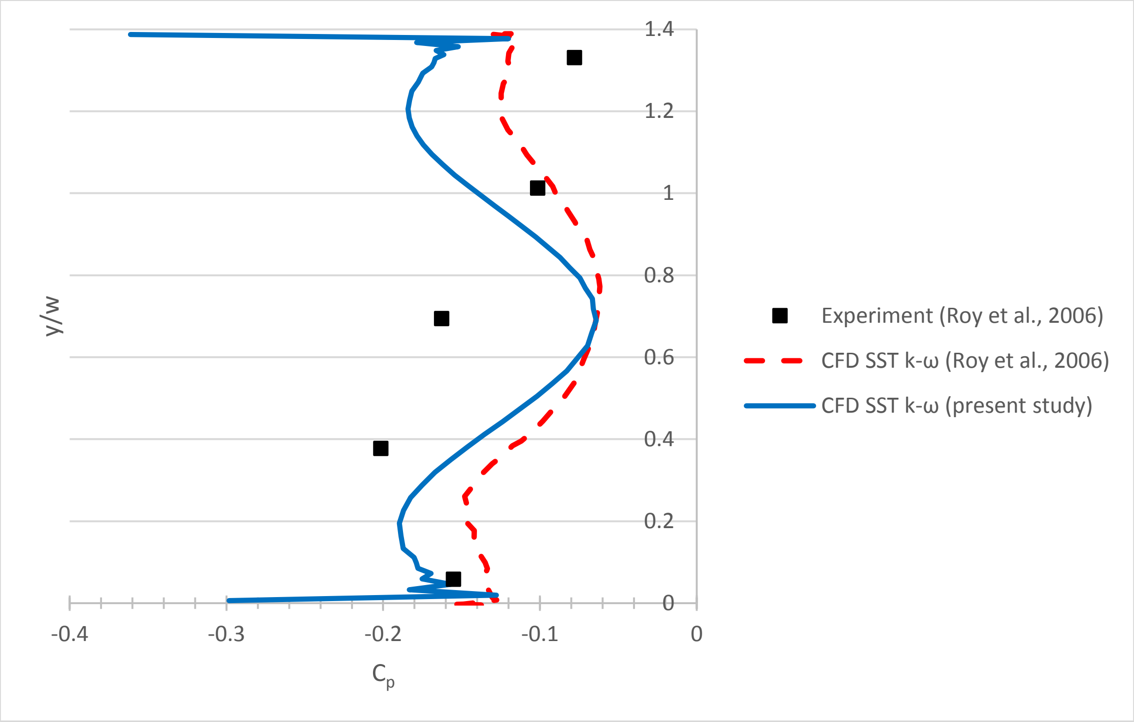

Fig. 4.26. Vertical centreline (*z*/*w*=0.0) surface pressure distributions on the GTS base face showing a comparison between the results from the fine, fully-structured mesh and both simulation and experimental data from Roy et al., (2006).

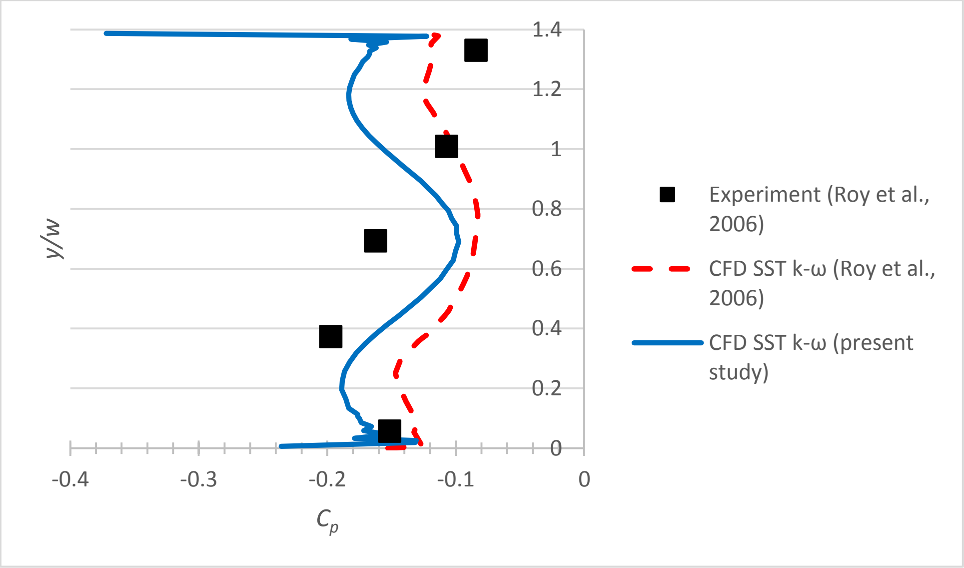

Fig. 4.27. Vertical surface pressure distributions at a transverse position just less than midway between the centreline and outer edge of the trailer (*z*/*w*=0.2206) on the GTS base face showing a comparison between the results from the fine, fully-structured mesh and both simulation and experimental data from Roy et al., (2006).

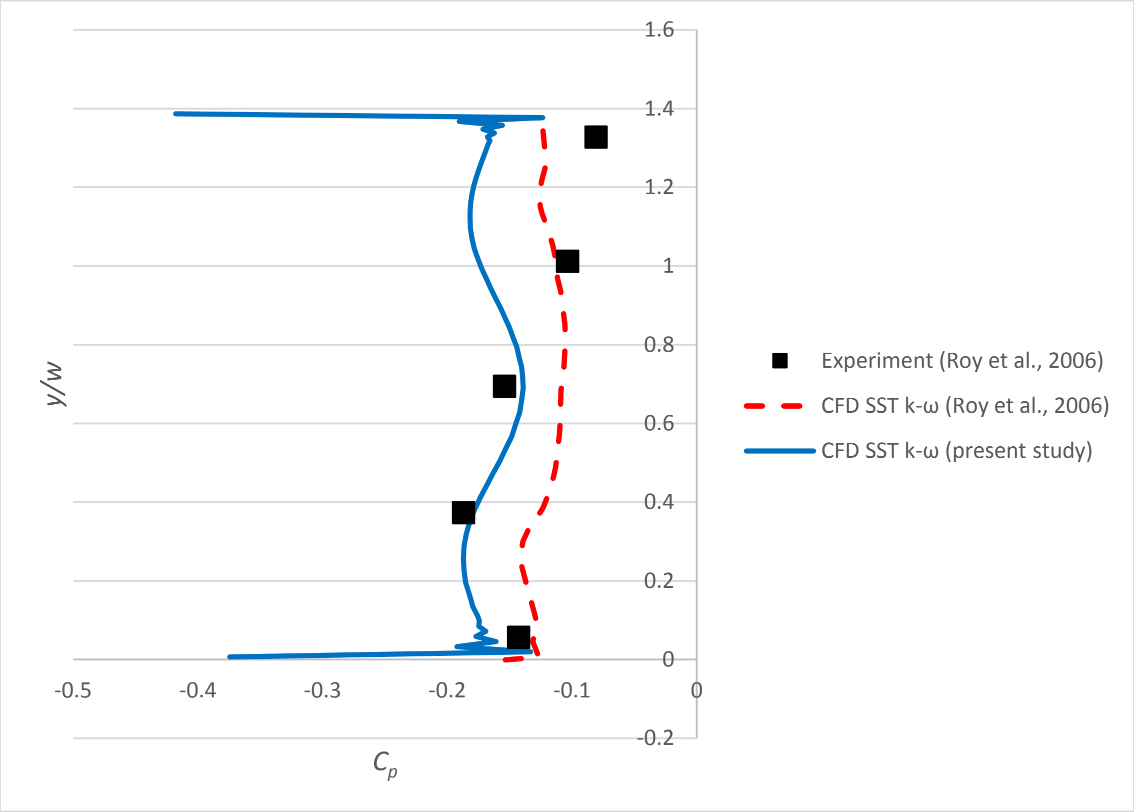

Fig. 4.28. Vertical surface pressure distributions just inboard of the outer edge of the trailer (z/w=0.4412) on the GTS base face showing a comparison between the results from the fine, fully-structured mesh and both simulation and experimental data from Roy et al., (2006).

Fig. 4.29 and Fig. 3.30 show centreline surface pressure distributions on the top and bottom of the GTS model, respectively. The pressure profile on the top of the model reveals a suction peak of about C_p =-0.5 which coincides with the acceleration over the curved front of the GTS. This is an over-prediction compared to both experimental and simulation results from Roy *et al.* (2006) where they found the peak to be smaller at C_p =-0.4. Despite the discrepancies in the suction peak, the overall pressure distribution shows that the correct trends are being predicted by the CFD approach adopted in this thesis. Similarly, the pressure distributions on the bottom surface of the GTS show good agreement between the present study and experiments; the overall pressure distribution is shown in Fig. 4.30 with a close-up of the pressure gradients in Fig. 4.31 (note different y-axis).

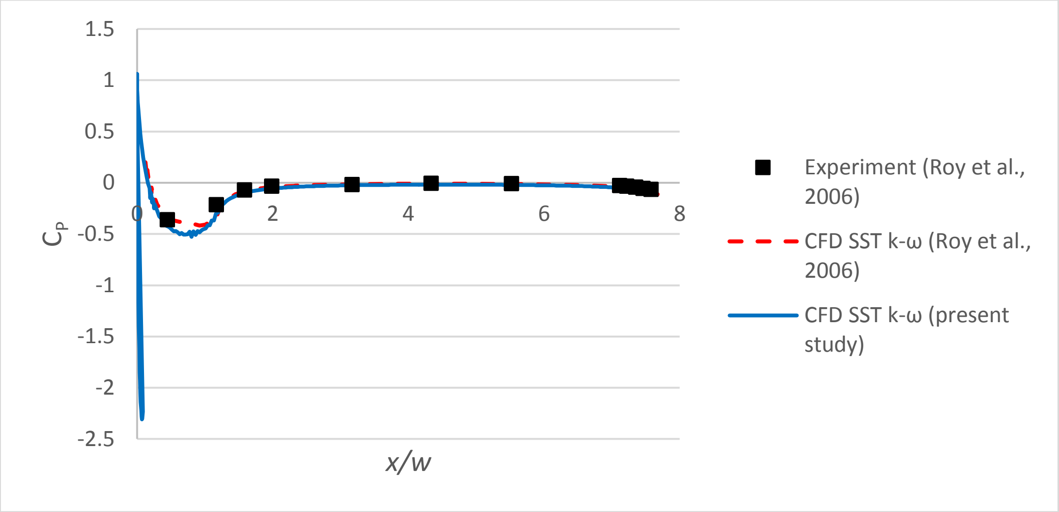

Fig. 4.29. Centreline surface pressure distributions on the top of the GTS model showing a comparison between the results from the fine, fully-structured mesh and both simulation and experimental data from Roy et al., (2006).

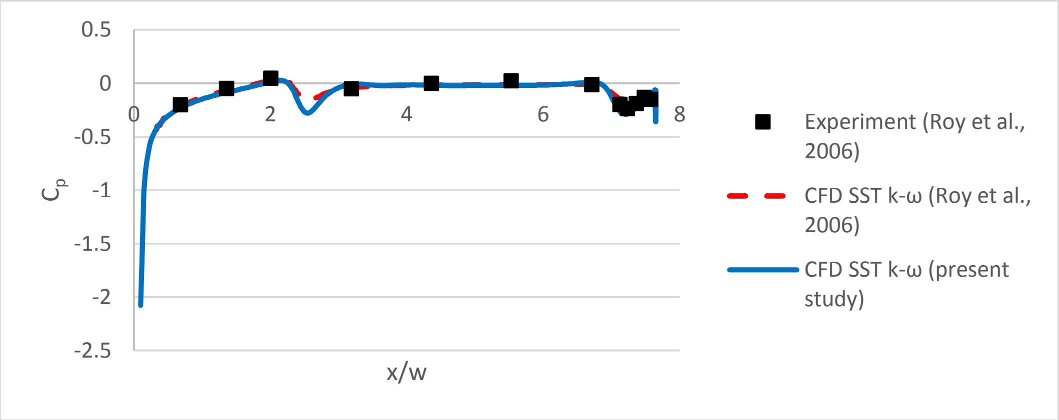

Fig. 4.30. Centreline surface pressure distributions on the bottom of the GTS model showing a comparison between the results from the fine, fully-structured mesh and both simulation and experimental data from Roy et al., (2006).

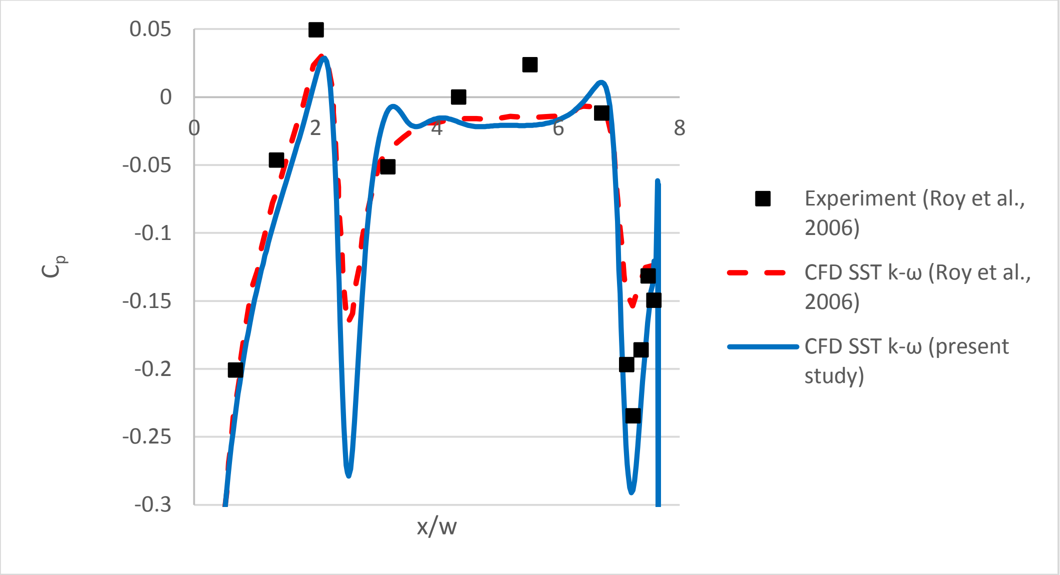

Fig. 4.31. Centreline surface pressure distributions (close-up view) on the bottom of the GTS model showing a comparison between the results from the fine, fully-structured mesh and both simulation and experimental data from Roy et al., (2006).

4.6 **Summary**

The results in this chapter showed that a fully-structured mesh design produces better results than a hybrid one when simulating the aerodynamics of the GTS model. The fine structured mesh (10mm) has been chosen to use in later chapters as it has enough accuracy, based on experimental comparisons. Also, the simulation time for results computed on this mesh structure is manageable considering the required number of simulations for this study. It has been demonstrated that the SST k-ω turbulence model is capable of simulating the salient features of massive flow separation which are very important in this work. The near-wall mesh structure accounts for viscous effects in the boundary layer region so the mesh parameters identified in this chapter are retained for all further simulations.

Chapter 5 : Analysis of typical wind angles and HGV design parameters

This chapter begins with analysis of a typical UK haulage route from Leeds to London to determine the expected wind directions experienced by an HGV. As explained in earlier chapters, one of the gaps in knowledge of HGV design is that they are not designed to accommodate side winds. Therefore, understanding the expected wind angles is crucial before designing HGV's which can perform better in these conditions. Following this, the CFD method explained in chapter 4 is applied to a generic heavy goods vehicle which is very similar to the GTS model introduced earlier. A series of preliminary parametric studies will explore the impact of geometric changes to the roof section on aerodynamic drag. These will be used in the next chapter as part of a rigorous design optimisation study to identify suitable HGV designs.

5.1 Wind direction analysis for a typical UK haulage route

The route from Leeds to London along the M1 motorway is used in this analysis because it is one of the largest haulage routes in the UK. A key assumption in this analysis is that the prevailing background wind speed of 3.5 m/s, in a south-westerly direction, is used (Lapworth and McGregor, 2008). Gusts are not considered as they are beyond the scope of this work. Another assumption is that the speed of a typical HGV is equal to the speed limit of 56 mph which is equivalent to 25 m/s. Equations (2.18) and (2.19) are used to calculate the resultant wind speed, V_{res}, and direction, β, as a result of an HGV travelling down the M1 motorway, negotiating the many changes in direction of this route. Fig. 5.1 shows a typical velocity vector diagram for the HGV travelling South and another travelling North.

$$V_{res} = \sqrt{V_D^2 + V_S^2 + 2V_D V_S \cos\beta} \tag{2.18}$$

$$\beta = \frac{V_{res}^2 - V_D^2 - V_S^2}{2V_{res}V_D} \tag{2.19}$$

The distance from Leeds to London on the M1 motorway is 315 km (196 miles) and, using GIS software, this route was split into 1000 equal parts. By using the coordinates of these points along the route, the angle between the HGV and the wind direction, δ, is easily calculated. This then enables β to be calculated which is the angle between the resultant velocity vector and the direction of travel of the HGV. This side-slip or wind angle (β) is of interest because it has a significant effect on aerodynamics and stability. Therefore, knowing how this varies for a typical journey will allow for relevant aerodynamic analysis to be conducted.

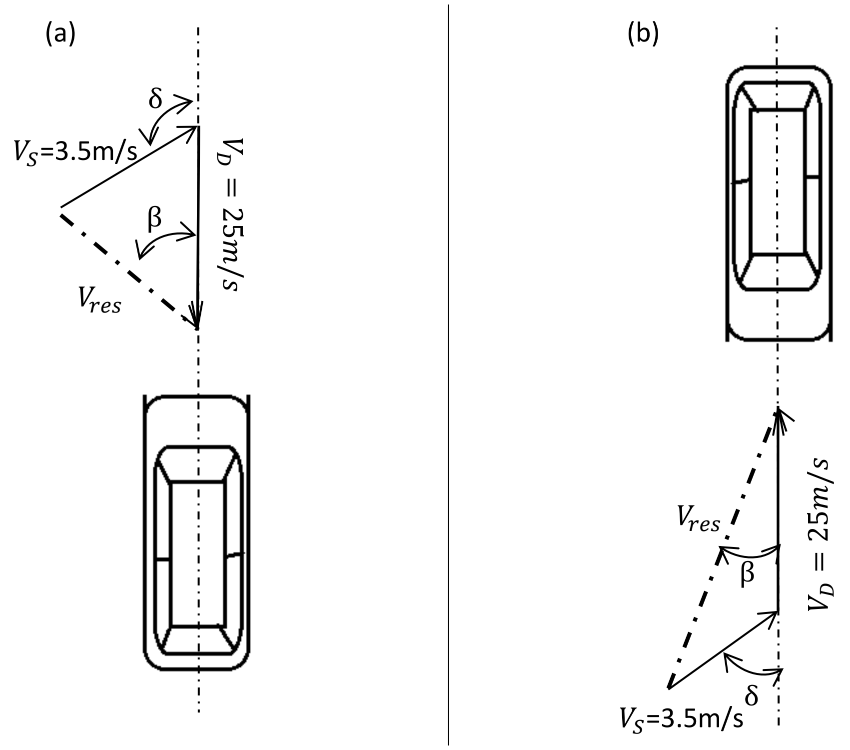

Fig. 5.1. Typical velocity vector diagrams for a vehicle travelling (a) North from London-Leeds and (b) South from Leeds-London. Both vehicle speed, V_D, and the side wind, V_S, have the same magnitude and V_S has the same direction (diagram not to scale).

Fig. 5.2 shows histograms of the frequency distribution of $|\beta|$ for the Leeds-London route. It can be seen that the mode average is eight degrees, so this angle is of significant interest. Further to this, the study by Holt et al., (2015) showed that the behavior of drag reduction from curved vehicles changes dramatically at around 5°. A decision was also made to study a wind angle of 6°, which is just less than the mean average wind angle, so for the purposes of the optimisation study in Chapter 6, the three wind angles of interest are 5°, 6° and 8°.

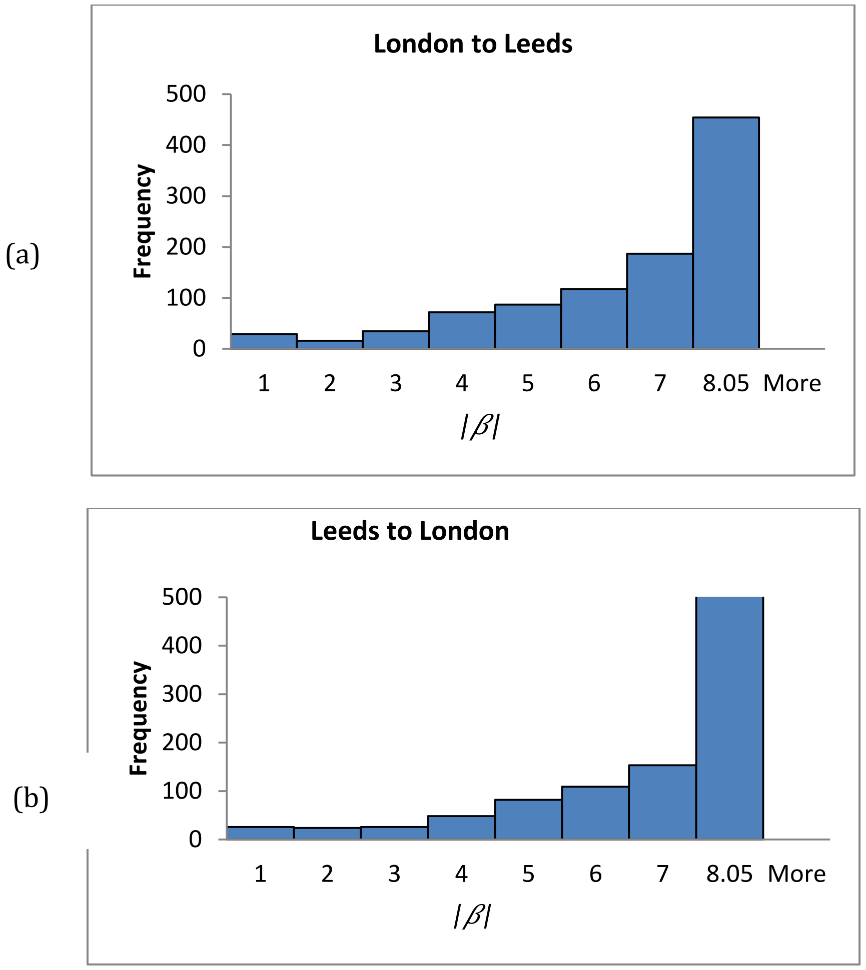

Fig. 5.2. histograms of, $|\beta|$, the angle between the resultant and the direction of HGV at the M1 motor way. (a) from London-Leeds and (b) from Leeds-London..

5.2 Preliminary parametric studies

Before starting to conduct intensive CFD simulations in search of optimal designs, a logical step is to explore individual design variables to assess their suitability in the full design optimisation cases described in Chapter 6. In order to avoid the “curse of dimensionality” (Forrester et al., 2008), only three design variables will be explored. These are chosen based on inspiration from relevant past literature and they are also designed to effectively reduce drag in both zero yaw conditions and for side winds. The GTS model is used as the basic representation of a generic HGV because the overall aim of this thesis is to provide conceptual design guidance for the over-body shape. Therefore, aspects such as a towing gap, wheels and underbody components are not considered.

5.2.1 Side edge radius

As described in the literature review, the application of curved edges on bluff bodies is a useful method for avoiding flow separation which is beneficial for reducing aerodynamic drag. Using the GTS model as a basis, attention was focused on the two sharp longitudinal edges where the roof meets the side panels. It was postulated that rounding these sharp edges could prevent flow separation at the junction of the roof and side panels in cross-winds. Therefore, these two edges are modified but all the other dimensions remain constant. Fig. 5.3(a) shows the baseline GTS model with the sharp edges and Fig. 5.3(b) and (c) show two modified versions. As can be seen, the radius of the side edge is only changed at the rear of the vehicle because it seamlessly blends into the radius of curvature, R_0, where the front section of the GTS (cab) joins into the rectangular trailer section. Therefore, by keeping R_0 constant and changing the radius at the rear of the vehicle, a range of curvatures can be evaluated. Fig. 5.3(b) shows the largest radius considered ($3.5R_0$) and Fig. 5.3(c) shows the smallest one ($0.5R_0$). This range of values was determined from some initial simulations not reported here. In all cases the radius has a smooth transition from R_0 to the rear of the vehicle.

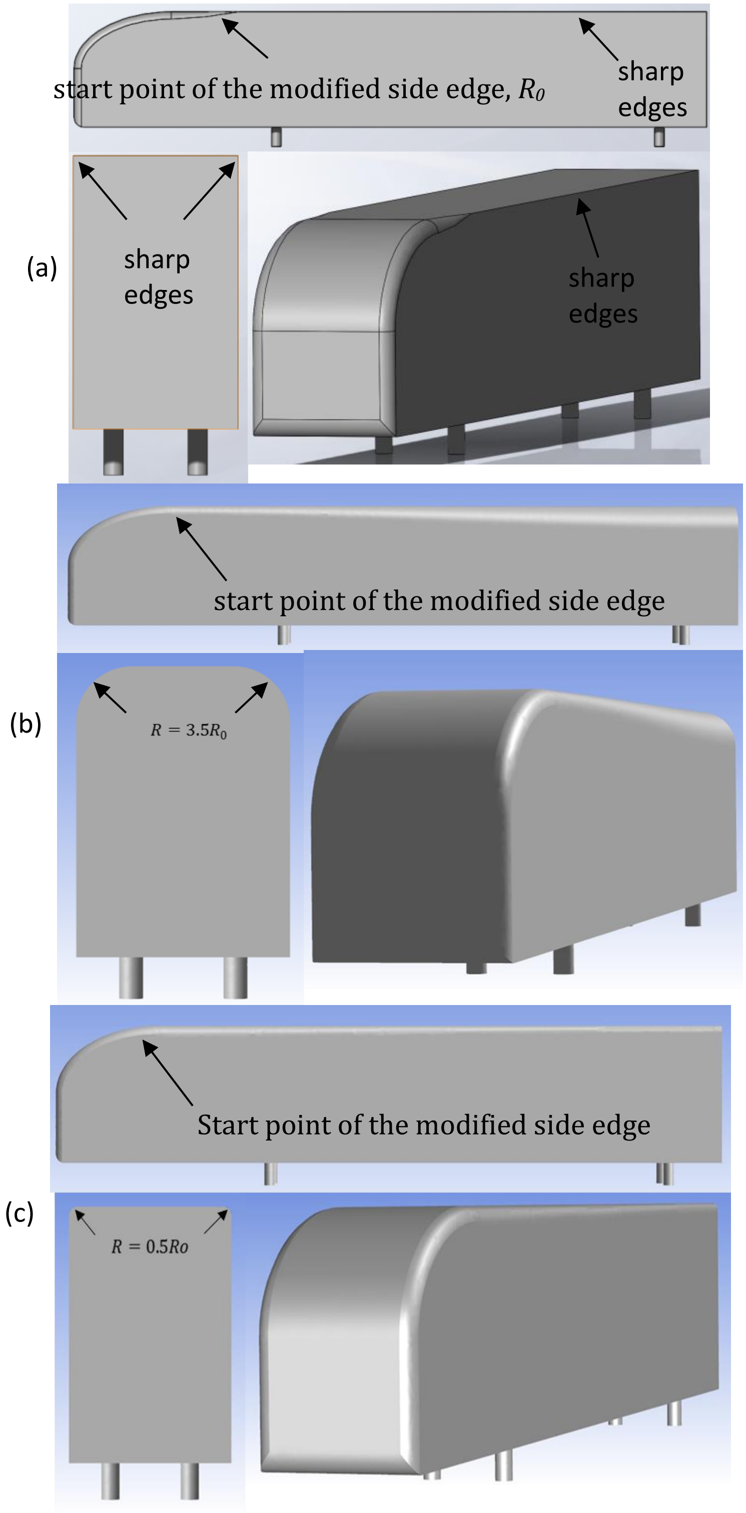

Fig. 5.3. Illustration of a) baseline GTS model and two different modified GTS models with curved side edges for b) R=3.5R_0 and c) R=0.5R_0.

The same general method and procedures used in chapter 4 were implemented to generate the mesh and the subsequent CFD results. Before conducting parametric simulations on rounded side edges, it was necessary to investigate scale effects. Recalling the validation study in Chapter 4, the 1/8th GTS model was surrounded by a relatively small wind tunnel which gave a Reynolds number of 2 million. The Mach number was slightly over the limit of incompressible flow (0.3) with a Mach number of 0.35. Table 5.1 shows the results from four simulations. The first row of data is for the validation case (wind tunnel) for comparison with three other cases at full scale for various free-stream velocities. Due to the fact that the scale has increased by a factor of 8, the velocity reduces in proportion, which dramatically lowers the Mach number well into the incompressible regime. Of the three free-stream velocities investigated, the greatest is equal to the speed of an HGV traveling at the speed limit of 56 mph = 25 m/s. It is seen that the Reynolds number is high in all cases and in the turbulence regime. The drag coefficient does reduce from the confined wind tunnel to the larger domain but only by approximately ΔC_D = -0.02, so it is relatively small.

Table 5.1. Comparison of drag data at different scales and free-stream velocities.

	Scale of model	free-stream velocity	Re	Mach number
Wind Tunnel	(1/8)	90m/s	2.00E+06	0.34799
Large extended domain	1	11.25	2.00E+06	0.04121
Large extended domain	1	18	3.03E+06	0.06593
Large extended domain	1	25	4.21E+06	0.09158

Full-scale, three dimensional models were built with different radii ranging from R_0 to $3.5R_0$ in increments of $0.5R_0$, giving five different models in total. Then, the fine (10mm) hybrid mesh structure explained in Chapter 4, was applied. Then inlet boundary conditions were set so that the free-stream velocity was equal 25 m/s. The solver settings used in chapter 4 and the SST k-ω turbulence model was used. Furthermore, the inlet boundary conditions were changed to simulate a range of different wind angles from $\beta = 0^\circ$ to $\beta = 10^\circ$ in increments of 1°. As expected, the rounding of sharp edges has an impact on the aerodynamic characteristics of the vehicle. Fig. 5.4 shows the variation of drag coefficient, C_D, with side wind angle for the five different models and these are compared to the standard (unmodified) GTS model for comparison. All results broadly follow those from Holt et al., (2015) with drag increasing with yaw angle for all configurations. It can be seen that in the side wind range of 0-7°, for the modified model with the two smallest radii ($R=R_0$ and $R=1.5R_0$) the drag coefficient is less than the baseline case, whereas for all other (larger) values of R tested, the drag is greater. Interestingly, a small step change in drag ($\Delta C_D \approx 0.03$) occurs when the radius is $R > 1.5R_0$ this is because larger radii leads to suction on the leeward face of the vehicle which influences the strength of the trailing vortex and contributes extra drag. Based on these results, the range of radii to be considered in the later optimisation study is R=0.5R_0 to R=2.5R_0. This is a wide enough range of radii to possibly find an optimum combination of design variables later.

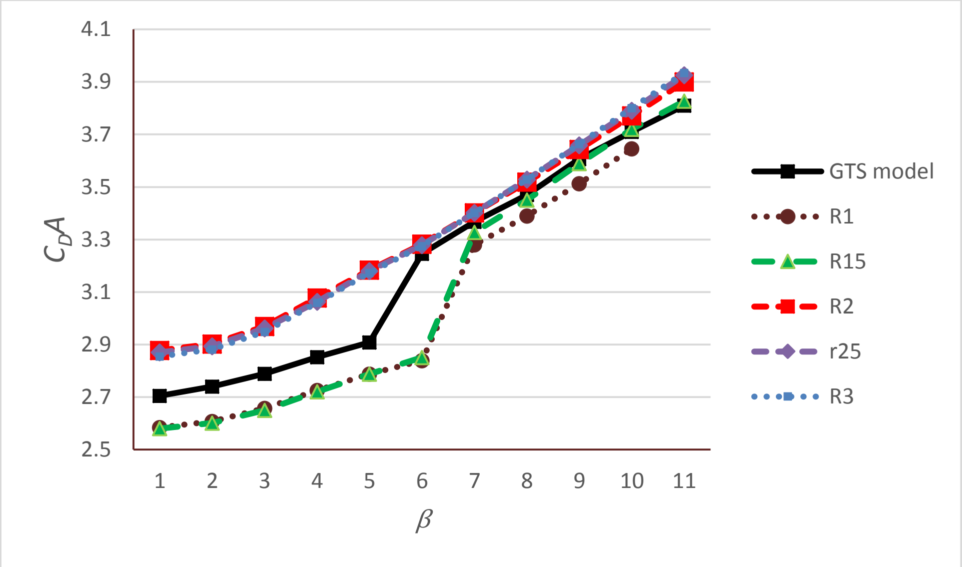

Fig. 5.4. Variation of the drag coefficient, C_DA, as a function of the side wind angle, β, for a range of rear radii, R, compared to the baseline GTS model.

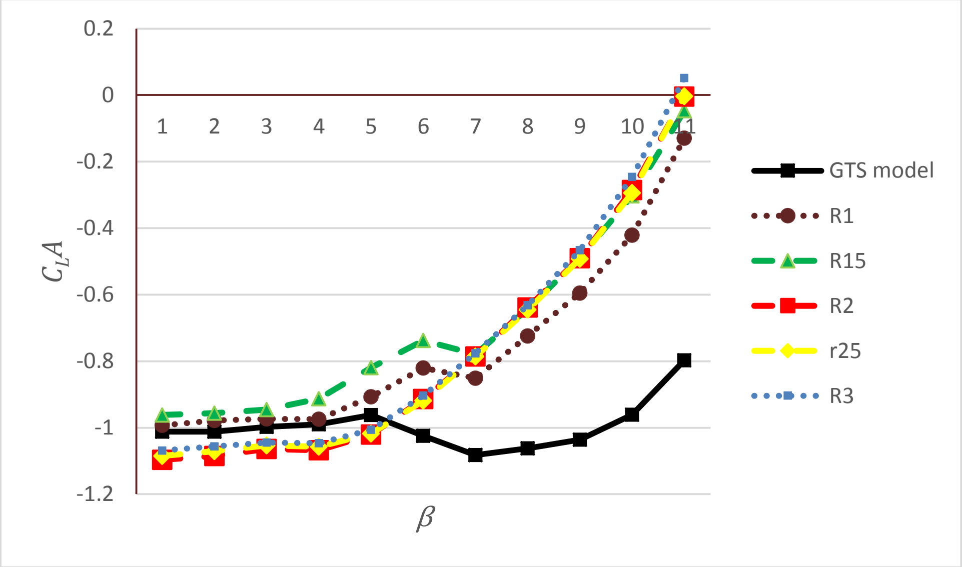

Fig. 5.5. Variation of the lift coefficient, C_LA, as a function of the side wind angle, β, for a range of rear radii, R, compared to the baseline GTS model.

5.2.2 Over-body shape exploration

In section 5.2.1 the side edge radii (*R1* and *R1.5*) showed merit for reducing aerodynamic drag in a side wind. A range of other parameters also need to be considered to provide the contours of the over-body shape because this also affects drag, particularly for zero yaw cases. In particular, over-body contouring will affect how the flows over the roof interact with the wake so this requires careful consideration. Here, a number of 2D CFD simulations are carried out to choose which method will be suitable to control the curvature of the roof shape and positively influence the aerodynamics of the vehicle. Clearly, 2D analysis will neglect 3D flow effects but this preliminary analysis is designed to give an indication of which parameters to choose prior to the detailed 3D optimisation study present later. In the following sub-sections, five different methods for modifying the side profile of the GTS model are tested and compared. These 2D CFD simulations are carried out by using Fluent version 17 and the grid was created by using the specification of the fine (10mm) hybrid mesh, as explained in Chapter 4.

5.2.2.1 Method 1: trailer aerofoil integration

As described in Chapter 2, Holt et al., (2015) modified the over-body profile of a small van using the known low-drag characteristics of aerofoils. Here, the side profile of the standard GTS model is modified by integrating symmetric aerofoils so that the over-body profile is controlled from the intersection of the cab-trailer to the rear of the trailer itself. Fig. 5.6 shows how the NACA0010 aerofoil is overlaid on the GTS side profile and then this is used to give the final shape (in Fig. 5.6(b)). Using this method, the side profile is changed by varying the thickness, *t*, of the aerofoil and the final shape of the front is the original front shape of the GTS baseline geometry. The height and frontal projected area of this modification and the baseline are the same.

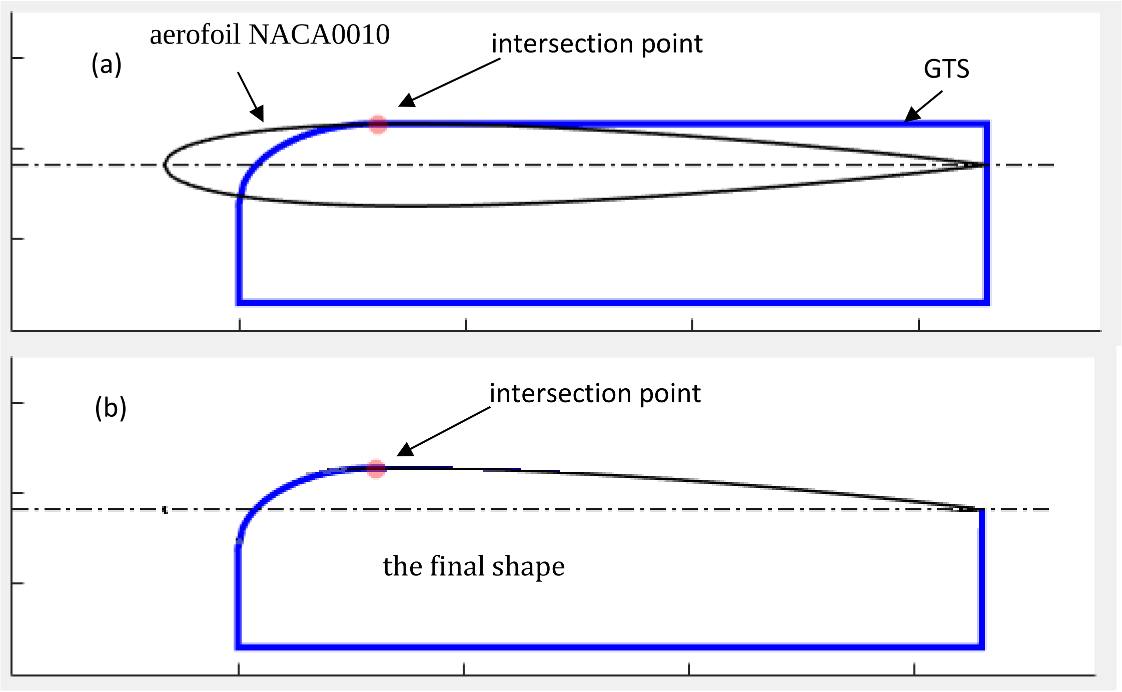

Fig. 5.6. Illustration showing (a) geometry construction and (b) the final side profile of one of the modified GTS models for method 1 using a NACA0010 aerofoil as an example.

Table 5.2 shows the drag coefficient of the baseline GTS model compared to five variants of method 1. It can be seen that the drag coefficient decreases as the thickness increases. To explain this effect Fig. 5.7 shows velocity contours for these modified vehicles and the baseline GTS. Clearly, the wake is smaller as the curvature of the roof section increases. It is important to note that all of these simulations were carried out with the same conditions as the validation case i.e. 1/8th scale and higher free-stream velocities. These tests were carried out before those in section 5.2.1 (full-scale) but the results are still representative of the overall effects of curvature.

Table 5.2. Drag data for method 1.

	H(%)	C_D
Baseline	100.0	0.385
NACA0002	93.4	0.342
NACA0006	86.7	0.264
NACA0008	80.1	0.230
NACA0010	66.8	0.202

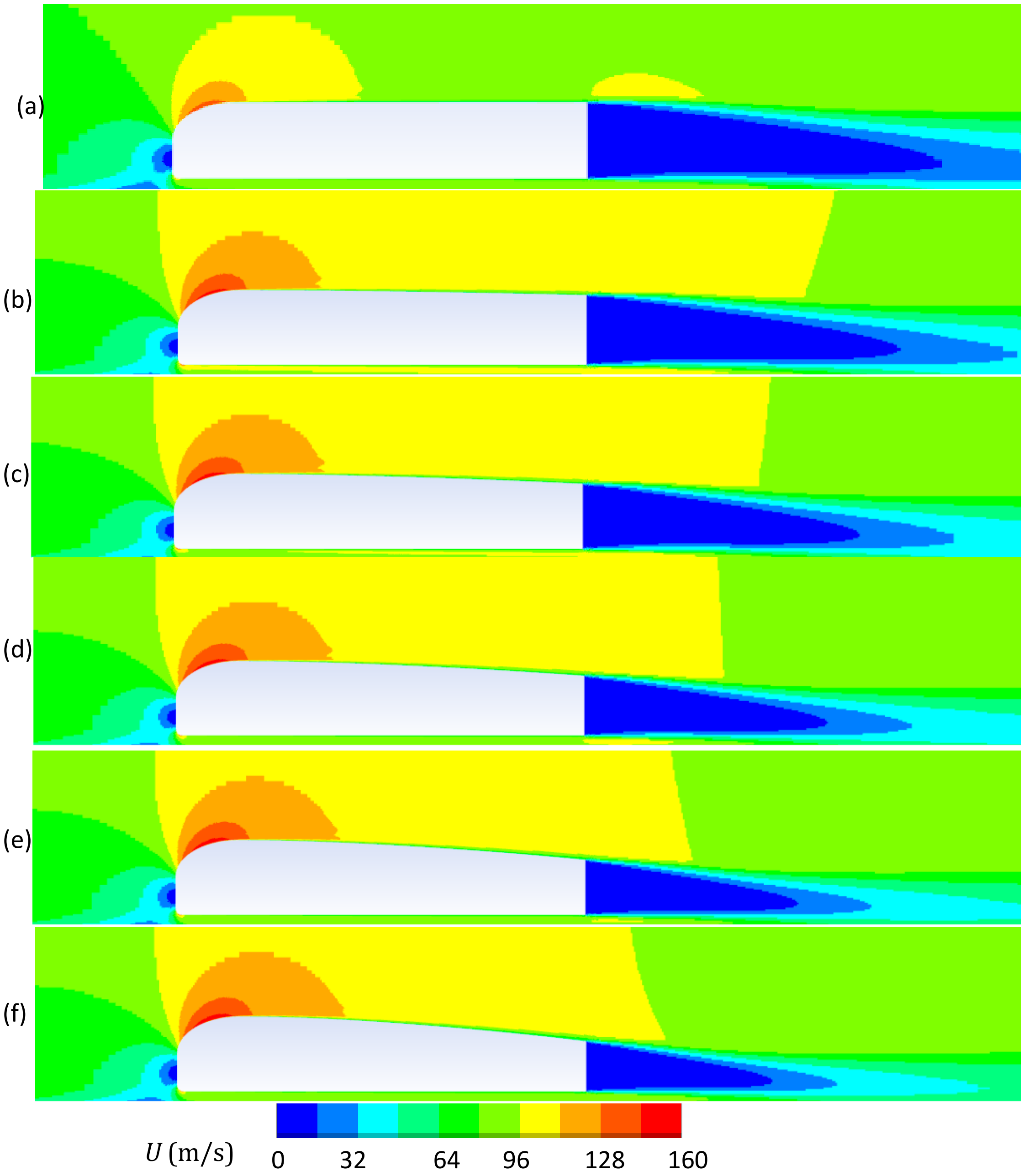

Fig. 5.7. Velocity magnitude contours for Method 1 (a) baseline GTS (b) *t*=2% (c) *t*=4% (d) *t*=6%, (e) *t*=8% and (f) *t*=10%.

5.2.2.2 **Method 2: whole vehicle aerofoil integration**

This method is a variation of method 1 and it reproduces the work of Holt et al., (2015) where the top section of a symmetric aerofoil is used to construct the whole of the upper HGV side profile, see Fig. 5.8. The motivation for this concept is to carefully control the geometry from the very front of the cab section all the way to the base region.

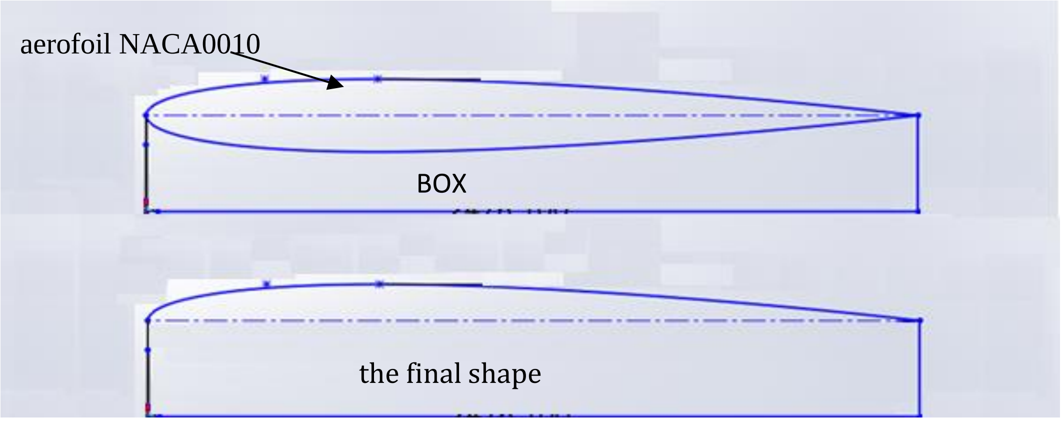

Fig. 5.8. Illustration showing (a) geometry construction and (b) the final side profile of one of the modified GTS models for method 2 using a NACA0010 aerofoil as an example.

Table 5.3 shows the drag coefficient of the baseline GTS model compared to five variants for method 2. Here, the over-body shape is determined by symmetric aerofoils which have thicknesses, *t*, changing from 2% to 10%. It is seen that the drag is only reduced when the thickness of the modified design is quite large at around 8% or more. As with method 1, only thick aerofoils are able to influence the size of the wake by directing flow downwards as it leaves the trailing edge of the over-body profile.

Table 5.3. Method 2.

	H (%)	C_D
Baseline	100	0.385
NACA0002	94.5	1.060
NACA0004	89.0	0.876
NACA0006	83.5	0.561
NACA0008	78.0	0.254
NACA0010	72.5	0.223

Fig. 5.9 also reveals that the front of the modified designs are inherently less-rounded than the baseline GTS model with small thicknesses. In such cases, it can be seen that there is a local acceleration region near the top of the cab at the leading edge and a greater front stagnation region; these observations all contribute to a higher drag for small thicknesses. Benefits are only realised when the thickness is large enough to minimise the stagnation area at the front and the size of the wake in the base region. However, increasing the thickness too much does have implications for either how tall the vehicle will be, or, for how flat the front of the vehicle can be which has further implications for driver visibility i.e. having a conventional flat windscreen.

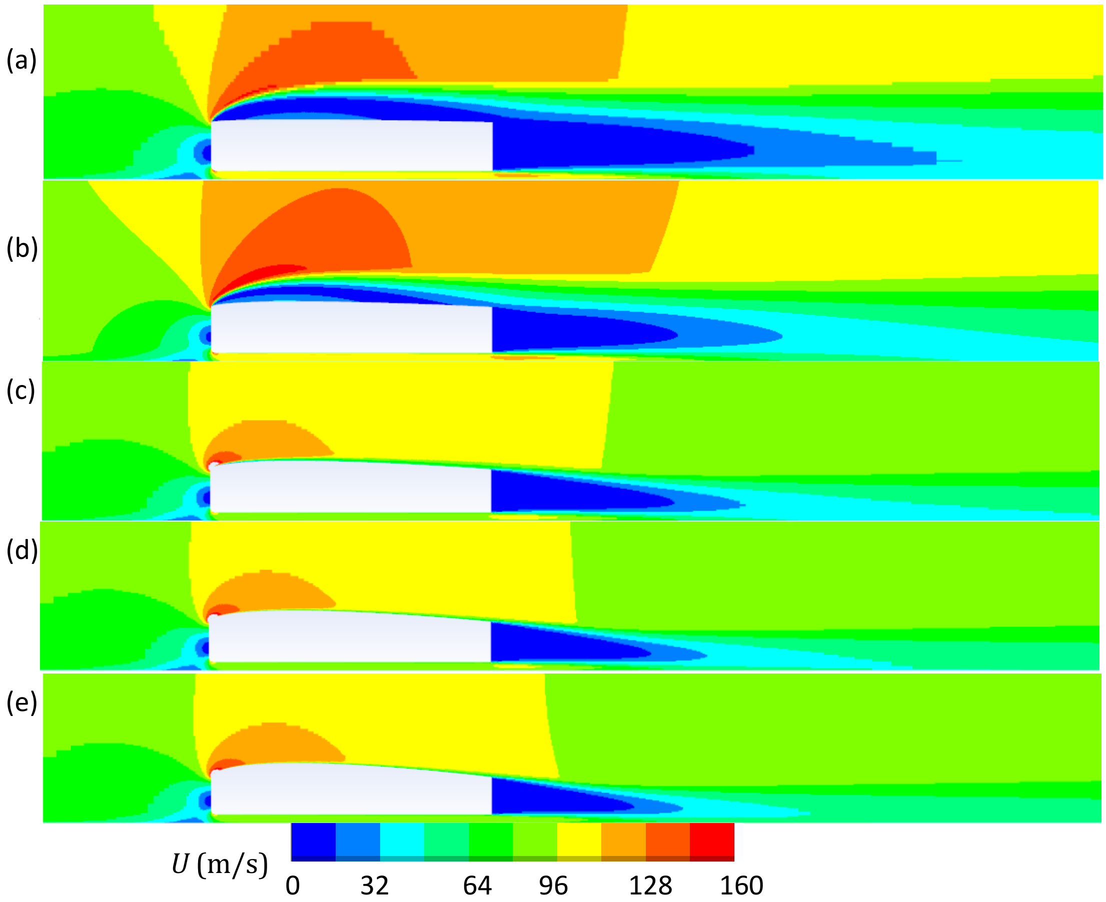

Fig. 5.9. Velocity magnitude contours for Method 2 (a) *t*=2% (b) *t*=4% (c) *t*=6%, (d) *t*=8% and (e) *t*=10%.

5.2.2.3 **Method 3: GTS-aerofoil hybrid**

Following on from the previous two methods, this third idea was proposed to try to integrate the smooth GTS baseline design with symmetrical NACA aerofoils again. The purpose was to see if a hybrid of methods 1 and 2 would yield any potential benefits. Fig. 5.10 shows an example of this method using the NACA0010 aerofoil. The final shape is changed by varying the thickness of the NACA aerofoil. As shown in Fig. 5.10, the front intersection point is more forward compared to method 1 so part of the front shape of the vehicle is determined by the shape of the aerofoil when viewed from the front. However, the height of and the projected front area is the same as the baseline GTS model.

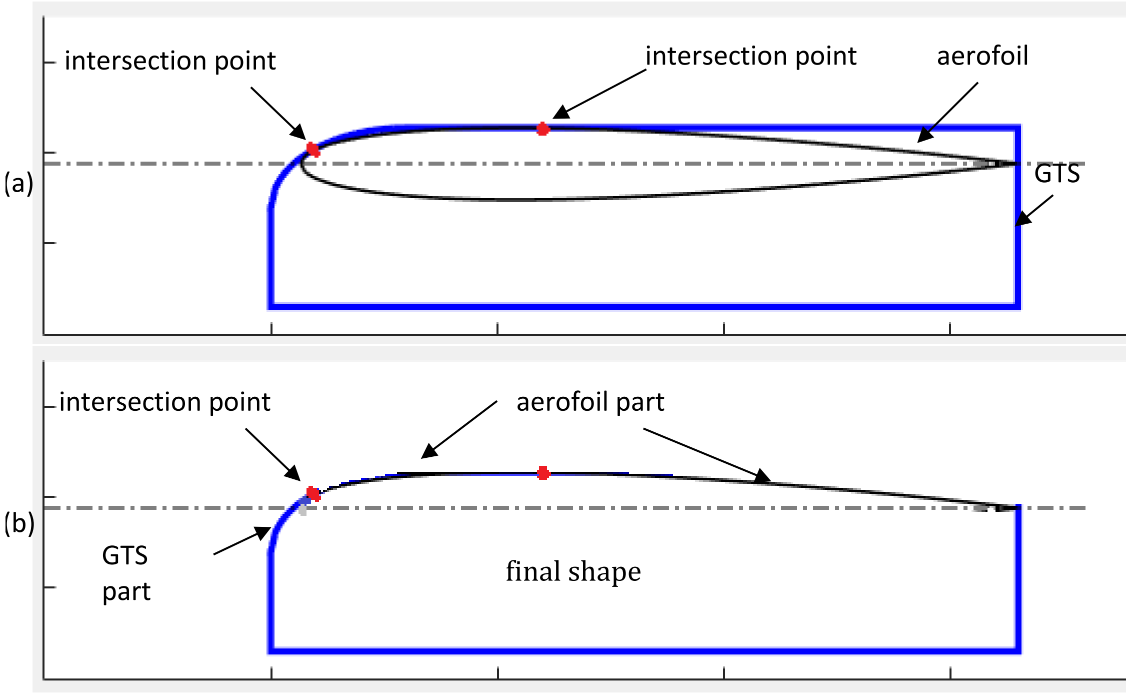

Fig. 5.10. Illustration showing (a) geometry construction and (b) the final side profile of one example of the modified vehicle, for method 3 using a NACA0010 aerofoil as an example.

Table 5.4 shows the drag coefficient of the baseline GTS model compared to five variants of method 3. It can be seen, as with the earlier methods, that the drag coefficient decreases as the thickness increases. To explain this effect Fig. 5.11 shows velocity magnitude contours for these modified designs and the baseline GTS. As with method 1, it can be seen that the size of the wake reduces behind the rear as the thickness increases. The results show that method 3 also directs flow downwards as it leaves the trailing edge of the over-body profile, making the wake smaller.

Table 5.4. Method 3.

	H (%)	C_D
Baseline	100	0.039
NACA0002	95.0	0.351
NACA0004	89.7	0.315
NACA0006	84.3	0.281
NACA0008	78.8	0.249
NACA0010	73.1	0.222

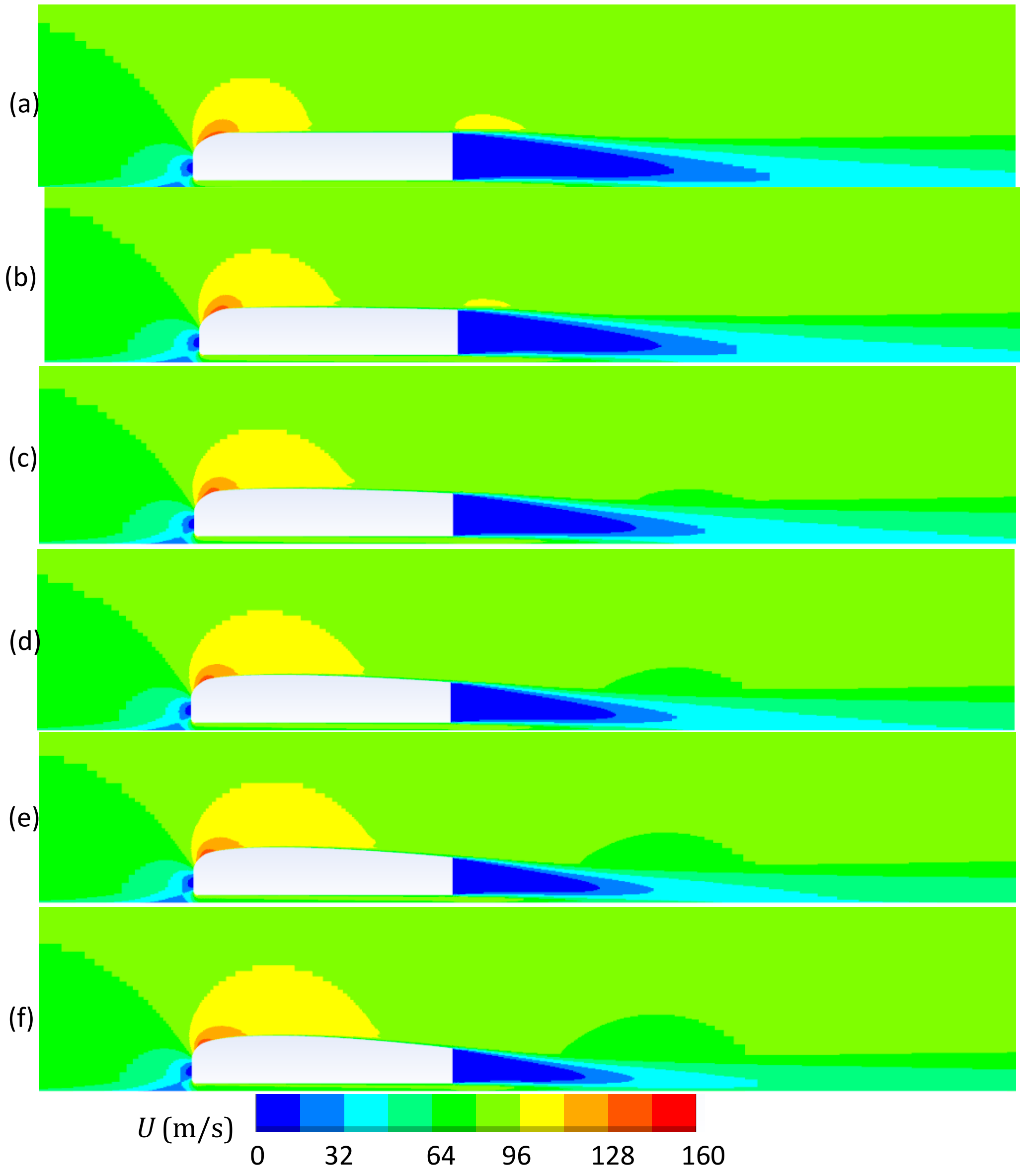

Fig. 5.11. Velocity magnitude contours for Method 3 (a) baseline GTS (b) t=2% (c) t=4% (d) t=6%, (e) t=8% and (f) t=10%.

From analysis of aerodynamic drag data for methods 1-3, Fig. 5.12 shows that method 3 gives very similar results to method 1 with the same observations in the flow field i.e. smaller wake and smaller stagnation region at the front. These two methods also reduce drag compared to the baseline GTS. Method 2 is not suitable for HGV design, unless thickness is large.

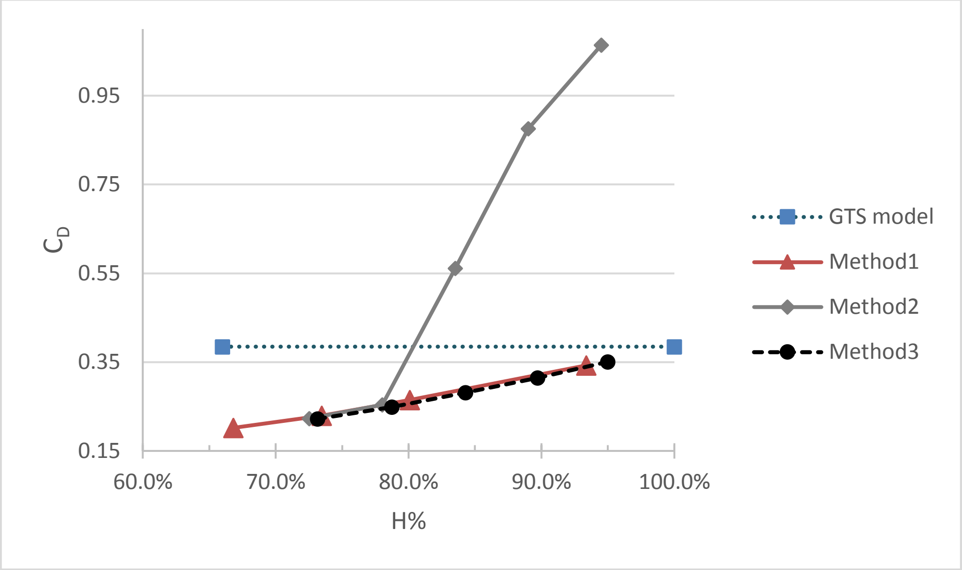

Fig. 5.12. Plot of aerodynamic drag as a function of percentage thickness for methods 1, 2 and 3, compared to the baseline.

5.2.2.4 **Method 4: front-rear parameterisation**

Although methods 1-3 show some potential for reduced drag using aerofoil profiles, it is apparent that there is a limit to how thick symmetric aerofoils can be. Therefore, a more sophisticated approach is required. In evaluating methods 1-3, it is clear that the angle, θ, of the trailing edge of the over-body profile (with respect to the horizontal axis) has a significant bearing on the size of the wake. Generally, as this angle increases, the drag reduces, provided that the flow remains attached over the top of the vehicle. Similarly, the amount of rounding at the front of the vehicle has an impact on the size of the stagnation region and the size of the acceleration area over the cab of the vehicle. If the acceleration is too strong this leads to low pressure on the forward portion of the rounded front, which leads to some drag contribution. As already explained, a further difficulty is that any changes to the over-body of the vehicle does have an impact on overall height which is governed by tight regulations (Butcher, 2009).

A solution was proposed to target the drag reduction at the front and the rear by influencing parameters in both of these locations. This was done using a third-order polynomial to give the new shape of the over-body profile, namely:

$$y = a + bx + cx^2 + dx^3 \tag{5.1}$$

where a, b, c and d are constants which determine the shape of the over-body profile. The value of these coefficients can be found for each value of, H, the height of the base of the vehicle and the angle of the trailing edge, θ. Therefore, by changing H and θ, the over-body profile is changed, see Fig. 5.13. For each value of H and θ, there is one unique over-body profile with unique coefficients a-d. Mathematically, from Fig. 5.13 there are two points (x_0,y_0) and (x_1,y_1) which are required to solve the equation that produces the over-body profile. Therefore, two equations and be written based on these unique points:

$$y_0 = a + bx_0 + cx_0^2 + dx_0^3 \tag{5.2}$$

$$y_1 = a + bx_1 + cx_1^2 + dx_1^3 \tag{5.3}$$

Furthermore, the slope of the trailing edge is equal to the tangent of θ at (x_1,y_1) so another equation can be written to relate these parameters:

$$\tan\theta = b + 2cx_1 + 3dx_1^2 \tag{5.4}$$

Because the edge at point (x_0,y_0) is horizontal, the slope at this point is equal to zero. Therefore another equation can be written:

$$0 = b + 2cx_0 + 3dx_0^2 \tag{5.5}$$

By keeping the point (x_0,y_0) and x_1 constant and by setting the height of the base (y_1 or H), and the angle of the trailing edge, the four equations (5.2), (5.3), (5.4) and (5.5) can be solved, providing the required four coefficients a-d. This method has the flexibility to influence the height of the front of the vehicle and the slope of the trailing edge of the roof. Literature has shown that changing the slope in particular (boat-tailing) is crucial for reducing drag (Choi et al., 2014, Yi et al., 2007). It should be noted that method 4 is unique; to the author's knowledge nothing like this has ever been tried before for an over-body profile of a bluff body. As was explained in the literature review, a significant proportion of drag reduction technologies have focused on the front, rear and underbody of large bluff vehicles. Fig. 5.14 and Fig. 5.15 shows a range of different designs from this parameterisation method.

Fig. 5.13. Parameterisation of the modified GTS model using method 4.

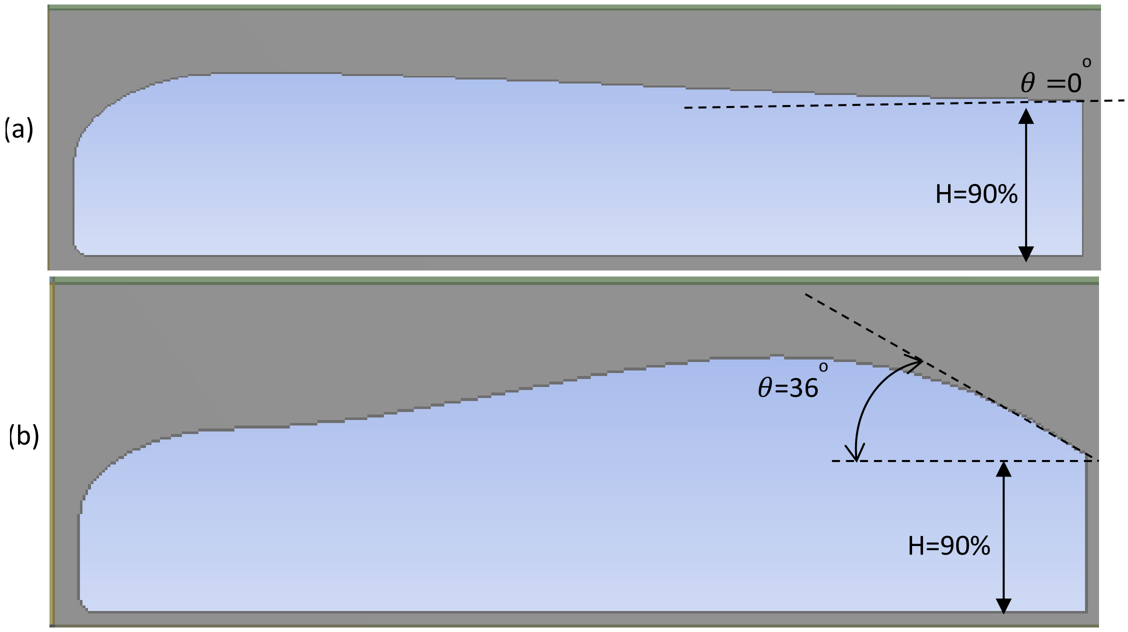

Fig. 5.14. Illustration showing two examples of parameterisation of the modified GTS model using method 4 with a constant relative height, *H*=90% and (a) a flat trailing edge, $\theta = 0^{\circ}$ and (b) a highly sloped trailing edge $\theta = 36^{\circ}$.

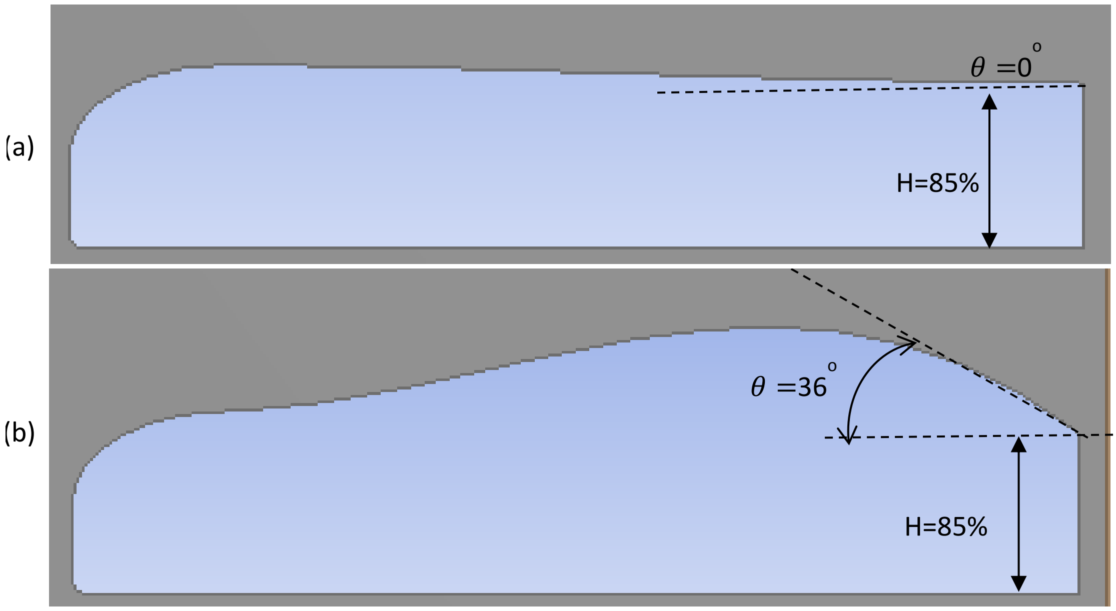

Fig. 5.15. Illustration showing two examples of parameterisation of the modified GTS model using method 4 with a constant relative height, H=85% and (a) a flat trailing edge, $\theta = 0^{\circ}$ and (b) a highly sloped trailing edge θ=36°.

A parametric study was conducted to show the effect of this parameterisation on the drag coefficient area, as a function of θ for two different heights, see Fig. 5.16. Note that the drag coefficient area is a fair comparison of actual aerodynamic load on the vehicle because the front projected area can change by varying these two parameters. It can be seen that the values of the two parameters have a noticeable effect on the drag coefficient area. Overall drag is less as H decreases. Furthermore, drag reduces as θ increases until a minimum value is attained at 28^{0}; further increases in this angle cause drag to rise. To explain this effect Fig. 5.17 shows velocity magnitude contours to highlight the change in size of the wake for this modified GTS design compared to the baseline GTS. It can be seen that for a given height, increasing the slope of the rear of the vehicle reduces the size of the wake. As seen in earlier methods, high angles direct flow downwards as it leaves the trailing edge of the over-body profile. However, for high θ, the flow can separate off the rear of the HGV, before it reaches the trailing edge. Furthermore, there is a local acceleration towards the rear of the over-body profile and because this is rearward-facing, the low pressure contributes to a higher drag. Therefore, there must be an optimum angle to reduce drag which will be explored in more detail in Chapter 6.

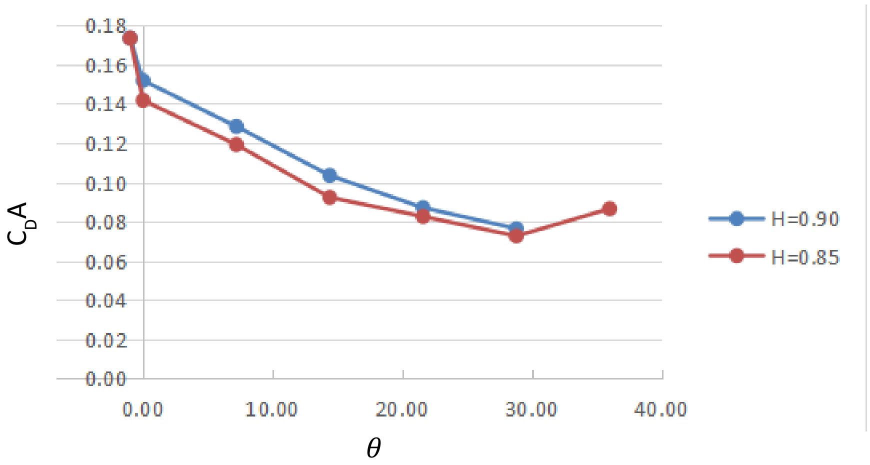

Fig. 5.16. Plot of drag area as a function of rear slope angle for two rear heights, for method 4.

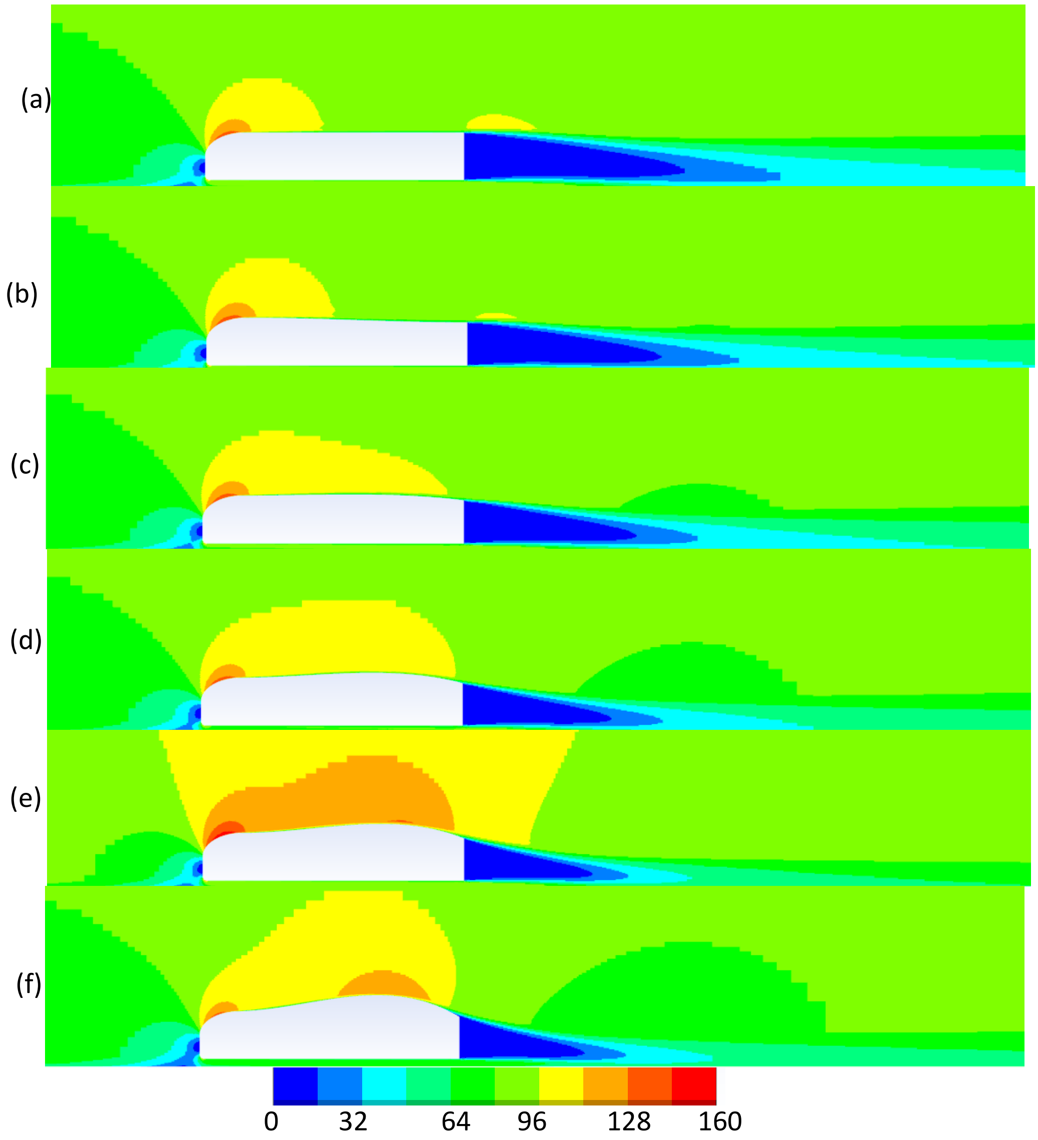

Fig. 5.17. Velocity Contours for Method 4 modified GTS showing contours of the wake in (a) baseline GTS (b) θ =0° (c) θ =7.2° (d) θ =14.4°, (e) θ =21.6° and (f) θ =28.8°.

5.3 Summary

The analysis of a typical UK haulage route from Leeds to London found that considering yaw angles of up to 8° is representative of a typical journey. The mode average angle is 8° and this occurs for 45% of a typical journey. The mean wind angle is about to 6°. As already concluded in section 5.1, there are three wind angles of interest to take forward into an optimisation study, they are: 5°, 6° and 8°.

As detailed above, a series of preliminary parametric studies explored the impact of geometric changes on aerodynamic drag using different methods. It was concluded that geometric changes controlled by the height of the rear of the vehicle and the slope of the trailing edge of the roof are sufficient to show effective drag reduction. Side edge rounding of the longitudinal edges of the over-body was also found to reduce drag in the presence of a side wind. These three parameters will be explored in 3D in the next chapter as part of a rigorous design optimisation study.

Chapter 6 : Aerodynamic shape optimisation of a generic heavy goods vehicle

As described in the previous chapter, analysis of a typical UK HGV haulage route showed that resultant velocities between the vehicle and the free-stream are expected to vary between 0 and 8 degrees. Furthermore, is was shown from some basic preliminary design analysis that rounding the upper side edges of a typical HGV can reduce drag in a side wind, as well as altering the front and rear of the HGV with a suitable polynomial parameterisation. All of these findings are used in this chapter as part of a rigorous design optimisation study to identify suitable HGV designs. Note that this work only considers an isolated vehicle and not a platoon of vehicles. Firstly, the problem formulation is presented and then both single and multi-objective optimisation is explored for a selected number of typical wind angles. The purpose of this work is to identify a range of design solutions offering low drag and improved stability. The chapter concludes with a summary of key design solutions and guidance for the industry, thereby addressing objectives 4 and 5 outlined in chapter 1.

6.1 Problem formulation

As explained in the early chapters, HGVs are extensively used in the UK transport sector, and this has a great cost in terms of fuel consumption. Therefore, changing HGV design to positively influence the aerodynamics can make a valuable contribution to this problem. In the past, different strategies have been used such as shape optimisation (Sharma et al., 2015) or the use of add-on devices at various positions on the vehicle to reduce fuel consumption (Choi et al., 2014), however, these methods usually focus on aerodynamic drag without considering potential vehicle instabilities. To the author's knowledge, little attention has been paid to enhancing the design of HGVs to reduce drag whilst simultaneously improving vehicle stability, handling and safety operation, especially in challenging conditions such as in gusts or side winds. Therefore, the problem formulation is to identify potential designs for typical HGV concepts which minimise drag and maximise stability.

6.1.1 Design variables and parameterisation

As explained in the previous chapter, only three design variables are used to avoid the "curse of dimensionality" (Forrester et al., 2008) whilst still allowing a large design space to be explored. Based on the preliminary work in section 5.2, the three design variables (inputs) are:

1. Relative height of the trailing edge of the HGV, D_1, expressed relative to the baseline GTS height;
2. Angle of the trailing edge, D_2, in degrees, with respect to the horizontal axis;
3. Normalised radius of the upper side edges of the HGV, $\mathbf{D_3}$, relative to the baseline value, R_0 = 0.22792m.

The first two of these are shown in sample designs compared to the baseline GTS model in Fig. 6.1. Recall from the previous chapter that the parameterisation of the side profile requires the height, H, and the angle of the trailing edge of the roof profile, θ. In this chapter, $D_1 = H$ and $D_2 = \theta$. There is a unique side profile for each combination of D_1 and D_2 as explained in Chapter 5. An important consideration is the maximum height limit of HGVs which according to UK transport regulations is 4.9m (Butcher, 2009). This is the major physical constraint in this study i.e. the maximum height of all designs to be evaluated should not exceed this value at any point along the vehicle length. This limit is indicated by the grey dashed line in Fig. 6.1 and the red dashed line is the outline of the baseline GTS vehicle.

Fig. 6.1 shows the baseline GTS vehicle contrasted with three modified examples showing the effect of changing D_1 and D_2 on the overall side profile. Fig. 6.1(b) and (c) show acceptable designs whereas the input parameters for the vehicle shown in Fig. 6.1(d) is unacceptable because it violates the maximum height limit. It is important to note that the baseline GTS model which is modified in this chapter has been re-scaled. This is because the original GTS model (Roy et al., 2006) is based on a 1/8th scale US transport vehicle size and so, in this study, the baseline vehicle is slightly modified in proportion to be relevant to UK HGV dimensions and scaled up to full-scale. Accordingly, the height of the full-scale baseline vehicle, H_0, has been slightly increased from 4.213m to 4.556m. Within the physical constraints of the problem, this height allows for different types of the side-profile curvature of the over-body shape to be considered, including both concave (Fig. 6.1(b)) and convex (Fig. 6.1(c)) designs. Furthermore, the length of the baseline vehicle has been reduced from 19.8m to 16.5m to reflect the smaller sizes of UK HGVs. The standard width of a UK HGV is 2.55m but it can be as large as 2.60m if there are refrigeration units present (Butcher, 2009). Because these are both close to 2.59m, the width has not changed from the scaled-up GTS design which is 2.5904m.

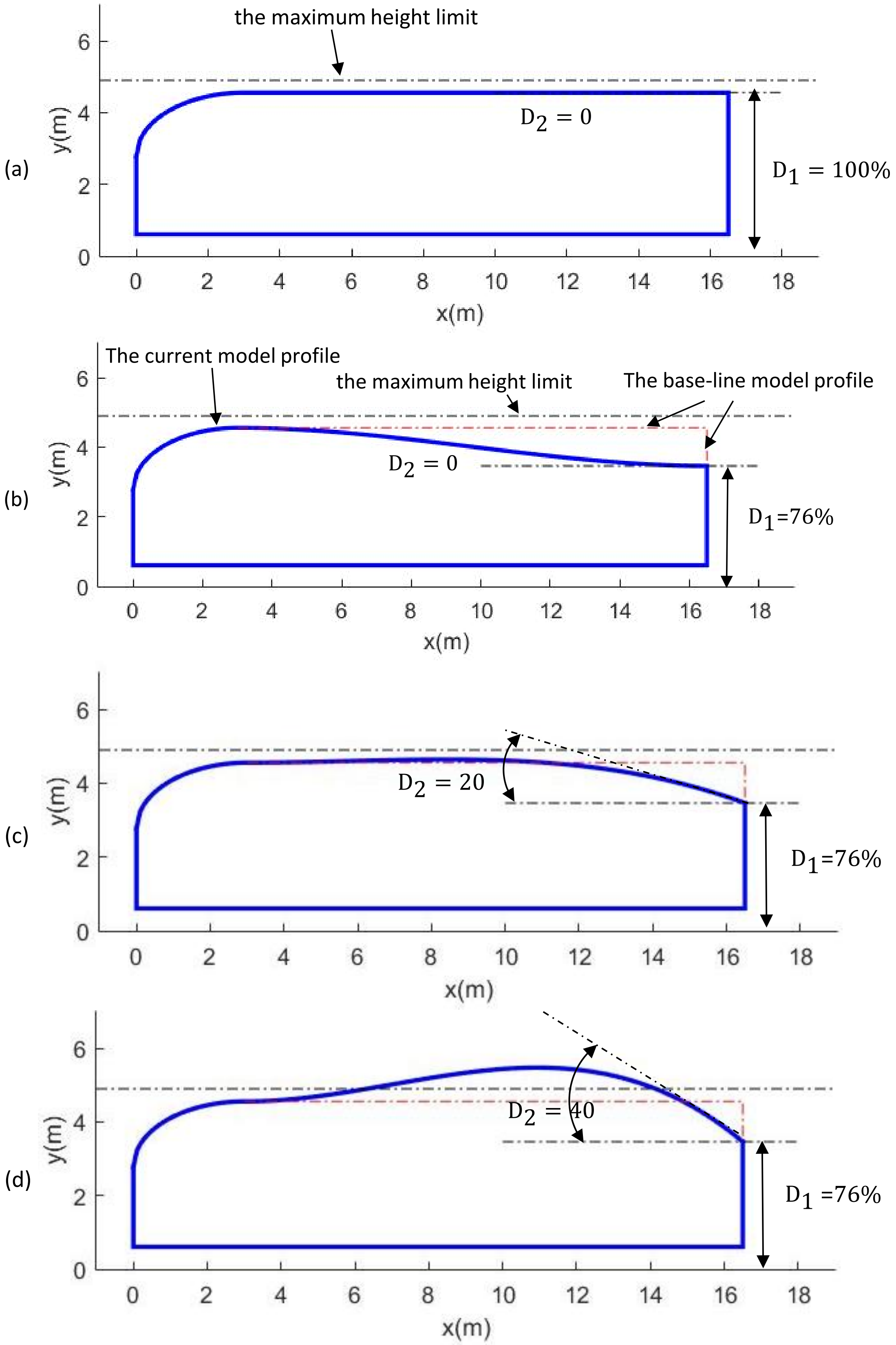

Fig. 6.1. Illustration showing the design variables used to modify the GTS model with the maximum permissible height indicated by the grey dashed line: (a) modified re-scaled GTS, (b) a typical concave design, (c) a typical convex design and (d) an unacceptable model violating the height constraint.

In order to decide on a suitable range for the design variables, the physical constraints had to be considered. As explained above the maximum height of 4.9m is a consideration and the minimum height of the trailing edge, D_1, must not be too small, otherwise goods would not be able to be loaded in and out of the rear loading doors of the vehicle. After careful consideration of these constraints, the following ranges for the design variables were identified:

1. $0.76 \leq D_1 \leq 0.95$
2. $0^{\circ} \leq D_2 \leq 14^{\circ}$
3. $0.50 \leq D_3 \leq 2.50$

Table 6.1 shows how the above ranges were chosen in this study. Each cell contains the maximum height of the vehicle (m), the first column contains values of D_1 (%) and the first row shows the angles of the trailing edge in degrees. Blue cells indicate the design space which can be explored without violating the physical constraints. Red cells show invalid designs (see Fig. 6.1(d) for an example of one) and yellow ones are still feasible, but this would involve further constraint functions to account for possible invalid designs. For simplicity, a cubic design space was chosen, therefore the blue cells indicate the range of design variables D_1 and D_2 used in the remainder of this study. The range of values used for D_3 was determined from the work in Chapter 5.

Table 6.1 Range of feasible designs (blue cells), invalid designs (rad cells) and excluded designs (yellow cells) for a range of design variables, D_1 and D_2.

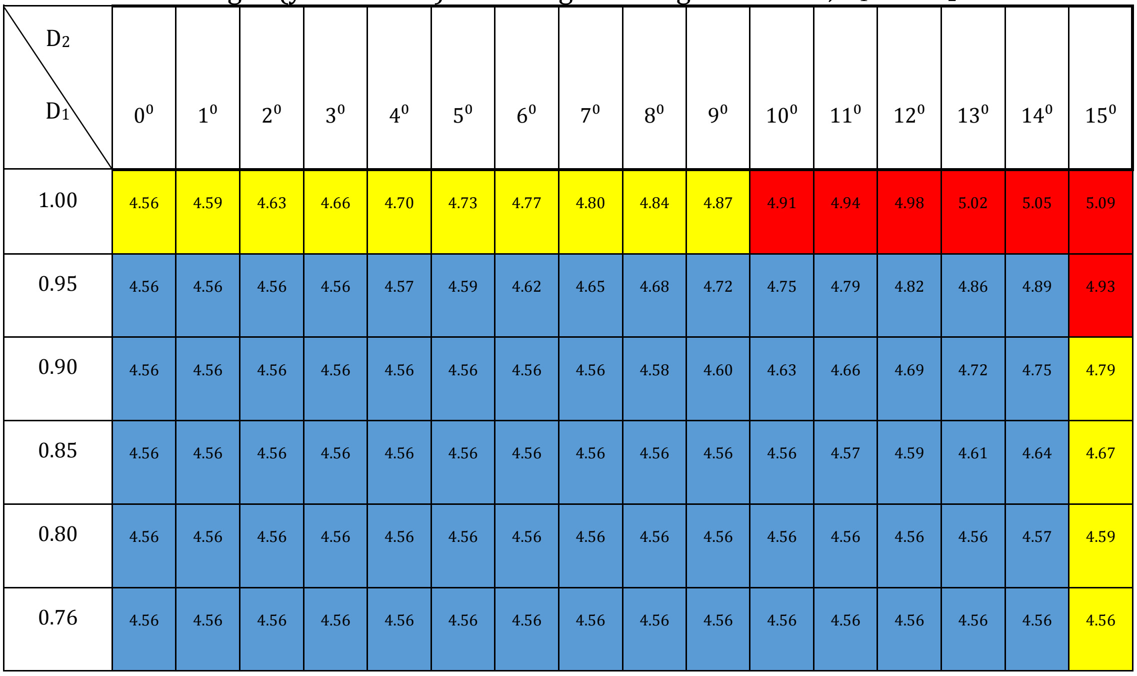

D2 D1	0^0	1^0	2^0	3^0	4^0	5^0	6^0	7^0	8^0	9^0	10^0	11^0	12^0	13^0	14^0	15^0
1.00	4.56	4.59	4.63	4.66	4.70	4.73	4.77	4.80	4.84	4.87	4.91	4.94	4.98	5.02	5.05	5.09
0.95	4.56	4.56	4.56	4.56	4.57	4.59	4.62	4.65	4.68	4.72	4.75	4.79	4.82	4.86	4.89	4.93
0.90	4.56	4.56	4.56	4.56	4.56	4.56	4.56	4.56	4.58	4.60	4.63	4.66	4.69	4.72	4.75	4.79
0.85	4.56	4.56	4.56	4.56	4.56	4.56	4.56	4.56	4.56	4.56	4.56	4.57	4.59	4.61	4.64	4.67
0.80	4.56	4.56	4.56	4.56	4.56	4.56	4.56	4.56	4.56	4.56	4.56	4.56	4.56	4.56	4.57	4.59
0.76	4.56	4.56	4.56	4.56	4.56	4.56	4.56	4.56	4.56	4.56	4.56	4.56	4.56	4.56	4.56	4.56

6.1.2 **Design of Experiments**

With the design variables and their ranges chosen, another important consideration is the number of designs to be evaluated. For three dimensional CFD of bluff body aerodynamics, Gilkeson et al., (2013) found that 50 designs gave sufficient coverage of a 3D design space using an optimal Latin hypercube Design of experiments (DoE). One problem with this was that the corner points, side faces and edges of the design space were not sampled in the initial DoE which meant that the optimisation search took longer. Therefore, in this study, a full factorial DoE comprised of five divisions on all three axes of the design space leads to 125 points. Each of these points, shown in Fig. 6.2, represents a different HGV design with a unique combination of the three design parameters, D_1, D_2 , and D_3. To illustrate the range of HGV shapes, Fig. 6.2, Fig. 6.3 and Fig. 6.4 shows the unique CAD model for all eight corner points of the design space. It is clear that there is a wide range of possible of designs which all satisfy the physical constraints of the problem described above.

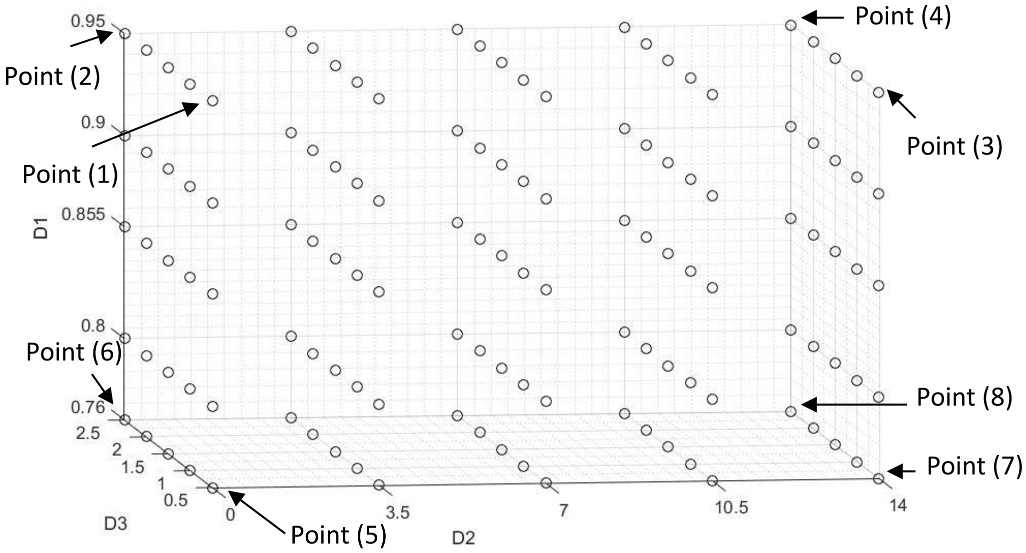

Fig. 6.2. Illustration of the 125-point design space including eight selected designs (labelled).

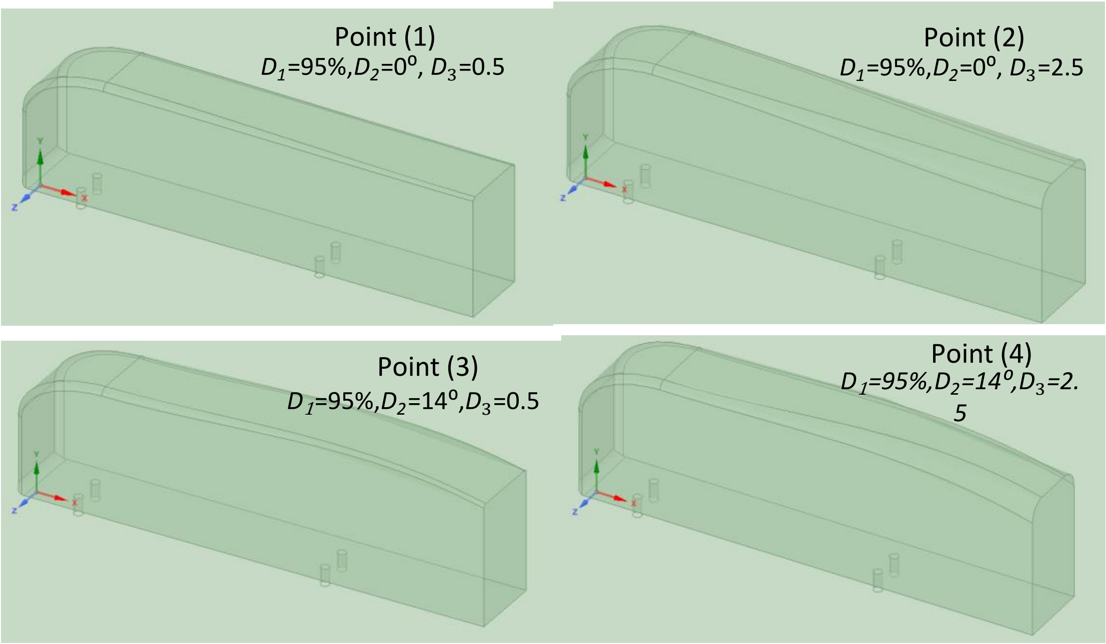

Fig. 6.3. Illustration showing the top four corner points of the design space.

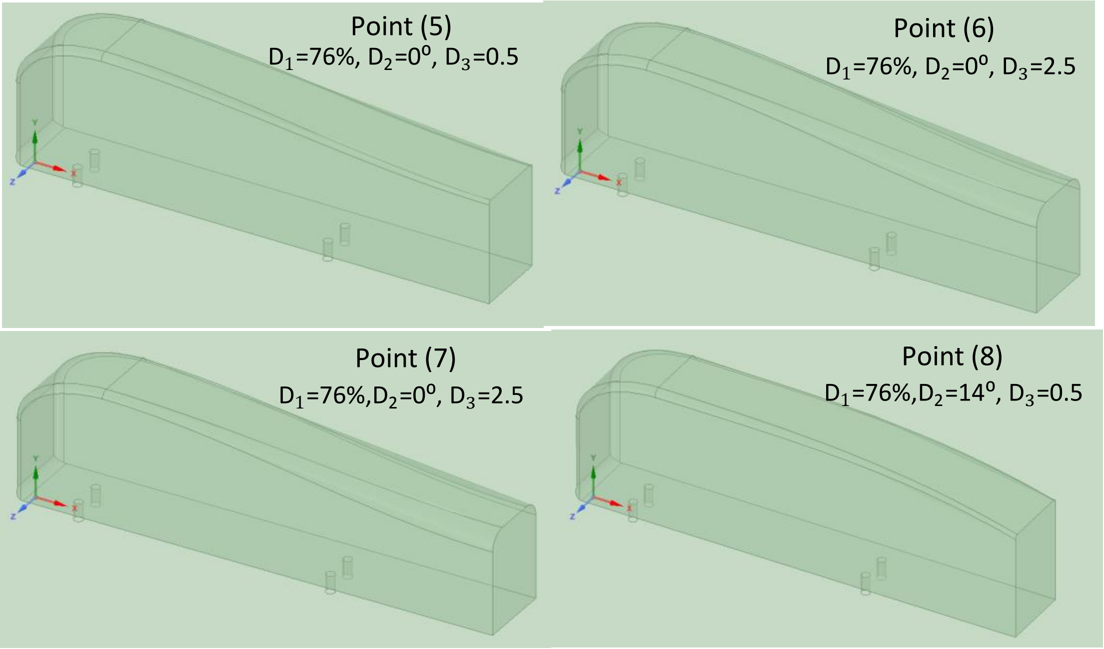

Fig. 6.4. Illustration showing the lower four corner points of the design space.

6.1.3 **Objective functions**

The objective functions (outputs) of this problem relate to the aerodynamics and vehicle stability. In later sections, both single and multi-objective optimisation formulations will be explored but the five individual functions of interest are:

a) The drag coefficient area, C_DA, as a fair indicator of aerodynamic drag;

b) The gradient of the yawing moment coefficient with respect to slip angle multiplied by the product of frontal area and a reference length, $\frac{dc_N}{d\beta}AL$, as a fair indicator of yaw stability (recalling that a positive gradient is unstable, negative is stable);

c) Side force coefficient area, C_YA, as a fair indicator of likelihood of the vehicle toppling over;

d) Rolling moment coefficient area, $|C_RAL|$, as a fair indicator of roll stability;

e) Yawing moment coefficient area, C_NAL, as another indicator of yaw stability.

For objective function (b) the purpose is to ensure that it is increasingly negative (more stable) and all other functions are minimised. The individual problems, whether single or multi-objective, will be described one-by-one in later sections. Objective functions (a)-(e) are calculated based on either forces or moments about the centre of gravity of the vehicle. The centre of gravity of a real on-road HGV is dependent on geometry and especially the distribution of the load inside the trailer (if there is one). Evaluating different CG positions is beyond the scope of this study, therefore, for simplicity, it is assumed that CG is located in geometric centre of the vehicle (8.25m, 1m, 0m); this is a reasonable assumption for a fully-loaded HGV. It is important that the CG point does not change during the study, so that the stability of the model can be studied. Note that objective function (b) must be calculated from yawing moments, for at least two different yaw angles in order to determine the gradient $dC_N/d\beta$. This aspect will be described in more detail later when results for this function are presented.

For each of the initial 125 designs evaluated, CAD models were created for every HGV shape. Each design was then placed in a solution domain and discretised using the mesh size and structure matching the fine mesh explained in chapter 4; recall that this gave grid independent solutions with small discretisation errors. For each mesh, the global cell count was in the region of 11 million cells.

As explained in chapter 5, assuming that the forward velocity, V_D, of a typical HGV is equal to the speed limit of 56 mph (25 m/s), the resultant wind velocity experienced by the vehicle, V_{res}, depends on the direction of travel relative to a prevailing average wind speed, V_S. As explained in section 5.1 in this study, the slip angle, β, of 0°, 5°, 6° and 8° are considered. Fig. 6.5 illustrates these velocity vectors for the four slip angles.

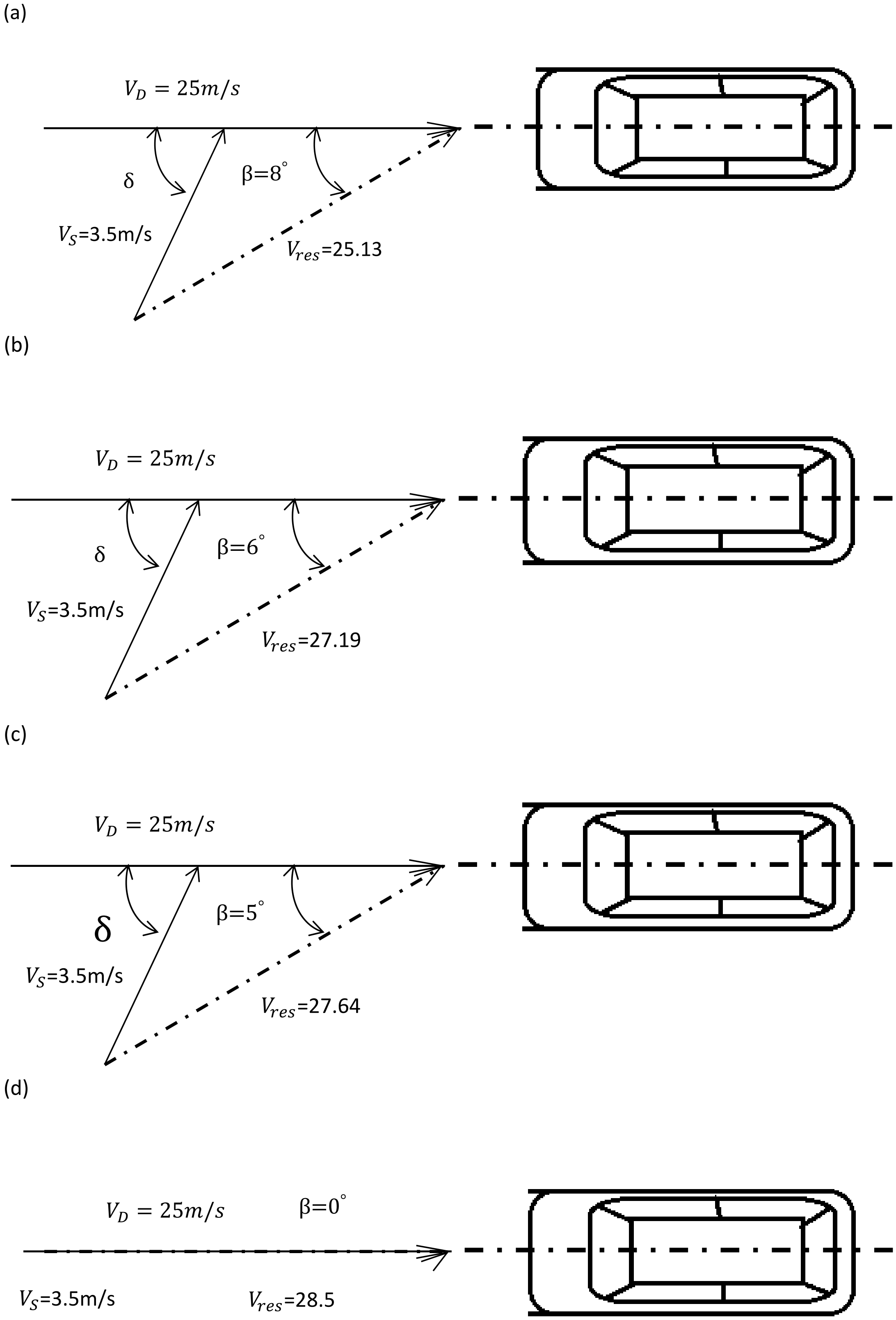

Fig. 6.5. Illustration of the vector diagram for each of 0,5, 6 and 8 degrees showing the vehicle forward velocity and the wind direction, plus the resultant velocity vector.

The magnitude and direction of the resultant vectors shown in Fig. 6.5 are used to set the inlet boundary conditions in subsequent simulations. Accordingly, all 125 3D geometries were evaluated with a high-fidelity CFD solution at each of the four slip angles, leading to 500 simulations in total. For each one, the five objective functions described on the previous page were calculated. In each simulation, convergence was achieved within 2,500 iterations with typical simulation times of about 2.5 hours on 32 processors.

6.1.4 Moving Least Squares Metamodel Development

As explained in chapter 2, in design optimisation there are various methods of finding the best design. The approach used in this thesis is to run CFD simulations for all 125 designs, at all 4 slip angles, and to post-process the solutions to obtain values for the 5 objective functions described above. Then, using these outputs, a metamodeling approach can be used to act as a surrogate for the outputs, relating these to the design variables (inputs). An example metamodel, fitted through relevant data points, is shown in Fig. 6.6 for illustrative purposes. Data points obtained from CFD simulations are shown as black dots and the surface contour plot is the whole function, represented by the metamodel. It was explained in chapter 2 that moving least squares (MLS) metamodels are particularly useful for dealing with numerical noise which is often generated from CFD solutions (Gilkeson et al., 2014) and the method has been useful in bluff body vehicle aerodynamic shape optimisation (Gilkeson et al., 2013) , therefore, this method is used here.

A feature of the MLS method is that it can provide a continuous representation of the objective function throughout the design space based on limited individual points (from the DoE) as a function of the independent design variables, see Fig. 6.6. The advantage of metamodels is that they can provide this functional relationship based on a limited number of CFD simulations. The metamodels themselves can then be searched using traditional optimisation methods such as Genetic Algorithms to find candidates for the global minimum, providing the design variables which should lead to this predicted optima. Any such optima can be validated with further CFD simulations to check if the predicted design variables are able to replicate the metamodel prediction.

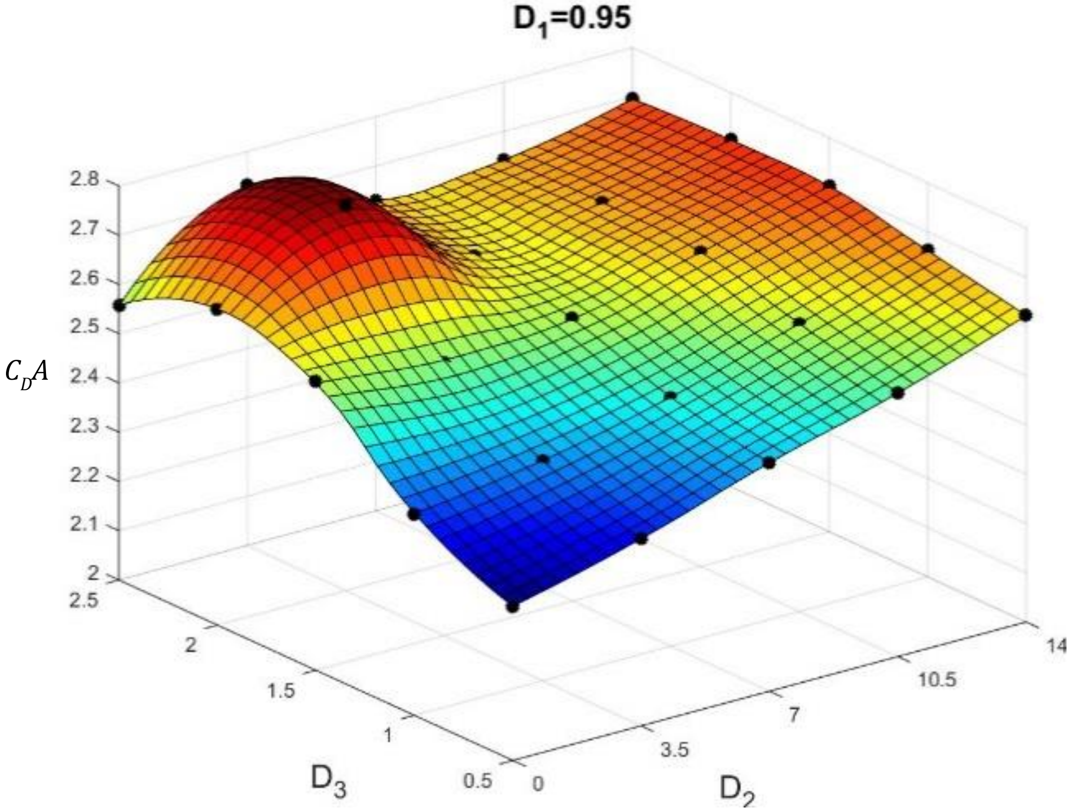

Fig. 6.6. An example of a metamodel of the drag coefficient area, C_DA, for a range of values of D_2 and D_3 with $D_1 = 0.95$.

If there are large differences between the CFD result and the metamodel prediction, the metamodel can be rebuilt and further refined by adding additional CFD (validation) data points. The refined metamodel can then be searched again to locate a new candidate for the global minimum and an additional CFD simulation performed to validate this. The process is repeated iteratively until the CFD result matches the metamodel prediction for the optimum design. Note that the function shown in Fig. 6.6 is relatively simple, and the global minimum is easily ascertained. However, there will be cases where the function is very complicated and this is where the advantage of metamodels can be crucial for finding optimum solutions, because this may not be very easy to do visually.

In the current study, the MLS method (Toropov et al., 2005) was used to build objective functions based on CFD results corresponding to all 125 DoE points. Next, MLS metamodels were built using these results, with one metamodel per objective function being obtained. As discussed before one great strength of the MLS technique is that it can handle numerical noise in the input data by selecting an appropriate closeness of fit parameter, θ, for a given data set (Gilkeson et al., 2014). For instance, if the noise levels are high then the metamodel can be loosely fitted to the points, whereas a close fit can be implemented if the noise levels are low. The closeness of the fit parameter is embedded within the MLS method using a Gaussian weight decay function given by:

$$w_i = exp^{-\boldsymbol{\theta} r_i^2} \tag{6.1}$$

where the parameter, r_i, is the Euclidean distance of the metamodel prediction location from the *i*th DoE point. For the specific case of θ = 0, the MLS approximation reduces to a conventional least-squares polynomial response surface fitting. In all other cases, the value of θ can either be specified *a priori* or optimized to produce the best fitting metamodel for the given CFD responses (Toropov et al., 2005). Since the value of θ used in each metamodel has a significant impact on its shape, it is important to choose a sensible value. Manually selecting θ is not recommended and there are more sophisticated methods for doing this.

A common technique is to analyse a random subset of *n* points used in the construction of a given metamodel (validation points). For example, a metamodel could be built using 50 points and 10 points are analysed. The purpose is to systematically rebuild a new metamodel with each one of these validation points removed. By analysing the differences in resulting *n* metamodels, θ can be tuned so that the root mean square error between metamodels can be minimised. Once a suitable value of θ has been obtained, this is then used to construct a final tuned metamodel. The process is repeated for each objective function. A similar but more rigorous technique is the Leave-One-Out Cross Validation technique (LOOCV)(Loweth et al., 2011, De Boer et al., 2016) which will be used in this work. It works in the same manner as above, however, every single point in the original metamodel is analysed instead of a random sample of points.

If the best θ value for a given metamodel is found to be zero or tends to infinity then the choice of the metamodel is probably incorrect for the data series. When θ = 0, the metamodel takes the form of a least squares approximation (no local refinement) whereas if θ is infinity then overfitting occurs (no global refinement). One solution is to change the polynomial order or decay function in equation 6.1, or, more data points should be added to the metamodel to improve its prediction.

6.2 Single Objective Design Optimization

In this section, individual optimisation of the five objective functions is presented to illustrate which is the best vehicle design for each of these. Only in section 6.3 will multi-objective optimisation be considered to understand the best compromise between certain objective functions.

6.2.1 Optimum C_DA

The investigation to find the global minimum for the drag area, C_DA, was undertaken to identify which shapes provide the lowest drag and thus minimise fuel consumption. Note that the drag area is used in place of C_D because the parameterisation can increase the projected frontal area so the drag coefficient alone is not a fair comparison, whereas drag area is. Initially a metamodel of C_DA was constructed based on CFD data points for the zero slip angle i.e. $\beta = 0^\circ$ cases. Based on the wind angle analysis in Chapter 5, it was decided to create three more metamodels with one produced for each of $\beta = 5^\circ$, 6° and 8°. Each metamodel required the full set of 125 CFD simulation results for each respective slip angle.

By using Matlab codes written and developed by Dr. Gregory de Boer (Loweth et al., 2011, De Boer et al., 2016), each metamodel was generated from the relevant set of 125 CFD data points. Each metamodel was then tuned to find the optimum fitness parameter, θ, using the LOOCV method described above. The initial metamodels were then searched using the Genetic Algorithm (GA) optimisation tool which is available in Matlab's optimisation toolbox (MATLAB R2015a). The GA method was used to find a candidate for the global minimum drag area, for each slip angle, β. Following the global search, a commonly-used local gradient search method, known as fmincon(MATLAB R2015a) was used to refine the prediction because although the GA is an excellent global search method, it doesn't always find the exact optima on its own; it is good practice to use a global and then a local search (Gilkeson et al., 2013). It should be noted that fmincon is designed to work with continuous objective functions (MATLAB R2015a) which is what the MLS metamodel provides.

As this point, the proposed global minimum for C_DA was found, for each metamodel (i.e. one metamodel per set of slip angles). In practice, the repetition of the global-local search steps did not always change the position of the proposed global minimum for C_DA and this increased the likelihood that the global minimum had been found. For each metamodel, the input parameters it proposed for the minimum drag design were used to generate a CAD model and a CFD simulation was subsequently run. In some cases a number of points near the predicted global minimum were evaluated. Once the new data points were obtained from the CFD analysis, refined metamodels were rebuilt with this extra information and the same optimisation search steps (outlined above) were followed. In some cases this process had to be repeated until the CFD data and the metamodel predicted the same vehicle design, for each slip angle. In total, an extra 13 data points were obtained from this process and these were evaluated for all slip angles, even though not all of them were needed in some cases. Table 6.2 shows final results for each of the metamodels with all 138 data points.

Table 6.2. Comparison of the 138 point metamodel prediction and corresponding CFD results for the minimum drag roof design.

Side slip angle (β)	Design Variables			C_DA		
	D_1	D_2(°)	D_3	MLS	CFD	δ
0	0.76	2.11	0.5	1.798	1.801	-0.45%
5	0.76	0.97	0.5	2.046	2.047	0.04%
6	0.76	0.0	0.5	2.074	2.075	0.01%
8	0.76	0.0	0.5	2.011	2.012	0.02%

It can be seen that the minimum drag roof design for β = 6° and 8° is the corner point (5) shown in Fig. 6.4. Furthermore, the percentage difference between the MLS metamodel prediction and the CFD result, δ, is less than 0.5% in all cases and far below this for the three yawed cases. It is interesting to observe that for all four slip angles considered, the minimum C_DA design requires the minimum height at the rear of the trailer unit (D_1) and the minimum side edge radius (D_3). Furthermore, for the highest slip angle cases of 6° and 8° the minimum angle of the rear of the trailer roof profile (D_2) was 0°. Even for the symmetric case (β = 0°) and β = 5° the angle of the roofline was small at 2.11° and 0.97°, respectively. Recalling the design space in Fig. 6.2 and Fig. 6.4, it is clear that the minimum C_DA design is in a corner point (5) for the two largest slip angles considered and it is close to this corner, along an edge, for the symmetric case and the smallest slip angle of 5°.

To illustrate the objective function landscape, Fig. 6.7 shows various slices of the β = 8° metamodel of drag coefficient area, C_DA. It is shown as a function of D_2 and D_3 for three given values of D_1 at the maximum, minimum and the middle value for this design variable. It is necessary to present the metamodel in this way because it is four dimensional. Visually, it is clear that the global minimum, C_DA = 2.012, which is shown in blue, is in the corner point of the design space, Fig. 6.7(c). The other C_DA metamodels look broadly the same but Fig. 6.7 is representative of how C_DA varies in response to design variable changes. See, for example, Fig. 6.8 for the β = 6° metamodel.

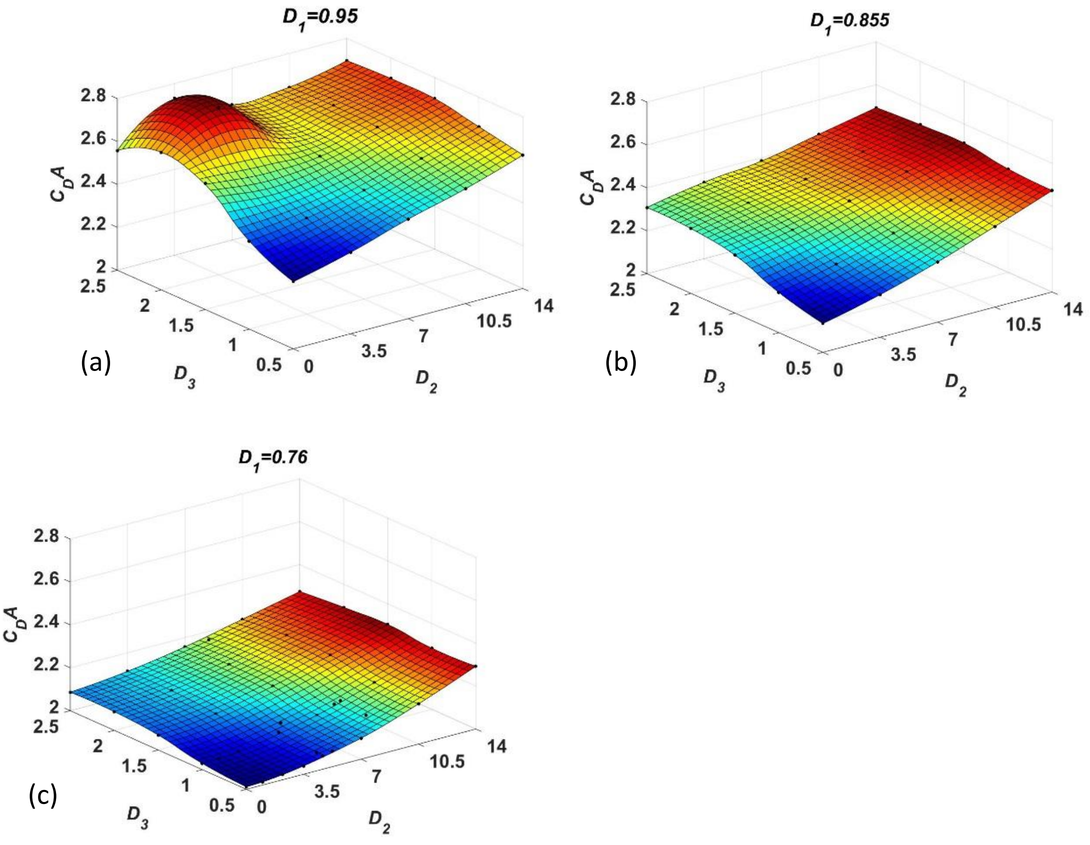

Fig. 6.7. The MLS metamodel of the drag coefficient area, C_DA, for a sideslip angle, $\beta = 8^{\circ}$. The metamodel shows C_DA as a function of D_2 and D_3 for (a) the maximum of D_1, (b) the middle value of D_1 and (c) the minimum of D_1. Black points represent data points.

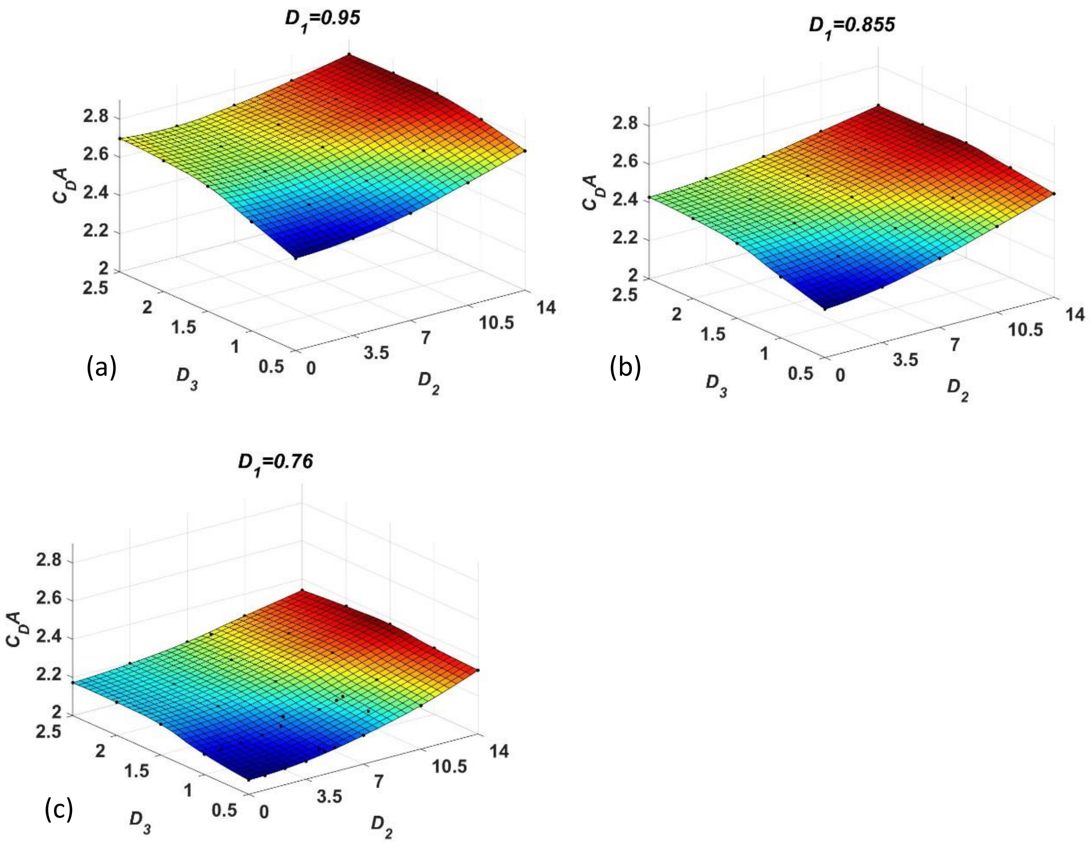

Fig. 6.8. The MLS metamodel of the drag coefficient area, C_DA, for a sideslip angle, $\beta = 6^{\circ}$. The metamodel shows C_DA as a function of D_2 and D_3 for a) the maximum of D_1, b) the middle value of D_1 and c) the minimum of D_1. Black points represent data points.

Fig. 6.9 shows the shape of the best design for the $\beta = 5^{\circ}$ case which is very similar to all minimum C_DA designs and Fig. 6.4 shows the corner point (5) which is the minimum C_DA design for $\beta = 6^{\circ}$ and 8°.

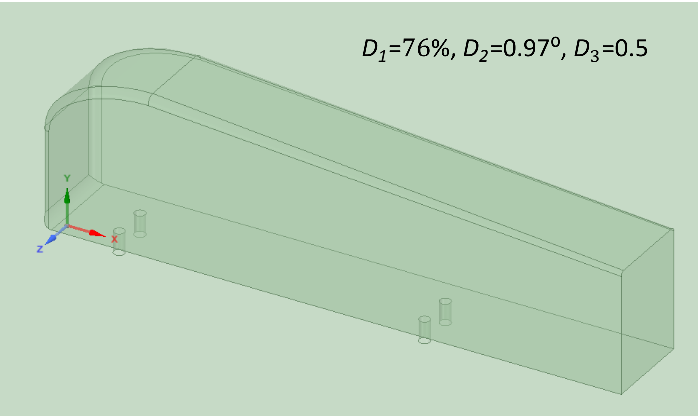

Fig. 6.9. Illustration of the minimum-drag roof design predicted by the metamodel and validated by CFD for β = 5o where D_1=76%, D_2=0.97^0 and D_3=0.5

It is crucial to compare between the baseline and the optimised designs to quantify the benefit of the optimisation. Table 6.3 shows comparison between the baseline and optimised designs for different slip angles. Note that the baseline is the rescaled GTS design. It is clear that the optimisation process has produced a substantial reduction in aerodynamic drag.

Table 6.3. Comparison between the baseline and optimised designs C_DA.

Side slip angle (β)	Baseline (CFD)	Optimised designs (CFD)	δ
0	3.0168	1.801	40.30%
5	3.3086	2.047	38.13%
6	3.4218	2.075	39.36%
8	3.4537	2.012	41.74%

Now that a generic optimum design has been found, some postprocessing is necessary in a comparison between the baseline and optimised designs to find some evidence for why the optimum designs are better. As explained in detail in the literature review, the flow structure around a road vehicle is directly related to its shape and this has an impact on the overall aerodynamic forces and moments, including drag. Fig. 6.10-Fig. 6.17 show the comparison of the wake structure between the baseline design (rescaled GTS) and the minimum-drag design predicted by the metamodel for β = 0^{o} , 5^{o} , 6^{o} and 8^{o}. Similar to Khalighi (2012), these figures show that the design parameters proposed by the metamodel result in a smaller base area which leads to a smaller wake size. For the zero yaw case, the wake was characterised by a velocity magnitude isosurface of 10 m/s (Gilkeson et al., 2013), see Fig. 6.10.

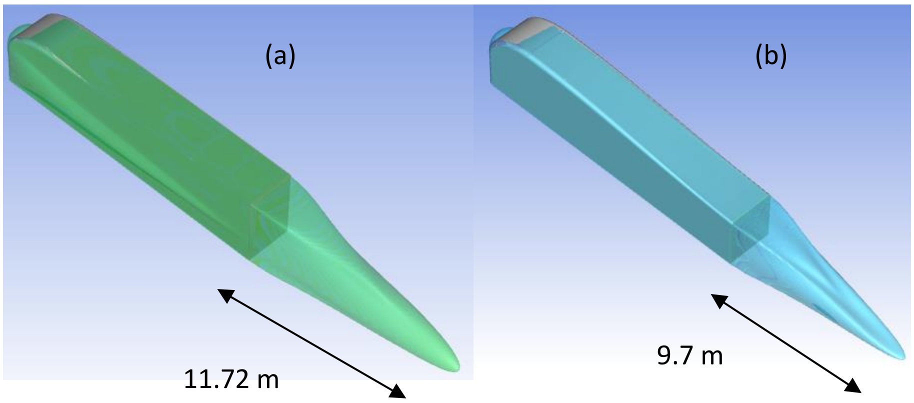

Fig. 6.10. Comparison of the wake structure visualised by a velocity magnitude isosurface of 10m/s for (a) the baseline model and (b) the minimum-drag roof design predicted by the metamodel, for β = 0^{o}. ($D_1 = 0.76, D_2 = 2.1, D_2 = 0.5$).

By measuring the length of the maximum downstream extent of the isosurface, a measure of the wake length is found. In this case, the minimum drag design reduced the size of the wake by approximately 7%. The differences are also seen in Fig. 6.11 and Fig. 6.12 which show contours of the velocity magnitude from the side and the top of the vehicles, respectively. It is clear that the wake is smaller and more compact. It is obvious that the reduction in the height of the vehicle at the base of the trailer (D_1) consequently reduces the height of the wake immediately downstream of the vehicle. This produces a smaller recirculation region which has a positive influence further downstream.

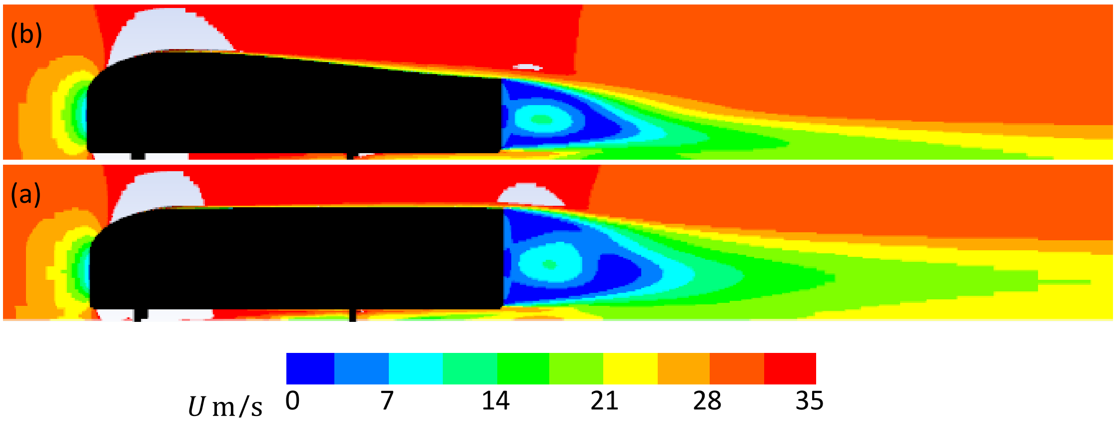

Fig. 6.11. Comparison of the streamwise velocity magnitude contours on the symmetry plane for (a) the baseline model and (b) the minimum-drag roof design predicted by the metamodel for β = 0°. ($D_1 = 0.76, D_2 = 2.1, D_2 = 0.5$).

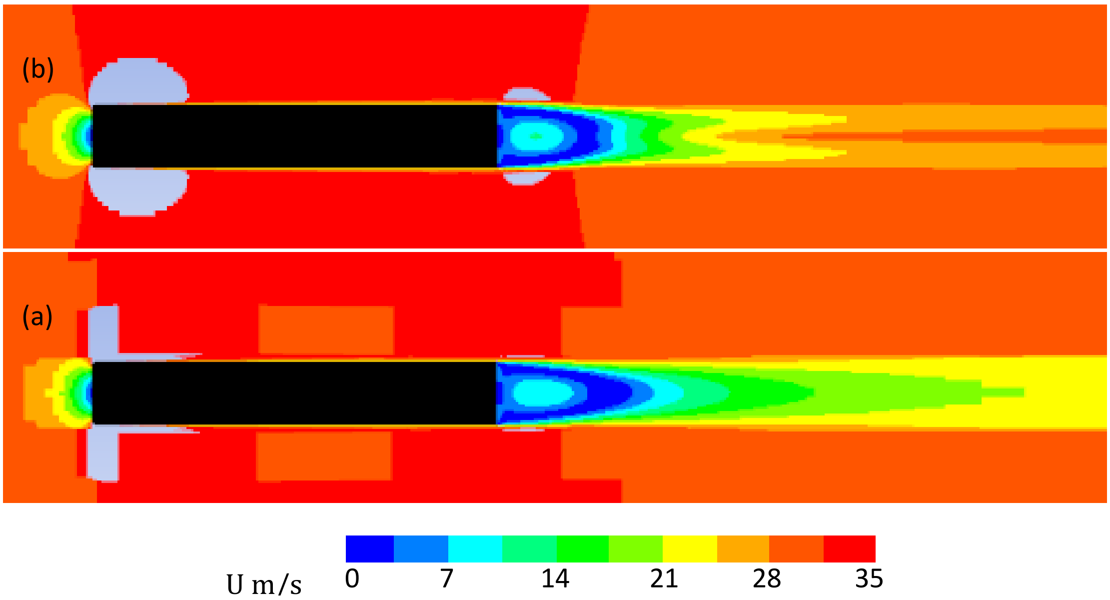

Fig. 6.12. Comparison of the streamwise velocity magnitude contours on a horizontal plane approximately halfway up the vehicle (y = 2m) for (a) the baseline model and (b) the minimum-drag roof design predicted by the metamodel for β = 0°. ($D_1 = 0.76, D_2 = 2.1, D_2 = 0.5$).

Fig. 6.13, Fig. 6.14 and Fig. 6.15 show the same results for the smallest yaw case of $\beta = 5^{\circ}$. Again, the wake size is visualised by a 10 m/s velocity magnitude isosurface and as for the zero yaw case, the wake reduces in size, this time by around 8%. As expected, the wake structure skews to one side due to the side wind but the same overall trend of a smaller wake is evident. This trend continues for the two larger yaw angle cases and these wakes are visualised in Fig. 6.16 and Fig. 6.17.

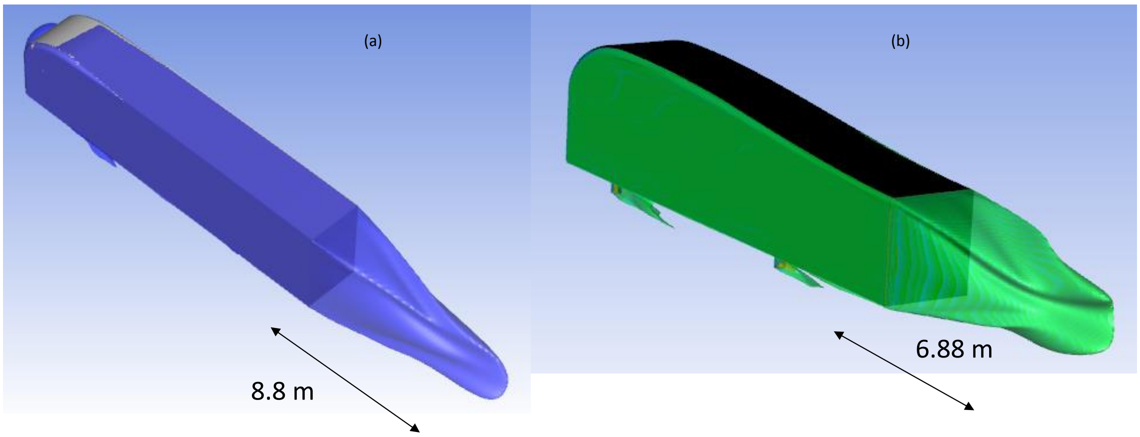

Fig. 6.13. Comparison of the wake structure visualised by a velocity magnitude isosurface of 10m/s for (a) the baseline model and (b) the minimum-drag roof design predicted by the metamodel for $\beta = 5^{o}$. $(D_1 = 0.76, D_2 = 1, D_2 = 0.5)$

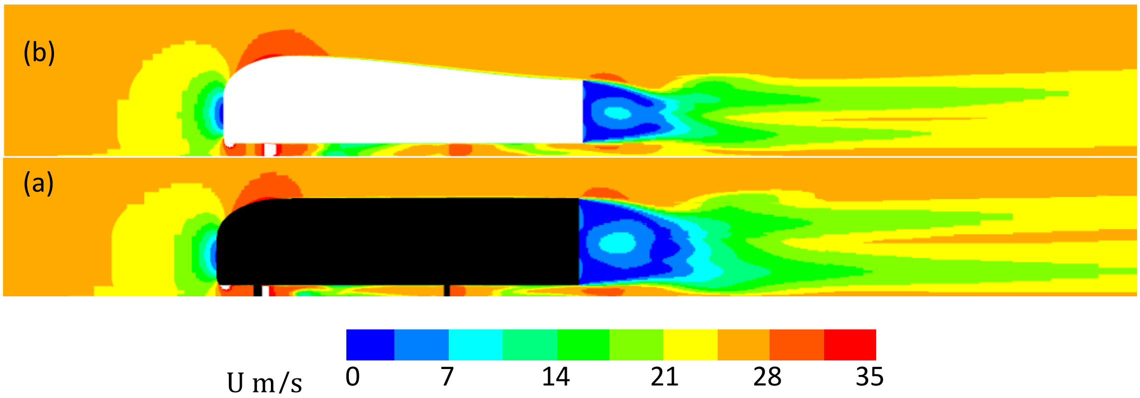

Fig. 6.14. Comparison of the streamwise velocity magnitude contours on the symmetry plane for (a) the baseline model and (b) the minimum-drag roof design predicted by the metamodel for $\beta = \mathring{5}$ $(D_1 = 0.76, D_2 = 1, D_2 = 0.5)$.

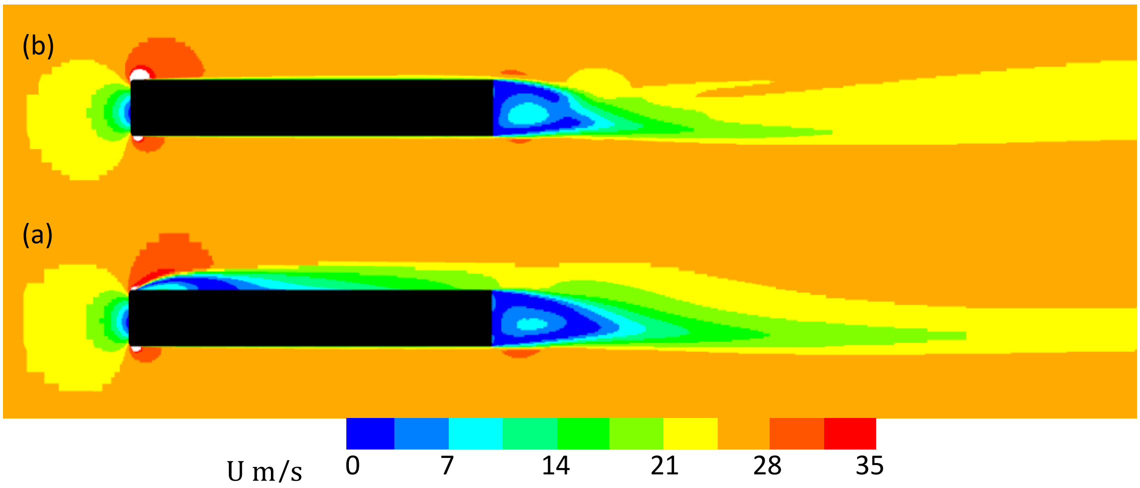

Fig. 6.15. Comparison of the streamwise velocity magnitude contours on the horizontal plane (y=2m) for (a) the baseline model and (b) the minimum-drag roof design predicted by the metamodel for $\beta = 5^{\circ}$ ($D_1 = 0.76, D_2 = 1, D_2 = 0.5$).

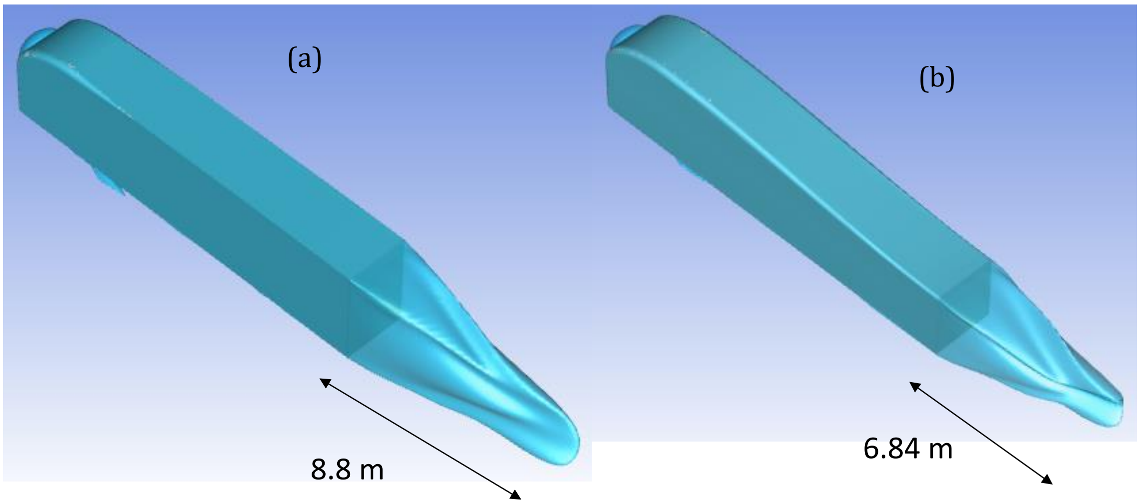

Fig. 6.16. Comparison of the wake structure visualised by a velocity magnitude isosurface of 10m/s for (a) the baseline model and (b) the minimum-drag roof design predicted by the metamodel for $\beta = 6^{\circ}$. ($D_1 = 0.76, D_2 = 0, D_2 = 0.5$).

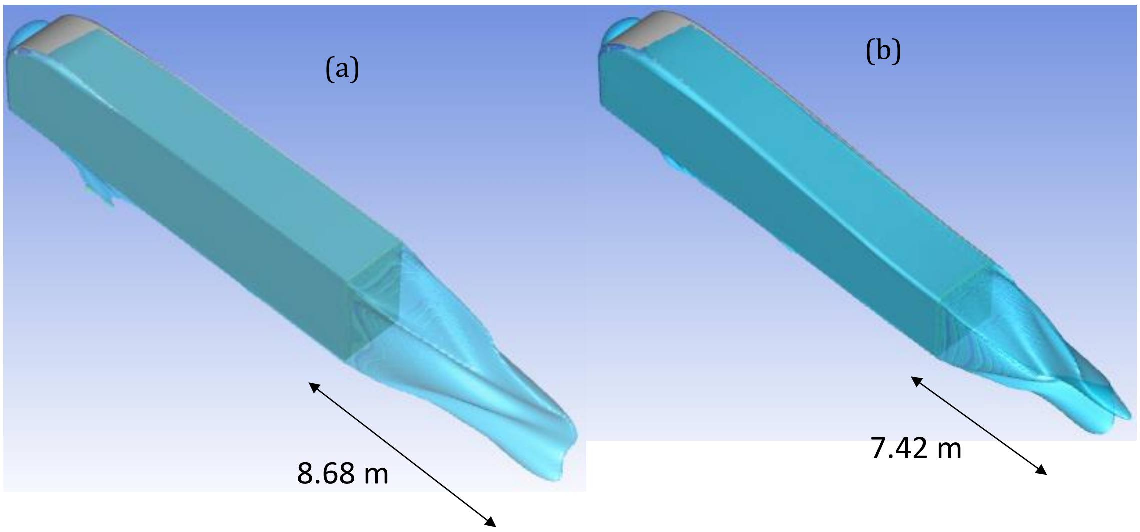

Fig. 6.17. Comparison of the wake structure visualised by a velocity magnitude isosurface of 10m/s for (a) the baseline model and (b) the minimum-drag roof design predicted by the metamodel for β = 8°. $(D_1 = 0.76, D_2 = 0, D_2 = 0.5)$.

6.2.2 Optimum $\frac{dc_N}{d\beta}$AL

As described in the literature review, mathematically, a road vehicle is statically stable when the condition $\frac{dc_N}{d\beta} < 0$ is satisfied. The approximation $\frac{dc_N}{d\beta} \cong \frac{\Delta c_N}{\Delta\beta}$ can be used by calculating the differences in C_N and β from the range of yaw angles (β = 5°,6° and 8°) considered. For the β = 5° cases, the gradient is calculated by assuming that C_N = 0 when β = 0° and so the values of C_N at β = 5° is used to find $\frac{dc_N}{d\beta}$. Similarly, the gradient for β = 6° cases is found using C_N data at β = 5° and β = 6° (i.e. $\Delta\beta$ =1°) etc. As before, obtaining the global minimum for $\frac{dc_N}{d\beta}$ at each yaw angle was found by constructing a new metamodel and iteratively searching for each minima. Table 6.4 shows the comparison of the metamodel prediction and corresponding CFD results for the minimum $\frac{\mathrm{d}c_N}{\mathrm{d}\beta}AL$ roof design, per side slip angle. Recall that the stability parameter $\frac{dc_N}{d\beta}$ is multiplied by the frontal area, A, for consistency and the length of the vehicle, L, as the characteristic length. Here, the optimum design for all side angles has the following parameters: D_1 =95%, D_2 = 0^0 and D_3 = 0.5. This HGV design is shown in Fig. 6.18 and it is a corner point in the design space (point (1) in Fig. 6.2 and Fig. 6.3).

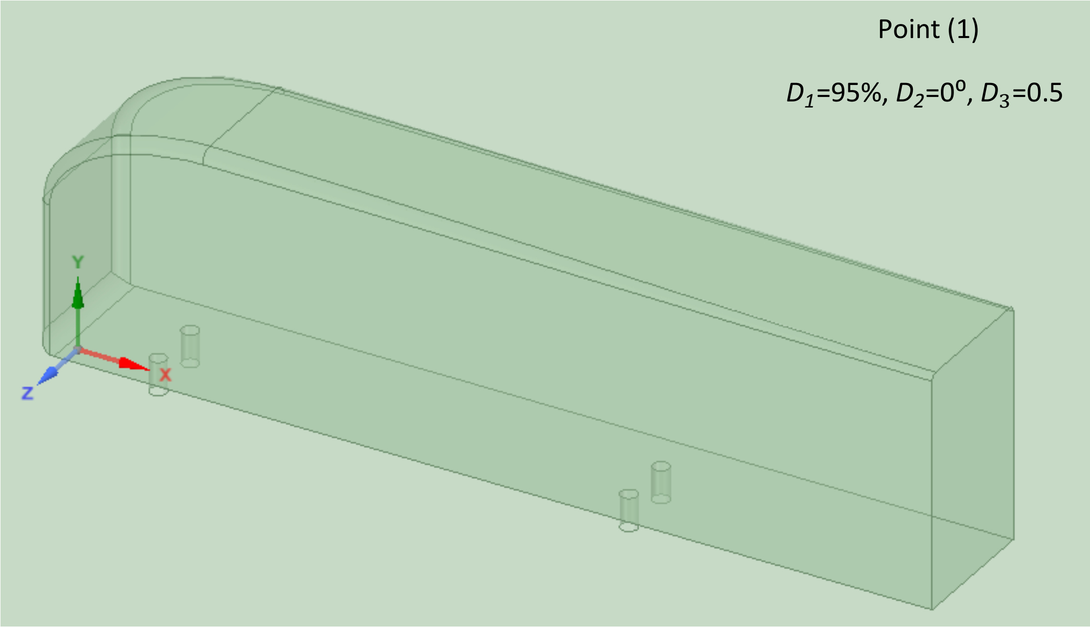

Fig. 6.18. Illustration of the minimum-$\frac{dc_N}{d\beta}AL$ roof design predicted by the metamodel and validated by CFD for β = 0° , 5° , 6° and 8° . Corner point (1) relates to Fig. 6.2 and Fig. 6.3.

Unfortunately, all these optimum designs are statically unstable because $\frac{dc_N}{d\beta} > 0$, however, so is the baseline design. It is worth mentioning that all the moments, including the yawing moment, are calculated about the geometric centre of the vehicle (recall section 6.1.3). If the moments are taken from a point closer to the front, then the vehicle becomes stable because of weathercock stability i.e. there is more side area behind the centre of gravity. As already mentioned, setting the centre of gravity to be the geometric centre of the vehicle is a reasonable assumption which is used in this thesis, however, future work may need to consider different centre of gravity positions; this will be explained in the discussion. As with the minimum drag design shown previously, Table 6.4 shows a close agreement between the MLS metamodel prediction and the CFD result, whereby δ is less than 0.6%.

Table 6.4. Comparison of the metamodel prediction and corresponding CFD results for the minimum $\boldsymbol{\frac{dc_N}{d\beta}}AL$ roof design.

Side slip angle (β)	Design Variables			$\frac{dc_N}{d\beta}AL$		
	D_1	D_2	D_3	MLS	CFD	δ
5^0	0.95	0^0	0.5	4.6179	4.6208	0.06%
6^0	0.95	0^0	0.5	4.2000	4.2232	0.55%
8^0	0.95	0^0	0.5	3.1477	3.1504	0.09%

Furthermore, Fig. 6.19 shows various slices of the metamodel of $\boldsymbol{\frac{dc_N}{d\beta}}AL$ plotted as a function of D_2 and D_3 for three different values of D_1. This figure clearly indicates that the global minimum (best stability) occurs in a corner point (1) of the design space i.e. the maximum height (D_1 = 95%), the minimum possible angle of the base of the roof (D_2 = 0^0) and the minimum possible side edge curvature (D_3 = 0.5). The trends from Fig. 6.19 confirm that the stability improves (less positive $\frac{dc_N}{d\beta}AL$) with an increase in the base height (D_1) which makes sense because this means there is more side area at the rear, leading to better weathercock stability. Stability is also better as the base angle of the roof (D_2) reduces. If the angle is high, this leads to a concave shape with greater side area in the centre of the HGV and not as much side area at the rear, so the restoring moment and thus weathercock stability is less effective. The final parameter, the side edge curvature (D_3) is not very sensitive to yaw stability, however, static stability improves slightly as the edge radius reduces.

An important point is that unlike the minimum drag design, the maximum yaw stability design (Table 6.4) is less stable than the baseline one. This is shown in Table 6.5 which compares the baseline with the optimum design for each of the three side slip angles considered. This is not surprising considering that the parameterisation limits the maximum height at the base of the optimised design to only 95% of the baseline value. Consequently, there is less side area available at the base of the optimised HGV and so there is less weathercock stability. This is an unfortunate consequence of the physical constraints which limit the parameterisation and therefore the scope of the design space. However, the design presented in Table 6.4 and shown in Table 6.5 still has the best yaw stability of all the designs tested in this optimisation study.

Table 6.5. Comparison between the baseline and optimised designs $\frac{dc_N}{d\beta}AL$.

Side slip angle (β)	Baseline (CFD)	Optimised designs (CFD)	δ (%)
5^0	4.2553	4.6208	-8.59%
6^0	3.5415	4.2232	-19.25%
8^0	2.5142	3.1504	-25.30%

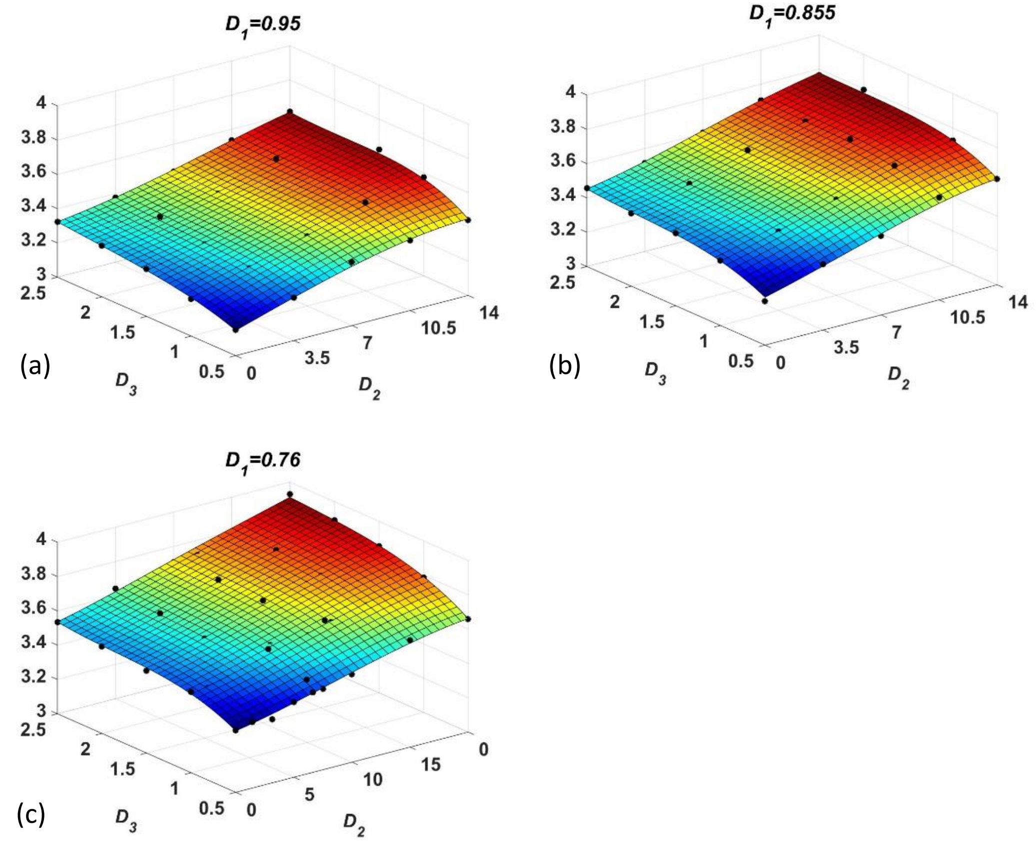

Fig. 6.19. The MLS metamodel of $\frac{dc_N}{d\beta}AL$, for a sideslip angle, $\beta = 8^\circ$. The metamodel shows $\frac{dc_N}{d\beta}AL$ as a function of D_2 and D_3 for (a) the maximum of D_1, (b) the middle value of D_1 and (c) the minimum of D_1. Black points represent data points.

Now that a generic optimum within the design space has been found, further analysis is necessary to understand how it compares to the baseline design and others in the design space. Fig. 6.20 shows a comparison between the slope of the curve of $C_N AL$ as a function of β for the baseline and optimum designs and three other DoE corner points (2),(3) and (5) (recall Fig. 6.2-6.4). As already mentioned, it is clear that all the designs are statically unstable because gradients of the curves ($\frac{dc_N}{d\beta}$) are positive. This means that the yawing moment generated due to the aerodynamics has the tendency to rotate the vehicle away from the wind direction; the yawing moments further exaggerate the disturbance making the designs statically unstable if the centre of gravity is in the centre of the vehicle. It is important to note that the baseline design is also unstable but not by as much.

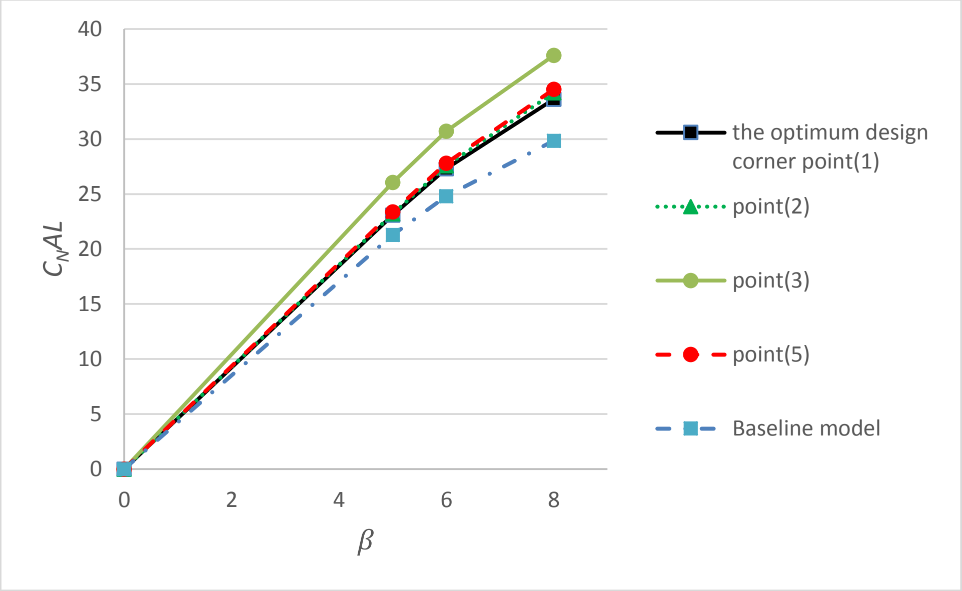

Fig. 6.20. Comparison between the slope of the curve of C_NAL for the baseline and optimum designs as well as corner points (2), (3) and (5).

From Fig. 6.20 it is clear that there is no significant difference between the stability of the optimum design (which is corner point 1) and corner points (2) and (5). On the contrary, there is a significant difference when compared to corner point (3) which is less stable. This is clearer in Table 6.6 which shows the results for all 8 corner points in the design space, for all three slip angles evaluated.

Table 6.6. CFD results for the $\frac{dc_N}{d\beta}AL$ roof design for all eight corner points.

Model name	Design Variables			Side slip angle (β)			
	D_1	D_2	D_3	0^0	5^0	6^0	8^0
corner point(1)	0.95	0^0	0.5	0	4.6208	4.2232	3.1504
corner point(2)	0.95	0^0	2.5	0	4.6451	4.3509	3.3220
corner point(3)	0.95	14^0	0.5	0	5.2107	4.6739	3.4394
corner point(4)	0.95	14^0	2.5	0	5.3356	4.7435	3.6147
corner point(5)	0.76	0^0	0.5	0	4.6791	4.4086	3.3623
corner point(6)	0.76	0^0	2.5	0	4.7738	4.5939	3.5334
corner point(7)	0.76	14^0	0.5	0	5.2203	4.8439	3.6586
corner point(8)	0.76	14^0	2.5	0	5.4706	5.0653	3.9302

Furthermore, recalling the design space in Fig. 6.2, it can be concluded that the effect of design variable D_2 is more influential than the other two variables. Moreover, from Fig. 6.20, Table 6.6 and Fig. 6.19, it is clear that the maximum $\frac{dc_N}{d\beta}AL$ design (least stable) is also a corner point (8) for the all slip angles. This least stable design has the lowest base height and the greatest rear slope angle. Both of these design characteristics mean the side area is distributed more to the front of the vehicle and therefore there is significantly less weathercock stability occurring.

6.2.3 Optimum $C_Y A$

The third objective function to be investigated is the side force coefficient area, $C_Y A$, which is another important stability parameter. The same optimisation process outlined above was followed to generate a metamodel for the three yaw angles (β = 5°, 6° and 8°). Table 6.7 shows the details for the minimum of $C_Y A$; again, the comparison between the CFD results and those predicted by the metamodel are shown with small differences of around 0.3% or less, giving continued confidence in the accuracy of the metamodel.

Table 6.7. Comparison of the metamodel prediction and corresponding CFD results for the minimum $C_Y A$ roof design.

Side slip angle (β)	Design Variables			$C_Y A$		
	D_1	D_2	D_3	MLS	CFD	δ
5^0	0.76	0^0	2.5	3.1180	3.1281	0.32%
6^0	0.76	0^0	2.5	3.7153	3.7260	0.29%
8^0	0.76	0^0	2.5	4.7015	4.7022	0.01%

It is clear from Table 6.7 that the side force (and thus $C_Y A$) is a minimum when D_1 and D_2 are at their smallest. These two parameters directly influence the side area; this is a minimum when D_1 and D_2 are a minimum i.e. flat and low roof profile at the rear, which is logical. The shape of the vehicle for minimum side force is shown in Fig. 6.21 which is corner point (6) in in the design space (recall Fig. 6.2 and Fig. 6.4).

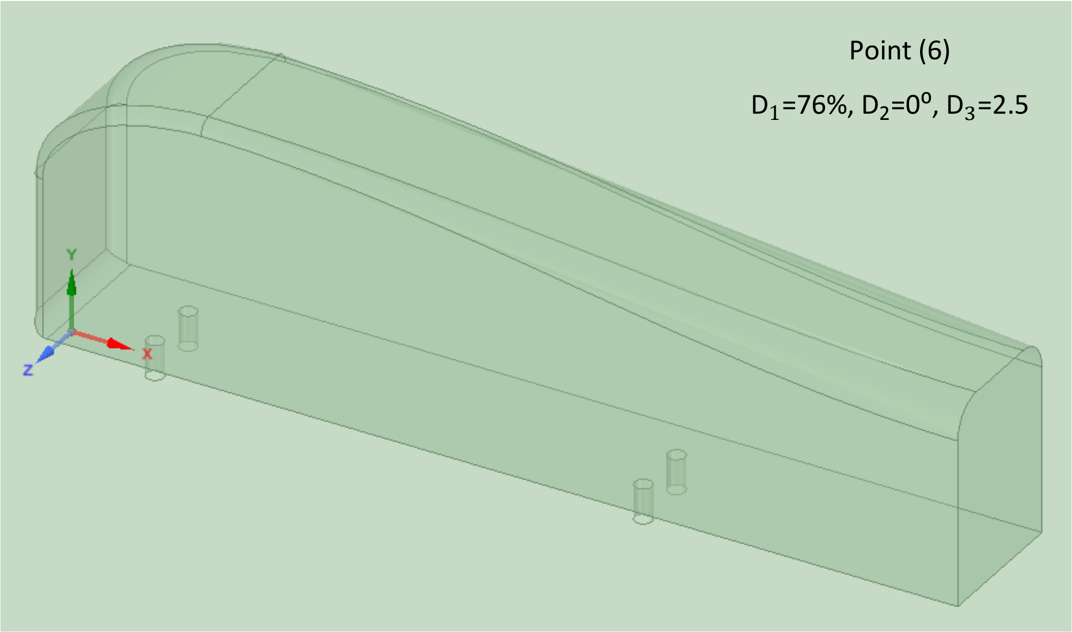

Fig. 6.21. Illustration of the minimum-$C_Y A$ roof design predicted by the metamodel and validated by CFD for $\beta = 0^o$, 5^o , 6^o and 8^o .

Furthermore, Fig. 6.22 shows various slices of the metamodel for one of the slip angles (β = 8°) and the trends are clear. The smaller D_1 and D_2 are, the smaller C_YA is. The side force area is not very sensitive to design variable D_3.

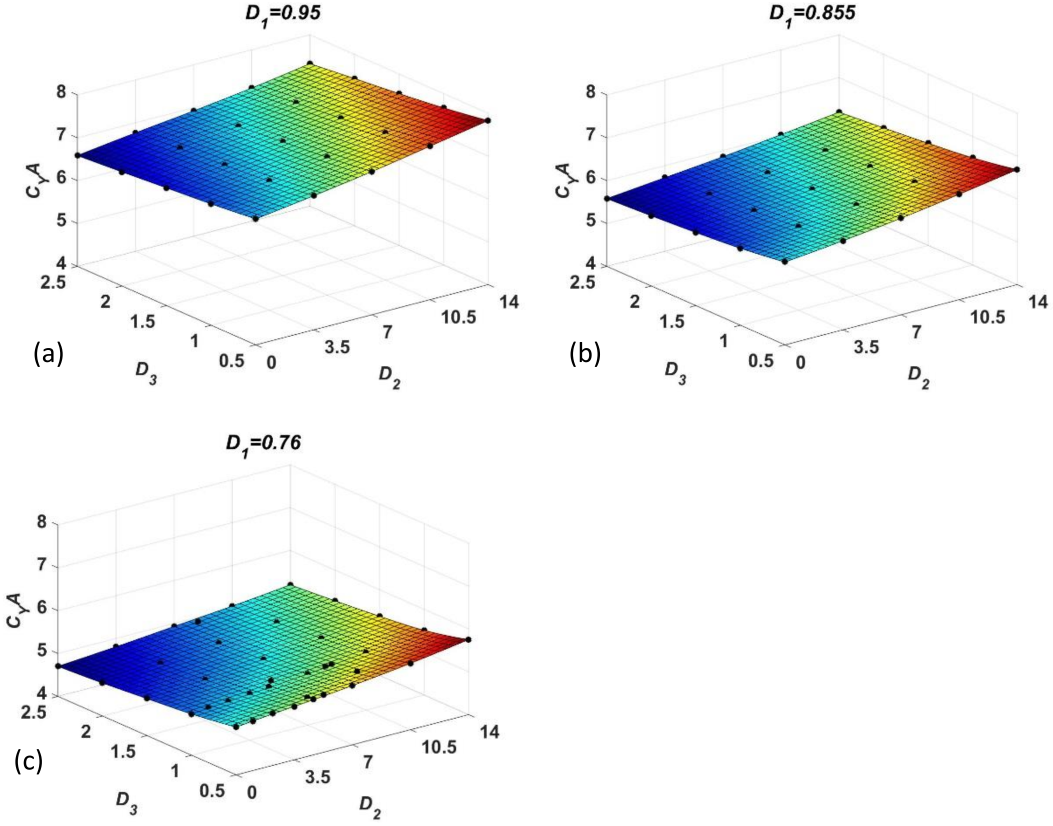

Fig. 6.22. the (MLS) metamodel of C_YA, for a sideslip angle, $\beta = 8^{\circ}$. The metamodel shows C_YA as a function of D_2 and D_3 for (a) the maximum of D_1, (b) the middle value of D_1 and (c) the minimum of D_1. Black points represent data points.

Now that an optimum design for side force area has been found, some postprocess is necessary to compare it to the baseline design to find some evidence for why this is better. Table 6.8 shows the comparison between the baseline and optimised designs of C_YA. Clearly, the side force is reduced by over 42% due to the decrease in side area.

Table 6.8. Comparison between the baseline and optimised designs for C_YA.

Side slip angle (β)	Baseline (CFD)	Optimised designs (CFD)	δ
5^0	5.4658	3.1281	42.77%
6^0	6.6066	3.7260	43.60%
8^0	8.5902	4.7022	45.26%

Unsurprisingly, the side edge radius, D_3, has comparatively little effect on C_YA because it has no impact on the projected side area, unlike D_1 and D_2. Nevertheless, as D_3 increases, C_YA

does still decrease because significant rounding of the two side edges creates a low-pressure region on the windward side of the vehicle and creates high pressure on the leeward side; this alters the sideways pressure distribution to reduce C_YA.

Fig. 6.23 Shows the effect of the side edge radius, D_3, by comparing the minimum-C_YA roof design which is corner point (6) in the design space and has the maximum D_3, and corner point (5) which has minimum D_3. Both of these designs have the same side area because D_1 and D_2 are the same; only D_3 is different. It can be seen that by increasing the radius of the side edges, the high-pressure area (stagnation) reduces in size on the windward side, especially at the rear and pressure increases at the leeward side; the combination of these effects is to reduce side force.

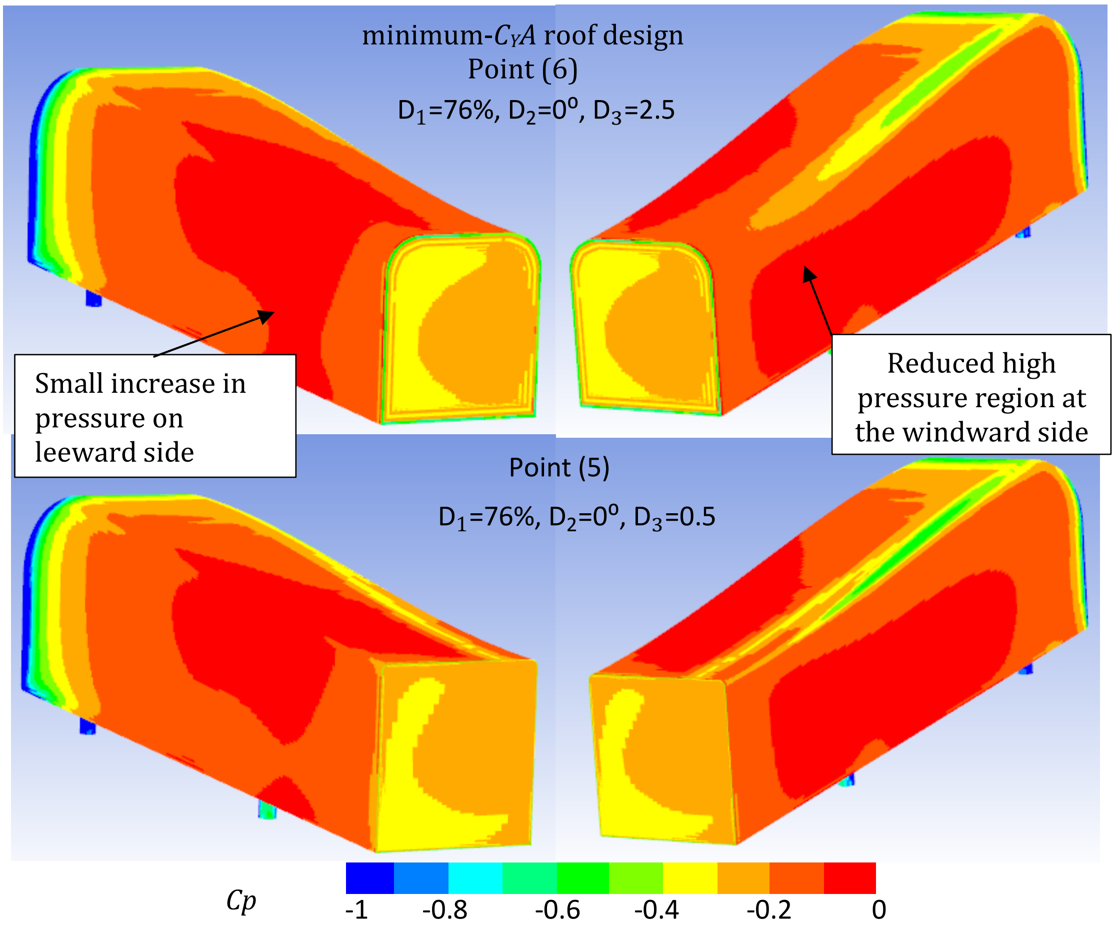

Fig. 6.23. Comparison of *Cp* on the surfaces of the minimum-C_YA roof design (top images) and corner point (5) (bottom images). Left images show leeward side, right images show the windward side.

6.2.4 **Optimum C_NAL**

The next single-objective optimisation considers the yawing moment coefficient area, C_NAL, which is another parameter describing stability and is related to objective function (b) i.e.

$\frac{\boldsymbol{dc_N}}{\boldsymbol{d\beta}}AL$. Table 6.9 shows the details of the global minimum of C_NAL. The same design was produced for all three yaw angles tested. It is clear that the minimum C_NAL design is the same as the minimum $\frac{\boldsymbol{dc_N}}{\boldsymbol{d\beta}}AL$ roof design as shown in Fig. 6.18, which is corner point (1) in the design space, see section 6.2.2.

Table 6.9. Comparison of the metamodel prediction and corresponding CFD results for the minimum C_NAL roof design.

Side slip angle (β)	Design Variables			C_NA		
	D_1	D_2	D_3	MLS	CFD	δ
5^o	0.95	0^o	0.5	23.0514	23.0518	0.00%
6^o	0.95	0^o	0.5	27.2565	27.2621	-0.02%
8^o	0.95	0^o	0.5	33.5453	33.5576	-0.04%

Table 6.9 again shows a close agreement between the MLS metamodel prediction and the CFD result, whereby δ is less than 0.05%. The relationship between the design variables and the objective function are illustrated in Fig. 6.24 which shows various slices of the β = 8° metamodel, which is representative of the others. The results are similar to the trends of the metamodel for $\frac{\boldsymbol{dc_N}}{\boldsymbol{d\beta}}AL$ in Fig. 6.19, clearly indicating that the global minimum occurs in a corner point of the design space i.e. the maximum height (D_1 =0.95), the minimum possible angle of the base of the roof (D_2 = 0^0) and the minimum possible side edge curvature (D_3 =0.5). The trends from Fig. 6.24 confirm that C_NAL decreases (better stability) with an increase in the base height (D_1) although this effect is small. The side edge curvature (D_3) is not very sensitive to C_NAL, however, as the base angle of the roof (D_2) increases, this significantly increases the size of the yawing moment and it is therefore less stable.

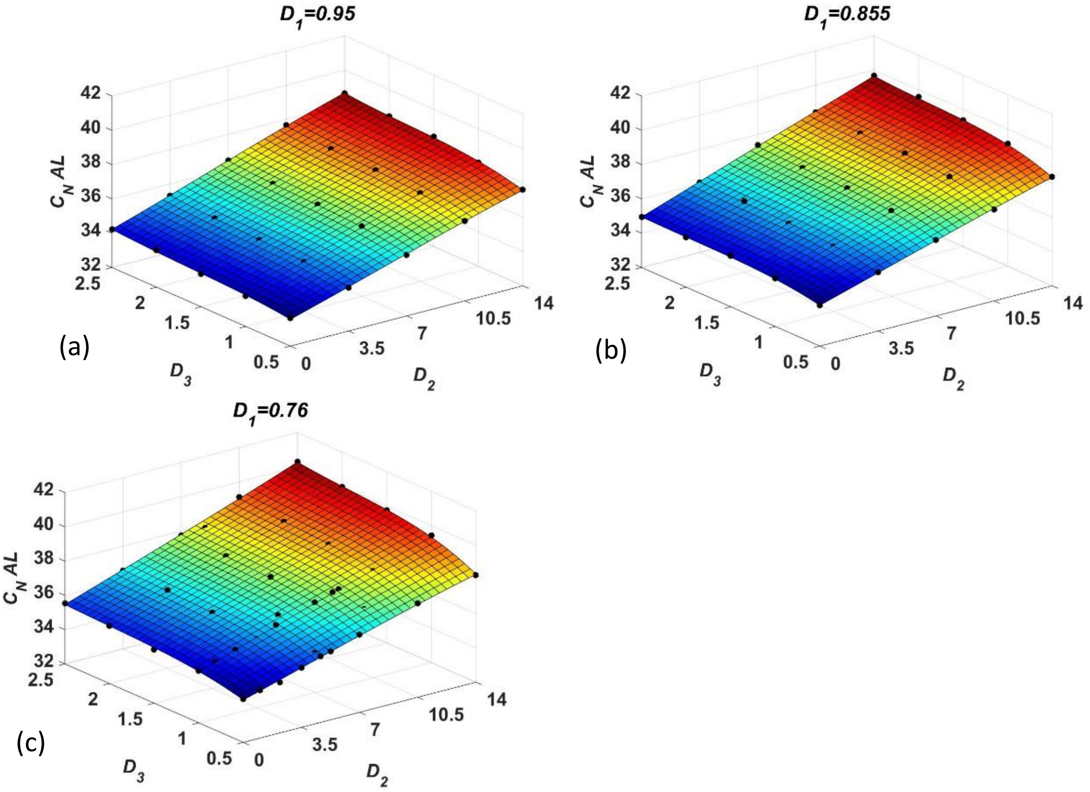

Fig. 6.24. The (MLS) metamodel of C_NAL, for a sideslip angle, $\beta = 8^{\circ}$. The metamodel shows C_NAL as a function of D_2 and D_3 for (a) the maximum of D_1, (b) the middle value of D_1 and (c) the minimum of D_1. Black points represent data points

Table 6.10 shows the comparison between the baseline and the optimum design for C_NAL. As with objective function (b), it is clear that the minimum yawing moment coefficient area is greater and therefore less stable than the baseline by between 8.3% and 12.4% for the three yaw angles considered.

Table 6.10. Comparison between the baseline and optimised designs C_NAL.

Angle of side force (β)	Baseline (CFD)	Optimised designs (CFD)	δ
5^0	21.2763	23.0518	8.34%
6^0	24.8178	27.2621	9.85%
8^0	29.8462	33.5576	12.44%

All three design variables affect C_NAL as well as the overall aerodynamic forces and moments in two ways. Firstly, these design variables change the side area of the vehicle and secondly, they change the pressure distribution over the roof section, which can dramatically change the flow structure. As already described, design variables D_1 and D_2 directly change the side area, whereas D_3 has very little effect. This is clearly seen in Fig. 6.25 which shows how changes in the rear height and the angle of the slope affect the projected side area. These four images show the extreme designs which would be on one face of the design space.

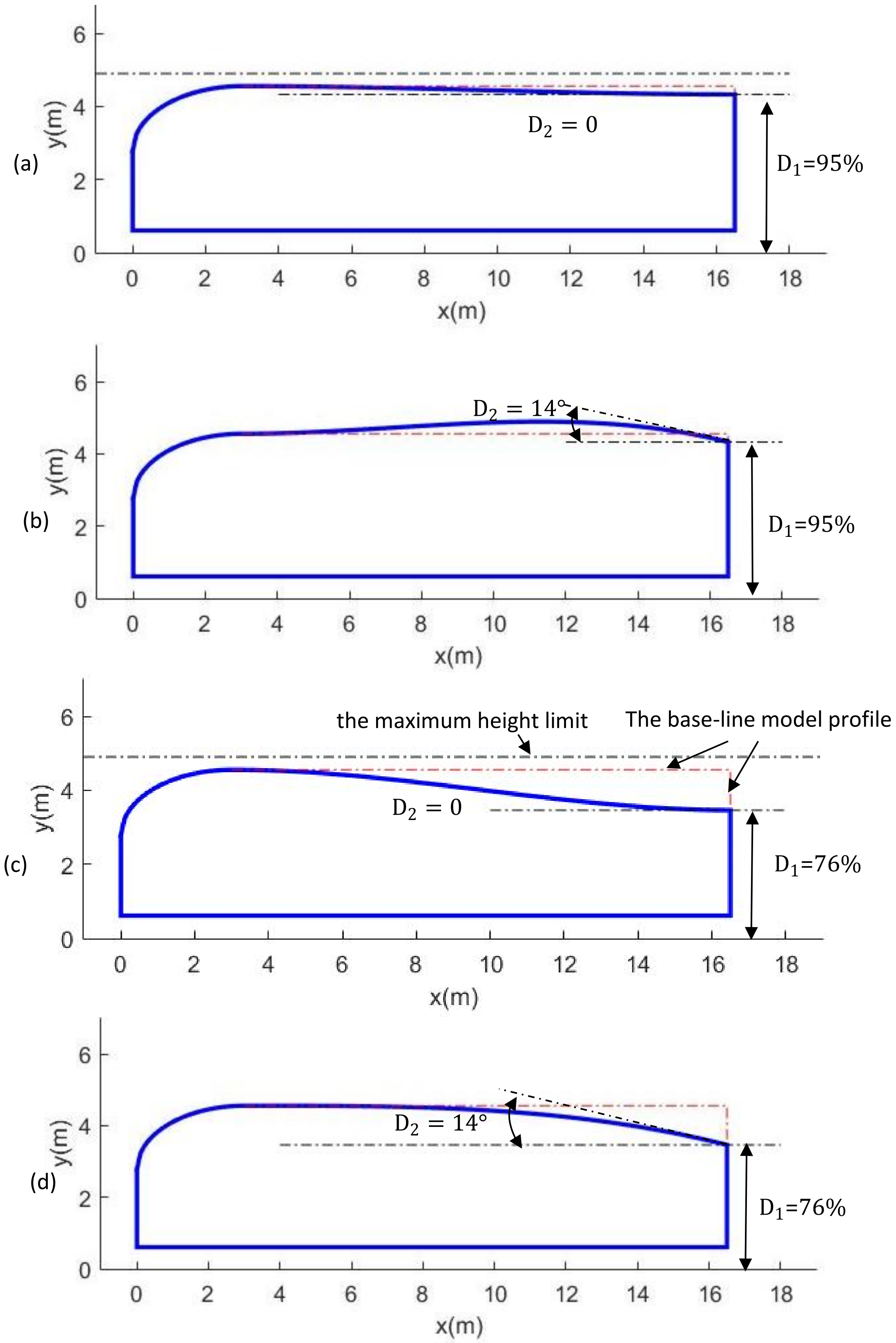

Fig. 6.25. Illustration showing the effect of design variables D_1 and D_2 on the side area of the vehicle

It is interesting to note that Fig. 6.25(a) shows the shape of the minimum C_NAL design which clearly has a larger rear area than, for example, the minimum drag design, Fig. 6.25(c). This is logical because the larger rear area produces a greater yawing moment leading to better weathercock stability. Therefore, it would be expected that the design shown in Fig. 6.25(b), which has even more area at the back, would be even more stable. However, this is not the case. To explore this further, the surface pressure distribution is compared for the baseline design, the minimum-C_NAL design (which is also corner point 1), corner point 2, 3 and 5, see Fig. 6.2

Although corner point 3 has the largest rear area for these designs (and in fact the largest in the whole design space), it is less stable than the baseline and minimum-C_NAL roof designs, even though they have less rear area than point 3. However it is clear from the pressure distribution that the high-pressure area on the windward side has shifted upstream which means the side force is greater at the front of the vehicle, pushing it away from the side wind, making the vehicle less stable. It can be concluded that the negative effect of shifting forward the high-pressure area overcomes the positive effect of increasing the side area at the rear of the vehicle.

Furthermore, regarding the impact of D_3, the side edge radius, it has been explained that it has a minimal effect on C_NAL because it cannot influence the side area and thus yaw of the vehicle. The vehicles shown in Fig. 6.26b and Fig. 6.26c have the same side area but the former has the smallest D_3 and the latter has the largest D_3. It can be seen that by increasing this side edge radius, this marginally reduces the stagnation pressure at the rear which is the same as shifting the high-pressure area upstream; this is indicated by there being less of the red contours at the rear of Fig. 6.26c. Therefore, greater side edge radius appears to decrease stability, as shown in the metamodel (Fig. 6.24), however, this effect is comparatively small.

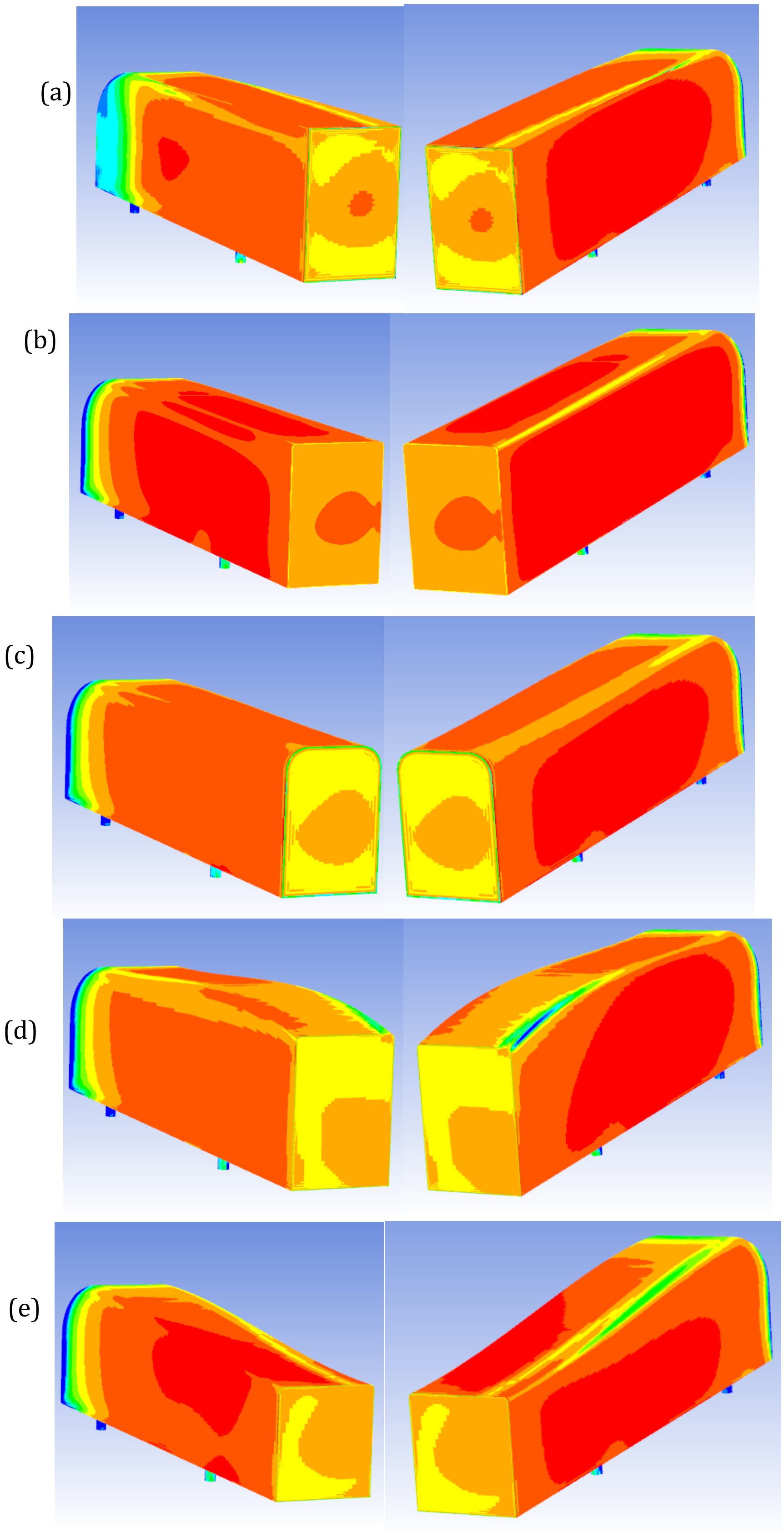

Fig. 6.26. Illustration showing C_p on the surface of (a) baseline (rescaled GTS), (b) min $C_N AL$ design, corner point 1, (c) corner point 2, (d) corner point 3 and (e) corner point 5. For all cases, β =8°. Left images show the leeward side of the vehicles, right images show windward side.

6.2.5 **Optimum** $|C_R AL|$

The final objective function to be investigated is the absolute value of the rolling moment coefficient area, $|C_RAL|$, which is another important stability parameter. The objective is to minimise this function which is equivalent to having no rolling taking place, making the vehicle easier to handle. The same optimisation process outlined before was followed to generate a metamodel for the three yaw angles (β = 5°, 6° and 8°). Fig. 6.27 shows various slices of the metamodel for one of the slip angles (β = 8°). These figures clearly indicate that the global minimum occurs near a corner point of the design space i.e. the maximum height (D_1 =0.95), near the maximum possible angle of the base of the roof (D_2) and the minimum possible side edge curvature (D_3 =0.5). The trends confirm that generally $|C_RAL|$ decreases (more stable) with increases in the base height (D_1) and the base angle of the roof (D_2), and a reduction in the side edge curvature (D_3).

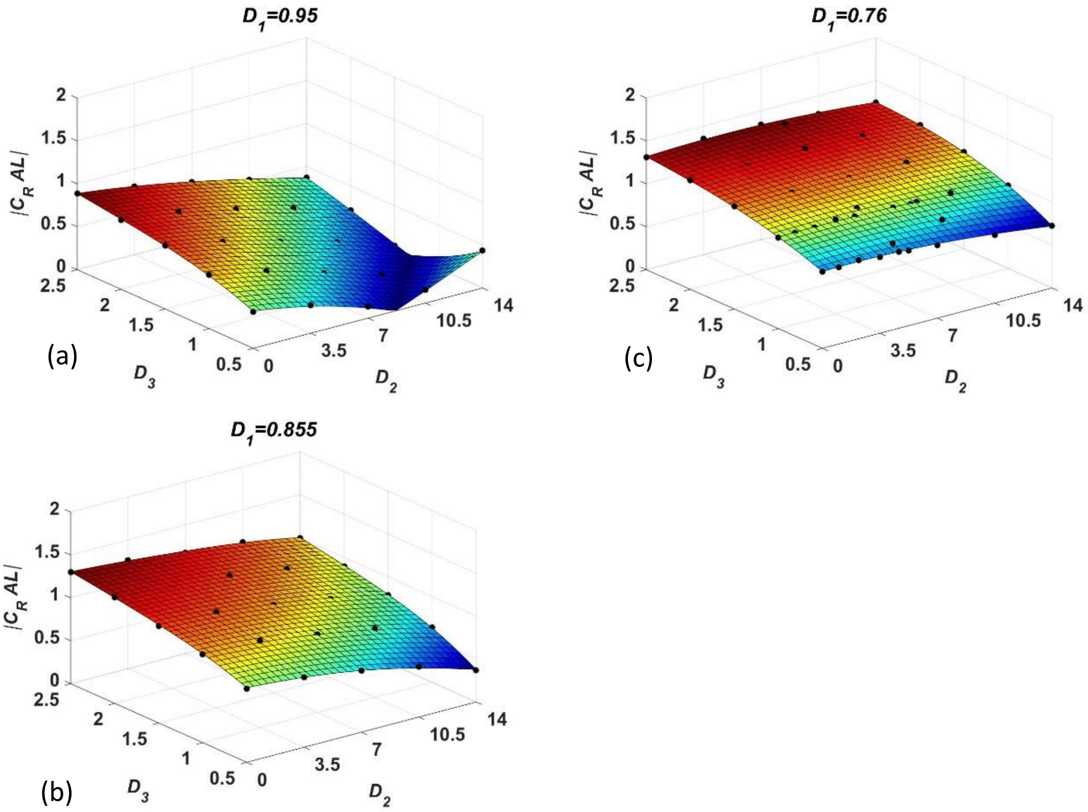
(a)

(c)

(b)

Fig. 6.27. Metamodel of $|C_RAL|$ for a sideslip angle, $\beta = 8^\circ$. The metamodel shows $|C_RAL|$ as a function of D_2 and D_3 for (a) the maximum of D_1, (b) the middle value of D_1 and (c) the minimum of D_1. Black points represent data points.

Fig. 6.28 shows contours of $|C_RAL|$ at the maximum of D_1 (0.95), for a sideslip angle, $\beta = 8^\circ$ as a function of D_2 and D_3. This is essentially a clearer view of Fig. 6.27(a). Interestingly, it can be seen that the global minimum occurs near a corner point and is shown as a valley (dark blue region). Here, the value of $|C_R AL|$, the rolling moment coefficient area, is zero along this valley which shows that certain combinations of design variables produce no rolling moment, however, this assumes that the centre of gravity is in the centre of the vehicle, as stated earlier. If the objective function was to minimise $C_R AL$ (and not its absolute value), then there would be negative rolling moments i.e. in the bottom right corner of Fig. 6.28. In practice the most negative rolling moment would occur for the vehicle design at corner point 3 within the design space; this is shown in Fig. 6.26d and it is clear that the stagnation pressure is greater at the bottom on the windward side. Because moments are taken about the geometric centre of the vehicle, there is a greater force at the bottom than the top, giving a negative rolling moment. However, the reaction forces on the HGV tyres would not allow this moment to dramatically affect vehicle performance.

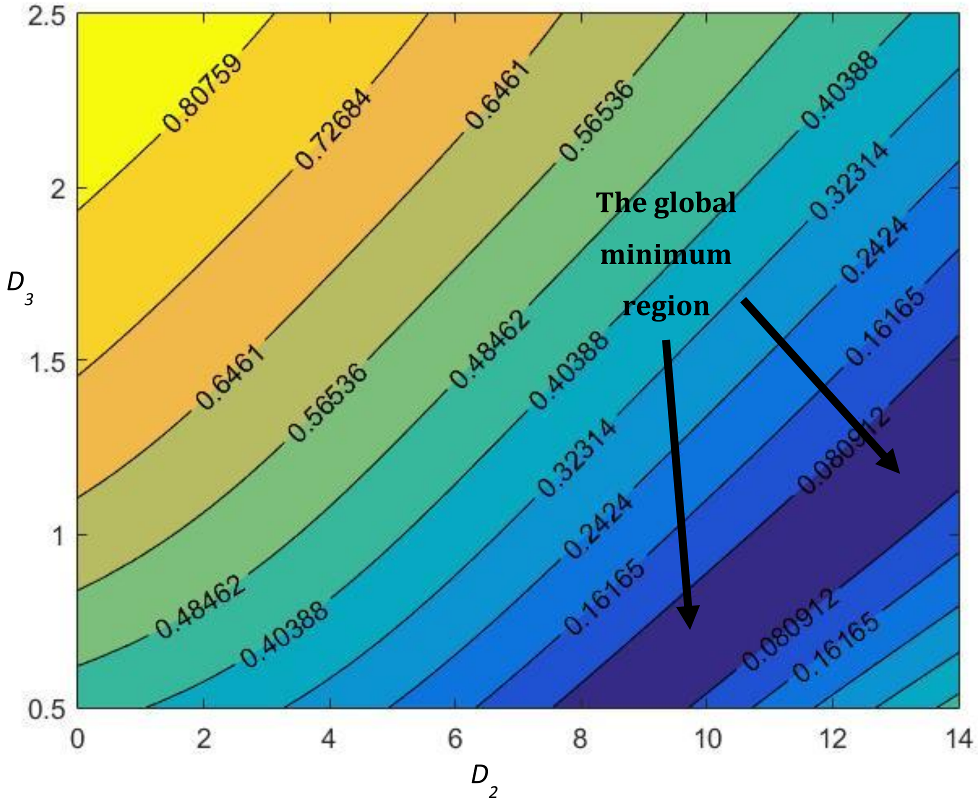

Fig. 6.28. Close up view of the (MLS) metamodel for $|C_R AL|$ for a sideslip angle, $\beta = 8^{\circ}$. The metamodel shows $|C_R AL|$ as a function of D_2 and D_3 for the maximum of D_1 (0.95).

Table 6.11 shows a comparison between the baseline and optimised designs for $|C_R AL|$, for all three side slip angles. As can be seen, the rolling moment is completely eliminated if the design variables are in the valley indicated in Fig. 6.28, for the reasons described above. No single combination of design variables can be identified because there is a range of designs which exists along the valley. However, the magnitude of the rolling moment on the baseline vehicle is significantly less than the yawing moment, for example, and so this objective function is less important for stability.

Table 6.11. Comparison between the baseline and optimised designs of $|C_R AL|$.

Side slip angle (β)	Baseline (CFD)	Optimised designs (CFD)
5°	1.0892	0
6°	1.4654	0
8°	2.2419	0

6.3 **Multi-objective optimization**

In the previous sub-sections, single objective optimisation was employed to find the best HGV design for five different objective functions. In this section, multi-objective optimisation will be presented to identify if there is a best compromise between different objectives such as drag and stability.

6.3.1 **Multi-objective optimization: $C_D A$ vs $\frac{dc_N}{d\beta}AL$**

Probably the most important multi-objective case is to investigate the effect of drag area, $C_D A$, and the stability using the yawing moment-slip angle derivative, $\frac{dc_N}{d\beta}AL$. Both of these objective functions have been optimised in previous sections. The minimum $C_D A$ design has inferior stability to the minimum $\frac{dc_N}{d\beta}AL$ design and likewise the minimum $\frac{dc_N}{d\beta}AL$ design (i.e. best stability) shows higher drag than the minimum $C_D A$ design. These two designs are shown in Fig. 6.29 which is a plot of the two objective functions, for each of the three yaw angles tested. These plots show the distribution of all 138 CFD responses together with the baseline design (i.e. the rescaled GTS). The most striking trend from Fig. 6.29 is that all of the designs show a significant improvement in terms of drag, compared to the baseline design. On the other hand, in terms of stability, all of the designs are less stable compared to the baseline design, for all three yaw cases considered. These plots also include a predicted Pareto front which is calculated from a multi-objective genetic algorithm approach using the “gamultiobj” MATLAB (R2015a) function.

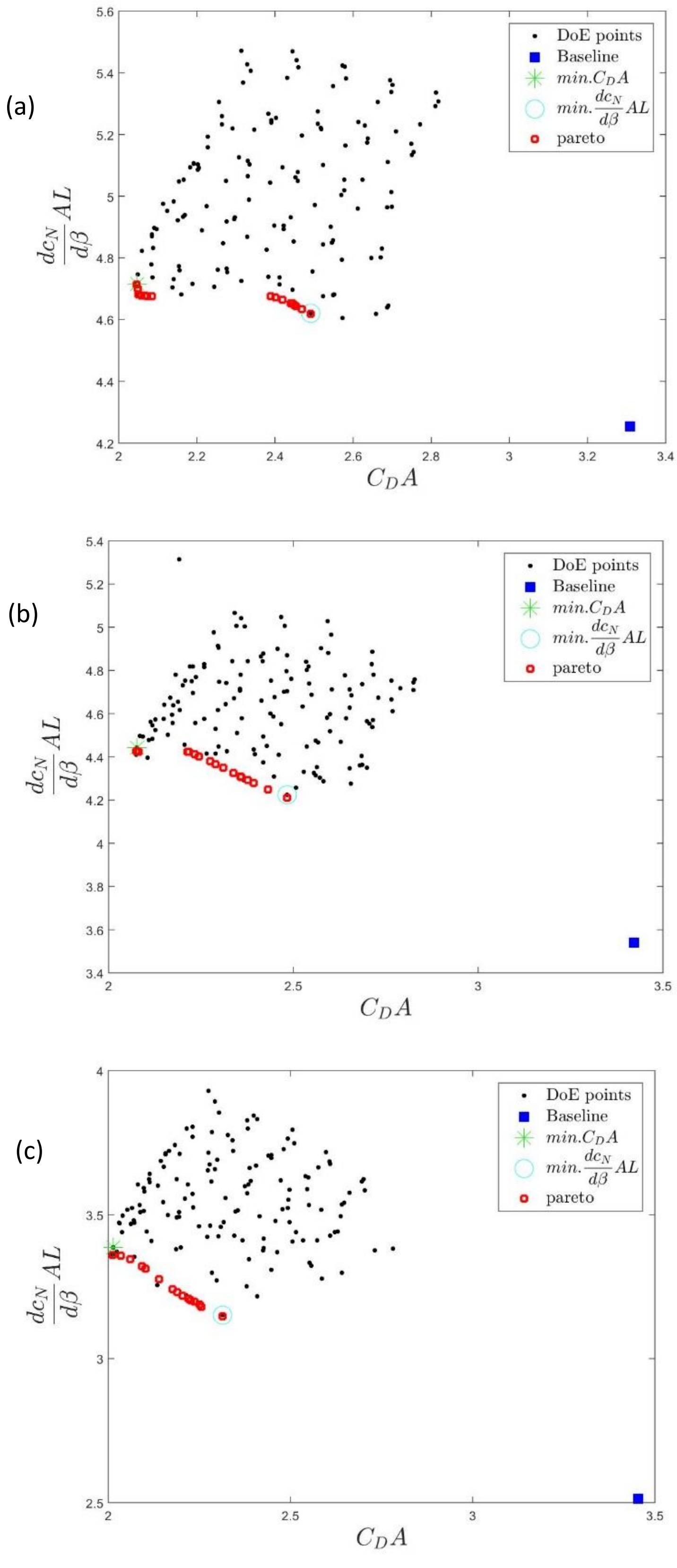

Fig. 6.29. Objective function plot showing the CFD results of the drag coefficient area, C_DA, as a function of the yawing moment coefficient-slip angle derivative, $\frac{\mathrm{dc_N}}{\mathrm{d\beta}}AL$ for (a) β = 5°, (b) β = 6° and (c) β = 8°.

It is important to know that each Pareto front presented in Fig. 6.29 (red circles) is not based on CFD data, but from the metamodel prediction, however, all other data points are based on CFD results. In theory, a Pareto front represents the best compromise between the two objective functions (Forrester et al., 2009). If minimum C_DA is favoured, the left-hand side of the Pareto front is the best location, whereas the right-hand side is better for minimum $\frac{dc_N}{d\beta}AL$. Anywhere in the middle of the Pareto is a compromise between the two objectives. The purpose of subsequent work is to identify some intermediate designs representing an acceptable compromise.

Table 6.12 shows 16 individual designs obtained from the predicted Pareto front in Fig. 6.29 (a) for the β = 5° case. Each of these points is constructed from the metamodels which predict the combination of design variables (D_1, D_2 and D_3) and the expected objective functions (C_DA and $\frac{dc_N}{d\beta}AL$), per design. Point 1 represents the minimum drag design (recall section 6.2.1) and point 16 is the best stability design (section 6.2.2). It is clear that the 16 points share approximately the same minimum for both the rear angle of the roof profile at the base, D_2 and the side edge radius, D_3. Interestingly, moving down the table from point 1 to 16, the metamodels predict that the base height, D_1, will increase as the design changes from low drag (point 1) to (comparatively) high stability (point 16). The same trends are seen for the other slip angle cases of β = 6° and β = 8° in Table 6.13 and Table 6.14, respectively.

Table 6.12. Sixteen points on the predicted Pareto front, with expected design variables and objectives functions predicted by the metamodels, for $\beta = 5^{\circ}$.

	D_1	D_2 (○)	D_3	C_DA	$\frac{dc_N}{d\beta}AL$
1	0.76	0.97	0.50	2.0462	4.7135
2	0.76	0.65	0.50	2.0490	4.7015
3	0.76	0.07	0.50	2.0503	4.6825
4	0.77	0.00	0.50	2.0580	4.6783
5	0.77	0.01	0.50	2.0675	4.6769
6	0.77	0.02	0.50	2.0731	4.6765
7	0.78	0.00	0.50	2.0853	4.6755
8	0.91	0.00	0.50	2.3897	4.6755
9	0.92	0.01	0.50	2.4010	4.6713
10	0.92	0.07	0.50	2.4199	4.6647
11	0.93	0.05	0.50	2.4408	4.6529
12	0.93	0.09	0.50	2.4447	4.6526
13	0.93	0.00	0.50	2.4492	4.6466
14	0.94	0.01	0.50	2.4534	4.6441
15	0.94	0.02	0.50	2.4694	4.6342
16	0.95	0.00	0.50	2.4915	4.6179

Table 6.13. Fourteen points on the predicted Pareto front, with expected design variables and objectives functions predicted by the metamodels, for $\beta = 6^\circ$.

	D_1	D_2 (○)	D_3	$C_D A$	$\frac{dc_N}{d\beta}AL$
1	0.76	0.00	0.50	2.0745	4.4263
2	0.76	0.00	0.64	2.0812	4.4245
3	0.84	0.00	0.50	2.2144	4.4245
4	0.84	0.01	0.52	2.2162	4.4242
5	0.85	0.00	0.51	2.2324	4.4117
6	0.86	0.01	0.51	2.2753	4.3785
7	0.87	0.00	0.50	2.2900	4.3656
8	0.88	0.01	0.51	2.3110	4.3499
9	0.89	0.00	0.50	2.3380	4.3254
10	0.90	0.00	0.50	2.3579	4.3085
11	0.91	0.00	0.50	2.3769	4.2915
12	0.91	0.00	0.50	2.3923	4.2795
13	0.93	0.00	0.50	2.4310	4.2482
14	0.95	0.00	0.50	2.4832	4.2100

Table 6.14. Fifteen points on the predicted Pareto front, with expected design variables and objectives functions predicted by the metamodels, for $\beta = 8^\circ$.

	D_1	D_2 (○)	D_3	$C_D A$	$\frac{dc_N}{d\beta}AL$
1	0.76	0.00	0.50	2.0114	3.3588
2	0.78	0.00	0.50	2.0339	3.3577
3	0.80	0.00	0.50	2.0603	3.3457
4	0.82	0.00	0.50	2.0926	3.3206
5	0.83	0.00	0.50	2.1020	3.3115
6	0.86	0.00	0.50	2.1390	3.2748
7	0.88	0.00	0.50	2.1768	3.2404
8	0.89	0.00	0.50	2.1888	3.2301
9	0.90	0.00	0.50	2.2042	3.2188
10	0.91	0.01	0.51	2.2209	3.2077
11	0.91	0.00	0.50	2.2273	3.2013
12	0.91	0.02	0.51	2.2364	3.1971
13	0.92	0.00	0.51	2.2502	3.1869
14	0.92	0.00	0.50	2.2559	3.1804
15	0.95	0.00	0.50	2.3132	3.1477

Although the design trends in Table 6.12, Table 6.13 and Table 6.14 appear to be sensible and logical, it is important to validate some of these points with CFD solutions. Accordingly, three of the predicted Pareto points were tested and combined with the minimum drag and the best stability designs, to give a 5-point Pareto front, based on CFD solutions (and not the metamodels). Table 6.15, Table 6.16 and Table 6.17 show the results for these designs with a comparison between the actual CFD results and the metamodel predictions. Agreement between the two approaches is good in all cases, further underlining the accuracy of the metamodeling approach and reinforcing the design trends described immediately above Table 6.12.

Table 6.15. Six key Pareto points including design variables and objective functions with results from actual CFD results and the metamodel predictions, for $\beta = 5^{\circ}$.

	D_1	D_2 (○)	D_3	C_DA	C_DA (CFD)	δ	$\frac{dc_N}{d\beta}A$	$\frac{dc_N}{d\beta}A$ (CFD)	δ
1	0.76	0.97	0.50	2.0462	2.0470	0.04%	4.7135	4.7164	0.06%
2	0.77	0.00	0.50	2.0580	2.0645	0.31%	4.6783	4.6898	0.25%
3	0.78	0.00	0.50	2.0853	2.0842	-0.05%	4.6755	4.6750	-0.01%
4	0.91	0.00	0.50	2.3897	2.3846	-0.21%	4.6755	4.6718	-0.08%
5	0.93	0.00	0.50	2.4492	2.4390	-0.42%	4.6466	4.6396	-0.15%
6	0.95	0.00	0.50	2.4915	2.4915	0.00%	4.6179	4.6208	0.06%

Table 6.16. Six key Pareto points including design variables and objective functions with results from actual CFD results and the metamodel predictions, for $\beta = 6^{\circ}$.

	D_1	D_2 (○)	D_3	C_DA	C_DA (CFD)	δ	$\frac{dc_N}{d\beta}A$	$\frac{dc_N}{d\beta}A$ (CFD)	δ
1	0.76	0.00	0.50	2.0745	2.0746	0.00%	4.4263	4.4086	0.40%
2	0.76	0.00	0.64	2.0812	2.0842	-0.15%	4.4245	4.4245	0.00%
3	0.84	0.00	0.50	2.2144	2.2228	-0.38%	4.4245	4.3429	1.84%
4	0.90	0.00	0.50	2.3579	2.3558	0.09%	4.3085	4.3228	-0.33%
5	0.93	0.00	0.50	2.4310	2.4287	0.09%	4.2482	4.1905	1.36%
6	0.95	0.00	0.50	2.4832	2.4832	0.00%	4.2100	4.2232	-0.31%

Table 6.17. Five key Pareto points including design variables and objective functions with results from actual CFD results and the metamodel predictions, for $\beta = 8^{\circ}$.

	D_1	D_2 (○)	D_3	C_DA	C_DA (CFD)	δ	$\frac{dc_N}{d\beta}A$	$\frac{dc_N}{d\beta}A$ (CFD)	δ
1	0.76	0.00	0.50	2.0114	2.0114	0.00%	3.3588	3.3623	-0.10%
2	0.83	0.00	0.50	2.1020	2.0986	0.16%	3.3115	3.2958	0.47%
3	0.90	0.00	0.50	2.2042	2.2106	-0.29%	3.2188	3.2161	0.08%
4	0.92	0.00	0.50	2.2559	2.2473	0.38%	3.1804	3.2001	-0.62%
5	0.95	0.00	0.50	2.3132	2.3132	0.00%	3.1477	3.1504	-0.09%

Fig. 6.30 also shows a close-up view of the predicted Pareto points (from the metamodel) compared with the five CFD data points and the actual Pareto front (in blue). The objective functions agree well between the two approaches and importantly, the design variables are the same for both.

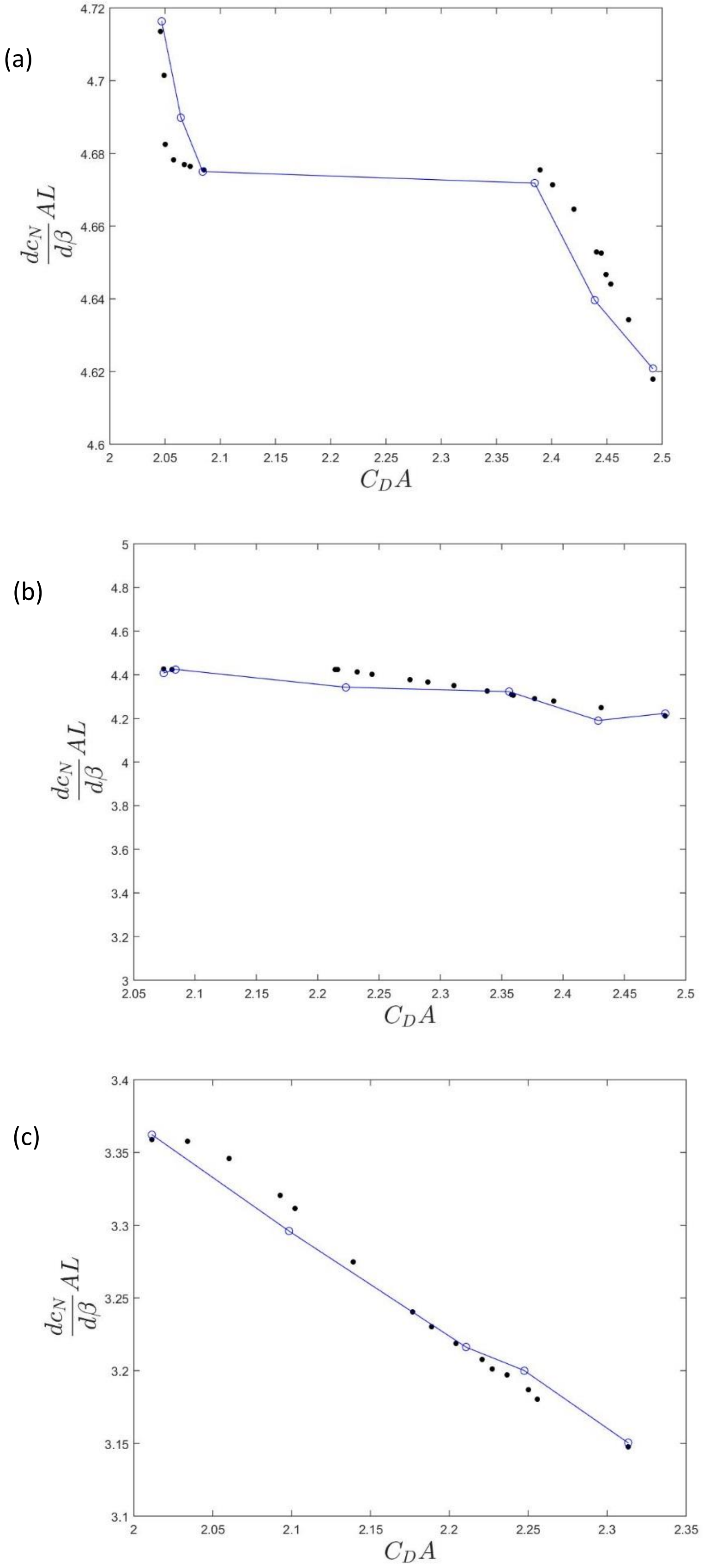

Fig. 6.30. Objective function plots showing the predicted Pareto front (black dots) from the metamodels and the actual Pareto front (blue circles and line) based on selected CFD results for (a) $\beta = 5^{\circ}$ (b) $\beta = 6^{\circ}$ and (c) $\beta = 8^{\circ}$.

What the Pareto fronts Table 6.14 show is that a compromise that must found when balancing low aerodynamic drag and greater yaw stability. It shows, for example, that achieving the best stability ($\frac{dc_N}{d\beta}$AL = 3.1477) design (P16), the drag increases by 15% compared to the minimum drag design (P1). Furthermore, the minimum drag design exhibits stability which is 6.3% worse than the best stability design. Ultimately, the most appropriate compromise depends on manufacturing requirements, operating costs and the functionality requirements HGV manufacturers and operators.

Although the overall quantitative data is conclusive, it is important to understand why these five Pareto optimum designs are better. Therefore, evidence was obtained from CFD postprocessing to show a comparison of flow fields between the baseline (rescaled GTS) design and the five optimum HGV shapes. As was explained in the literature review, the flow structure directly impacts aerodynamic drag and indeed all other forces and moments acting on the body of the vehicle. Accordingly, Fig. 6.31and Fig. 6.32 show comparisons of the wake structure for each of the 5 Pareto points for the β = 8 ° cases. Fig. 6.32 reveals that the flow structure in the wake looks broadly similar for all five Pareto optimum designs and it is clear that in all cases the side wind distorts the structure of wake of the model, skewing it to the right . Although the baseline design is not shown in Fig. 6.32, the results show that making the base area smaller leads to a smaller wake size which is consistent with, for example, Khalighi (2012).

In terms of velocity magnitude along the centreline of the HGVs, Fig. 6.31 shows a comparison of the baseline model with the five Pareto optimal designs. It is apparent that the area of lowest velocity (blue region) is smaller for the Pareto optimal designs and the wakes are generally shorter than that of the baseline because the height of the HGV is smaller. In all cases, the wake has two distinct longitudinal regions which occurs because there are two trailing vortices, one at the lower longitudinal edge and another at the upper one, along the trailer. This observation agrees with Krajnovic & Davidson (2003) who investigated the time-averaged wake behind a bluff vehicle, identifying these two distinct vortex structures (recall section 3.2.1).

Observing how the design changes moving down, Fig. 6.31, it is clear that the side profile of the HGV changes so that there is more side area at the rear of the vehicle, which coincides with improved yaw stability. This was observed in section 6.2.2 (single-objective optimisation) where it was found that increasing the side area at the rear, introduces more of a counteracting yawing moment to prevent a side wind moving the vehicle away from the wind direction. It was explained in section 2.8.3 that the stability of streamlined shapes with a large tail is better than a bluff vehicle. It follows, therefore, that a larger rear area on the HGV acts in the same way as a tail fin does on an aircraft from the weathercock stability principle (Anderson, 2011). This is a very important observation in the context of this thesis.

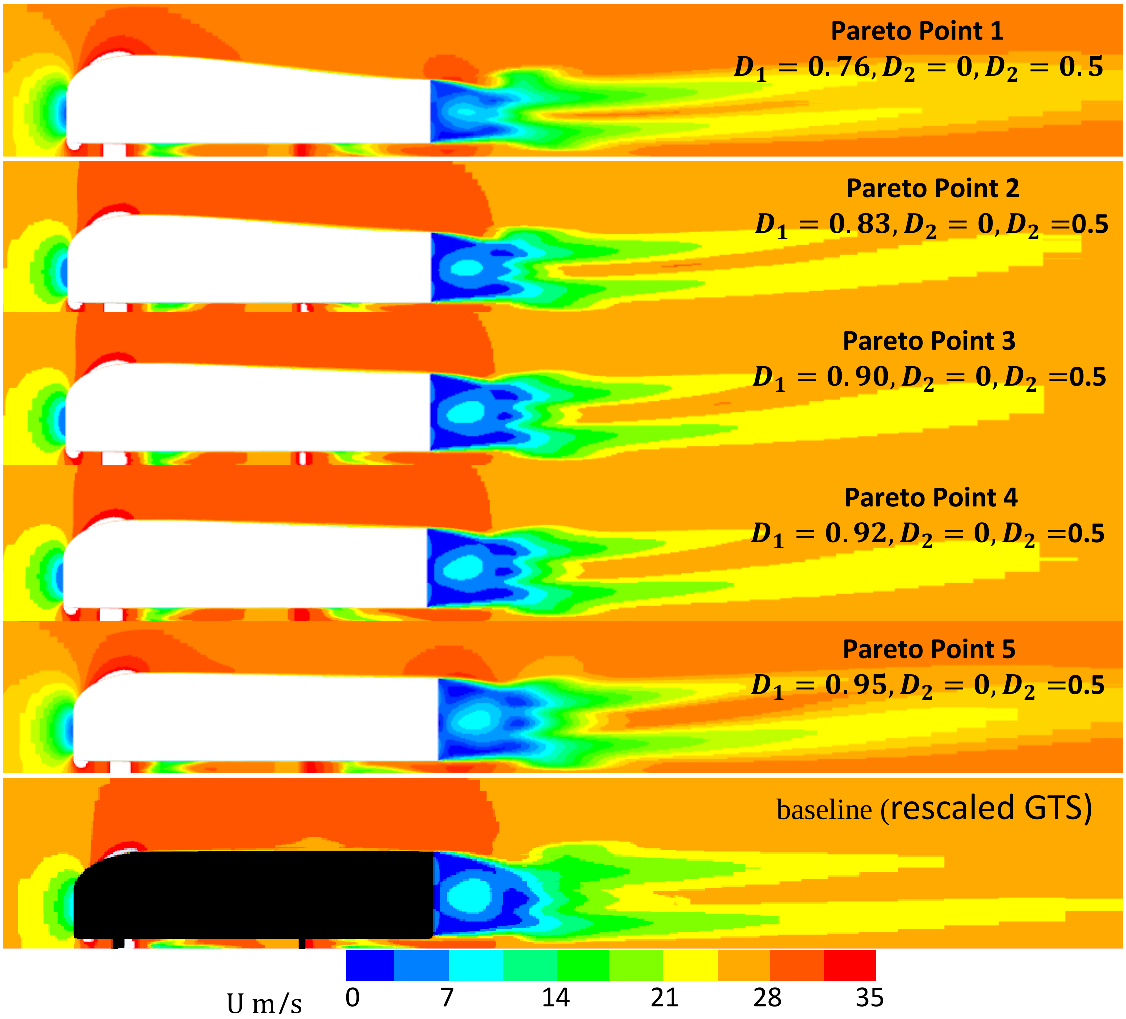

Fig. 6.31. Comparison of velocity magnitude contours on the central longitudinal axis for the baseline design (Roy et al.) and all five Pareto optimal designs, for $\beta = 8^{\circ}$

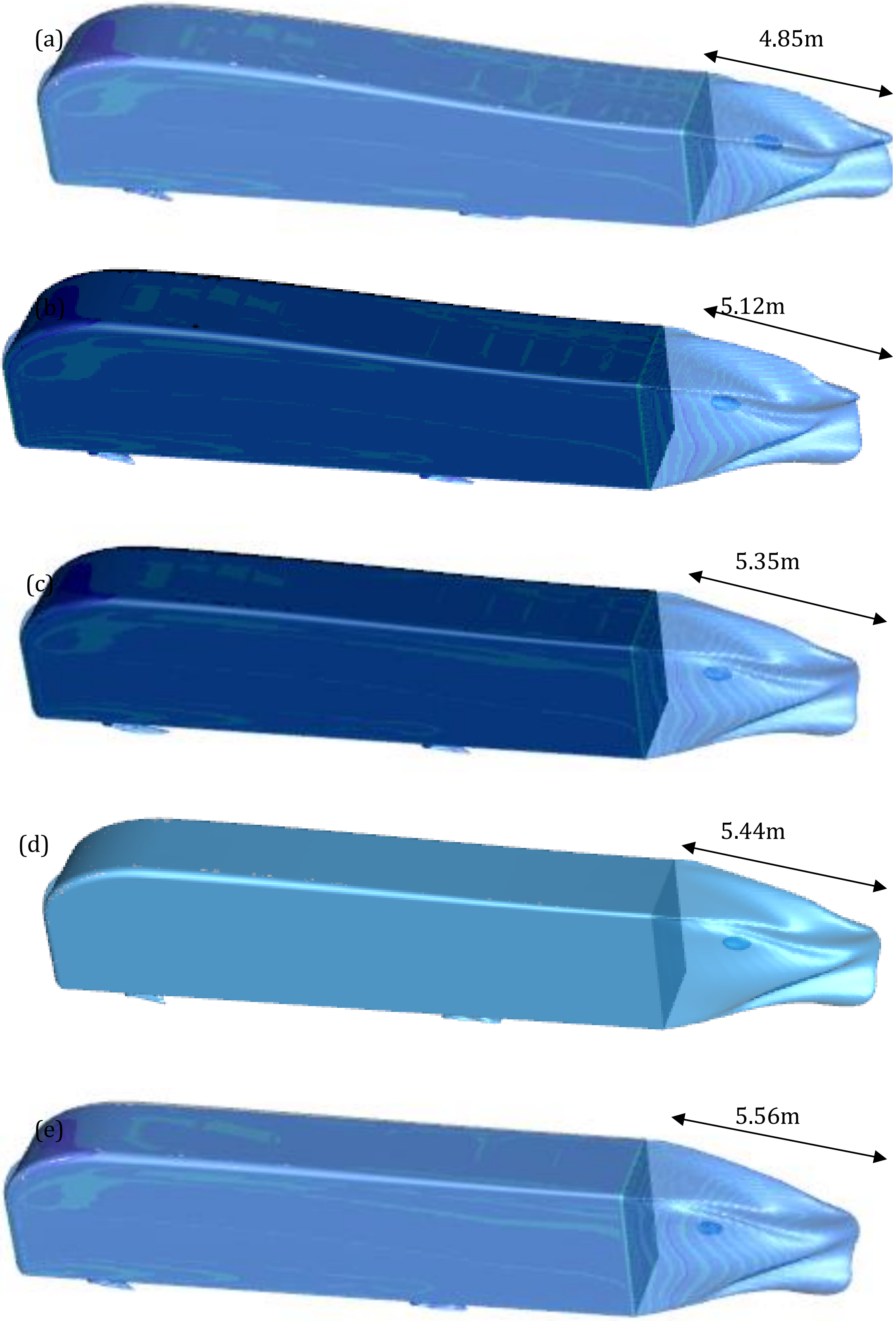

Fig. 6.32. Illustration of the wake structure for (a) the minimum-drag design, (b)-(d) Pareto points 2-4 and (e) the best stability design, for $\beta = 5^{\circ}$

6.3.2 Multi-objective optimization for C_DA and C_YA

The next multi-objective formulation is to compare C_DA (a measure of energy efficiency) with the side force coefficient area, C_YA (another measure of stability). The same approach as in section 6.3.1 was adopted to produce a predicted Pareto front of the two objective functions including all available CFD data. These are shown in Fig. 6.33 with a Pareto front constructed for each of the yaw angles of $\beta = 5^{\circ}, 6^{\circ}, 8^{\circ}$. The overall trend is that all of the designs show an improvement in both objective functions, compared to the baseline design which is shown by the blue square in the top right of each figure. An obvious difference though is that the range of drag area values along the Pareto front is much smaller in this multi-objective optimisation, compared to the last one. The trends are very similar for each of the three yaw angles tested.

It is important to remember that each Pareto front presented Fig. 6.33 (red circles) is not based on CFD data, but from the metamodel prediction, however, all other data points are based on CFD results. As previously, if minimum C_DA is favoured, the right-hand side of the Pareto front is the best location, whereas the lift-hand side is better for minimum-C_YA.

Table 6.18 shows 17 individual designs obtained from the predicted Pareto front in Fig. 6.33(a) for the $\beta = 5^{\circ}$ case. As before, each of these points is constructed from the metamodels which predict the combination of design variables and the expected objective functions (in this case C_DA and C_YA), per design. Point 1 represents the minimum drag design and point 16 is the best stability design (low C_YA) (recall section 6.2.3).

It is clear that the 17 points share the same minimum base height, D_1 and the rear angle of the roof profile at the base, D_2 is small and less than 1° in all cases. Interestingly, moving down the table, the metamodels predict that the side edge radius, D_3 is the dominant design variable to change the HGV design from minimum drag area to minimum side force area. The same trends are seen for the other slip angle cases of $\beta = 6^{\circ}$ and $\beta = 8^{\circ}$, see Table 6.19 and Table 6.20.

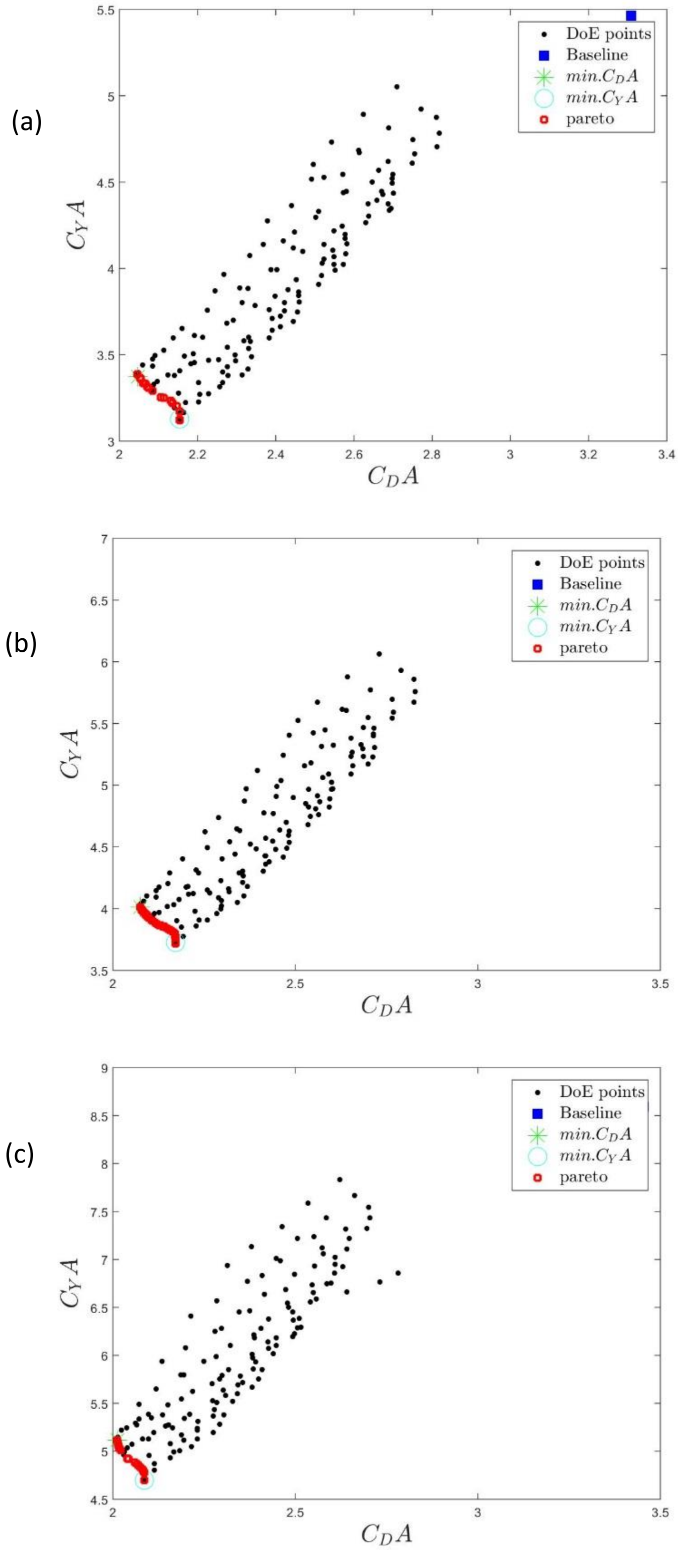

Fig. 6.33. Objective function plot showing the CFD results of the drag coefficient area, C_DA, as a function of the side force coefficient area, C_YA, for (a) β = 5°, (b) β = 6° and (c) β = 8°.

Table 6.18 Seventeen points on the predicted Pareto front, with expected design variables and objectives functions predicted by the metamodels, for the $\beta = 5^{\circ}$.

	D_1	D_2	D_3	C_DA	C_YA
1	0.76	0.97	0.50	2.0462	3.3852
2	0.76	0.26	0.56	2.0534	3.3675
3	0.76	0.87	0.63	2.0550	3.3590
4	0.76	0.40	0.72	2.0616	3.3351
5	0.76	0.96	0.80	2.0669	3.3320
6	0.76	0.46	0.85	2.0719	3.3143
7	0.76	0.38	0.88	2.0743	3.3078
8	0.76	0.44	1.00	2.0847	3.2904
9	0.76	0.13	1.20	2.1063	3.2534
10	0.76	0.44	1.27	2.1143	3.2500
11	0.76	0.28	1.39	2.1322	3.2329
12	0.76	0.09	1.46	2.1370	3.2183
13	0.76	0.01	1.58	2.1463	3.2042
14	0.76	0.00	1.88	2.1542	3.1709
15	0.76	0.15	2.50	2.1543	3.1241
16	0.76	0.00	2.50	2.1543	3.1221
17	0.76	0.00	2.50	2.1543	3.1221

Table 6.19 Seventeen points on the predicted Pareto front, with expected design variables and objectives functions predicted by the metamodels, for the $\beta = 6^{\circ}$.

	D_1	D_2	D_3	C_DA	C_YA
1	0.76	0.00	0.50	2.0745	4.0137
2	0.76	0.00	0.63	2.0806	3.9827
3	0.76	0.00	0.67	2.0829	3.9727
4	0.76	0.00	0.78	2.0894	3.9491
5	0.76	0.27	0.86	2.0954	3.9388
6	0.76	0.01	1.00	2.1065	3.9038
7	0.76	0.09	1.03	2.1089	3.9007
8	0.76	0.04	1.11	2.1167	3.8848
9	0.76	0.03	1.16	2.1216	3.8759
10	0.76	0.01	1.24	2.1310	3.8627
11	0.76	0.00	1.29	2.1389	3.8538
12	0.76	0.06	1.47	2.1578	3.8281
13	0.76	0.02	1.53	2.1619	3.8190
14	0.76	0.25	1.72	2.1696	3.7993
15	0.76	0.00	1.94	2.1722	3.7680
16	0.76	0.00	2.50	2.1722	3.7173
17	0.76	0.00	2.50	2.1722	3.7173

Table 6.20 fifteen points on the predicted Pareto front, with expected design variables and objectives functions predicted by the metamodels, for the $\beta = 8^{\circ}$.

	D_1	D_2	D_3	C_DA	C_YA
1	0.76	0.00	0.50	2.0114	5.1178
2	0.76	0.00	0.58	2.0130	5.0873
3	0.76	0.00	0.66	2.0147	5.0613
4	0.76	0.00	0.75	2.0175	5.0352
5	0.76	0.00	0.83	2.0219	5.0130
6	0.76	0.00	1.15	2.0394	4.9286
7	0.76	0.00	1.19	2.0429	4.9177
8	0.76	0.00	1.36	2.0599	4.8820
9	0.76	0.00	1.45	2.0669	4.8634
10	0.76	0.00	1.54	2.0725	4.8475
11	0.76	0.00	1.67	2.0784	4.8244
12	0.76	0.00	1.81	2.0829	4.8018
13	0.76	0.00	1.90	2.0854	4.7859
14	0.76	0.00	1.95	2.0864	4.7789
15	0.76	0.00	2.50	2.0864	4.7015

The Pareto fronts show that a compromise must found when balancing low aerodynamic drag and reduced side force. It shows, for example, that achieving the best stability using this parameter (C_YA = 4.7015, design P15), the drag increases by 3.7% compared to the minimum drag design (P1). Furthermore, the minimum drag design exhibits stability which is 8.1% worse than the best stability design. Again, the most appropriate compromise depends on the requirements of HGV manufacturers and operators. As already explained, the dominant parameter in the transformation from minimum-C_DA to minimum-C_YA is the side edge radius which increases from its minimum value (minimum-C_DA design) to the maximum value (minimum-C_YA) in the design space. Observing the flow fields, was clear that as this radius increases, the extent of the high-pressure (stagnation) area reduces on the windward side, and the pressure also slightly increases on the leeward side of the vehicle; these effects lead to the small but notable improvement in side force stability.

6.3.3 Multi-objective optimisation for C_DA and C_NAL

Fig. 6.34 shows the objective function plots for C_DA and C_NAL. Unsurprisingly, these plots look similar to those from Fig. 6.29 which was the first multi-objective optimisation and this also depended on the yawing moment coefficient, C_N. As was seen in section 6.3.1, all of the designs show a significant improvement in terms of drag, compared to the baseline design, however, in terms of stability, all of the designs are poorer.

Using the same method as before, tables were produced to show the different designs on the Pareto front. Only one table is presented, Table 6.21, for the 5° slip angle case, but the others were very similar. The same trends as section 6.3.1 are seen i.e. moving from the minimum-C_DA (P1) to minimum-C_NAL design (P17), the height of the vehicle increases from its minimum to the maximum value. All Pareto designs share the minimum side edge radius, D_3, and a very small rear angle at the rear, D_2, which is zero for most cases and no greater than 1° for any single design.

Results for the 8° slip angle case (table not shown) that achieving the best stability (C_NAL=33.5576) design is at the expense of a 15% drag increase, compared to the minimum drag design. Conversely, the minimum drag design exhibits stability which is only 2.7% worse than the minimum-C_NAL design.

(a)

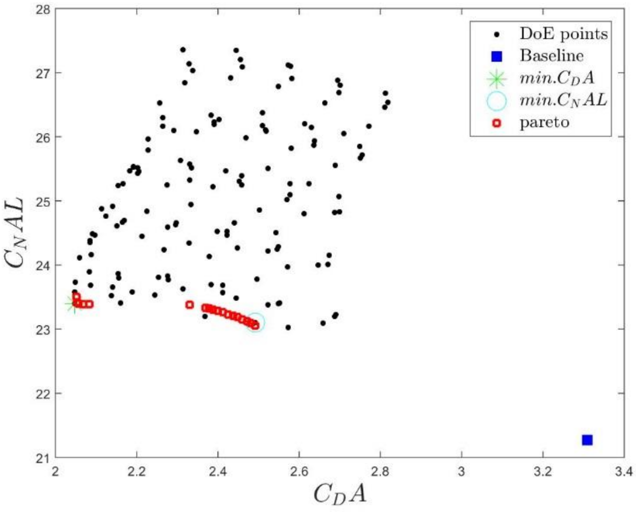

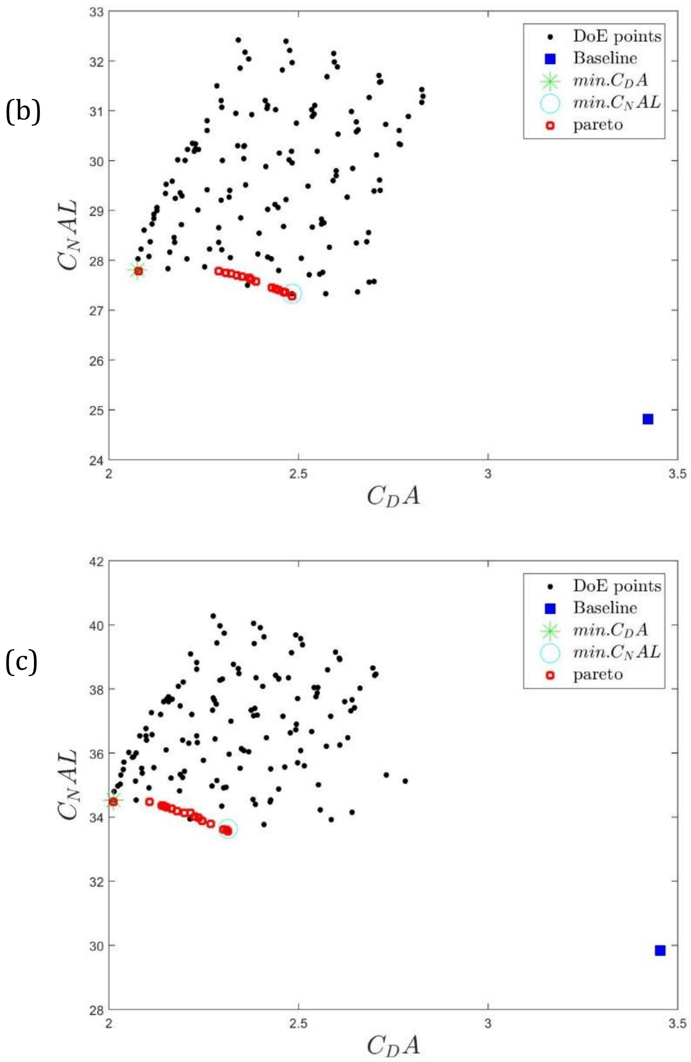

Fig. 6.34. Objective function plot showing the CFD results of the drag coefficient area, C_DA, as a function of the yawing moment coefficient area, C_NA for (a) $\beta = 5^\circ$(b) $\beta = 6^\circ$and (c) $\beta = 8^\circ$.

Table 6.21 Seventeen points on the predicted Pareto front, with expected design variables and objectives functions predicted by the metamodels, for the $\beta = 5^\circ$.

	D_1	D_2	D_3	C_DA	ABS(C_NAL)
1	0.76	0.96	0.50	2.0463	23.5614
2	0.76	0.17	0.50	2.0480	23.4192
3	0.77	0.20	0.50	2.0601	23.4172
4	0.78	0.00	0.50	2.0763	23.3807
5	0.88	0.00	0.50	2.3195	23.3805
6	0.89	0.00	0.50	2.3226	23.3776
7	0.89	0.00	0.50	2.3463	23.3514
8	0.90	0.00	0.50	2.3644	23.3270
9	0.90	0.00	0.50	2.3734	23.3136
10	0.91	0.00	0.50	2.3867	23.2917
11	0.92	0.06	0.50	2.4098	23.2608
12	0.92	0.00	0.50	2.4123	23.2443

13	0.93	0.00	0.50	2.4331	23.2003
14	0.93	0.00	0.50	2.4427	23.1783
15	0.94	0.00	0.50	2.4748	23.0976
16	0.95	0.00	0.50	2.4862	23.0669
17	0.95	0.00	0.50	2.4915	23.0518

6.3.4 **Multi-objective optimization for C_DA and $|C_RAL|$**

The final multi-objective consideration is the compromise between minimum drag and minimum absolute rolling moment $|C_RAL|$. Using the same method as before, Fig. 6.35 shows these objective functions at the three yaw angles considered. All of the designs show an improvement in terms of drag and $|C_RAL|$ compared to the baseline design, for all yaw angles.

Table 6.22 shows 16 individual designs obtained from the predicted Pareto front in Fig. 6.35 (a) for the β = 5° case. Each of these points is constructed from the metamodels which predict the combination of design variables and the expected objective functions (C_DA and $|C_RAL|$), per design. Point 1 represents the minimum drag design and point 16 is the best stability design (based on $|C_RAL|$). In this case the family of designs on the Pareto front both share practically same minimum the side edge radius, D_3. Moving down the table from point 1 to 16, the metamodels predict that both base height, D_1 and the rear angle of the roof profile at the base, D_2 and will increase as the design changes from minimum-C_DA (P1) to the minimum-$|C_RAL|$ design (P16). Very similar trends are seen for the other slip angle cases of β = 6° and β = 8° in Table 6.23 and Table 6.24, respectively, however, the side edge radius is a bit higher in some cases.

(a)

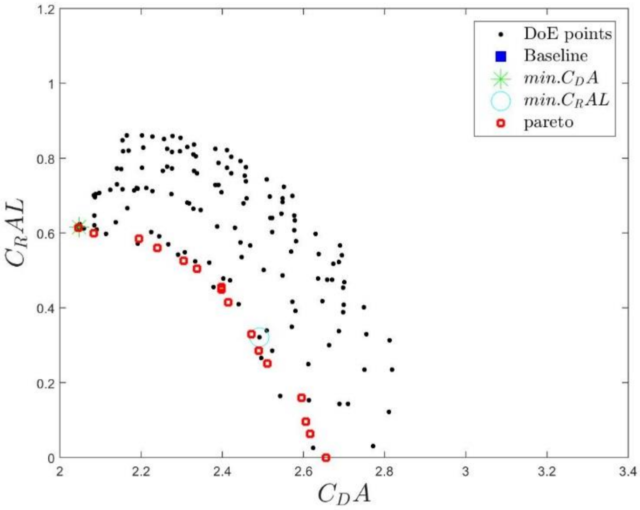

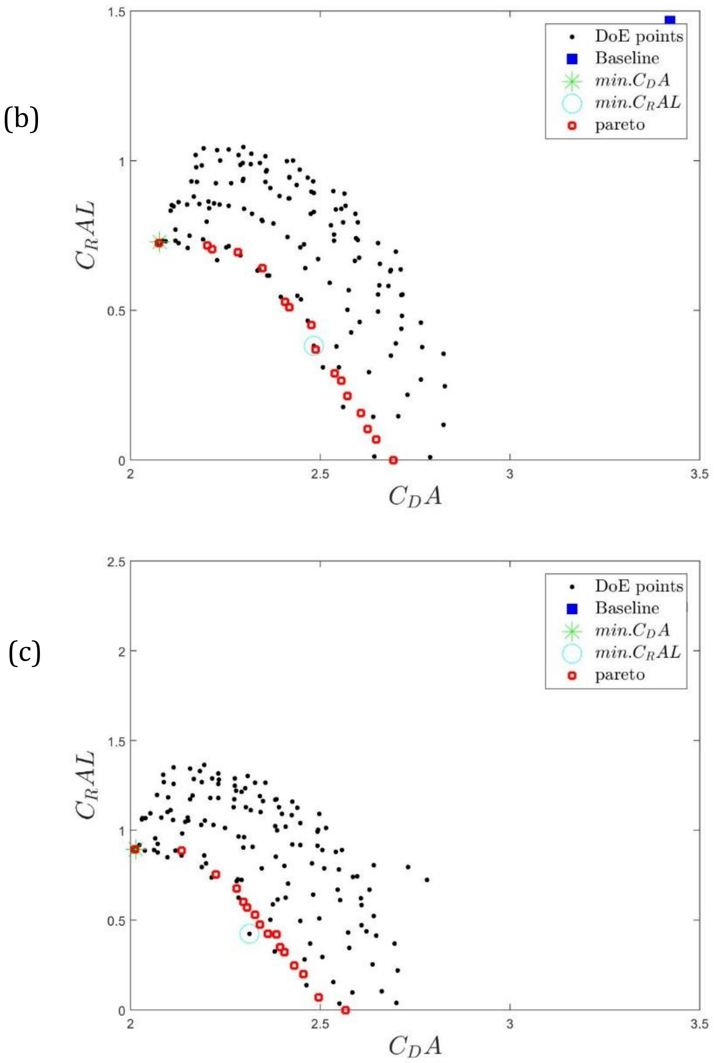

Fig. 6.35. Objective function plot showing the CFD results of the drag coefficient area, C_DA, as a function of the rolling moment area, C_RAL for (a) $\beta = 5^\circ$, (b)$\beta = 6^\circ$and (c) $\beta = 8^\circ$.

Table 6.22 Sixteen points on the predicted Pareto front, with expected design variables and objectives functions predicted by the metamodels, for $\beta = 5^\circ$.

	D_1	D_2	D_3	C_DA	ABS(C_RAL)
1	0.76	0.97	0.50	2.0462	0.6141
2	0.78	1.81	0.50	2.0841	0.5988
3	0.83	1.81	0.52	2.1942	0.5849
4	0.84	3.53	0.51	2.2408	0.5600
5	0.86	5.23	0.50	2.3046	0.5253
6	0.89	2.01	0.50	2.3380	0.5044
7	0.88	7.23	0.52	2.3976	0.4560
8	0.89	6.52	0.52	2.3989	0.4493
9	0.90	5.37	0.52	2.4154	0.4137
10	0.92	6.56	0.52	2.4725	0.3296
11	0.93	5.97	0.52	2.4904	0.2858
12	0.94	6.82	0.52	2.5109	0.2503

13	0.92	11.56	0.54	2.5947	0.1594
14	0.94	10.53	0.52	2.6056	0.0955
15	0.95	10.46	0.52	2.6161	0.0623
16	0.95	12.01	0.54	2.6559	0.0000

Table 6.23 Sixteen points on the predicted Pareto front, with expected design variables and objectives functions predicted by the metamodels, for $\beta = 6^{\circ}$.

	D_1	D_2	D_3	C_DA	ABS(C_RAL)
1	0.76	0.00	0.50	2.0745	0.7237
2	0.78	7.50	0.50	2.2025	0.7173
3	0.77	8.63	0.50	2.2159	0.7047
4	0.86	1.05	0.50	2.2825	0.6935
5	0.82	9.47	0.51	2.3476	0.6408
6	0.91	3.18	0.50	2.4069	0.5292
7	0.92	2.91	0.51	2.4187	0.5094
8	0.92	5.74	0.57	2.4759	0.4497
9	0.93	4.67	0.52	2.4881	0.3682
10	0.94	6.85	0.56	2.5379	0.2897
11	0.94	7.66	0.57	2.5561	0.2640
12	0.93	8.74	0.53	2.5721	0.2141
13	0.93	10.62	0.52	2.6071	0.1570
14	0.94	10.66	0.53	2.6248	0.1034
15	0.93	12.17	0.52	2.6473	0.0681
16	0.94	13.02	0.60	2.6929	0.0000
17	0.94	13.02	0.60	2.6929	0.0000

Table 6.24 Sixteen points on the predicted Pareto front, with expected design variables and objectives functions predicted by the metamodels, for $\beta = 8^{\circ}$.

	D_1	D_2	D_3	C_DA	ABS(C_RAL)
1	0.76	0.00	0.50	2.0114	0.8951
2	0.84	1.51	0.51	2.1339	0.8873
3	0.88	2.73	0.50	2.2254	0.7545
4	0.92	0.96	0.64	2.2804	0.6745
5	0.93	1.16	0.60	2.2975	0.6023
6	0.93	1.56	0.59	2.3074	0.5694
7	0.93	2.79	0.57	2.3281	0.5308
8	0.93	3.97	0.51	2.3415	0.4766
9	0.94	3.66	0.55	2.3623	0.4237
10	0.94	4.37	0.62	2.3847	0.4198
11	0.93	5.48	0.51	2.3945	0.3497

12	0.94	5.78	0.51	2.4054	0.3216
13	0.94	6.73	0.50	2.4316	0.2482
14	0.94	7.82	0.53	2.4559	0.1998
15	0.94	9.56	0.53	2.4962	0.0703
16	0.94	11.62	0.73	2.5667	0.0000

The Pareto fronts reveal that a compromise must be found when balancing low aerodynamic drag and greater Rolling stability. For the high yaw angle cases, for example, achieving the best stability design (P16) is at the expense of a 30% drag increase, compared to the minimum drag design (P1).

6.4 **Engineering Insight and Over-body Design Guidance**

The final research objective of this thesis (objective 6) is to take the results from the optimisation studies and understand how the insights can be used to help the design of overall HGV shapes. Of course, these insights relate to the over-body design parameterisation developed in this thesis, however, the range of designs tested exceeds the relatively simple range of shapes seen on our roads. It is hoped that some design universality can be achieved from these findings.

6.4.1 **Drag vs Yaw Stability**

As explained in section 6.3.1, probably the most important relationship is the one between minimum aerodynamic drag and the best yaw stability. Although the yawing moment, C_N, is an objective function in its own right, the yawing moment-slip angle derivative parameter, $\frac{dc_N}{d\beta}AL$, accounts for the change in C_N with respect to yaw angle, so it is a more sophisticated stability parameter because it encompasses more information. To reiterate what was explained in section 6.3.1, the design trends actually remain the same, irrespective of the yaw angle studied, whether 5°, 6° or 8°. Furthermore, from the work carried out on the Leeds-London motorway journey analysis (Chapter 5), it is expected that considering yaw angles of up to 8° (as was done in this thesis) is representative of 45.5% of a typical journey. Therefore, analysing how C_DA and $\frac{dc_N}{d\beta}AL$ vary in response to design variable changes, should provide a good approximation of the operation (energy vs stability) of over-body designs. This relationship is shown in Fig. 6.36.

The trends shown in Fig. 6.36 are based on the metamodels, which themselves are based on over 138 CFD solutions. Looking at each design variable one at a time, recall that D_1 is the height of the rear of the HGV, D_2 is the angle of the base of the roof section and D_3 is the radius of the upper side edge. As has already been shown, by far the most influential parameter is the height of the rear of the HGV. In simple terms, the lowest height leads to the minimum drag within the design space considered, whereas the greatest allowable height improves yaw (weathercock) stability by virtue of the increased side area at the rear of the vehicle. Although the yaw stability for the optimum design was found to be inferior to the baseline design, this was largely because the parameterisation limited the height of the generic HGV to be no greater than 95% of the baseline vehicle height. When selecting the most appropriate rear height, a compromise must be reached, depending on the relative importance of reducing aerodynamic drag (and thus energy) and improving stability (driver comfort and safety).

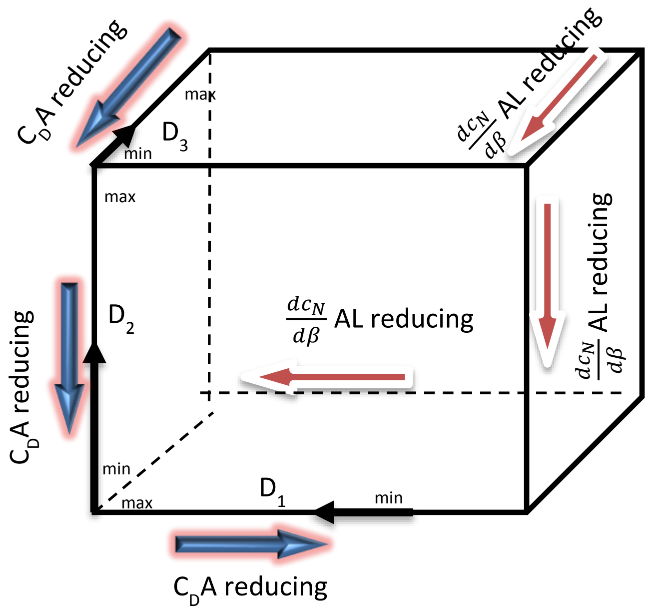

Fig. 6.36. Illustration of the design space, showing how changes in the design variables affect the objective functions of aerodynamic drag and yaw stability.

Moving onto the other two design variables, as the values of both D_2 and D_3 decrease, both aerodynamic drag and yaw stability improves. Therefore, from these results, a suitable design rule is to minimise the angle of the base of the HGV, D_2, as much as possible to 0˚ (horizontal roof), interestingly, this is in contrast to the approach taken by curved over-body designs currently on the UK transport network (recall chapter 1). It follows that another suitable design rule is to minimise the radius of the upper side edge curvature as much as possible. It is important to note that the minimum radius considered in this investigation was $0.5R_0$ where R_0=0.228m so the radius of the upper side edge curvature is recommended to be no greater than 0.114m. Whether the trend would continue for even smaller values has not been proven in this investigation. Vehicle stability improves by decreasing the radius of the upper side edges because significant rounding of these creates a low-pressure region over the leeward-facing radiused surface to assist with weathercock stability, i.e. turning the vehicle towards the wind direction.

In the work shown in section 6.3.1, five Pareto optimal designs were identified, representing a family of generic HGV designs exhibiting various compromised between low aerodynamic drag and improvements in yaw stability. Based on these, the following design guidance is proposed:

1. If low aerodynamic drag and improved stability are both sought, the angle of the base of the HGV should be flat (0˚) and the radius of the upper side edge should be

as low as possible, with a practical lower limit being around 0.1m. The height of the rear of the vehicle should probably be in the middle of the range 3.46 – 4.33m.

2. If low aerodynamic drag is sought from an over-body design, the following is recommended:
    a. HGV trailer units should have as a low a rear height as possible, with a practical lower limit being around 3.46m.
    b. The top of the vehicle should be shaped so that it is convex over the front half of the vehicle, morphing into a concave shape until it becomes flat immediately upstream of the base region.
    c. The radius of curvature of the longitudinal side edges of the over-body profile should be small.
    d. An improvement in drag of 40% is possible, compared to a baseline vehicle with a completely flat over-body, however, yaw stability is 11% poorer at a slip angle of 5° increasing to 35%, at 8°.
3. If improvements in yaw stability are required, the following suggestions are recommended:
    a. The top of the vehicle should be shaped so that it is convex over the front half of the vehicle until it becomes flat immediately upstream of the base region; this maximises the rear side area which assists with yaw stability.
    b. The base height should be around 4.33m, based on the parametrisation explored in this investigation, however, increasing this further towards the maximum allowable limit of 4.9m would likely lead to better yaw stability, at the expense of increased drag.
    c. The radius of curvature of the longitudinal side edges of the over-body profile should be small.
    d. These guidelines lead to the best yaw stability in the design space, however it is still 8% poorer than the baseline at 5° of yaw and 25% worse at 8°.
    e. An improvement in drag of 33% is possible, compared to a baseline (rectangular) vehicle.

To summarise, Fig. 6.37 shows the side profile of the minimum drag and maximum stability designs and Fig. 6.38 shows a 3D comparison of these, to illustrate the differences in side-edge curvature. Profiles in between these two shapes (refer to section 6.3.1) will provide a compromise between the two designs presented. The design parameters for three intermediate designs presented in Table 6.17 can be referred to, with expected drag and stability quantified.

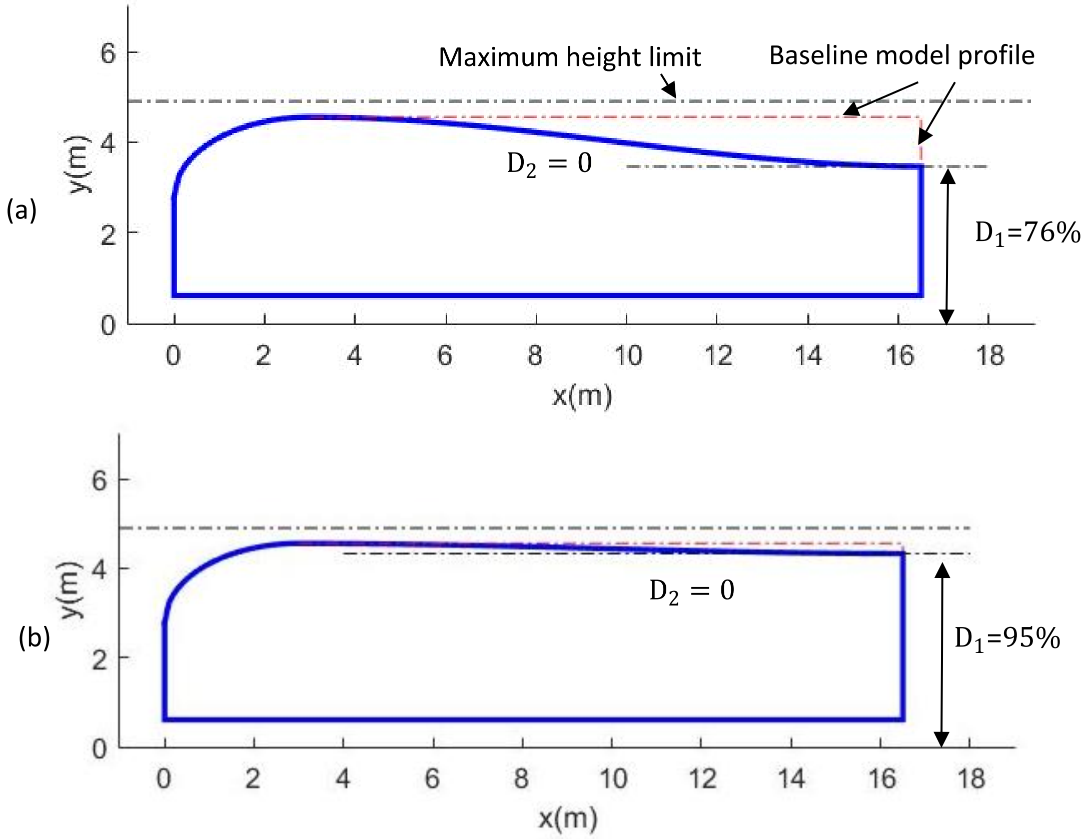

Fig. 6.37. Illustration showing the difference in side profile of (a) minimum drag and (b) maximum stability designs.

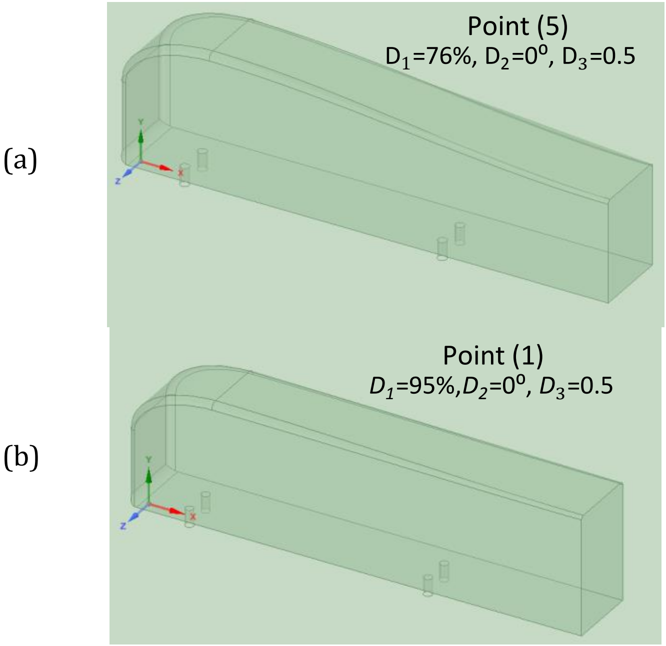

Fig. 6.38. Illustration showing the difference in 3D appearance of (a) minimum drag and (b) maximum stability designs viewed from the rear.

6.4.2 **Other Design Considerations**

The design guidance in the previous section is an important contribution to knowledge and these are the most important aspects of this work. However, the nature of the metamodels means that other design trends can be seen by making different comparisons. Fig. 6.39 shows how different locations in the design space affect drag and the yawing moment area parameter. This relationship is exactly the same as the one in section 6.4.1. Both drag and the yawing moment area require a low a value for both D_2, the angle of the base of the HGV, and D_3, the radius of the upper side edge curvature. The base height, D_1, leads to an inverse relationship in the two objective functions; drag rises but the yawing moment area decreases (increasing the stability). Therefore, the design guidance in section 6.4.1 still applies.

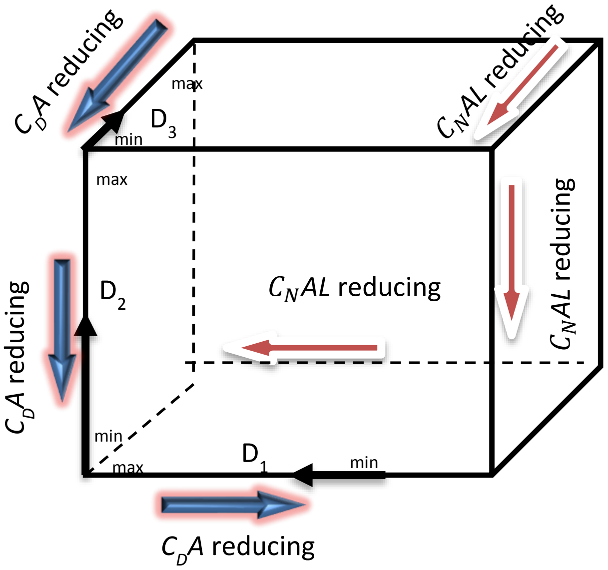

Fig. 6.39. Illustration of the design space, showing how changes in the design variables affect the objective functions of aerodynamic drag and yawing moment area.

Another exploration of the design space with aerodynamic drag and side force area is presented in Fig. 6.40. This shows how different locations in the design space affect drag and the side force area parameter. In this relationship, both drag and side force area require a small base height and a small base angle of the over-body of the HGV. The dominant parameter is the radius of the upper side edges; if it is small, drag is less, if it is large, stability is improved in another inverse relationship.

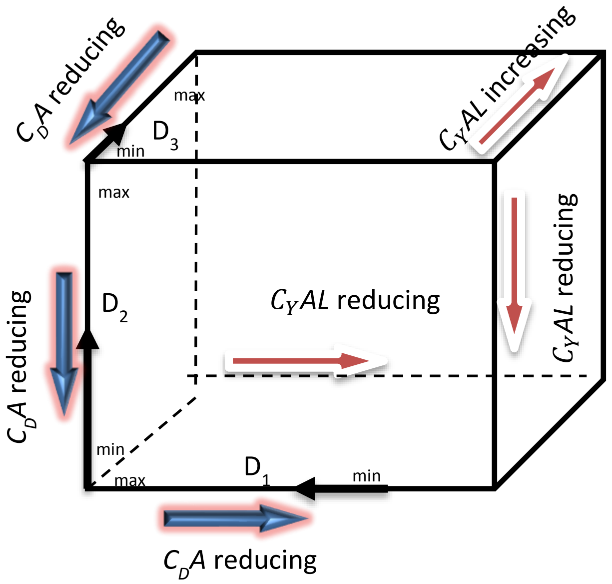

Fig. 6.40. Illustration of the design space, showing how changes in the design variables affect the objective functions of aerodynamic drag and side force area.

One final exploration of the design space is for aerodynamic drag and rolling moment area, as presented in Fig. 6.41. It shows how different locations in the design space affect drag and the rolling moment area parameter. In this relationship, both drag and rolling moment require low a value for, (*D*$_3$), the radius of the upper side edge curvature. whereas increases in the other two design variables, (*D*$_1$) and (*D*$_2$), leads to the inverse relationship in the two objective functions; drag rises but rolling moment area decreases (increasing the stability).

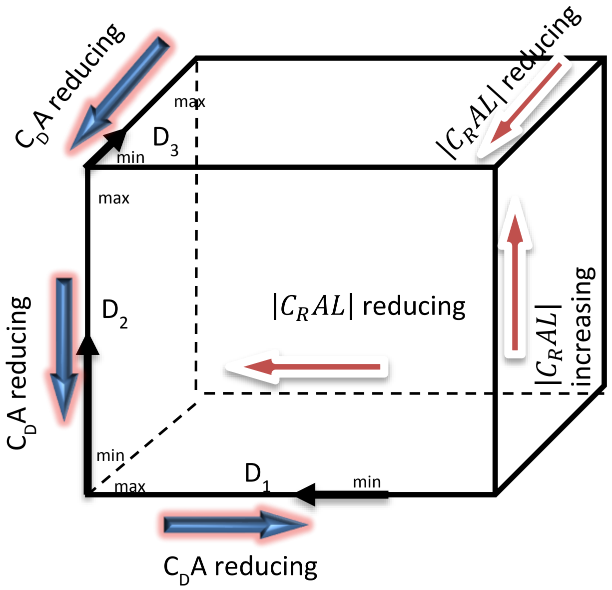

Fig. 6.41. Illustration of the design space, showing how changes in the design variables affect the objective functions of aerodynamic drag and rolling moment area.

6.5 **Summary**

To sum up the observations in this important section of the thesis, Table 6.25 shows the relationship between the three design variables and all five objective functions. As each of the design variables is reduced (within the ranges set out in section 6.1.1), the impact on the aerodynamic forces, moments and stability parameters of interest is clear to see that, for example, the C_DA and C_YA are decreasing as the first design variable decreases. The findings in Section 6.4.1 give more focused guidance on the relationship between HGV design and the impact on energy and stability, but Table 6.25 is a useful quick reference guide for the overall design sensitivities.

Table 6.25: Relationship between the three design variables and all five objective functions.

	C_DA	$\frac{dc_N}{d\beta}AL$	C_YA	$\lvert C_R\, AL\rvert$	C_NAL
D_1 ↓	↓	↑	↓	↑	↑
D_2 ↓	↓	↓	↓	↑	↓
D_3 ↓	↓	↓	↑	↓	↓

Chapter 7 : Discussion

7.1 Scope

The main focus of this PhD was to explore over-body (roof) curvature of generic HGVs using aerodynamic shape optimisation to form practical design recommendations. As explained in Chapter 1 and 2, many different solutions to minimise the aerodynamic drag on bluff road vehicles have been explored over many decades. The focus for HGVs has primarily been on cab reflectors, devices in the gap to trailer units and base region solutions (see e.g. Choi et a., 2014). However, to the authors knowledge, only the study by Holt et al. (2015) has systematically explored the concept of curving the over-body shape to provide aerodynamic benefits. This is despite the prevalence and variety of such designs currently on UK road networks (recall section 1.4). Another point is that literature on the aerodynamic design of HGVs tends to focus on drag reduction at a zero yaw angle and stability is often a secondary consideration, if it is even considered. Therefore, the purpose of this thesis was to minimise the aerodynamic drag of a generic HGV without negatively impacting the static stability at different yaw angles. The following sub-sections highlight some of the major discussion points of the work carried out.

7.2 Verification and validation

The vehicle used in this study was the Ground Transportation System (GTS) model which is representative of a generic European HGV and is broadly representative of those used in the UK. In order to develop an accurate numerical model to predict aerodynamic forces, a rigorous verification and validation (V&V) exercise was completed and detailed in Chapter 4. Here, three dimensional, isothermal, steady-state airflow simulations were performed using the finite volume solver, ANSYS Fluent (version 19.1). The double precision solver was used to minimise round-off error and simulations were run until residuals were completely flat, thereby eliminating convergence error.

Discretisation error was assessed from a detailed mesh independence study. It was found that a fully-structured mesh design produced better results than a hybrid one when simulating the aerodynamics of the GTS model. A "fine" mesh with a cell count of 8.7 million gave a satisfactory drag result with an over-prediction of 15% compared to the experimental results of Roy et al (2009), however, this prediction was better than the RANS prediction (also Roy et al., 2009). The drag prediction was even closer with an over-estimate of around 8% for a “finer” mesh (15.2 million cells), however, these simulations took much longer than the fine mesh, which had implications for the large number of simulations (around 700) conducted in later chapters. In any case, irrespective of the drag predictions, the pressure distributions produced by the fine mesh were very encouraging, often matching experimental data and out-performing the results from Roy et al (2009). Overall, results produced by the SST k-ω turbulence model were able to capture the salient features of the flow field, including massive flow separation, which is very important in this work. Two other turbulence models were evaluated as well, however, they gave inferior performance.

7.3 Influence of wind angle

In Chapter 5, some analysis on the influence on the wind angle for a typical journey was carried out. The route from Leeds to London along the M1 motorway was chosen as this is an essential haulage route in the UK. The analysis assumed that a typical HGV travelled the 315km from Leeds to London and back again, along the M1 which was calculated with 1000 points equally spaced points i.e. 0.315km apart. The prevailing background wind speed was assumed to be 3.5 m/s, in a south-westerly direction (Lapworth and McGregor, 2008) and the forward speed the HGV was assumed to be equal to the speed limit of 56 mph. Histograms of the resultant wind speed and direction allowed for the range of side-slip or wind angles, β, to be calculated.

Statistical analysis of the range of wind angles, which have a significant effect on aerodynamics and stability, showed that the mode average angle is 8° and this occurs for 45% of a typical journey, therefore, this angle is of significant interest. Furthermore, the mean wind angle was about to 6°. It should be noted that the study by Holt et al., (2015) showed that the behavior of drag reduction from vehicles with curved roof sections changes dramatically at around 5°. Therefore, a decision was made to study a wind angle of 5° as well as the aforementioned 6° and 8° in a subsequent design optimisation investigation. In most cases, the impact of the magnitude of the wind angle (i.e. 5°, 6° or 8°) did not significantly change the shape of the optimum designs, based on the results in Chapter 6. However, the wind angle is still an important consideration and it should be accounted for in future studies.

7.4 Parameterisation

As well as considering the range of expected wind angles, Chapter 5 also explored different shape parameterisations using the GTS model as a basic representation of a generic HGV.

For the first parameter, attention was focused on the two sharp longitudinal edges where the roof section meets the side panels. Normally, HGVs have rectangular cross-sections with no longitudinal edge radii running the length of the vehicle. It was postulated that the addition of radii on these roof-side-panel intersections may offer aerodynamic and/or stability benefits by minimising flow separation in the presence of side winds. Accordingly, a 3D parametric study for a range of wind angles was carried out. As expected, the rounding of sharp edges had an impact on the aerodynamic characteristics of the vehicle. Using the baseline radius of R_0=0.22792m from the forebody region of the GTS model, a number of different radii were tested in the presence of side winds. Analysis of the results identified the range of radii to be considered in the later optimisation study to vary from R=0.5R_0 to R=2.5R_0. This was considered a wide enough range of radii to find an optimum combination of design variables later.

As well as the radius of longitudinal edges, attention was focused on over-body contouring. Four different approaches were explored in 2D which included transplanting the upper surface of symmetrical NACA aerofoils onto the vehicle and integrating aerofoil shapes with cab sections. Though offering some benefits, these ideas did not allow much flexibility in design. This led to the idea of using a third-order polynomial to provide a range of over-body shapes including fully convex and convex-concave shapes, as well as seamlessly fitting to the front section of the baseline GTS model which is constructed from an ellipse in side view. Eventually, this method allowed two design parameters to be specified which determined the shape of the over-body. These were (a) the height of the rear of the trailer section and (b) the angle of the over-body at the trailing edge, with respect to the horizontal axis. Combining these two parameters with the side edge radii discussed above led to three design variables to be carried forward to a formal design optimisation study. Having this many design variables meant that a wide range of shapes could be explored without suffering the "curse of dimensionality" (Forrester et al., 2009) which implies that the design space is too large to adequately sample.

7.5 Optimisation

As already discussed, little attention has been paid to enhancing the design of HGVs to reduce drag whilst simultaneously improving vehicle stability, especially in challenging conditions such as in gusts or side winds. Therefore, the optimisation problem formulation was to identify potential designs for typical HGV concepts which minimise drag and maximise stability.

There is usually a physical upper limit for how large each given design variable can be (Gilkeson et al., 2013). The major physical constraint in this study was the maximum height limit for HGVs which must not exceed 4.9m (Butcher, 2009). Ultimately, this requirement meant that physical constraints had to be put on the design variables such that the maximum height of the rear of the HGV could not exceed 95% of the height of the baseline shape and the angle of the trailing edge had an upper limit of 14°. The rear height constraint had later implications for stability as will be discussed in the next section. In total, five objective functions were assessed including the drag coefficient area, C_DA, the gradient of the yawing moment coefficient, $\frac{dc_N}{d\beta}AL$, the side force coefficient area, C_YA, the rolling moment coefficient area, $|C_RAL|$ and the yawing moment coefficient area, C_NAL.

Moving Least Squares metamodels (Toropov et al., 2005) were constructed for each of these objective functions which were determined from CFD solutions. A 125-point full factorial Design of Experiments was used to set the design variables for each CFD solution. Each metamodel needed updating with extra data points because optimisation searches invariably highlighted new designs which needed evaluating. Individual metamodels were tuned to the dataset using Leave-One-Out Cross Validation (Loweth et al., 2011, De Boer et al., 2016). Overall, the metamodeling technique was very effective at finding the best designs for each objective function as well as for multi-objective problems whereby two different objectives were optimised to obtain Pareto optimal solutions.

In addition to finding optimum HGV designs, the metamodels were very effective at illustrating design sensitivities. For example, the height of the rear of the HGV needs to be small for low drag and larger for better static stability. This led to very encouraging drag predictions, however, weathercock stability was inferior to the baseline value.

Despite this, the design sensitivities in the relevant metmodel shows that further increases in vehicle height will eventually led to a high value of weathercock stability, compared to the baseline. However, as will be described in the next section, too much weathercock stability may potentially blow HGVs off the road, thereby reducing *vehicle* stability. If maximising weathercock stability is the objective, then the trade-off would be increased drag and of course further rear height increases would invalidate the current parametrisation, risking the vehicle exceeding the maximum height restriction. A potential solution for future work would be to introduce further design constraints so that the design space is not cubic and any given design would not violate height restrictions.

7.6 Design Guidance

Following the design optimisation searches, section 6.4 summarised the engineering insights from over 700 high-fidelity CFD simulations and design guidelines were suggested. Probably the most important relationship is the one between minimum aerodynamic drag and the best yaw stability. It was found that the smaller the rear height of the HGV is, the better the drag reduction. Within the design constraints of this problem, a potential drag reduction of around 40% may be possible and this is for a base height of 76% of the baseline value i.e. 3.46m. Conversely, the best yaw stability design was 8-25% inferior to the baseline value, depending on the yaw angle, however, it too exhibited excellent drag reduction of 33%.

This shows that the parameterisation is biased towards find low-drag designs with limited potential for finding better stability configurations. However, as already discussed, the design directions are clear if the trends in the metamodels can be extrapolated beyond the design space; this would provide a theme for future work.

7.7 Weathercock vs Directional Stability

Another aspect which warrants discussion here is the important distinction between vehicle directional stability and weathercock stability. In the present study the focus was purely on aerodynamics with aerodynamic drag and yaw (weathercock) stability being the main considerations. Consider a vehicle such as an HGV travelling along a straight section of road at a constant speed. Without a side wind, the vehicle will be directionally stable if there are no disturbances, however, if a side wind occurs then the manner in which the vehicle responds will determine how stable it is. In this thesis, the assumption has been that if the vehicle opposes the disturbance in yaw then it is stable i.e. the concept of static stability. As described above, the optimisation process identified a design which has the best yaw stability but this was significantly less than the baseline vehicle which has a greater concentration of side area at the rear. From this, it was determined that the baseline vehicle exhibits greater weathercock stability than the maximum-stability design. Therefore, from this point of view the maximum-stability design was less stable than the baseline.

However, whilst it is important to have a certain amount of static (weathercock) stability, if it is too high then it could cause the vehicle to align with the wind. If the weathercock effect is too great then it will cause the vehicle to align with the overall wind direction whereas vehicle directional stability aligns with the road direction. Clearly, a high level of weathercock stability is unwanted because this could prevent the vehicle from travelling in a straight line on the road. Therefore, in terms of vehicle directional stability, it is more beneficial to have a reduced value of weathercock stability, provided that the vehicle still opposes any side wind disturbances. It follows that the maximum stability design found in this thesis may in fact be a better design than the baseline both in terms of aerodynamic drag and yaw stability. To better quantify this, the interaction between the wheels and the road would need to be considered in future work to understand the optimum amount of yaw stability which is helpful for vehicle directional stability as well.

7.8 **Limitations, Future Work and Recommendations**

It is important to recognise the limitations of the work carried out in this thesis. Firstly, all simulations are based on a simplified vehicle i.e. the GTS model. This does not account for rotating wheels or the cab-trailer towing gap which is normally present on UK HGVs. Therefore, adding these details and others such as the undercarriage should be accounted for in future studies.

In terms of the simulation approach used in this thesis, every effort was made to increase accuracy from verification and validation (Chapter 4). A steady-state RANS-based approach was adopted which gave satisfactory results overall, but aerodynamic drag was over-predicted by 15%. Although pressure distributions were generally good, the accuracy of the method could be improved. This could be achieved by using a transient method such as LES or DES (e.g. Krajnovic and Davidson, 2003). Such methods provide greater accuracy and insight into the flow structure around bluff vehicles, accounting for phenomena such as vortex shedding. However, these accuracy improvements come with significant computational cost and so the balance between accuracy and speed of computation remains a challenge (Spalart, 2000).

The present research focussed on over-body curvature, however, it mainly modified the middle to rear section, with the front of the GTS model retained. It is known from literature that about 45% of the total drag force is generated at the front part of a typical tractor-trailer vehicle (Choi et a., 2014). Therefore, implementing another design method to extend along the whole side profile from front to rear, may realise greater benefits, particularly for yaw stability. A variation on this method may allow for studying the effect of combining a curved over-body roof profile with cab roof deflector or with other known drag reduction devices which have actually been adopted on the road. Looking forward, there are many potential research avenues for HGV shape design improvements.

An important point about the present study is that drag reduction for the minimum drag design was very high with a reduction of over 40% in some cases. The base region height was 24% smaller than the baseline value, which made the wake significantly smaller and it would be expected that the drag would be significantly smaller. However, without carrying out experimental validation on this shape, it is difficult to comment on how accurate this figure is. Certainly, the drag reduction is very promising but it does appear to be very optimistic and this would need to be investigated further. Having said this, as described in section 3.3.2, experimental studies into boat-tail devices have realised drag reduction of up to 50% (Choi et al., 2014, Yi et al., 2007), and the shape of the minimum drag design in this study has a very similar effect to the boat-tail philosophy; this adds some confidence to the drag reduction figure of 40%.

As already discussed, the best stability design showed the best performance of the shapes tested within the design space, but even this exhibited stability which is 8% worse than the baseline value at 5° of yaw, increasing to 24% worse at 8°. It is very important to appreciate that stability was evaluated assuming that the centre of gravity was in the geometric centre of the whole vehicle. This of course will vary considerably, depending on the load distribution of within a typical HGV and nature of load itself. If the centre of gravity shifts forward then yaw stability will be significantly better, whereas a rearward shift would have the opposite effect (e.g. Hucho, 1998). Therefore, in future, extending the problem to account for changes in centre of gravity position, as another design variable, may be worthwhile. Furthermore, it may be beneficial to investigate three-objective optimisation strategies (rather than two-objective) to identify if there is a design exhibiting the best compromise between different objectives such as drag, yaw stability and rolling stability, or others which may arise.

Finally, as outlined in section 7.7, the work carried out in this thesis did not account for the interaction between the wheels of the HGV and the road surface to determine vehicle direction stability. Instead, it only focussed on aerodynamics and stability considerations were essentially only based on static stability. In future, dynamic stability should be considered to ensure optimum vehicle directional stability and this may involve substantially more investigation.

7.9 Conclusion

This study explored design changes to a generic HGV to influence over-body shape with the aim of minimising aerodynamic drag and maximising static stability. The Ground Transportation System (Roy et al., 2006) was investigated in this thesis because it closely resembles a UK HGV. A commercial Computational Fluid Dynamics (CFD) package, ANSYS Fluent was used to simulate the aerodynamics. A steady-state RANS approach using the SST k-ω turbulence model gave satisfactory results, predicting aerodynamic drag to be 15% greater than experimental results with good agreement to known pressure distributions.

Subsequently, single and multi-objective aerodynamic shape optimisation was employed using a 125-point Design of Experiments (DoE) and Moving Least Squares (MLS) metamodels. Around 140 different HGV designs were evaluated based on changes to the base height, the angle of the trailing edge of the over-body contour (viewed from the side) and the radius of curvature of the longitudinal roof-side panel edges. Each design was evaluated at simulated yaw angles of 0°, 5°, 6° and 8°. Results show that a minimum-drag design can accomplish drag reduction of around 40% compared to a baseline (rectangular) vehicle, however, yaw stability is 11% poorer at a slip angle of 5° increasing to 35%, at 8°. The best stability design was found to achieve a 33% drag improvement, compared to the baseline and yaw stability is between 8% and 25% worse, for 5° and 8° of yaw, respectively. The height of the base of the vehicle is the dominant design parameter with small values leading to improved drag but large values inducing greater weathercock stability due to increased rear side area.

REFERENCES

AERONAUTICS, A. I. O. & ASTRONAUTICS 1998. *AIAA guide for the verification and validation of computational fluid dynamics simulations*, American Institute of aeronautics and astronautics.

AHMED, S. R., RAMM, G. & FALTIN, G. 1984. Some salient features of the time-averaged ground vehicle wake. *SAE Transactions*, 473-503.

AIDER, J.-L., BEAUDOIN, J.-F. & WESFREID, J. E. 2010. Drag and lift reduction of a 3D bluff-body using active vortex generators. *Experiments in fluids,* 48, 771-789.

ALLAN, J. 1981. Aerodynamic drag and pressure measurements on a simplified tractor-trailer model. *Journal of Wind Engineering and Industrial Aerodynamics,* 9, 125-136.

ANDERSON, J. 2011. Classical Thin Airfoil Theory. *Fundamentals of Aerodynamics, 5th ed., McGraw–Hill, New York*, 338-357.

ANDERSON JOHN, D. 1995. Computational fluid dynamics: the basics with applications. *Science/Engineering/Math. McGraw-Hill Science*.

ANSYS, R. 18.0 User's Guide. 2017.

BABUSKA, I. & ODEN, J. T. 2004. Verification and validation in computational engineering and science: basic concepts. *Computer methods in applied mechanics and engineering,* 193, 4057-4066.

BALKANYI, S. R., BERNAL, L. P. & KHALIGHI, B. Analysis of the near wake of bluff bodies in ground proximity. ASME 2002 International Mechanical Engineering Congress and Exposition, 2002. American Society of Mechanical Engineers Digital Collection, 705-713.

BEAUDOIN, J.-F. & AIDER, J.-L. 2008. Drag and lift reduction of a 3D bluff body using flaps. *Experiments in fluids,* 44, 491.

BUTCHER, L. 2009. Lorry sizes and weights. *House of Commons Briefing SN/BT/654*.

CASEY, M. & WINTERGERSTE, T. 2000. *Best Practices Guidelines: ERCOFTAC Special Interest Group on" Quality and Trust in Industrial CFD"*, Ercoftac.

CENGEL, Y. A., KLEIN, S. & BECKMAN, W. 1998. *Heat transfer: a practical approach*, McGraw-Hill New York.

CHOI, H., LEE, J. & PARK, H. 2014. Aerodynamics of heavy vehicles. *Annual Review of Fluid Mechanics,* 46, 441-468.

COOPER, K. R. 2004. Commercial vehicle aerodynamic drag reduction: historical perspective as a guide. *The Aerodynamics of Heavy Vehicles: Trucks, Buses, and Trains.* Springer.

DE BOER, G., GAO, L., HEWSON, R., THOMPSON, H., RASKE, N. & TOROPOV, V. 2016. A multiscale method for optimising surface topography in elastohydrodynamic lubrication (EHL) using metamodels. *Structural and Multidisciplinary Optimization,* 54, 483-497.

DFT 2019. Transport statistics Great Britain:(2018). London DfT.

ENGINEERS, A. S. O. M. 2009. *Standard for Verification and Validation in Computational Fluid Dynamics and Heat Transfer: An American National Standard*, American Society of Mechanical Engineers.

ENGLAR, R. J. 2001. Advanced aerodynamic devices to improve the performance, economics, handling and safety of heavy vehicles. SAE Technical Paper.

FORRESTER, A., SOBESTER, A. & KEANE, A. 2008. *Engineering design via surrogate modelling: a practical guide*, John Wiley & Sons.

FOX, R., PRITCHARD, P. & MCDONALD, A. 2010. Introduction to Fluid Mechanics. John Wiley & Sons Asia Pte Ltd Singapore.

GENTA, G. 1997. *Motor vehicle dynamics: modeling and simulation*, World Scientific.

GILKESON, C., TOROPOV, V., THOMPSON, H., WILSON, M., FOXLEY, N. & GASKELL, P. 2013. Multi-objective aerodynamic shape optimization of small livestock trailers. *Engineering Optimization,* 45**,** 1309-1330.

GILKESON, C., TOROPOV, V., THOMPSON, H., WILSON, M., FOXLEY, N. & GASKELL, P. 2014. Dealing with numerical noise in CFD-based design optimization. *Computers & Fluids,* 94**,** 84-97.

GILKESON, C., WILSON, M., THOMPSON, H., GASKELL, P., BARNARD, R., HACKETT, K. & STEWART, D. Ventilation of small livestock trailers. 6th MIRA International Vehicle Aerodynamics Conference: Real World Aerodynamics, 2006. MIRA.

GILKESON, C. A. 2009. *Analysis and optimization of ventilation and drag in small livestock trailers using computational fluid dynamics.* University of Leeds.

GILLESPIE, T. D. 1992. *Fundamentals of Vehicle Dynamics,* Society of Automotive Engineers.

GILLIÉRON, P. & KOURTA, A. 2010. Aerodynamic drag reduction by vertical splitter plates. *Experiments in fluids,* 48**,** 1-16.

GRIFFIN, O. M. 1995. A note on bluff body vortex formation. *Journal of Fluid mechanics,* 284**,** 217-224.

HEFNY, M. M. & OOKA, R. 2009. CFD analysis of pollutant dispersion around buildings: Effect of cell geometry. *Building and Environment,* 44**,** 1699-1706.

HIRSCH, C. 2007. *Numerical computation of internal and external flows: The fundamentals of computational fluid dynamics*, Elsevier.

HOLLAND, J. H. 1992. *Adaptation in natural and artificial systems: an introductory analysis with applications to biology, control, and artificial intelligence*, MIT press.

HOLT, J. C., GARRY, K. P. & VELIKOV, S. 2015. A wind tunnel investigation into the effects of roof curvature on the aerodynamic drag experienced by a light goods vehicle.

HUCHO, W.-H. 1986. Aerodynamics of Road Vehicles. *SAE International*.

HUCHO, W. & SOVRAN, G. 1993. Aerodynamics of road vehicles. *Annual review of fluid mechanics,* 25**,** 485-537.

HYAMS, D. G., SREENIVAS, K., PANKAJAKSHAN, R., NICHOLS, D. S., BRILEY, W. R. & WHITFIELD, D. L. 2011. Computational simulation of model and full scale Class 8 trucks with drag reduction devices. *Computers & Fluids,* 41**,** 27-40.

KHALIGHI, B., ZHANG, S., KOROMILAS, C., BALKANYI, S., BERNAL, L. P., IACCARINO, G. & MOIN, P. 2001. Experimental and computational study of unsteady wake flow behind a bluff body with a drag reduction device. *SAE transactions***,** 1209-1222.

KRAJNOVIĆ, S. & DAVIDSON, L. 2005. Flow around a simplified car, part 1: large eddy simulation.

LAPWORTH, A. & MCGREGOR, J. 2008. Seasonal variation of the prevailing wind direction in Britain. *Weather,* 63**,** 365-368.

LAUNDER, B. E. & SPALDING, D. B. 1983. The numerical computation of turbulent flows. *Numerical prediction of flow, heat transfer, turbulence and combustion.* Elsevier.

LEE, J. & CHOI, H. Large eddy simulation of flow over a three-dimensional model vehicle. Sixth international symposium on turbulence and shear flow phenomena, 2009. Begel House Inc.

LITTLEWOOD, R. & PASSMORE, M. A. 2012. Aerodynamic drag reduction of a simplified squareback vehicle using steady blowing. *Experiments in fluids,* 53**,** 519-529.

LO, K. H. & KONTIS, K. 2017. Flow around an articulated lorry model. *Experimental Thermal and Fluid Science,* 82**,** 58-74.

LOCK, A. 2007. Computational fluid dynamics development of the JCB DIESELMAX land speed record vehicle. SAE Technical Paper.

LOWETH, E., DE BOER, G. & TOROPOV, V. Practical recommendations on the use of moving least squares metamodel building. Proceedings of the Thirteenth International Conference on Civil, Structural and Environmental Engineering, Chania, Crete, Greece, 2011.

MADDOX, S., SQUIRES, K. D., WURTZLER, K. E. & FORSYTHE, J. R. 2004. Detached-eddy simulation of the ground transportation system. *The aerodynamics of heavy vehicles: trucks, buses, and trains.* Springer.

MALVIYA, V., MISHRA, R. & FIELDHOUSE, J. 2009. CFD investigation of a novel fuel-saving device for articulated tractor-trailer combinations. *Engineering Applications of Computational Fluid Mechanics,* 3**,** 587-607.

MEHTA, U. B. 1998. Credible computational fluid dynamics simulations. *AIAA journal,* 36**,** 665-667.

MENTER, F. R. 1994. Two-equation eddy-viscosity turbulence models for engineering applications. *AIAA journal,* 32**,** 1598-1605.

MORAN, M. J., SHAPIRO, H. N., MUNSON, B. R., DEWITT, D. P. & THERMODYNAMICS, F. M. 2003. Introduction to thermal systems engineering. *Thermodynamics, Fluid Mechanics, and Heat Transfer*.

NARAYANAN, A., TOROPOV, V., WOOD, A. & CAMPEAN, I. 2007. Simultaneous model building and validation with uniform designs of experiments. *Engineering Optimization,* 39**,** 497-512.

NODUM. 2018. *Why semi-trucks in US and Europe are so different?* [Online]. Available: https://nodum.org/why-semi-trucks-in-us-and-europe-are-so-different/ [Accessed 28 April 2020.

OBERKAMPF, W. L. & TRUCANO, T. G. 2002. Verification and validation in computational fluid dynamics. *Progress in aerospace sciences,* 38**,** 209-272.

ORTEGA, J. & SALARI, K. An experimental study of drag reduction devices for a trailer underbody and base. 34th AIAA Fluid Dynamics Conference and Exhibit, 2004. 2252.

ORTEGA, J., SALARI, K. & STORMS, B. 2009. Investigation of tractor base bleeding for heavy vehicle aerodynamic drag reduction. *The Aerodynamics of Heavy Vehicles II: Trucks, Buses, and Trains.* Springer.

ORTEGA, J. M., DUNN, T., MCCALLEN, R. & SALARI, K. 2004. Computational simulation of a heavy vehicle trailer wake. *The aerodynamics of heavy vehicles: trucks, buses, and trains.* Springer.

PATANKAR, S. V. 1980. Numerical heat transfer and fluid flow, Hemisphere Publ. *Corp., New York,* 58.

PATANKAR, S. V. & SPALDING, D. B. 1983. A calculation procedure for heat, mass and momentum transfer in three-dimensional parabolic flows. *Numerical prediction of flow, heat transfer, turbulence and combustion.* Elsevier.

PENISTONE, A. 2018. 2017 UK greenhouse gas emissions, provisional figures. *Department for Business, Energy & National Strategy, National Statistics, OGL*.

PENISTONE, A. 2019. 2018 UK greenhouse gas emissions, provisional figures. *Department for Business, Energy & National Strategy, National Statistics, OGL*.

PUJALS, G., DEPARDON, S. & COSSU, C. 2010. Drag reduction of a 3D bluff body using coherent streamwise streaks. *Experiments in fluids,* 49**,** 1085-1094.

QUEIPO, N. V., HAFTKA, R. T., SHYY, W., GOEL, T., VAIDYANATHAN, R. & TUCKER, P. K. 2005. Surrogate-based analysis and optimization. *Progress in aerospace sciences,* 41**,** 1-28.

RAJPUT, R. 2002. A textbook of fluid mechanics and hydraulic machines, S1 Version, S. *Chad and Company Ltd, New Delhi*.

ROACHE, P. J. 1994. Perspective: a method for uniform reporting of grid refinement studies.

ROY, C. J., PAYNE, J. & MCWHERTER-PAYNE, M. 2006a. RANS Simulations of a Simplified Tractor/Trailer Geometry. *Journal of Fluids Engineering,* 128**,** 1083-1089.

ROY, C. J., PAYNE, J. & MCWHERTER-PAYNE, M. 2006b. RANS simulations of a simplified tractor/trailer geometry.

SCHUETZ, T. C. 2015. *Aerodynamics of Road Vehicles, Fifth Edition*, SAE International.

SCIBOR-RYLSKI, A. J. 1984. *Road vehicle aerodynamics*.

SHARMA, S., BANGA, S., DUNGRIYAL, R. S., ZUNAID, M., ANSARI, N. A. & LAL, S. 2015. CFD Analysis and Optimization of Geometrical Modifications of Ahmed Body. *IOSR Journal of Mechanical and Civil Engineering (IOSR-JMCE) e-ISSN***,** 2278-1684.

SHIH, T.-H., LIOU, W. W., SHABBIR, A., YANG, Z. & ZHU, J. 1994. A new k-epsilon eddy viscosity model for high Reynolds number turbulent flows: Model development and validation.

SPALART, P. & ALLMARAS, S. A one-equation turbulence model for aerodynamic flows. 30th aerospace sciences meeting and exhibit, 1992. 439.

SPALART, P. R. 2000. Strategies for turbulence modelling and simulations. *International Journal of Heat and Fluid Flow,* 21**,** 252-263.

STORMS, B., SATRAN, D., HEINECK, J. & WALKER, S. A study of reynolds number effects and drag-reduction concepts on a generic tractor-trailer. 34th AIAA Fluid Dynamics Conference and Exhibit, 2004. 2251.

STORMS, B. L., ROSS, J. C., HEINECK, J. T., WALKER, S. M., DRIVER, D. M., ZILLIAC, G. G. & BENCZE, D. P. 2001. An experimental study of the ground transportation system (GTS) model in the NASA Ames 7-by 10-ft wind tunnel.

THACKER, A., AUBRUN, S., LEROY, A. & DEVINANT, P. Unsteady analyses of the flow separation on the rear window of a simplified ground vehicle model. 28th AIAA Applied Aerodynamics Conference, 2010. 4569.

THÉVENIN, D. & JANIGA, G. 2008. *Optimization and computational fluid dynamics*, Springer Science & Business Media.

TOROPOV, V. V., SCHRAMM, U., SAHAI, A., JONES, R. D. & ZEGUER, T. 2005. Design optimization and stochastic analysis based on the moving least squares method. *6th World Congresses of Structural and Multidisciplinary Optimization*.

TSUBOKURA, M., KOBAYASHI, T., NAKASHIMA, T., NOUZAWA, T., NAKAMURA, T., ZHANG, H., ONISHI, K. & OSHIMA, N. 2009. Computational visualization of unsteady flow around vehicles using high performance computing. *Computers & Fluids,* 38**,** 981-990.

TU, J., YEOH, G.-H. & LIU, C. 2013. Chapter 2 - CFD Solution Procedure—A Beginning. *Computational Fluid Dynamics (Second Edition).* Butterworth-Heinemann.

TU, J., YEOH, G. H. & LIU, C. 2018. *Computational fluid dynamics: a practical approach*, Butterworth-Heinemann.

VELDHUIS, C., GORNICZ, T. & SCHOLCZ, T. 2016. Ship optimization using viscous flow computations in combination with generic shape variations and design of experiments [C]. *Proceedings of PRADS 2016*.

VERSTEEG, H. K. & MALALASEKERA, W. 2007. *An introduction to computational fluid dynamics: the finite volume method*, Pearson education.

VIANA, F. A. & HAFTKA, R. T. Using multiple surrogates for metamodeling. Proceedings of the 7th ASMO-UK/ISSMO International conference on engineering design optimization, 2008. 1-18.

VINCHURKAR, S. & LONGEST, P. W. 2008. Evaluation of hexahedral, prismatic and hybrid mesh styles for simulating respiratory aerosol dynamics. *Computers & Fluids,* 37**,** 317-331.

WILCOX, D. C. 1998. *Turbulence modeling for CFD*, DCW industries La Canada, CA.

WONG, D.-M. & MAIR, W. 1983. Boat-tailed afterbodies of square section as drag-reduction devices. *Journal of wind engineering and industrial aerodynamics,* 12**,** 229-235.

WOOD, R. M. A discussion of a heavy truck advanced aerodynamic trailer system. Int. Symp. Heavy Veh. Weights Dimens., 9th, University Park, PA, 2006.

YI, W., SAGONG, W. & CHOI, H.-C. Drag reduction of a three-dimensional car model using passive control device. Proceedings of the KSME Conference, 2007. The Korean Society of Mechanical Engineers, 2868-2872.